Sheffield Hallam University

A Sheffield Hallam University thesis

ProQuest Number: 10701204
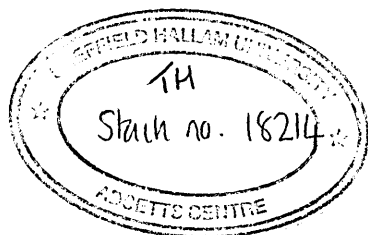
ProQuest 10701204

A Computer Simulation Study of Tilted Smectic Mesophases

IAN MICHAEL WITHERS, BSc (Hons.), Grad. Inst. Phys.

A thesis submitted in partial fulfilment of the requirements

of Sheffield Hallam University for the degree of

Doctor of Philosophy

18 May, 2000

Abstract

Results are presented from a series of simulations undertaken to determine the effect of a novel form of molecular biaxiality upon the phase behaviour of the well established Gay-Berne (GB) liquid crystal model.

Firstly, the simulation of a bulk system interacting via the Internally-Rotated Gay-Berne (IRGB) potential, which offers a single-site representation of a molecule rigidly constrained into a *zig-zag* conformation, is presented. The results of simulations performed for systems of IRGB particles with an aspect ratio of 3:1 confirm that the introduction of biaxiality into the model results in the destabilisation of the orientationally ordered phases. For particles with a sufficiently pronounced *zig-zag* conformation, this results in the complete destabilisation of the smectic A phase and the smectic B phase being replaced by the tilted smectic J phase. Following these observations, the effect upon the phase behaviour of increasing molecular elongation is also considered, with an increase in the aspect ratio from 3:1 to 4:1 resulting in the nematic and smectic J phases being replaced by smectic A and smectic G phases respectively.

Secondly, a version of the IRGB potential modified to include a degree of molecular flexibility is considered. Results obtained from bulk systems interacting via the flexible IRGB for 3:1 and 4:1 molecules show that the introduction of flexibility results in the destabilisation of the smectic A phase and the stabilisation of the nematic and tilted hexatic phases.

Finally, the effect upon the phase behaviour of the rigid IRGB model of the inclusion of a longitudinal linear quadrupole is examined. These results show that increasing quadrupole moment results in the destabilisation of the tilted hexatic phase, although the biaxial order parameter is increased with increasing quadrupole moment. There is no clear correlation between quadrupole magnitude and the other observed phase transitions, with the nematic and smectic A phases being variously stabilised and destabilised with increasing quadrupole magnitude. For the 4:1 molecules with large quadrupole moments, buckled smectic layers are observed where some molecules are tilted with respect to a local layer normal. Of all the systems considered here, this buckled structure is the one which most closely resembles the elusive smectic C phase.

The great tragedy of Science - the slaying of a beautiful hypothesis by an ugly fact

Thomas Henry Huxley

Acknowledgements

Advanced Studies

As part of the course of study a number of postgraduate courses within the MRI at Sheffield Hallam University were attended. These included the topics Simulation and Phase Diagrams, and Polymers and Liquid Crystals.

A number of relevant external courses and conferences were participated in. These were, along with any work presented at them, in chronological order;

- CCP5 Annual Meeting, University of Bristol (September 1996)

- BLCS Winter Workshop, University of Hull (December 1996)

- CCP5 Spring School, University of Bristol (March 1997) - Poster presentation, *Computer Simulation of Smectic C Liquid Crystals*

- BLCS Annual Meeting, University of Southampton (April 1997)

- Structured Fluids Conference, University of Durham (September 1997)

- Modelling of liquid crystals at interfaces - one day workshop, Sheffield Hallam University (November 1997)

- BLCS Annual Meeting, University of Leeds (April 1998) - Poster presentation, *Computer Simulation of Tilted Liquid Crystal Phases*

- NATO ASI Advanced in the computer simulation of liquid crystals, Erice, Italy (June 1998) - Poster presentation, *Computer Simulation of Tilted Liquid Crystal*

Phases

- BLCS Annual Meeting, University of Durham (March 1999) – Poster presentation,

A Computer Simulation Study of a Biaxial Variant of the Gay-Berne Model

Contents

Chapter 1

Introduction

Liquid crystalline phenomena are observed in a wide range of areas in the physical and biological sciences. Ranging from such obvious technological applications as the twisted nematic and ferroelectric display devices, and the wide-spread use of surfactants in the cleaning industry, through to the importance of self-assembly in a large number of biological processes, mesogenic behaviour is clearly a worthy topic of investigation.

However, despite having been under investigation since their discovery more than 100 years ago [1–3], there is still much which is not known about the underlying physics [4, 5] of many liquid crystalline effects. In the last three decades there has been considerable experimental characterisation of liquid crystals. This has been relatively successful in determining the underlying structures of the various liquid crystalline phases, and in locating the transitions and phase diagrams which char-

acterise such systems [6]. It is by systematic investigation of these that the viability of new liquid crystals for various applications is tested, and also, occasionally, novel behaviour is uncovered opening up the possibility of new applications.

That said, it is important to realise that for the complicated statistical mechanics of phase transitions experimental techniques can sometimes be of limited success in providing understanding of the origins of various phenomena. Also, the assumptions needed for the theoretical treatments of these effects can mean that they are too far removed from the real situation to provide useful information. It is here that computer simulation [7, 8] can come into its own - essentially lying in between the realms of theory and experiment, simulation can be of great use in gaining insight into phenomena which are difficult to access using other techniques.

1.1 Aims

To date, the major application of thermotropic liquid crystals has been in the liquid crystal display (LCD), which takes advantage of the anisotropic optical and electrical properties of these molecules in low powered switching devices, initially in the twisted nematic display, and more recently in ferroelectric devices which offer faster switching times, larger field of view and higher complexity displays than were previously available. These ferroelectric displays are manufactured from materials in which the molecules form a layered structure with the molecular long axes being tilted with respect to the layer normal, known as the smectic C phase. Whilst there

2

are a large number of considerations to be taken into account, which effect the operational performance of such devices, the more fundamental mechanism of molecular tilting within these phases is not fully understood. A wide variety of diverse theories having been proposed to explain this phenomenon.

The work described in this thesis relates to computer simulations performed with the aim of promoting greater understanding of the mechanisms responsible for this tilting process, mainly from a theoretical perspective, since no single theoretical model has completely described the tilting process satisfactorily. Specifically, attention has been focussed on the bulk phase behaviour of the much studied liquid crystal model, the Gay-Berne [9], which has been modified in a novel manner so as to offer a single-site approximation of a molecule rigidly constrained in a *zig-zag* conformation. This modification, known as the Internally-Rotated Gay-Berne potential, thereby offers a method of comparing theoretical models which assume that tilted smectic phases are formed purely due to steric effects (the shape of the molecules), in particular those which assume that the molecular tilt within each layer originates from the packing requirement of *zig-zag* shaped molecules. Following this, two perturbations of the Internally-Rotated Gay-Berne model have been considered.

Firstly, the model was modified such as to introduce a degree of molecular flexibility. This modification has been incorporated since experimental studies into the formation of liquid crystalline phases have concluded that molecular flexibility is important factor to consider, since it both promotes reasonably low melting points and is thought to stabilise the molecular alignment within the liquid crystalline

3

structures.

Secondly, the effect of electrostatic interactions upon the observed phase behaviour has been examined, with a longitudinal linear quadrupole being attached to each particle. The motivation for this work has been provided by theoretical models which seek to explain the formation of tilted smectic phases in term of intermolecular electrostatic interactions. Initially, these theories considered the effect of dipole-dipole interactions upon the phase behaviour. However, more recently, serious doubt has been cast upon the validity of this approach and attention has been focussed upon quadrupole-quadrupole interactions.

1.2   Summary of Thesis

Aside from this introduction, this thesis is organised as follows.

In Chapter 2, an introduction to liquid crystals in given, concentrating on the types of molecules which exhibit such phases and details of the structures involved. The next two chapters consider previous attempts to model liquid crystalline behaviour, using theoretical techniques in Chapter 3 and simulation techniques in Chapter 4, together with a brief description of the simulation methods used both in previous studies and later in this body of work. Attention is focussed on work which is relevant to the results presented here, although some effort has been made to give a wider consideration of experimental liquid crystals.

Within Chapter 5 the model being used here is described, followed by the results of a series of simulations of bulk liquid crystalline materials performed in order to determine the effect of introducing a *zig-zag* type interaction upon the phase diagram. Based upon these results, simulations which introduce a degree a molecular flexibility into the model are described in Chapter 6 and the effect upon the phase behaviour of the inclusion of a quadrupole moment upon each molecule is considered in Chapter 7.

Finally the implications of this work are considered in Chapter 8, from theoretical, experimental and simulation angles. The success of the program of work is assessed and suggestions are presented for future investigations.

Chapter 2

Experimental Liquid Crystalline

Behaviour

In this chapter, a brief introduction is given to the physical properties of liquid crystals. Firstly the bulk phase behaviour is described, including details of the microscopic structure of the liquid crystalline phases of interest here. This is followed by a brief review of the molecular structure of compounds which exhibit tilted smectic phases. Finally a discussion of the physical and technological importance of these tilted phases is given.

2.1 Liquid Crystals

The term liquid crystals, or *mesogens*, refers to materials which exhibit intermediate phases between the isotropic liquid and crystalline solid states. Mesogenic materials have been reported and investigated since their discovery in the late 19th Century [1–3]. The unique properties of such materials have been exploited in many devices, notably in liquid crystal displays (LCDs), as well as having applications in data storage. However, many of the properties and underlying physics are not fully understood, and there remains scope for improvement of their utilisation.

Mesogenic phases may be classified into two distinct categories [5]; disordered crystal mesophases and ordered fluid mesophases. The former have their constituent molecules arranged upon a lattice with orientational freedom, and are termed plastic crystals. In the latter, the constituent molecules have long ranged orientational order and may have some, but not complete, long ranged translational order. These are termed liquid crystals (LCs). Further to this classification, there are generally two further categories; thermotropic and lyotropic. Thermotropic LCs form different mesophases with varying temperature, whereas lyotropic LCs do so by changes in concentration as well.

Thermotropic mesophases have been found to be produced by two distinct types of molecular shape, rod-like - called *calamitic liquid crystals* - which were the first to be discovered, and disk-like - called *discotic liquid crystals* - which have been discovered relatively recently [10].

7

Since this work is primarily concerned with thermotropic calamitics, a brief description of only these phases will be given. The familiar phases of liquid and solid are represented below (Figure 2.1). As can be seen, in the isotropic liquid the molecules are completely disordered, whereas in the crystalline solid their long axes are all parallel and they are confined to a regular lattice structure.

Isotropic Liquid   Crystalline Solid

Nematic   Smectic A   Smectic C
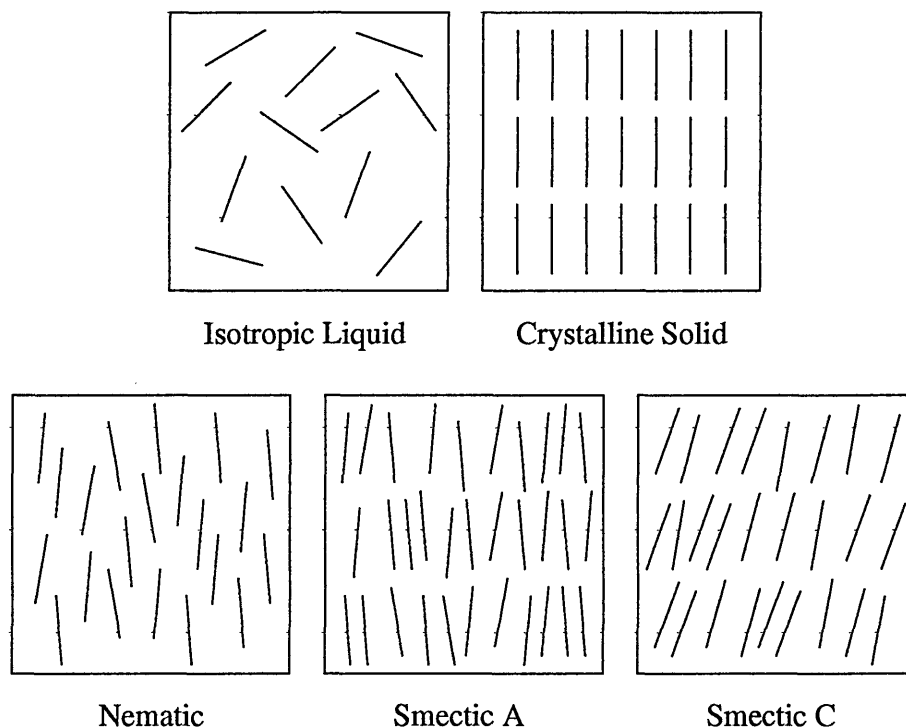
Figure 2.1: Schematics of various phases

The intermediate mesogenic phases are characterised by varying degrees of orientational and positional order, being split into two main types. The first, nematic, occurs where there is orientational order such that the long axes of the molecules are aligned in a preferred direction but there is no long range translational order. The second, smectic, occurs where the molecules are arranged in regularly spaced layers, such that there is a density wave running through the material. Brief schematics of these phases are also given in Figure 2.1.

8

Various classes of smectic phase exist; their classification is dependent upon the degree of ordering within the layers and the presence of any tilt with respect to the layer normal. Figure 2.2 shows idealised plan views of the molecular organisation within the different smectic mesophases, where triangles indicate a molecular tilt within the layer towards the apex of the triangle.
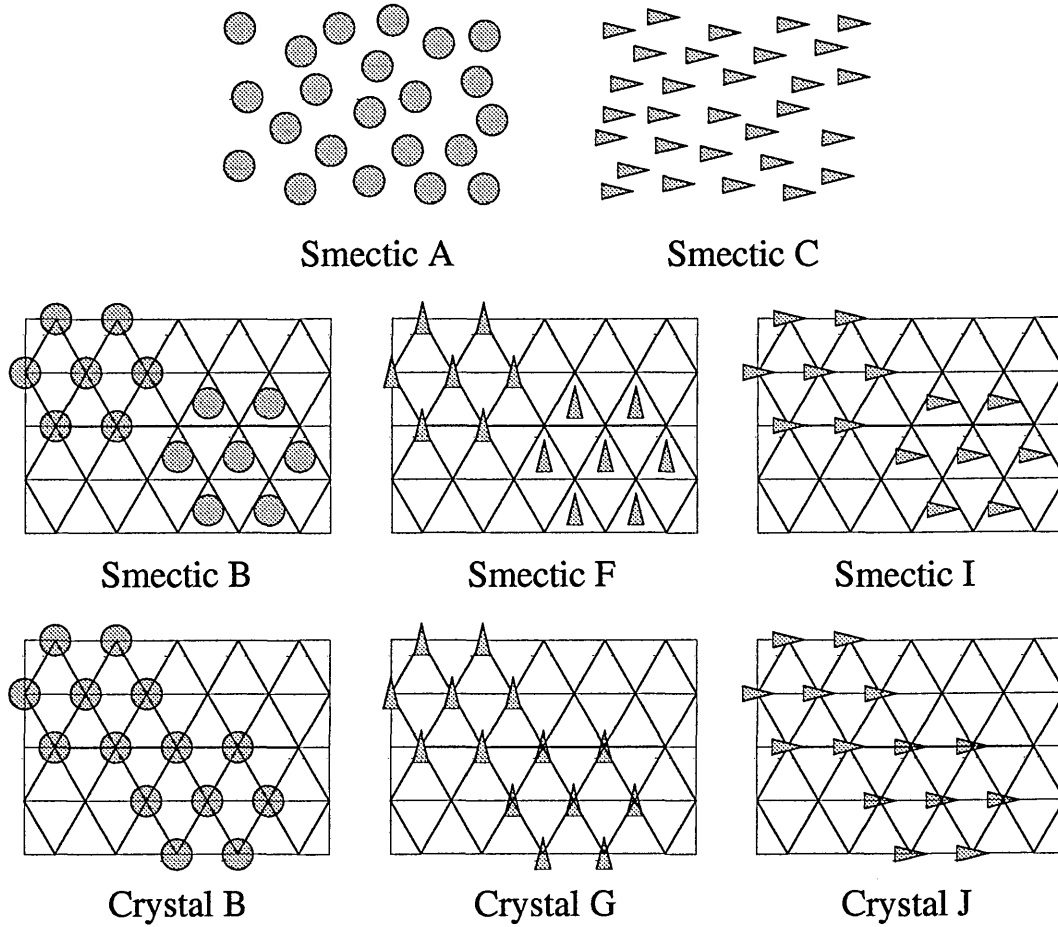
Figure 2.2: Plan views of smectic mesophase structures [11]

The simplest smectic phase, where each layer is a two dimensional liquid with no correlations between the layers and no tilt is known as the smectic A (S_A) phase. The tilted analogue of this is the smectic C (S_C) phase, with the director being tilted with respect to the smectic layer normal in an overall averaged direction over

9

all layers.

The smectic B (S_B) phase is more ordered than the S_A phase with the constituent molecules adopting hexagonal ordering within the layer, with repeat positional order of $\sim 150 - 600$ Å, and bond-order over macroscopic distances [4]. There are, however no inter-layer correlations, and hence the phase possesses liquid properties. The hexagonal nature of the S_B phase generates two tilted analogues called the smectic F (S_F) and smectic I (S_I) where the molecules are tilted towards the side and apex of the hexagonal lattice respectively (direction of tilt is depicted by the *triangular* molecules in Fig. 2.2). The tilting process causes the hexagonal lattice to become distorted in the direction of tilt. The structure of this pseudo-hexagonal close packed unit cell for the S_F phase has been determined by Doucet *et al* [12]. These tilted phases also have no interlayer correlations, short-range in-layer correlations, and long-range bond orientational order, with a correlated direction of tilt. The plastic crystal mesophases B, G and J, shown in Figure 2.2, are highly correlated analogues of the S_B, S_F and S_I phases respectively, with the repeat positional order being predictable over a long range in three dimensions [11].

It has been shown, via NMR techniques [13, 14], that thermal rotation of the molecules is unhindered for all of the mesophases mentioned above. However, later studies [15] have concluded that the molecular long axis is not, on average, a rotation axis for the entire molecule in the S_C phase, with rotational motion being observed for different parts of the molecule which do not share a common axis of rotation. Such observations support the view that the molecules within the tilted layer do

10

not adopt linear conformations. Two such conformations confined within a smectic layer are shown in Figure 2.3.
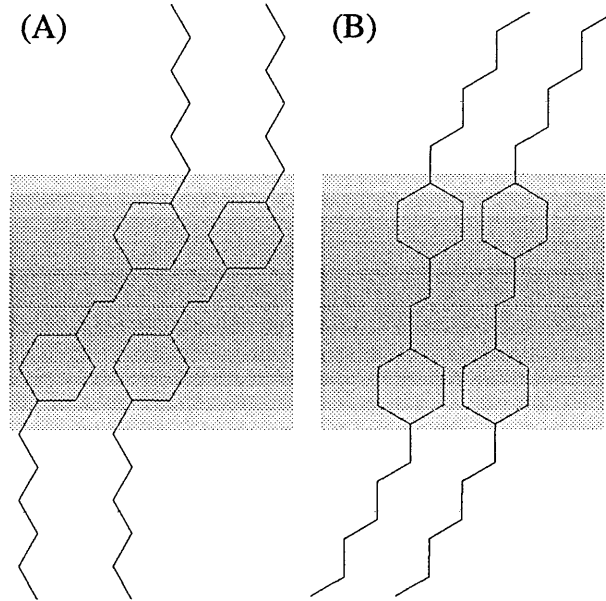
Figure 2.3: Two possible conformations in a S_C layer, (A) tail director is tilted less than the core, or (B) the tails tilt more than the core. (Experimental evidence to distinguish between these two cases is surprisingly meager, see for example [16,17].)

A large number of different molecules have been shown to display various calamitic LC phases. All of these share a geometrical anisotropy in shape. Figure 2.4 shows a general template that can be used to describe the structure of calamitic liquid crystals.
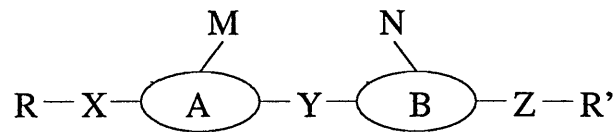
Figure 2.4: General structural template for calamitic liquid crystals

The constituent units within this general structure and their combinations determine the type of LC phase (if any) and the physical properties exhibited by a

compound [6]. A certain rigidity is required to provide the anisotropic molecular structure, which is achieved by linearly linked ring systems (A and B), which may be connected directly, or joined by a linking group (Y) which maintains the linearity of the central core. This core is not usually sufficient to generate a LC phase and a certain degree of flexibility is often present, to ensure low melting points and to help stabilise the molecular alignment within the mesophase structure. This flexibility is provided by terminal substituents (R and R'), which are usually alkyl or alkoxy chains; however, one terminal unit may be a small polar substituent. These terminal units may be joined directly to the central core or linked via groups X and Z. The lateral substituents (M and N), whilst generally detrimental to the formation of LC phases, are used to modify the mesophase morphology and the physical properties of LCs to generate enhanced properties for applications.

Since the smectic phases form a lamellar structure, the molecular structure must allow lateral intermolecular attractions. It has therefore been concluded that, in general, the smectic phases are favoured by a symmetrical molecular structure; i.e. molecules with a wholly aromatic core with two terminal alkyl/alkoxy chains compatible with the core tend to pack well into a smectic phase. Any breaking of the symmetry, such as the inclusion of lateral substituents or broadening of the core, or extension of the core to make it long relative to the overall molecular length tends to destabilise smectic formation and favour the nematic phase.

The general molecular template shown above may be used to generate all types of smectic mesophases, although the S_A phase is the most common smectic phase

exhibited (most probably due to it being the most disordered). When special structural requirements are satisfied, the tilted smectic phases may be observed, with the S_C being the most common, again probably because of the relatively high degree of disorder.

Whilst the vast majority of the literature concerned with the tilted smectic phases focusses upon the S_C phase, the more ordered hexatic phases should not be overlooked. These phases are always observed at temperatures lower than the S_A, S_B and S_C phases; with the less ordered S_F and S_I phases being observed above the plastic crystal mesophases upon cooling. Due to the fact that these more ordered phases are not of practical use, little interest seems to have been taken in them. In fact, in many studies these phases are not classified and simply listed as S_X. It should, however, be noted that the molecular structure responsible for the formation of these phases fits the same general structure that describes molecules which exhibit the S_C phase. It is on these structural requirements that attention will now be focussed.

2.2 Molecular Structural Factors Influencing the Smectic C Phase

Numerous studies have been undertaken concerning the effects of small changes in molecular structure upon the temperature range of stability of the S_C phase. These effects may be demonstrated by examining the phase sequences exhibited by

certain homologous series. From these investigations it is apparent that no one single structural factor is responsible for the formation of the S_C phase.

Compounds which exhibit the S_C phase must have a molecular structure favourable for smectic phase formation, i.e. approximately symmetrical and with two terminal alkyl or alkoxy chains. The effect of varying the chain length for various compounds has been investigated (for example, 4-n-alkoxyphenyl 4'n-octyloxy-biphenyl-4-carboxylates shown in Figure 2.5). These studies have shown that the observed mesophases are strongly dependent upon terminal chain length, with longer chains stabilising the smectic phases and the S_C phase being injected at certain terminal chain lengths. In general, the S_C phase is observed for molecules with chain lengths between approximately 4 and 15 carbon atoms, being often seen in molecules with chain lengths which are approximately equal (the phase sequence for a general structure is shown in Figure 2.6).

Modifications may be made to the terminal chains, such as the introduction of a double bond or chain branching. The former modification reduces the flexibility of the alkyl chain. If the double bond is positioned such that molecule remains in an approximately linear conformation, then the transition temperatures may be reduced and the S_C range increased. Branching of the alkyl chain, along with introducing chirality into the molecule, causes a disruption in the molecular packing which may also reduce transition temperatures and increase the S_C range.

The other key molecular feature which leads to the formation of the S_C phase is the inclusion of polar groups into the molecular structure. Goodby, Gray and Mc-

14
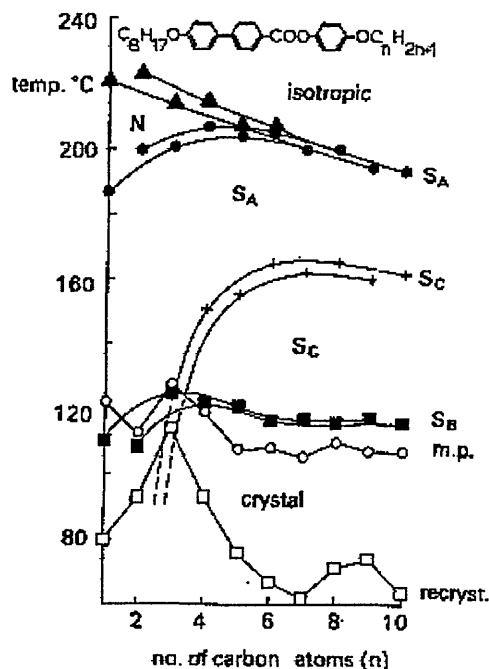
Figure 2.5: Plot of the transition temperatures against number of carbon atoms (n) in the alkyl chain of the 4-n-alkoxyphenyl 4'n-octyloxy-biphenyl-4-carboxylates. Redrawn from [18].

Donnell [20] studied a series of materials with a range terminal dipoles (shown in Figure 2.7). All of these compounds exhibited S_C or chiral S_C phases, with the stability of the phase being enhanced by terminal outboard dipole moments; that said, this feature is by no means a necessity.

The inclusion of alkoxy chains and carboxylate linking groups is not the only method of inducing a dipole moment into the molecular structure. The structures of some other common compounds which exhibit the S_C phase are shown in Figure 2.8.

The use of nitrogen substitution in the phenyl ring (as in compounds I and II of Figure 2.8) also results in the observation of the S_C phase. Here the formation of the tilted phase is believed to be due to the combination of the lateral dipole
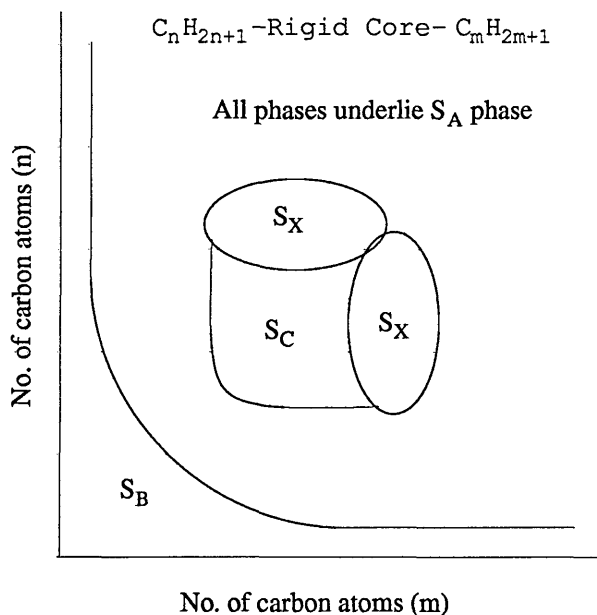
Figure 2.6: Expected mesophases for an ideal n-alkyl-Rigid core-alkyl-n system. S_X refers to tilted hexatic phases. Redrawn from [19].

moment from the ether oxygen and the hetrocyclic nitrogens. Once again, the phase characteristics may be altered by varying the length of the terminal chain, and extending the chain may enhance the S_C phase stability (e.g. compound **II**) .

Cores that are bent may also generate smectic mesophases, provided that the overall molecular shape is still approximately linear. When combined with suitable polar groups and long terminal chains (as in compound **III**) the S_C phase may be observed. The bent structure is also thought to enhance molecular tilting. The inclusion of a polar ester linkage (compound **IV**) is believed to aid lamellar packing, and, when in conjunction with sufficiently long alkoxy chains, the S_C phase is observed. Finally, the structure may be modified by lateral substituents. In particular, lateral fluoro substitution has been widely used to generate materials that exhibit the S_C phase (compounds **V** and **VI**). Whilst the inclusion of lateral substituents destabilises the

16

$C_8H_{17}O$—⬡—⬡—$CO.O$—⬡—OC_8H_{17}

Crystal 110 S_B 116 S_C 165 S_A 200 I

$C_8H_{17}O$—⬡—⬡—$CO.O$—⬡—C_8H_{17}

Crystal 110 S_B 110.5 S_C 132.5 S_A 184 I

$C_2H_5\overset{*}{C}H(CH_3)(CH_2)_3$—⬡—⬡—$CO.O$—⬡—$C_7H_{15}$

Crystal 91.5 S_C^* 93 S_A^* 112 N^* 131 I
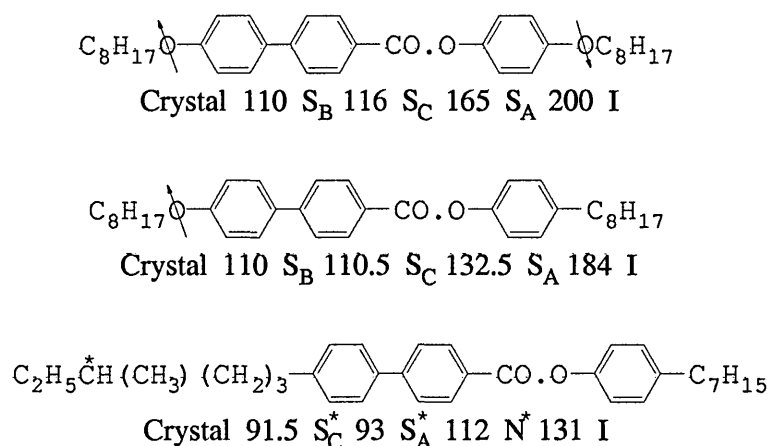
Figure 2.7: Phase sequences observed with progressive elimination of terminal outboard dipole moments. * indicates chiral carbon atom [20].

smectic phases, the use of fluorine provides a strong lateral dipole moment which is thought to aid the tilting process.

The conclusion that the S_C phase is favoured by linear molecules, with relatively long terminal chains with polar groups, preferably providing a terminal outboard dipole moment, is only general and may not necessarily be correct for all species which exhibit the S_C phase.

Having now described the types of molecules which exhibit the S_C phase, attention will now be focussed upon the properties and technological importance of the S_C phase.

2.3   Properties of the Smectic C Phase

From early characterisation of the S_C phase by means of X-ray diffraction patterns, it has been shown that the tilt angle varies with temperature for all S_C phases

C_8H_{17}—[pyrimidine]—[benzene]—$OC_{10}H_{21}$ **I**

Crystal 32.0 S_C 59.5 S_A 65.5 N 69.5 I

$C_{10}H_{21}$—[pyrimidine]—[benzene]—$OC_{10}H_{21}$ **II**

Crystal 36.0 S_C 73.0 S_A 77.0 I

C_5H_{11}—[benzene]—[thiadiazole]—[benzene]—OC_8H_{17} **III**

Crystal 80.0 S_C 167.0 N 182.0 I

C_8H_{17}—[benzene]—C(=O)O—[benzene]—$OC_{10}H_{21}$ **IV**

Crystal 63.0 S_C 74.0 N 91.0 I

C_5H_{11}—[benzene]—[difluorobenzene]—[benzene]—OC_8H_{17} **V**

Crystal 48.5 S_C 95.0 N 141.5 I

C_5H_{11}—[difluorobenzene]—[benzene]—[benzene]—OC_8H_{17} **VI**

Crystal 89.0 S_C 155.5 S_A 165.0 N 166.0 I

Figure 2.8: Example compounds which exhibit the smectic C phase [6].

observed below the S_A phase, as shown in Figure 2.9.

It has since been confirmed that the $S_A - S_C$ transition is continuous [4] with the tilt angle θ decreasing continuously to zero, with the temperature dependence being will represented by

$$\theta = A \left(T_{S_A S_C} - T \right)^\gamma \tag{2.1}$$
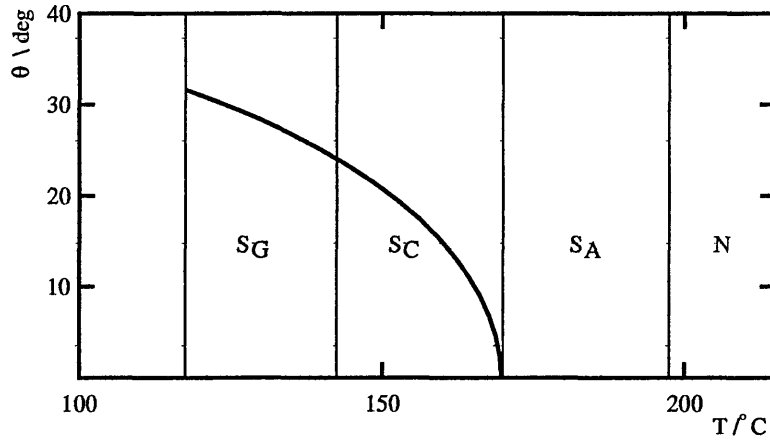
Figure 2.9: Temperature dependence of the tilt angle as a function of temperature for Terephthal-Bis-Butylaniline (TBBA) [12]

where $T_{S_A S_C}$ is the temperature of the $S_A - S_C$ transition, A is a material dependent constant and $\gamma \simeq 0.35$.

The temperature dependence of the tilt angle is different when the S_C phase is observed below the nematic or isotropic phases, where first order phase transitions are observed. With reducing temperature, a large tilt angle $(25^0 \lesssim \theta \lesssim 45^0)$ is observed at the transition, which increases only slightly with decreasing temperature.

An interesting modification of the S_C phase is the chiral (S_C^*) phase, in which a slight and gradual change in the direction of the molecular tilt is observed from layer to layer, gradually describing a helix. Due to the chirality of the constituent molecules, the space symmetry is reduced from a centre of inversion, a mirror plane orthogonal to the layers and a two-fold axis of rotation (for achiral molecules), to only the two-fold axis of rotation. This reduction of symmetry leads to a ferroelectric ordering within the layers [21], with a net polarisation perpendicular to the direction of tilt within each layer. Due to the helical structure of the chiral phase, over the

19

bulk the net polarisation reduces to zero, and hence the S_C^* phase is truly defined as helielectric.

The invention of fast optical switching devices [22] makes use of these ferroelectric S_C^* materials. To construct such a device, the ferroelectric material is constrained between properly prepared pieces of glass separated by only several micrometres, such that the director is parallel to the glass surfaces and uniform throughout the liquid crystal. When this arrangement is achieved, the smectic planes are perpendicular to the glass surfaces and the spontaneous polarisation is along the normal to the glass surfaces for the whole device (as illustrated in Figure 2.10). To achieve this texture an electric field must be applied to orient the spontaneous polarisation, with a reversal of the direction of the applied electric field inverting the direction of polarisation, with the director maintaining the same tilt angle but rotating around the cone centred on the normal to the smectic planes by 180^0.
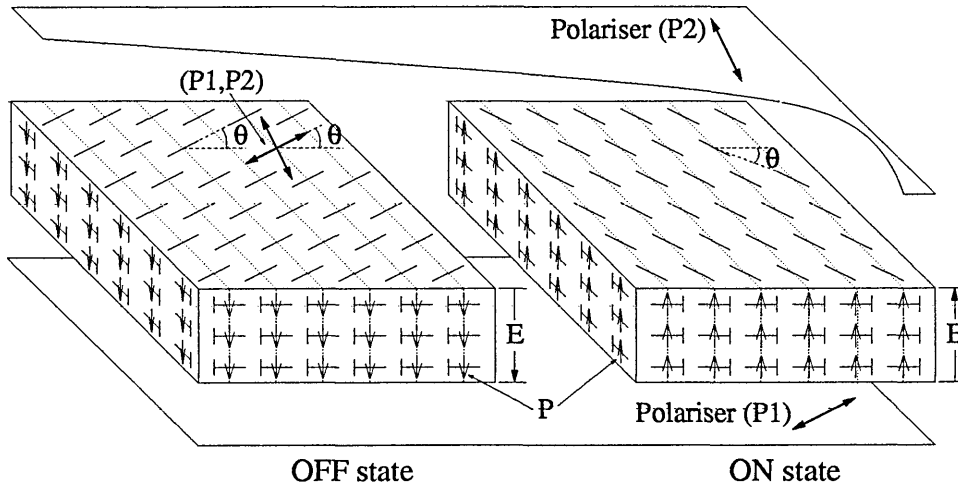
Figure 2.10: Schematic representation of a ferroelectric LCD; dotted lines indicate the smectic layers and ⊣ indicates a molecule whose right end projects outwards

To complete the device, cross polarisers are added to the outside of the two pieces of glass, such that the bottom polariser (P1) is aligned parallel to the director when the cell is in the *OFF* state of Figure 2.10 and the top polariser (P2) is perpendicular to the bottom polariser. Thus light entering the bottom of the device in the *OFF* state is polarised parallel to the director, thus suffering no change in its polarisation state and is extinguished by the top polariser so the cell appears dark. If the ideal case of $\theta = 22.5^0$ is achieved then light entering the bottom of the device in the *ON* state is polarised at an angle of 45^0 to the director. If the cell thickness and optical anisotropy of the liquid crystal are just right then the light undergoes a phase retardation such that it passes through the top polariser and the cell appears bright.

Before the invention of such devices, the smectic phases were regarded as a curiosity and any research performed was fundamental. However, since the realisation that the S_C phase is of technological importance, much research has been undertaken with the aim of understanding and enlarging the phase envelope of the S_C phase, in both bulk and in a confined geometry. The goal here is to discover materials which offer a wide temperature range of S_C stability, strong surface anchoring (to keep the smectic layers in an untwisted state), a low viscosity and large dielectric biaxiality (to reduce switching time). To further complicate the issue, very few materials are known to exhibit the S_C^* phase and those that do are not suitable for commercial applications. Therefore devices are manufactured from a ferroelectric mixture consisting of an achiral host (possibly even a mixture itself, displaying the S_C phase with the desired physical properties) and a small quantity ($\approx 10\%$) of a highly polar chiral material. Further details of these material properties will not

be given here as this work is concerned with investigating the nature of the tilting

process.

Chapter 3

Theoretical Models of Liquid

Crystals

This chapter provides an overview of the theoretical treatments which have been

proposed to explain the formation of the calamitic mesophases.

The statistical mechanics of liquid crystals is complex [4], with no exact solution

having been worked out for even the simplest physical models considered.

A number of different analytical techniques are available to the theorist, which may

be broadly classified into two fields. Phenomenological theories attempt to model an

observed behaviour empirically, but do not consider *a priori* molecular interactions.

Molecular theories, on the other hand, start from a consideration of inter-particle

effects and predict the macroscopic behaviour in some way from these. Due to the

complexity of these problems, approximations and assumptions have to be made in

molecular theories to make them analytically tractable. One of the most widely used approximations in the theoretical treatment of mesogenic systems is that employed in a mean-field calculation. For these calculations the molecular interactions are not considered individually but approximated to give an average local effect - i.e. a mean field. This approach greatly simplifies the solution of these theories, but results in an incorrect treatment of local correlations, which leads to erroneous predictions, especially in the vicinity of phase transitions where the correlation length scale can be of primary importance.

Before considering the theoretical treatments which have been proposed to explain the mechanism of molecular tilting as the S_C phase is formed, a brief review of the molecular theories of the nematic and smectic A phases, which underlie most of the more complicated theories of the S_C phase, will be given.

3.1   Nematic and Smectic A Phases

The vast majority of mesogenic materials are rod-like in shape. In the 1940's, Onsager [23] showed that a system of hard rods will show orientational order above a certain concentration. This model used a simple form of density functional theory, with a mean field type approximation, and made the following assumptions; the only forces of importance corresponded to steric repulsion (the rods could not interpenetrate each other), the volume fraction was much less than one (sparse system) and the rods were very long.

Within these limits, it was shown that such a system undergoes a first order phase transition from the isotropic to nematic phase. This provided the first evidence that attractive forces are not necessary for a system to display spontaneous alignment. However, the predictions of Onsager's theory differ from actual observations of thermotropic systems; the transition density is too low, the jump in density is too large and the nematic order parameter at the transition is too large. Like all models involving only infinitely repulsive forces (so called hard particle models), the system is independent of temperature.

Maier and Saupe [24] developed a theory which takes into account the attractive intermolecular interaction. This was done using a system of classical spin vectors, and by solving this within a mean field approximation, a first order isotropic to nematic phase transition is predicted at a temperature dependent upon the intermolecular potential. In particular, the nematic order parameter at the ordering transition is less than that predicted by Onsager and closer to experimentally observed values.

Later simulation results obtained using this spin system [25,26] showed the isotropic to nematic transition to be weakly (as observed experimentally), rather than strongly first order, indicating that mean field theory is not a very good guide for such characterisation.

McMillan [27] proposed a description of the smectic A phase by extending Maier-Saupe theory to include an additional order-parameter to describe a one-dimensional translational periodicity of a layered structure. Using this model, the isotropic and nematic to smectic A phase transitions were observed, with broad agreement with

experimental data, however the smectic A to nematic transition entropy was too great. To improve agreement, McMillan used, in a later study [28] a modified pair potential. Whilst a number of other refinements and extensions have been proposed, McMillan's model remains the simplest which brings out all the qualitative features of the nematic and isotropic to smectic A transitions.

3.2   Smectic C phase

Over the last 30 years a number of theoretical studies have been undertaken to attempt to describe the smectic C phase, with no one model completely describing the phase satisfactorily.   These models fall into two categories; those which rely upon electrostatic interactions between the constituent molecules to induce a tilted phase, and those which consider purely steric interactions. It is to the former which attention will be focussed initially.

3.2.1   Electrostatic Interaction Models

The first readily accepted theory of this type was proposed by McMillan [29]. The model used relied on the evidence, at the time, that materials which exhibit the S_C phase were approximately symmetrical in shape, with dipole moments associated with the ends of the central core.

The model assumes that the smectic A order is well established with the molecules

being parallel to each other within a single smectic layer. Each molecule is represented as a cylindrical rod with three dipoles moments rigidly attached to the central axis; one dipole of magnitude μ_1 at the centre and two anti-parallel dipoles, each of magnitude μ_2, at a distance $d/2$ above and below the centre (as shown in Figure 3.1(a)).

(a) (b) (c) (d)
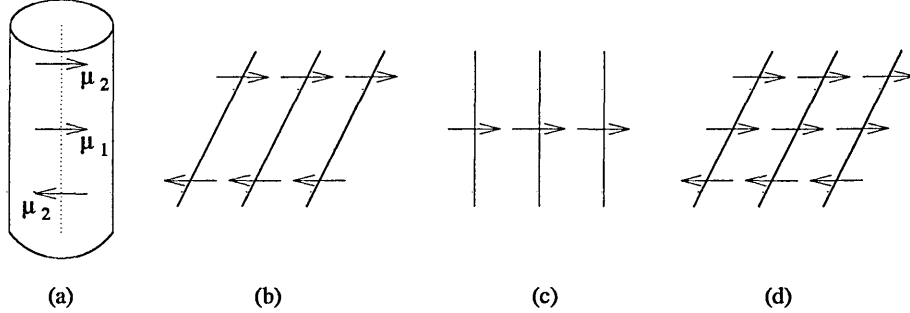
Figure 3.1: (a) Molecular model proposed by McMillan [29] with three electric dipoles attached to the central axis, (b) molecular order in the C phase with outboard dipoles aligned, (c) molecular order in the C_1 phase with central dipoles aligned, (d) molecular order in the C_2 phase with all dipoles aligned.

The resulting model presents a physical picture of the mechanism of the tilting within the smectic C phase where the tilt angle plays only a secondary role. The primary role is played by a freezing out of the rotation of the molecules about their long axes in the smectic A phase at T_{AC} as a result of the dipole moments becoming aligned. If the dipole moments are not quite perpendicular to the molecular long axes, a torque is created parallel to the layer planes, thus tilting the molecules with respect to the layer normal.

By examining these rotational phase transitions within the mean-field approximation, McMillan showed that this model would form three rotationally ordered phases

27

below the smectic A phase. Within the first of these phases (labelled C, with $\mu_1 < \mu_2$) the structure is dominated by two outboard oppositely directed dipoles and the central dipoles (if any) are randomly oriented, as shown in Figure 3.1(b). This phase has the physical properties associated with the S_C phase; tilted director, optical biaxiality and second order A to C phase transition.

For $\mu_1 > \mu_2$ the molecular structure is dominated by the central dipole and a ferro-electric phase is predicted (labelled C_1, shown in Figure 3.1(c)), with the outboard dipoles being randomly orientated. There is, however, no experimental evidence that such a phase exists. The final structure is observed at temperatures below the C and C_1 phases where all three dipole moments align (labelled C_2, shown in Figure 3.1(d)), thus displaying the physical properties of a single layer of a chiral S_C material.

In an extension of this model, Meyer and McMillan [30] included a soft-core repulsive interaction and only considered the effect of the outboard dipole moments. With this adaptation the smectic B and a tilted hexatic phase are introduced into the phase diagram. However, as no inter-planar interactions were considered it is not know whether the latter phase is a smectic G or J.

More recent experimental evidence has cast a number of doubts upon the validity of the McMillan model. As has been shown in Section 2.2, whilst the inclusion of two terminal outboard dipole moments does help to stabilise the S_C phase, their presence is not a necessity. The prediction that there is freezing out of free rotation of the molecules about their long axes is also in contradiction to experimental findings [13–

15].

Cabib and Benguigui [31] proposed a model which also considers the electrostatic interaction between polar groups, but does not assume that the free rotation about the molecular long axes is frozen out in the S_C phase. To achieve this, only components of two oppositely opposed outboard dipole moments parallel to the molecular long axis are considered, with free rotation assumed to average out the perpendicular components in both the S_A and S_C phases. Whilst this uniaxial model, solved via the mean field approximation for a single smectic layer, displays a S_C phase below the S_A phase, the model has not been widely accepted due to the commonly held view that terminal dipole moments are necessary for the formation of the S_C phase [20,32].

In a later publication Van der Meer and Vertogen [33] proposed a model in which a permanent dipole moment in one molecule induces a dipole in a neighbouring molecule. When solved within the mean field approximation, the induction forces between outboard dipoles and the polarisable centres of neighbouring molecules induces a tilt, with resistance to tilt originating from a combination of Van der Waals' forces and hard core repulsions. For sufficiently strong induction forces the resistance to tilt is overcome and a second-order S_A to S_C transition results. A further increase in the induction forces destabilises the S_A phase, leading to a first-order N to S_C transition. Calculations of the force between a dipole and a neighbouring point polarisability showed that the strength of the induction force is strongly dependent on the position of the dipole within the molecule; acentral, and in particular transverse

acentral, dipole moments contribute significantly to the induction forces, for which there is an optimal location within the molecule. Rotation about the molecular long axis is unhindered in this model as the induction forces do not simply average out.

Whilst the theory of Van deer Meer and Vertogen satisfies the criteria presented from experimental studies, doubt upon the validity of all the models of the S_C phase mentioned so far has been cast from a mathematical perspective [34]. Within this paper a criterion is set which states that there must be a molecular tilt dependence upon the entropy of the system, otherwise the tilted phase constitutes the same thermodynamic phase as the S_A phase. The theories of Cabib and Benguigui [31] and Van deer Meer and Vertogen [33] have no such dependence. Therefore the predicted tilted phases must be referred to as tilted S_A and not S_C. Whilst the theory of McMillan [29] does include a relationship between tilt angle and entropy, a rigourous calculation of the temperature dependence of the tilt angle reveals a complex and unphysical behaviour. It was therefore concluded that whilst the phase transitions described do exist, that the dipole-ordered smectic phases should not be classified as the S_C phase [34].

The theory of Priest [35,36] is based on general coupling between second rank tensors and does not discuss the relation between coupling constants and molecular struc- ture. Whilst it has been shown that this theory also produces a tilted S_A rather than a S_C phase [34], the model is worthy of note as it was the first case where the angular dependence of the intermolecular interaction was assumed to be the same as that between two axially symmetric quadrupoles.

Following the criticism of theoretical models based upon the dipole-dipole interaction, attention was shifted onto models involving quadrupole-quadrupole interactions. A number of studies having been undertaken [37–40] using different theoretical techniques. In all cases, the model used have consisted of a quadrupole moment located at the centre of mass of a linear molecule and leads to the prediction of second-order smectic A to smectic C phase transition, with the later studies also finding a first-order nematic to smectic C transition. The energetically most favourable configuration of a quadrupole-quadrupole interaction is the T configuration (when only the 224-term in the spherical expansion of the interaction energy is considered, as in [39, 40] and in this work). However, for a system of perfectly ordered molecules, the interaction energy between a pair of quadrupole moments is minimised with an angle of $\approx 50^0$ between the molecular long axes and intermolecular vector. Thus the *parallel staggered* configuration is more favourable than the T configuration when orientational order is imposed upon the molecules.

It therefore appears that, for a sufficiently long molecules, Van der Waals' forces and hard core repulsions are responsible for the formation of orientationally ordered phases, with the polar constituents of the molecular structure (by inducing a quadrupole moment upon each molecule) being responsible for the tilting. These conclusions are supported by a recent simulation study [41] which has shown that a bulk Gay-Berne fluid with a longitudinal quadrupole moment attached will display a S_C phase.

31

3.2.2 Steric Repulsion Models

Unlike the models considered thus far, the Wulf [42] model is based upon purely steric factors. This model considers the packing requirements for zig-zag shaped molecules (as shown in figure 2.3), where the shape arises from the end chains not being collinear with the central core.

The steric contribution to the pair potential is given as

$$
-A_1(r)(\hat{\mathbf{u}}_i^{(3)} \cdot \hat{\mathbf{u}}_j^{(3)})(\hat{\mathbf{u}}_i^{(2)} \cdot \hat{\mathbf{u}}_j^{(2)}) - \frac{A_2(r)}{r_2^2} \left[(\hat{\mathbf{u}}_i^{(3)} \cdot \hat{\mathbf{r}}_{ij})(\hat{\mathbf{u}}_i^{(2)} \cdot \hat{\mathbf{r}}_{ij}) + (\hat{\mathbf{u}}_j^{(3)} \cdot \hat{\mathbf{r}}_{ij})(\hat{\mathbf{u}}_j^{(2)} \cdot \hat{\mathbf{r}}_{ij}) \right]
$$

$$(3.1)$$

where $\hat{\mathbf{u}}^{(3)}$ and $\hat{\mathbf{u}}^{(2)}$ denotes unit vectors along the molecular long axis and transverse axis respectively. The first term accounts for the fact that the potential energy is minimised if the particles long and short axes align together, resulting in a biaxial phase if the constituent molecules are biaxial. The second term represents the tendency for the molecules to tilt with respect to the intermolecular vector $\hat{\mathbf{r}}_{ij}$. The range of $A_2(r)$ is taken to be short compared with $A_1(r)$ and is controlled by r_2. This avoids the unphysical possibility that the molecules may tilt before the long and short axes of the molecules align.

When solved using the mean field approximation, this model predicts a second order S_A to S_C phase transition. A criticism of the the model has been that free rotation of the molecular long axis is not permitted. However, free rotation of individual

components of the molecule are permitted, with the central core and terminal chains not sharing a common axis of rotation, as as been observed experimentally [15].

A later study [43] has also shown that the S_C phase may formed by a biaxial hard body model. This was achieved by considering a system of parallel hard oblique cylinders, solved using density functional theory, with a S_C phase being predicted as a result of end-to-end packing effects.

Whilst the predictions of these theoretical studies support the idea that liquid-crystal structure and phase behaviour is largely driven by repulsions, it is not clear whether steric biaxiality of the constituent molecules is the cause or the result of the tilted phase.

3.3   Conclusions

Theoretical treatments of liquid crystalline systems have shown a reasonable degree of success in explaining experimental behaviour. The observation that repulsive interactions alone can give rise to mesogenic behaviour was an important early result. However, this hardly seems surprising now when it is known that most liquid structure is governed by hard core interactions, and that attractive effects can be regarded, with some reservations, as a perturbation away from this. Even in comparatively simple cases though, theoretical techniques have not been wholly successful. For example they tend to overestimate the strengths of mesogenic transitions, largely due to their inability to capture correctly the nature of orientational correlations.

For the more complicated tilted smectic phases, these problems have become more acute, and it is here that computer simulation can provide a useful comparison between the validity of a model and the theories used to predict its behaviour.

Chapter 4

Computer Simulation of Liquid

Crystals

In this chapter an overview of the computer simulation techniques used for liquid

phases is presented, together with a review of the current progress made with these

methods in the liquid crystal field. Details of the modelling methods used, both

in previous investigations and this work, are given initially, followed by a review of

previous simulations studies into liquid crystalline behaviour.

4.1   Simulation Techniques

The aim of computer simulation [7] is to predict the properties of real systems and

test theories based upon model systems by producing essentially exact results for a

relatively small idealised system of particles interacting through a given potential. The system may be replicated through space so as to reduce surface effects and enable a reasonable approximation to bulk behaviour to be made. This can, however, lead to problems, especially around phase transitions, due to the suppression of long range fluctuations.

There are two main techniques available, Metropolis Monte Carlo (MC) and molecular dynamics (MD). The former attempts to create a series of configurations for the system using random moves accepted with an appropriate probability, whereas the latter solves Newton's equations of motion (to an acceptable degree of accuracy) for the system, and can, therefore, be seen as representing the real evolution of the system through time. MD has a major advantage of allowing dynamical information to be obtained, though MC has the advantage that many different sorts of move (not necessarily realistic) may be attempted, and by a prudent choice of these, systems can be brought to equilibrium with greater ease.

A more detailed description of these techniques will now be given, starting with MC.

4.1.1 Monte Carlo Theory

The term Monte Carlo [7] has come into use to designate numerical methods in which specifically stochastic elements are introduced in contrast to the completely deterministic algebraic expression of the MD approach. The method was first used in the late 1940s to study the diffusion of neutrons in fissionable material. The

36

particular form used in liquid state physics was developed from this a few years later [44] and has generally become known as Metropolis Monte Carlo.

For the purposes of liquid state simulation, the MC method consists of generating a set of molecular configurations by random displacements of the particles within the system. A new configuration is accepted or rejected according to a criterion which ensures that, in the limit of an infinite number of transitions, a given configuration occurs with a probability proportional to the Boltzmann factor for that configuration, which is independent of the initial configuration of the model. A more detailed analysis for the canonical ensemble is now given.

The canonical ensemble is a set of systems (the ensemble) each consisting of N particles in a fixed volume V and at a fixed temperature T (also referred to as constant NVT). The probability of a certain configuration, m, of particles occuring is proportional to the Boltzmann factor of the potential energy, U_m,

$$p_{NVT}(m) \propto \exp\left(\frac{-U_m}{k_B T}\right).$$
(4.1)

To normalise this, the partition function is introduced. This is simply the sum of the Boltzmann factors for all possible configurations of the system,

$$Z_{NVT} = \int \exp\left(\frac{-U_m}{k_B T}\right) dm.$$
(4.2)

Therefore the probability of the configuration m occuring is given by,

$$p_{NVT}(m) = \frac{\exp\left(\frac{-U_m}{k_BT}\right)}{Z_{NVT}}. \tag{4.3}$$

The partition function is the fundamental property in statistical mechanics from which all thermodynamic quantities can be obtained. However, for reasonable size systems its direct calculation is practically impossible, and what is needed is a way to sample the system effectively so that other quantities can be obtained accurately. The average of some function $f(m)$ in the canonical ensemble is given by

$$\langle f \rangle_{NVT} = \int p_{NVT}(m)f(m)dm. \tag{4.4}$$

By sampling configurations at random this integral can be estimated by

$$\langle f \rangle_{NVT} = \left\langle \frac{\sum_m^{trials} f(m)\exp\left(\frac{-U_m}{k_BT}\right)}{\sum_m^{trials} \exp\left(\frac{-U_m}{k_BT}\right)} \right\rangle \tag{4.5}$$

and the partition function may be estimated by

$$Z_{NVT} \approx \frac{V^N}{trials} \sum_m^{trials} \exp\left(\frac{-U_m}{k_BT}\right). \tag{4.6}$$

For an infinite number of trials, this random technique will give correct results; however for the finite number of trials possible with computer simulation it tends to converge very poorly. This is because it does not sample effectively the regions of configuration space where the potential energy is such that significant contributions

38

will be made to the summations. In practice most of the the terms tend towards zero and the value of interest is inaccurately estimated.

To allow only the parts of configuration space of interest to be considered, the Metropolis technique uses importance sampling where the configurations are chosen from a non-uniform distribution so that most of them make a significant contribution to the summations in Eqn. 4.5. By sampling configurations at random from a distribution p, the function of interest can be estimated by an MC trial average,

$$\langle f \rangle_{NVT} = \left\langle f(m) \frac{p_{NVT}(m)}{p} \right\rangle_{trials}. \tag{4.7}$$

For most functions the integrand will be significant where $p_{NVT}(m)$ is significant, and in these cases choosing $p = p_{NVT}(\tau)$ should give a good estimate of the integral, such that

$$\langle f \rangle_{NVT} = \langle f(m) \rangle_{trials}. \tag{4.8}$$

The problem, thus, becomes one of finding a method of generating a random sequence of states such that by the end of the simulation each state has occured with the appropriate probability. The solution is to set up a *Markov chain* of states, which is constructed so that it has the limiting distribution of p_{NVT}. A Markov chain series of trials satisfies two conditions; the outcome of each trial belongs to a finite set of outcomes, $\{\Gamma_1, \Gamma_2, ..., \Gamma_n, \Gamma_m, ...\}$, called the state space, and the outcome of each trial depends only on the state that immediately precedes it.

π is defined as the transition matrix, with the element π_{mn} being the probability of moving from state m to state n. The probability that a system is in a particular state is given by a state vector $\mathbf{p} = \{p_1, p_2, ..., p_m, p_n, ...\}$. What is required is a transition matrix such that the limiting distribution of the chain,

$$p = \lim_{\tau \to \infty} p^1 \pi^\tau \tag{4.9}$$

is equal to the desired distribution, p_{NVT}. The limiting distribution of p is independent of the starting guess, p^1, and satisfies the eigenvalue equation

$$\sum_m p_m \pi_{mn} = p_n \tag{4.10}$$

with eigenvalue unity. This can be achieved by satisfying *microscopic reversibility*,

$$p_m \pi_{mn} = p_n \pi_{nm}. \tag{4.11}$$

The Metropolis solution is,

$$\pi_{mn} = \alpha_{mn} \qquad\qquad p_n \geq p_m \quad m \neq n$$

$$\pi_{mn} = \alpha_{mn} \left(\frac{p_n}{p_m} \right) \qquad p_n < p_m \quad m \neq n$$

$$\pi_{mm} = 1 - \sum_{n \neq m} \pi_{mn}$$

where α is a symmetrical stochastic matrix ($\alpha_{mn} = \alpha_{nm}$), often referred to as the underlying matrix of the Markov Chain. The symmetric properties of α ensure that

40

the Metropolis solution satisfies the condition of microscopic reversibility.

To implement the Metropolis solution it is necessary to specify α. The most common method used for generating a new configuration, n, from an old configuration, m, is to choose an atom i at random and displace it from its old position, $\mathbf{r}_i^m$, with equal probability to any point $\mathbf{r}_i^n$ within a sphere centred on $\mathbf{r}_i^m$. In a computer simulation there is a large finite number of new positions, N_R, and in this case α_{mn} can be defined as $\frac{1}{N_R}$. Care must be taken when choosing the size of displacement; too large and the acceptance rate will be too small, and too small and the system will sample phase space too slowly. The size of the maximum displacement is often adjusted during the simulation such that the acceptance rate of trial moves is approximately 50%.

The appropriate element of the transition matrix π depends upon the relative probabilities of the initial state m and the final state n. There are two cases to consider.

If the move in downhill in energy, ie $\Delta U = U_n - U_m \leq 0$, then $p_n \geq p_m$ and $\pi_{mn} = \alpha_{mn}$. Since the probability α_{mn} has already been incorporated in choosing the move, it can be accepted automatically.

If the move is uphill in energy, ie $\Delta U = U_n - U_m > 0$, then $p_n < p_m$ and $\pi_{mn} = \alpha_{mn}\left(\frac{p_n}{p_m}\right)$, so the move has to be accepted with a probability $\left(\frac{p_n}{p_m}\right)$. In order to recover the canonical ensemble, this ratio can be expressed as the Boltzmann factor of the energy change,

$$\frac{p_n}{p_m} = \frac{Z_{NVT}^{-1} \exp\left(\frac{Z_{NVT}^{-1} \exp}{k_B T}\right)}{Z_{NVT}^{-1} \exp\left(\frac{-U_m}{k_B T}\right)} = \exp\left(\frac{-\Delta U}{k_B T}\right). \tag{4.12}$$

To accept a move with this probability, a random number is generated uniformly between 0 and 1 and compared with $\exp\left(\frac{-\Delta U}{k_B T}\right)$. If the random number is less than the exponential, the move is accepted. If the move is rejected, the system remains in its current state in accordance with the finite probability π_{mm}, and this configuration is recounted as the new state in the chain.

A typical Monte Carlo scheme is as follows,

- Generate new configuration

- Calculate energy change, ΔE

- Calculate $\chi_{mn} = min\left(1, \exp\left(\frac{-\Delta E}{kT}\right)\right)$

- Generate random number ψ on [0,1]

- Accept move if $\psi \leq \chi_{mn}$

This procedure is relatively easy to implement on a computer and the method has been used extensively to perform simulations within the NVT ensemble.

For anisotropic systems, the underlying matrix of the Markov chain is altered to allow moves which usually consist of a combined translation and rotation of a molecule. This is relatively easy to implement, simply involving a simultaneous displacement of the translational coordinates (as already mentioned) and the orientational co-

42

ordinates (usually defined in terms of Euler angles or space fixed axes). However it is important not to bias the rotational part of the move by sampling uniformly from the Euler angles as might seem intuitively correct. Rather, this should be done either by choosing random displacements in the cosine of the angles [7], or by using the Barker-Watts algorithm [45], which involves rotating the molecule by a random amount about one of the three space-fixed axes (chosen at random). Both of these methods can be shown to satisfy microscopic reversibility, and the latter was used in this work.

It is also possible to generalise the Metropolis solution to other statistical mechanical ensembles, by means of an appropriate modification of the transition matrix so that the correct thermodynamic distribution of states is given. For example, in the isothermal-isobaric (constant NPT) ensemble, the configuration integral is given by

$$Z_{NPT} = \int \exp\left(\frac{-PV}{k_B T}\right) dV \int \exp\left(\frac{-U_m}{k_B T}\right) dm. \qquad (4.13)$$

The Metropolis scheme is implemented by generating a Markov chain of states which has a limiting distribution proportional to

$$p_{NPT} = \frac{\exp\left(\left(\frac{-U_m - PV}{k_B T}\right) + N \ln V\right)}{Z_{NPT}} \qquad (4.14)$$

by accepting trial moves with probability

43

$$\chi_{mn} = min\left(1, \exp\left(\frac{-\Delta H_{mn}}{k_B T}\right)\right) \qquad (4.15)$$

where

$$\Delta H_{mn} = \Delta U_{mn} + P\left(V_n - V_m\right) - \frac{N}{k_B T}\ln\left(\frac{V_n}{V_m}\right) \qquad (4.16)$$

and is closely related to the enthalpy change in moving from state m to state n.

4.1.2   Molecular Dynamics

4.1.2.1   Translational Motion

Molecular dynamics is a method [7] which solves the classical equations of motion for a system of N molecules interacting via a potential U. There are various ways of expressing these equations [46], perhaps the most fundamental being the Lagrangian equation of motion

$$\frac{d}{dt}\left(\frac{\partial L}{\partial \dot{q}_k}\right) - \left(\frac{\partial L}{\partial q_k}\right) = 0 \qquad (4.17)$$

where the Lagrangian,$L(q, \dot{q})$, is defined in terms of the kinetic and potential energies

$$L = K - U \qquad (4.18)$$

and is a function of the generalised coordinates q_k and their time derivatives $\dot{q}_k$. When considering a system of atoms with Cartesian coordinates, $\mathbf{r}_i$, and using the usual definitions of U and K, eqn. 4.17 becomes

$$m_i\ddot{\mathbf{r}}_i = \mathbf{f}_i \qquad (4.19)$$

where m_i is the mass of the atom i and

$$\mathbf{f}_i = \nabla_{r_i} L = -\nabla_{r_i} U \qquad (4.20)$$

is the force on that atom. These equations also apply to the centre of mass motion of a molecule, with $\mathbf{f}_i$ representing the total force acting upon molecule i. The equations of rotation take a similar form, and will be considered later. For anisotropic molecules, the form of the force is more complicated as the potential depends not only a function of $\mathbf{r}_i$ but also the relative orientation of the two molecules. Methods have been derived [47,48] which give explicitly the forces and torques necessary for the simulation of a fluid of anisotropic molecules. These are described in detail in Appendix A.

Computing the centre of mass trajectories requires solution of a system of $3N$ second order differential equations, eqn. (4.19). This is achieved by using finite difference methods. The general scheme is to take known molecular positions, velocities and other dynamical information at time t and attempt to obtain the positions, velocities, etc, at a later time $t + \delta t$, to a sufficient degree of accuracy. The choice of the time

45

interval δt depends upon the method used, but δt should be significantly smaller than the typical time taken for a molecule to travel its own length. There are a number of different algorithms which fall into the general category of finite difference methods. The most commonly used, and conceptually the simplest, method is the *Verlet* algorithm.

This method was initially developed to offer a direct solution to eqn. (4.19). The method is based upon the positions $\mathbf{r}(t)$, accelerations $\mathbf{a}(t)$, and positions $\mathbf{r}(t - \delta t)$ from the previous step. Although the algorithm is simple to program, exactly reversible in time and, given conservative forces, is guaranteed to conserve linar momentum, the handling of the velocities is awkward, and the algorithm may needlessly introduce some numerical imprecision.

Modifications to the basic Verlet scheme have been proposed to improve the algorithm. One such modification is known as the *leap-frog* scheme [49]. Since this algorithm has been used for this work a brief description will now be given. The algorithm is given by,

$$
\begin{aligned}
\mathbf{r}(t + \delta t) &= \mathbf{r}(t) + \delta t \mathbf{v}(t + \tfrac{1}{2}\delta t) \\
\mathbf{v}(t + \tfrac{1}{2}\delta t) &= \mathbf{v}(t - \tfrac{1}{2}\delta t) + \delta t \mathbf{a}(t).
\end{aligned}
\tag{4.21}
$$

This algorithm stores the current positions $\mathbf{r}(t)$, accelerations $\mathbf{a}(t)$ and mid-step velocities $\mathbf{v}(t - \tfrac{1}{2}\delta t)$. The velocity equation is applied first, such that the velocities leap over the positions to give the next mid-step values $\mathbf{v}(t + \tfrac{1}{2}\delta t)$. Subsequently the displacement equation is applied to advance the positions, and the new accelerations

are calculated for the next step. The on step velocities can be calculated using the formula

$$\mathbf{v}(t) = \frac{\mathbf{v}(t + \frac{1}{2}\delta t) + \mathbf{v}(t - \frac{1}{2}\delta t)}{2}. \tag{4.22}$$

It may be demonstrated that elimination of the velocities from these equations shows that the method is algebraically equivalent to Verlet's algorithm. The velocities now appear explicitly within the scheme, which is advantageous because, for example, control of simulation energy is achieved by appropriately scaling velocities.

4.1.2.2 Rotational Motion

4.1.2.2.1 Linear Molecules

In classical mechanics, it is natural to divide molecular motion into translation of the centre of mass and rotation about the centre of mass [46]. The rotational motion is governed by the torque, τ_i, about the centre of mass. This torque enters the rotational equations of motion in the same way that the force enters the translational equations. However, the nature of orientation space guarantees that the equations of re-orientational motion are not as simple as the translational equations.

For a linear molecule, only the angular velocity and the torque perpendicular to the molecular axis need be considered. Taking $\mathbf{u}$ as the unit vector defining the axis, the torque can be expressed as,

$$\boldsymbol{\tau} = \mathbf{u} \times \mathbf{g} \qquad (4.23)$$

where $\mathbf{g}$ can be determined from the intermolecular potential (shown in Appendix A). The vector $\mathbf{g}$ can always be replaced by its component perpendicular to the molecular axis, such that,

$$\boldsymbol{\tau} = \mathbf{u} \times \mathbf{g}^{\perp} \qquad (4.24)$$

where,

$$\mathbf{g}^{\perp} = \mathbf{g} - (\mathbf{g} \cdot \mathbf{u})\mathbf{u}. \qquad (4.25)$$

The equation of rotational motion can then be expressed using the second order differential equation [50]

$$\ddot{\mathbf{u}} = \frac{\mathbf{g}^{\perp}}{I} + \lambda \mathbf{u} \qquad (4.26)$$

where I is the moment of inertia perpendicular to $\mathbf{u}$ and λ is a Lagrange multiplier, which constrains $|\mathbf{u}|$ to be a constant of motion. A proposed solution to this equation uses a leap-frog algorithm [51]. Firstly an expression for λ is obtained by considering the advancement of coordinates over a half time step

48

$$\dot{\mathbf{u}}(t) = \dot{\mathbf{u}}(t - \frac{1}{2}\delta t) + \frac{1}{2}\delta t \left[\frac{\mathbf{g}^{\perp}(t)}{I} + \lambda(t)\mathbf{u}(t) \right]. \qquad (4.27)$$

Taking the scalar product of both sides with the vector $\mathbf{u}(t)$, and using $\mathbf{u}(t) \cdot \dot{\mathbf{u}}(t) = 0$ and $\mathbf{u}(t) \cdot \mathbf{g}^{\perp}(t) = 0$ gives,

$$\lambda(t)\delta t = -2\dot{\mathbf{u}}(t - \frac{1}{2}\delta t) \cdot \mathbf{u}(t) \qquad (4.28)$$

and so

$$\delta t \ddot{\mathbf{u}}(t) = \delta t \frac{\mathbf{g}^{\perp}(t)}{I} - 2 \left[\dot{\mathbf{u}}(t - \frac{1}{2}\delta t) \cdot \mathbf{u}(t) \right] \mathbf{u}(t). \qquad (4.29)$$

This is then used to advance a full step in the integration algorithm

$$\dot{\mathbf{u}}(t + \frac{1}{2}\delta t) = \dot{\mathbf{u}}(t - \frac{1}{2}\delta t) + \delta t \ddot{\mathbf{u}}(t) \qquad (4.30)$$

and the step is completed using,

$$\mathbf{u}(t + \delta t) = \mathbf{u}(t) + \delta t \dot{\mathbf{u}}(t + \frac{1}{2}\delta t). \qquad (4.31)$$

This algorithm has been used in liquid crystal simulations and produces stable and accurate trajectories.

4.1.2.2.2 Non-Linear Molecules

When a non-linear molecule is considered, the method described above cannot be used to simulate rotational motion, due the molecule not possessing cylindrical symmetry. To integrate the equations of rotational motion we instead introduce the method of quaternions [52]. A quaternion $\mathbf{Q}$ is a set of four scalar quantities

$$\mathbf{Q} = (q_0, q_1, q_2, q_3) \tag{4.32}$$

satisfying the constraint

$$q_0^2 + q_1^2 + q_2^2 + q_3^2 = 1. \tag{4.33}$$

The orientation of a vector fixed in the molecule-fixed axes, $\mathbf{u}^b$, is related to the corresponding space-fixed axes, $\mathbf{u}^s$, by

$$\mathbf{u}^b = \mathbf{R}(\mathbf{Q})\mathbf{u}^s \tag{4.34}$$

where $\mathbf{R}(\mathbf{Q})$ is the rotation matrix,

$$\mathbf{R}(\mathbf{Q}) = \begin{pmatrix} q_0^2 + q_1^2 - q_2^2 - q_3^2 & 2(q_1 q_2 + q_0 q_3) & 2(q_1 q_3 - q_0 q_2) \\ 2(q_1 q_2 - q_0 q_3) & q_0^2 - q_1^2 + q_2^2 - q_3^2 & 2(q_2 q_3 + q_0 q_1) \\ 2(q_1 q_3 + q_0 q_2) & 2(q_2 q_3 - q_0 q_1) & q_0^2 - q_1^2 - q_2^2 + q_3^2 \end{pmatrix}. \tag{4.35}$$

The quaternion parameters are assigned to each molecule based on the Euler angle convention [46] (the definition of which is illustrated in Fig. 4.1),

$$q_0 = \cos\frac{1}{2}\theta\cos\frac{1}{2}(\phi + \psi) \tag{4.36}$$

$$q_1 = \sin\frac{1}{2}\theta\cos\frac{1}{2}(\phi - \psi) \tag{4.37}$$

$$q_2 = \sin\frac{1}{2}\theta\sin\frac{1}{2}(\phi - \psi) \tag{4.38}$$

$$q_3 = \cos\frac{1}{2}\theta\sin\frac{1}{2}(\phi + \psi). \tag{4.39}$$

The rotational motion of each molecule can then be expressed in terms of quaternions which evolve via

$$
\begin{pmatrix} \dot{q}_0 \\ \dot{q}_1 \\ \dot{q}_2 \\ \dot{q}_3 \end{pmatrix} = \frac{1}{2} \begin{pmatrix} q_0 & -q_1 & -q_2 & -q_3 \\ q_1 & q_0 & -q_3 & q_2 \\ q_2 & q_3 & q_0 & -q_1 \\ q_3 & -q_2 & q_1 & q_0 \end{pmatrix} \begin{pmatrix} 0 \\ \omega_x^b \\ \omega_y^b \\ \omega_z^b \end{pmatrix} \tag{4.40}
$$

where ω is the angular velocity. A modified leap-frog algorithm has been derived [53]. The method is based upon stored values of angular momenta, $\mathbf{j}$, quaternions and the torque, τ. The first step is to advance the angular momenta to time t,

$$\mathbf{j}^s(t) = \mathbf{j}^s(t - \frac{1}{2}\delta t) + \frac{1}{2}\delta t \tau^s(t). \tag{4.41}$$

The angular momenta can then be converted into molecule-fixed axes using eqn. (4.34),

51
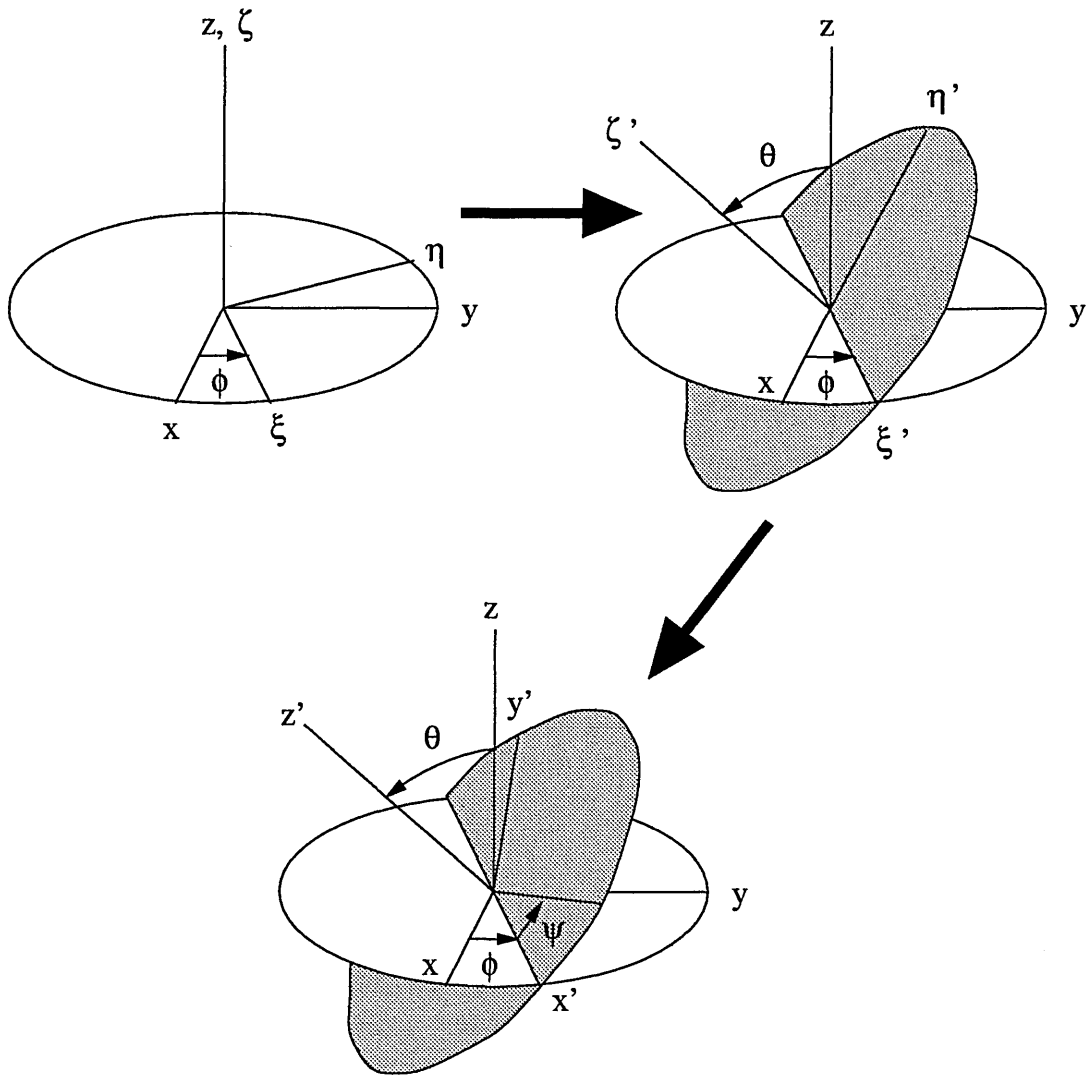
Figure 4.1: Schematic representation of the rotations defining the Eulerian angles

and the angular velocity can be calculated at time t,

$$\omega_\alpha^b(t) = \frac{j_\alpha^b}{I_{\alpha\alpha}} \tag{4.42}$$

where I_{xx}, I_{yy} and I_{zz} are the three principal moments of inertia. The time derivatives of the quaternions, $\dot{\mathbf{Q}}(t)$, can then be calculated using eqn. (4.40), and $\mathbf{Q}(t + \frac{1}{2}\delta t)$ is calculated by

$$\mathbf{Q}(t + \frac{1}{2}\delta t) = \mathbf{Q}(t) + \frac{1}{2}\delta t \dot{\mathbf{Q}}(t) \tag{4.43}$$

None of these values need be stored permanently, since the aim of these auxiliary equations is to obtain an estimate of $\mathbf{Q}(t + \frac{1}{2}\delta t)$ so that the transformation matrix and $\dot{\mathbf{Q}}$ can be calculated on the half-time step using eqns. (4.34) and (4.40). The main algorithm equations are,

$$\mathbf{j}^s(t + \frac{1}{2}\delta t) = \mathbf{j}^s(t - \frac{1}{2}\delta t) + \delta t \tau^s(t) \tag{4.44}$$

and

$$\mathbf{Q}(t + \delta t) = \mathbf{Q}(t) + \delta t \dot{\mathbf{Q}}(t + \frac{1}{2}\delta t). \tag{4.45}$$

The algorithm seems to be stable and accurate with a moderately large time step [53].

53

4.1.3 Periodic Boundary Conditions

In a real system it is common to have of the order 10^{23} particles, whereas a typical computer simulation will only have 10^2 to 10^6 particles due to the computational overhead involved when considering large systems. Confining the particles within a geometric shape will cause problems with surface effects for such a small system. Periodic boundary conditions are used to reduce this problem and involve effectively replicating the system box in all directions through space. If a particle leaves the system through one side then it will re-enter on the opposite side thus keeping the number of particles constant.

It is important to ask whether the properties of a small, infinitely periodic system and the macroscopic system which it represents are the same. This depends both on the range of the intermolecular potential and the phenomenon under investigation. If the range of the potential is large enough in comparison to the box size, then there will be a significant interaction between a particle and its own periodic image, imposing a degree of symmetry upon a structure which should in reality isotropic. There can also be problems in the vicinity of phase transitions, since these can involve the creation of long range fluctuations which are suppressed by periodic conditions. This can lead to a rounding and shifting of the phase transition, and transitions which are known to be first-order often exhibit the characteristics of higher order transitions when modelled in a small box due to suppression of fluctuations. The implications of this periodicity will be further discussed along with the relevant results in following Chapters.

4.1.4 Interaction Potentials

For a system of N interacting particles the potential energy can be divided into terms depending on the position (and orientation) of the individual atoms, pairs, triplets, etc,

$$U = \sum_i e_1(\mathbf{r}_i) + \sum_i \sum_{j>i} e_2(\mathbf{r}_i, \mathbf{r}_j) + \sum_i \sum_{j>i} \sum_{k>j>i} e_3(\mathbf{r}_i, \mathbf{r}_j, \mathbf{r}_k) + \ldots \qquad (4.46)$$

where e_1 represents the effect of an external field, e_2 represents a two body pair-wise potential and e_3 is a three body triplet-wise potential. The majority of the potential energy comes from the pair interaction term, however the triplet term is reasonably significant at liquid densities, accounting for about 10% of the total. It and higher terms are rarely used in computer simulations of liquids though, because they are extremely time consuming to calculate. Fortunately the pair-wise approximation used gives a remarkably good description of liquid properties [54], however it should be noted that the potentials used are effective pair potentials that represent all the many body effects, and are not necessarily the same as (or even similar to) the actual pair potentials in real systems [7].

4.1.5 Analysis

Within the field of molecular simulation, the variables to be analysed can be split into two groups

- Thermodynamic quantities - pressure, temperature, energy

- Structural quantities - order parameters, distribution functions

In general a number of the thermodynamic quantities will be fixed during a simulation, depending upon which ensemble is being used.

4.1.5.1 Energy

For both simulation techniques it is relatively simply to calculate the potential energy of the system from eqn. (4.46). However, kinetic energy can only be calculated from the molecular dynamics method as it is a dynamic quantity, and is calculated in the usual way from the stored velocities (both translational and rotational),

$$\mathcal{K} = \sum_{i=1}^{N} \sum_{k} \left[\frac{\mathbf{p}_{ik}^2}{2m_i} + \frac{\mathbf{j}_{ik}^2}{2I_{ikk}} \right] \tag{4.47}$$

where $j = x, y, z$. The first term gives the translational temperature whilst the second term gives the rotational temperature associated with particle i.

4.1.5.2 Temperature

From the kinetic energy it is possible to calculate the instantaneous temperature of the system, $\mathcal{T}$. For example, a biaxial rod like molecule has six degrees of freedom each with average kinetic energy of $\frac{k_B T}{2}$ per molecule, the temperature may be expressed as,

56

$$\mathcal{T} = \frac{\mathcal{K}}{3Nk_B} \qquad (4.48)$$

4.1.5.3 Pressure

The pressure can be calculated during the course of a simulation using the virial theorem,

$$\mathcal{P} = \mathcal{P}_{ideal} + \langle \mathcal{P}_{excess} \rangle = \rho k_B \mathcal{T} + \left\langle \frac{W}{V} \right\rangle \qquad (4.49)$$

where,

$$W = -\frac{1}{3} \sum_{i=1}^{N} \sum_{j<i}^{N} \mathbf{r}_{ij}.\mathbf{f}_{ij}. \qquad (4.50)$$

The observation of temperature and pressure during a simulation for which either or both are specified to provides a useful check of the program.

4.1.5.4 Orientational Order Parameters

Four second rank order parameters are used to characterise the uniaxial and biaxial ordering of rod like molecules,

$$Q_{00}^2 = \left\langle \tfrac{1}{2}(3\cos^2\theta - 1) \right\rangle$$

$$Q_{20}^2 = \left\langle \tfrac{1}{2}\sqrt{3}\sin^2\theta \cos 2\phi \right\rangle$$

$$Q_{20}^2 = \left\langle \tfrac{1}{2}\sqrt{3}\sin^2\theta \cos 2\psi \right\rangle \tag{4.51}$$

$$Q_{22}^2 = \left\langle \tfrac{1}{2}(1 + \cos^2\theta)\cos 2\phi \cos 2\psi - \cos\theta \sin 2\phi \sin 2\psi \right\rangle$$

where θ, ϕ and ψ are the Euler angles of a typical molecule with respect to the laboratory axes. In practice only Q_{00}^2 and Q_{22}^2 are needed to characterise the observed system, the former being the uniaxial (nematic) order parameter measuring the alignment of the principal molecular axis (z) with the director (taken to define the laboratory $\mathbf{Z}$ direction), with the latter being sensitive to the alignment of the subsidiary (x and y) molecular axes along the laboratory $\mathbf{X}$ and $\mathbf{Y}$ directions. Writing ordering matrices along each of the axes of a molecule, for all molecules, as,

$$Q_{\alpha\beta}^{xx} = \frac{1}{N}\sum_{i=1}^{m}\left(\frac{3}{2}\hat{x}_{i\alpha}\hat{x}_{i\beta} - \frac{1}{2}\delta_{\alpha\beta}\right), \quad \alpha,\beta = 1,2,3 \tag{4.52}$$

where $\delta_{\alpha\beta}$ is the Kronecker delta, with similar definitions for $Q_{\alpha\beta}^{yy}$ and $Q_{\alpha\beta}^{zz}$, the order parameters may be expressed as,

$$Q_{00}^2 = \left\langle \mathbf{Z} \cdot \mathbf{Q}^{ZZ} \cdot \mathbf{Z} \right\rangle$$

$$Q_{22}^2 = \tfrac{1}{3}\left\langle \mathbf{X} \cdot \mathbf{Q}^{XX} \cdot \mathbf{X} + \mathbf{Y} \cdot \mathbf{Q}^{YY} \cdot \mathbf{Y} - \mathbf{X} \cdot \mathbf{Q}^{YY} \cdot \mathbf{X} - \mathbf{Y} \cdot \mathbf{Q}^{XX} \cdot \mathbf{Y} \right\rangle \tag{4.53}$$

Apart from finite-size corrections, Q_{00}^2 should be zero in an isotropic phase, and non-zero, increasing towards its maximum value of 1, in a uniaxial (or biaxial)

phase. Similarly Q_{22}^2 should be zero in an isotropic or uniaxial phase, and non-zero, increasing towards its maximum value of 1, in a biaxial phase.

The problem is now, that during the course of a simulation, the subsidiary molecular axes and the laboratory directions need to be determined. A unambiguous procedure for this has been developed [55] based solely on the assumption that the appropriate molecular axes may be identified with the axes of symmetry of the molecule, rather than being arbitrarily orientated within the molecule.

Initially the three ordering matrices are calculated. By diagonalising each of these, three eigenvalues and eigenvectors are determined, with the largest eigenvalue λ_+ and its corresponding eigenvector being of interest. The molecular axis with the largest λ_+ is then identified to the principal molecular axis z. The corresponding eigenvector is identified as the laboratory $\mathbf{Z}$ direction (giving the director $\hat{n}$) and the eigenvalue is equal to $\mathbf{Z} \cdot \mathbf{Q}^{ZZ} \cdot \mathbf{Z}$. This procedure is the same as that usually undertaken to calculate the nematic order parameter [56] with the added complication of needing to decide amongst the possible molecular axes. The second largest λ_+ is taken to identify the secondary molecular ordering axis y with the corresponding eigenvector being used to construct the second laboratory axis $\mathbf{Y}$, which is then constrained to be orthogonal to $\mathbf{Z}$. The remaining molecular axis is taken to be x, while $\mathbf{X}$ is constructed perpendicular to $\mathbf{Y}$ and $\mathbf{Z}$. With these axes defined, the instantaneous order parameters are straightforwardly calculated from Eqn. 4.53.

59

4.1.5.5   Radial Distribution Function

The radial distribution function $g(r)$ provides structural information about the system. It is defined as the probability of finding a pair of molecules a distance r apart, relative to the probability expected for a completely random distribution at the same density.

Within a computer simulation, it is calculated by compiling a histogram. The volume around each particle is divided into concentric spherical shells, and the number of particles in each shell is counted and divided by the shell volume (given by the difference between two spherical volumes), to obtain the local density. The densities at each distance are then averaged over all particles, and normalised with the overall density to obtain $g(r)$. Thus,

$$g(r) = \frac{1}{\rho^* \frac{4}{3} \left((r + dr)^3 - (r - dr)^3 \right)} \frac{1}{N} \sum_{i=1}^{N} N_j \tag{4.54}$$

where N_j is the number of particles j such that $r + dr > |\mathbf{r}_i - \mathbf{r}_j| > r - dr$.

A more detailed investigation of the structure is available from the radial pair distribution functions resolved relative to the layer normal $\hat{\mathbf{l}}$. To calculate the layer normal a *local* layer normal $\hat{\mathbf{l}}_i$ is calculated for each molecule i by diagonalising the tensor

$$Q'_{i\alpha\beta} = \frac{1}{n(n-1)} \sum_{j}^{n} \sum_{k \neq j}^{n} \left[\frac{3}{2} (\hat{\mathbf{r}}_{ij} \times \hat{\mathbf{r}}_{ik})_\alpha (\hat{\mathbf{r}}_{ij} \times \hat{\mathbf{r}}_{ik})_\beta - \frac{1}{2} \delta_{\alpha\beta} \right] \tag{4.55}$$

60

where $\hat{\mathbf{r}}_{ij}$ and $\hat{\mathbf{r}}_{ik}$ are unit vectors between molecule i and two of its n near neighbours (such that $\hat{\mathbf{r}}_{ij} < 2\sigma_0$ and $\hat{\mathbf{r}}_{ik} < 2\sigma_0$). The layer normal $\hat{\mathbf{l}}$ is then given by the eigenvector corresponding to the largest eigenvalue obtained by diagonalising the tensor,

$$Q_{\alpha\beta} = \frac{1}{N} \sum_{i=1}^{N} \left[\frac{3}{2} \hat{\mathbf{l}}_{i\alpha} \hat{\mathbf{l}}_{i\beta} - \frac{1}{2} \delta_{\alpha\beta} \right] \qquad (4.56)$$

For the purposes of characterisation of liquid crystalline phases it is convenient to resolve $g(r)$ into two functions; $g_{\parallel}(r_{\parallel})$ dependent upon $r_{\parallel} = \mathbf{r}_{ij} \cdot \hat{\mathbf{l}}$, the pair separation parallel to the layer normal, and $g_{\perp}(r_{\perp})$ dependent upon $r_{\perp} = \sqrt{\mathbf{r}_{ij}^2 - r_{\parallel}^2}$, the transverse separation.

It should be noted that pairs of molecules with considerably different $r_{\parallel}$ may contribute to $g_{\perp}(r_{\perp})$. Therefore this function is not a two-dimensional distribution. For this reason, other functions may be used to determine the intralayer and interlayer structures. Since the phase and periods of the density wave along $\hat{\mathbf{l}}$ is known, each particle can be assigned into a specific layer, $m = 1, 2, 3$, etc. Calculation of $g_{\perp}(r_{\perp})$ can now be resolved according to its layer index, $g_{\perp}^{(\Delta m)}(r_{\perp})$, where the index refers to the number of adjacent layers between molecules i and j, i.e $g_{\perp}^{(0)}(r_{\perp})$ is a two-dimensional distribution function averaged over pairs of molecules i and j in the same layer, $g_{\perp}^{(1)}(r_{\perp})$ is defined for molecule i in a given layer and j in an adjacent layer. For these cases an overall average over i (and hence all layers) is taken.

This type of in-plane distribution function has been shown to be an effective method

for the determination of the structure of the S_A and S_B phases. However, for the purpose of identifying tilted smectic phases such two-dimensional distribution functions will not allow the distinction between tilted hexatic phases, which are classified by their direction of tilt within the hexagonal lattice, to be made. In order to allow these phases to be classified the in-plane distribution function must be resolved into two one-dimensional distribution functions parallel $g_{\perp\parallel}(r_{\perp\parallel})$ and perpendicular $g_{\perp\perp}(r_{\perp\perp})$ to the direction of tilt. Then comparison of these distribution functions with an ideal hexagonal lattice will allow these phases to be classified. In order to define vectors in the layer which can be used to resolve these functions, the property that the average orientation of the molecules, defined by the director $\hat{n}$, and the layer normal, $\hat{l}$, will be orientated in different directions within a tilted phase is used. Therefore the components resolved perpendicular and parallel to the direction of tilt may be made dependent upon $r_{\perp\perp} = \mathbf{r}_{ij} \cdot (\hat{l} \times \hat{n})$ and $r_{\perp\parallel} = \mathbf{r}_{ij} \cdot ((\hat{l} \times \hat{n}) \times \hat{l})$ respectively.

In these cases the normalising volume needs to be modified appropriately; instead of considering two spheres and using their difference as the volume, a sub-space of each of these spheres is used, such that each sub-space defines the correct volume element for the distribution function being used. The difference in volume of these sub-spaces is then again used as the normalising volume (replacing $\frac{4}{3}((r + dr)^3 - (r - dr)^3)$ in Eqn. 4.54).

4.1.6 Reduced Units

Within computer simulations it is normal to take the mass of the molecules as a fundamental unit, i.e. set $m_i = 1$. As a consequence, the particle momenta and velocities become numerically identical, as do the forces and accelerations. For molecules interacting via a relatively simple pair potential this approach can be extended further. For example, the Lennard-Jones potential is completely defined by the parameters ϵ and σ and from these definitions other units may be defined;

$$\text{Density} \quad \rho^* = \rho\sigma^3 \tag{4.57}$$

$$\text{Temperature} \quad T^* = k_B T/\epsilon \tag{4.58}$$

$$\text{Energy} \quad E^* = E/\epsilon \tag{4.59}$$

$$\text{Pressure} \quad P^* = P\sigma^3/\epsilon \tag{4.60}$$

$$\text{Time} \quad t^* = (\epsilon/m\sigma^2)^{1/2}t \tag{4.61}$$

$$\text{Quadrupole} \quad Q^* = Q/(4\pi\epsilon_0\sigma^5\epsilon)^{1/2} \tag{4.62}$$

Since the Gay-Berne potential is an anisotropic form of the Lennard-Jones potential, the reduced units used in this work are all defined in the same way.

The use of reduced units avoids any possible embarrassment of conducting essentially duplicate simulations. There are also technical advantages in that when parameters such as ϵ and σ are given a value of unity, they will not appear in the program at all, saving some time in the calculation of energies, forces, *etc.*

63

4.2 Liquid Crystal Simulation

Liquid crystals present a particular challenge to the computer simulator. Firstly the molecules are complex, having flexible or semi-flexible structures and often possessing interesting electronic charge distributions, making them computationally expensive to model realistically. Secondly, liquid crystal phenomena occur over relatively large time and length scales, requiring, in some circumstances, lengthy simulations of large systems. For these reasons a great deal of powerful CPU time is required, and it is not surprising that early attempts to simulate mesogens in the 1970's suffered greatly from insufficient computer time preventing any definite conclusions being drawn. It was not until the 1980s that there was sufficient computer power for mesogenic phases to be observed unambiguously.

The types of model used to simulate liquid crystals off lattice can be broadly split into two main types - hard and soft particle models - each of which have been studied extensively. Both types are discussed in this review, concentrating exclusively on bulk systems and the history of liquid crystal simulations, with particular emphasis on previous studies using the Gay-Berne model, which has been used as the basis for the work presented in this thesis.

4.2.1 Hard Particle Models

A hard particle model simply consists of an infinitely repulsive core within which no penetration is possible. It contains no attractive region, and is expressed math-

ematically for a sphere as,

$$U^{HS}(\mathbf{r_{ij}}) = \begin{cases} \infty & (\sigma > r) \\ 0 & (\sigma \leq r) \end{cases} \qquad (4.63)$$

where σ is the diameter of the sphere. It is the simplicity of Eqn. (4.63) that makes this class of model so useful to the computer simulator. The first liquid simulations were carried out using hard particles and were surprisingly effective at reproducing features of the liquid state, showing that the main driving forces behind liquid structure are excluded volume effects. Models of liquid crystals using hard particles have shown that an essential reason for mesogenic behaviour is the degree of shape anisotropy. That said, attractive interactions can certainly effect the phase behaviour drastically.

As described in section 3.1, the work of Onsager showed that orientational ordering will be seen in a system of needle-like hard bodies when the density increases above a critical value, so its was known that these particles were capable of forming mesophases. This was first verified by Frenkel and Eppenga [57], who also performed Monte Carlo simulations on a system of thin hard discs to show that this system undergoes an isotropic to nematic transition. However, because the discs had zero volume the system could not crystallise thus ensuring that the nematic phase would be observed at sufficiently high densities.

4.2.1.1 Ellipsoids

An ellipsoid is one of the simplest shapes to be studied. It is simply a sphere subjected to elongation or compression. By defining semi-axes to be a, b and c, if $a = b = c$ then a sphere results, $a \neq b = c$ gives an axially symmetric molecule (ellipsoid of revolution) and $a \neq b \neq c$ gives a general biaxial molecule. When defining the shape of an axially symmetric molecule a factor e is used which is a measure of elongation or axial ratio ($e = a/b$). If e is less than 1 then the molecule is oblate and if e is greater than 1 then the molecule is prolate.

Frenkel and co-workers [58–60] explored the phase diagram of the hard ellipsoid system, considering a whole range of axial ratios from infinitely thin discs through hard spheres up to various lengths of rod-like molecules. It was found that the degree of anisotropy of the molecules determines the stability of the nematic phase, and that whilst a nematic phase was observed for $e = 1/2.75$ and 3, no nematic phase exists for less extreme ratios.

More extreme shapes, $e = 1/10$, $1/5$, 5 and 10 have been studied [61] and in each case a spontaneous ordering to the nematic phase being observed on uniform compression. It was also observed that upon transformation from oblate to prolate (e to $1/e$) the phase diagram is almost symmetrical, with the discotic molecules being slightly more aligned at a given density than the corresponding prolate molecules.

The effect of introducing biaxiality upon the isotropic-nematic transition has been investigated [55, 62] by transforming a prolate uniaxial ellipsoid ($e = 10$, $c/b = 1$)

through a biaxial ellipsoid ($e = 10$, $1 < c/b < e$) to an oblate uniaxial ellipsoid ($e = 10$, $c/b = e$). The resulting phase diagram is almost symmetric about $c/b = \sqrt{e}$ (where the ellipsoid is neither prolate or oblate), with the nematic phase being replaced by a biaxial phase in the region of transformation from prolate to oblate. The most striking conclusion is that the strength of the isotropic-nematic transition is weakened dramatically by a modest degree of biaxiality, bringing these results into closer agreement with real experiments.

4.2.1.2 Spherocylinders

A calamitic molecule may also be described using a spherocylinder, that is a cylinder of length L and diameter D with hemispherical caps of diameter D. The length to breadth ratio is often given by $\gamma = L/D$ (whilst the overall length to breadth ratio is given by $L/D + 1$).

The first simulations using this model [63] considered a system of parallel spherocylinders with $5 \geq \gamma$, thus even at the lowest densities, the system was guaranteed nematic order. The most striking result of this work is that the system displays a stable smectic phase, the range of which was increased with the non-sphericity of the particles. More recent work [64] has examined the effect of the orientational degrees of freedom of the system by removing the parallel constraint for a $\gamma = 5$ system, and, later, for other aspect ratios [65]. This has shown that for $\gamma < 3$ only isotropic and crystalline phases can occur, and that for larger γ stable nematic and smectic are present.

An attempt has recently been made to trace out the whole of the density vs axial ratio phase diagram for hard spherocylinders using a combination of simulation and theoretical techniques [66]. It has been found that stable nematic and smectic phases only exist for $\gamma \geq 3.1$ and $\gamma \geq 3.7$ respectively. Also, the size of the density jump was seen to diminish at the nematic to smectic transition with increasing particle length, whereas it increases for the isotropic to nematic transition.

Since experimental studies have shown that the inclusion of polar groups into the molecular structure can have a dramatic effect upon the observed phase sequences, investigations into the effect upon the phase behaviour with the inclusion of dipole-dipole interactions have been considered. Following the results of molecular dynamics simulations [67, 68], which showed that a ferroelectric nematic phase may be formed by a system of dipolar soft spheres, simulations have been performed to determine the phase behaviour of spherocylinders with $\gamma = 5$ with the addition of a dipole-dipole interaction [69–71].

These results have shown that the inclusion of central point dipoles, both transverse and longitudinal, destabilises the nematic phase relative to the isotropic and smectic A phases. Whilst there is no evidence of ferroelectricity, short range anti-ferroelectric ordering is observed, with ring and chain domain structures being observed for transverse case. Simulations have also been performed upon a system with a terminal longitudinal point dipole located at the centre of the hemispherical cap. For this system, the opposite of the central dipole cases is observed, with the smectic phase being destabilised relative to the nematic, which appears to be a consequence of the

anti-parallel geometry of the dipoles in their minimum energy conformation causing a staggering of the molecules which cannot easily be accommodated into the smectic layers.

4.2.1.3 Conclusions

Despite the inherent problems of simulating mesogens, a surprising number of the features have been reproduced using hard core models. Of particular note is the establishment of stable smectic phases for systems of sufficiently elongated sphero-cylinders. The next logical step is the consideration of anisotropic particles with more realistic interactions, i.e. soft potentials.

4.2.2 Soft Particle Models

A realistic interaction between molecules is known to have both attractive and repulsive components, due to the fact that on one hand solids and liquids have the property of cohesion, but at the same time do not collapse indefinitely to a point singularity under the action of these forces. Soft interaction potentials attempt to model this by comprising both a repulsive inner and an attractive outer region. Unlike hard particles, they do not generally have an infinitely repulsive core, but rather a steeply rising potential within a certain distance, hence the term soft particle.

The Lennard-Jones pair potential is a commonly used model interaction for atomistic systems. It features an attractive tail at large intermolecular separations, to

model dispersive interactions due to correlation between electron clouds surrounding molecules. At shorter distances a negative well is present, which is responsible for cohesion in condensed phases, and finally a steeply rising repulsive section at short distances to model non-bonded overlap between the electron clouds. The Lennard-Jones pair potential is therefore given by,

$$U_{ij} = 4\epsilon_0 \left[\left(\frac{\sigma_0}{r_{ij}} \right)^{12} - \left(\frac{\sigma_0}{r_{ij}} \right)^6 \right] \tag{4.64}$$

with a long-range attractive tail of the form $- \left(\frac{1}{r} \right)^6$, a negative well of depth ϵ_0 and a steeply rising repulsive wall of the form $\left(\frac{1}{r} \right)^{12}$ at distances less than $r_{ij} \sim \sigma_0$.

This potential has proved exceedingly successful at reproducing real behaviour for a number of atomic systems, given an appropriate choice of ϵ_0 and σ_0. For the purpose of modelling an anisotropic molecule, several Lennard-Jones potentials would have to be used for each molecule to attempt to accurately reproduce the intermolecular interactions. For mesogenic systems, such models are computationally expensive and it is only very recently that such studies have been possible. This type of model will be discussed in more detail in Section 4.2.3.

To make efficient use of the computational power has resulted in a number of attempts, since the beginnings of computer simulation, to effectively model a site-site interaction with a single interaction. This alternative type of potential was first introduced in 1948 by Corner [72], who proposed a numerical fit to a multi-site Lennard-Jones potential with orientationally dependent range and energy parame-

ters.

Other potentials have since been proposed [73,74], however here attention will be

focussed purely upon the Gay-Berne potential, used for this work, and initially its

predecessor, the Berne-Pechukas potential.

4.2.2.1 Berne-Pechukas Potential

The Berne-Pechukas potential [75] is essentially an axially symmetric Gaussian over-

lap model generalised to a Lennard-Jones form. The potential contains the basic

12-6 part of the Lennard-Jones interaction, with angular dependence of σ determined

by the overlap of two Gaussian ellipsoidal functions,

$$\sigma(\hat{\mathbf{r}}_{ij}, \hat{\mathbf{u}}_i, \hat{\mathbf{u}}_j) = \sigma_0 \left[1 - \frac{\chi}{2} \left\{ \frac{(\hat{\mathbf{r}}_{ij} \cdot \hat{\mathbf{u}}_i + \hat{\mathbf{r}}_{ij} \cdot \hat{\mathbf{u}}_j)^2}{1 + \chi(\hat{\mathbf{u}}_i \cdot \hat{\mathbf{u}}_j)} + \frac{(\hat{\mathbf{r}}_{ij} \cdot \hat{\mathbf{u}}_i - \hat{\mathbf{r}}_{ij} \cdot \hat{\mathbf{u}}_j)^2}{1 - \chi(\hat{\mathbf{u}}_i \cdot \hat{\mathbf{u}}_j)} \right\} \right]^{-\frac{1}{2}} \quad (4.65)$$

where χ is a measure of the anisotropy which is determined by the length of the

major and minor axes of the anisotropic particle,

$$\chi = \frac{(\sigma_{ee}/\sigma_{ss})^2 - 1}{(\sigma_{ee}/\sigma_{ss})^2 + 1} \quad (4.66)$$

where σ_{ee} and σ_{ss} are proportional to the length and the cross section diameter of

the molecule respectively.

The energy parameter is also dependent upon χ, and is given by

$$\epsilon(\hat{\mathbf{u}}_i, \hat{\mathbf{u}}_j) = \epsilon_0 \left[1 - \chi^2 (\hat{\mathbf{u}}_i \cdot \hat{\mathbf{u}}_j)^2 \right]^{-\frac{1}{2}} \tag{4.67}$$

ϵ_0 and σ_0 are constants and $\hat{\mathbf{u}}_i$ and $\hat{\mathbf{u}}_j$ are unit vectors describing the orientations of the molecules. When these orientation dependent parameters are inserted into the Lennard-Jones potential, the Berne-Pechukas potential is obtained.

$$U(\hat{\mathbf{r}}_{ij}, \hat{\mathbf{u}}_i, \hat{\mathbf{u}}_j) = 4\epsilon(\hat{\mathbf{u}}_i, \hat{\mathbf{u}}_j) \left[\left(\frac{\sigma(\hat{\mathbf{r}}_{ij}, \hat{\mathbf{u}}_i, \hat{\mathbf{u}}_j)}{r_{ij}} \right)^{12} - \left(\frac{\sigma(\hat{\mathbf{r}}_{ij}, \hat{\mathbf{u}}_i, \hat{\mathbf{u}}_j)}{r_{ij}} \right)^{6} \right] \tag{4.68}$$

The model was first studied by Kushick and Berne [76] using constant temperature molecular dynamics in two and three dimensions. They applied an electric field to the isotropic phase which promoted orientational order and then monitored the system with the electric field removed. It proved easy to generate an ordered system when the electric field was applied, but in its absence a stable ordered state was difficult to achieve, and any observed order was lost after sufficiently long simulations.

The Berne-Pechukas potential suffers from some unrealistic features. Firstly, the strength parameter does not depend upon the intermolecular vector $\mathbf{r}_{ij}$, resulting in an equal interaction for configurations in which molecules are placed side-by-side and end-to-end, whereas a stronger interaction would be expected for the former. Secondly, the r-dependence scales as σ, which results in an overestimation of the width of the attractive well for those configurations in which σ is large [77].

4.2.2.2 Gay-Berne Potential

To address the problems of the Berne-Pechukas potential, Gay and Berne [9] compared it to the interaction between two molecules each composed of a linear array of four Lennard-Jones sites. To allow meaningful comparison, the potentials were normalised such that the well depth of side-by-side interactions was unity. Under these conditions, the two unrealistic features mentioned above were confirmed as the main discrepancies between the Berne-Pechukas potential and the multi-site potential. For the Lennard-Jones array, the side-by-side well depth was found to be approximately five times deeper than the end-to-end well depth, while in the Berne-Pechukas model they are equal. Also the multi-site potential had a well width which was approximately independent of molecular orientation, while in the Berne-Pechukas potential it is closely proportional to σ.

To rectify these anomalous features, Gay and Berne proposed two modifications. Firstly the energy parameter was modified to be explicitly dependent upon $\hat{\mathbf{r}}_{ij}$,

$$\epsilon(\hat{\mathbf{r}}_{ij}, \hat{\mathbf{u}}_i, \hat{\mathbf{u}}_j) = \epsilon_0 \epsilon_1^\nu(\hat{\mathbf{u}}_i, \hat{\mathbf{u}}_j)\epsilon_2^\mu(\hat{\mathbf{r}}_{ij}, \hat{\mathbf{u}}_i, \hat{\mathbf{u}}_j) \qquad (4.69)$$

where $\epsilon_1(\hat{\mathbf{u}}_i, \hat{\mathbf{u}}_j)$ is the strength parameter given in the Berne-Pechukas potential (Eqn. 4.67) and $\epsilon_2(\hat{\mathbf{r}}_{ij}, \hat{\mathbf{u}}_i, \hat{\mathbf{u}}_j)$ is a function taking the same form as the Berne-Pechukas $\sigma(\hat{\mathbf{r}}_{ij}, \hat{\mathbf{u}}_i, \hat{\mathbf{u}}_j)$ term (Eqn. 4.65),

$$\epsilon_2(\hat{\mathbf{r}}_{ij}, \hat{\mathbf{u}}_i, \hat{\mathbf{u}}_j) = 1 - \frac{\chi'}{2} \left\{ \frac{(\hat{\mathbf{r}}_{ij} \cdot \hat{\mathbf{u}}_i + \hat{\mathbf{r}}_{ij} \cdot \hat{\mathbf{u}}_j)^2}{1 + \chi'(\hat{\mathbf{u}}_i \cdot \hat{\mathbf{u}}_j)} + \frac{(\hat{\mathbf{r}}_{ij} \cdot \hat{\mathbf{u}}_i - \hat{\mathbf{r}}_{ij} \cdot \hat{\mathbf{u}}_j)^2}{1 - \chi'(\hat{\mathbf{u}}_i \cdot \hat{\mathbf{u}}_j)} \right\} \qquad (4.70)$$

where,

$$\chi' = \frac{(\epsilon_{ss}/\epsilon_{ee})^{1/\mu} - 1}{(\epsilon_{ss}/\epsilon_{ee})^{1/\mu} + 1} \qquad (4.71)$$

Here ϵ_{ss} is the minimum of the potential for a pair of parallel molecules arranged side-to-side and ϵ_{ee} is the minimum of the potential for two parallel molecules arranged end-to-end. The exponents μ and ν were originally adjusted to obtain a good fit to the four site Lennard-Jones potential. In their work Gay and Berne found that, for $\sigma_{ee}/\sigma_{ss} = 3$, $\epsilon_{ss}/\epsilon_{ee} = 5$, $\mu = 2$ and $\nu = 1$ gave good agreement to the Lennard-Jones array. However these variables can be varied to yield a wide range of anisotropic potentials.

The second modification involves a new functional form of the potential, such that the potential is displaced rather than dilated, and the Gay-Berne potential is expressed as

$$U(\hat{\mathbf{r}}_{ij}, \hat{\mathbf{u}}_i, \hat{\mathbf{u}}_j) = 4\epsilon(\hat{\mathbf{r}}_{ij}, \hat{\mathbf{u}}_i, \hat{\mathbf{u}}_j) \left[\left(\frac{\sigma_0}{r_{ij} - \sigma(\hat{\mathbf{r}}_{ij}, \hat{\mathbf{u}}_i, \hat{\mathbf{u}}_j) + \sigma_0} \right)^{12} \right. $$
$$\left. - \left(\frac{\sigma_0}{r_{ij} - \sigma(\hat{\mathbf{r}}_{ij}, \hat{\mathbf{u}}_i, \hat{\mathbf{u}}_j) + \sigma_0} \right)^{6} \right] \qquad (4.72)$$

where $\sigma(\hat{\mathbf{r}}_{ij}, \hat{\mathbf{u}}_i, \hat{\mathbf{u}}_j)$ is as defined for the Berne-Pechukas potential (Eqn. 4.65). It should be noted that if the anisotropy parameters, χ and χ', are set equal to zero,

corresponding to a spherical molecule, then the Gay-Berne potential reduces to the Lennard-Jones potential. In this way the potential can be regarded as a generalisation of the Lennard-Jones interaction to anisotropic systems.

The Gay-Berne potential has been widely studied for a number of parameterisations and can be regarded as one of the most important anisotropic potentials in use at present. As mentioned above, the first parameterisation suggested for the model was in the original work of Gay and Berne [9], who found satisfactory agreement to the 4 site linear Lennard-Jones array using the parameters $\sigma_{ee}/\sigma_{ss} = 3.0$, $\epsilon_{ss}/\epsilon_{ee} = 5.0$, $\mu = 2$ and $\nu = 1$. The dependence of this potential on intermolecular separation in the four main limiting configurations is shown in Fig 4.2, with the potential varying smoothly between these limiting behaviours for the intermediate configurations which occur in real simulations. This representation clearly shows that the side-by-side interaction is the most attractive; which promotes mesophase formation.

With this parameterisation, Adams *et al* [78] demonstrated a spontaneous isotropic to nematic transition for $\rho^* = 0.32$ and $1.7 \leq T^* \leq 1.8$ using MD in the *NVT* ensemble. This was established by observation of the second rank orientational pair correlation function and the radial pair distribution function.

Further work [79] was carried out using different exponents, $\mu = 1$ and $\nu = 2$, which were found to provide a potential with a greater propensity for mesophase formation; having deeper (i.e. more attractive) well-depths for the side-by-side configuration (shown in Fig. 4.3). Using this parameterisation, it was shown that the Gay-Berne
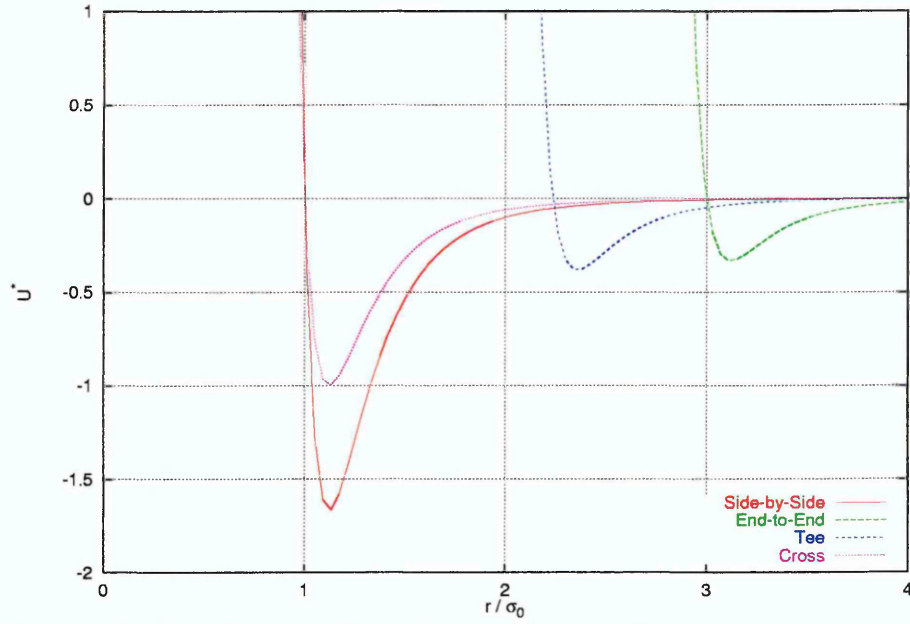
Figure 4.2: Gay-Berne well depths; $\sigma_{ee}/\sigma_{ss} = 3.0$, $\epsilon_{ss}/\epsilon_{ee} = 5.0$, $\mu = 2.0$ and $\nu = 1.0$
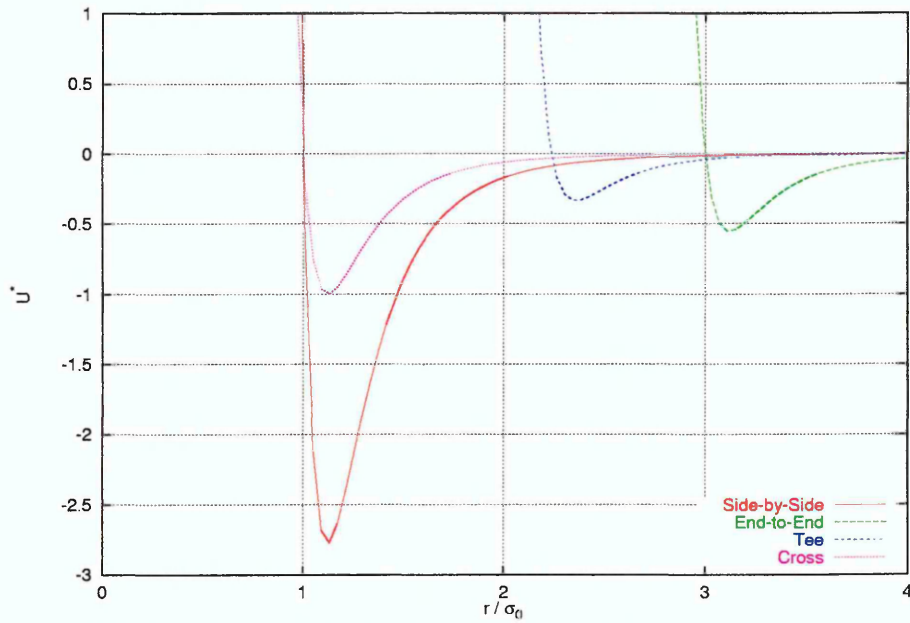

Figure 4.3: Gay-Berne well depths; $\sigma_{ee}/\sigma_{ss} = 3.0$, $\epsilon_{ss}/\epsilon_{ee} = 5.0$, $\mu = 1.0$ and $\nu = 2.0$

potential can exhibit isotropic, nematic, smectic A, smectic B and crystal phases. The phases were observed by monitoring appropriate correlation functions, order parameters, and also by graphical visualisation. One important point raised by this work is that when the Gay-Berne potential is viewed using a contour plot of the potential energy at the transition from positive to negative, the potential is found to be approximately elliptical in shape, and therefore according to the hard-particle models should not be capable of forming smectic phases. However, the strong side-by-side interactions stabilise the smectic phase allowing their observation.

Returning to the original Gay-Berne parameterisation, de Miguel *et al* carried out extensive simulations to construct an approximate phase diagram. The isotropic-vapour transition was located using the Gibbs Ensemble MC method [80], the isotropic-nematic transition by thermodynamic integration [81], and the remaining transitions were determined by observing specific order parameters along various isotherms [82,83].

Investigations into the system size dependence of Gay-Berne fluids [82] with regard to the isotropic-nematic transition have been undertaken. It was found that there was a slight shift ($< 1\%$) in the transition density and pressure with increasing system size from $N = 256$ to $N = 500$.

It has been attempted [84] to model a real material using the Gay-Berne potential. The material chosen was p-terphenyl because of its rigidity and non-polar characteristics. The total pair potential for the real molecule was constructed with 32 Lennard-Jones sites. As with the original Gay-Berne fitting, the parameters were

obtained from comparison of the Gay-Berne potential with the contours of a biaxial averaged set of multi-site interaction potentials. The resultant parameters were found to be, $\mu = 0.8$, $\nu = 0.74$, $\sigma_{ee}/\sigma_{ss} = 4.4$ and $\epsilon_{ss}/\epsilon_{ee} = 39.6$. Thus, the repulsive core is more elongated in shape and the well depth anisotropy is considerable greater than in the previous examples.

Investigations showed that this parameterisation successfully gave isotropic, nematic and smectic A phases. The next approach was to reduce the value of $\epsilon_{ss}/\epsilon_{ee}$, starting from the smectic A phase. It was found the system reverts to a nematic at sufficiently small $\epsilon_{ss}/\epsilon_{ee}$. However, without a full phase diagram, a true evaluation of this system cannot be given.

At this point, it should be mentioned that, except where explicitly stated, all of these simulations, have been performed using molecular dynamics techniques. There has, however, been some work done using the Monte Carlo technique on Gay-Berne fluids [85] with parameterisation to enhance the parallel interactions, $\mu = 1$ and $\nu = 3$. It was found that very long runs were required, especially around the transition regions due to long range fluctuations inherent within this system. Isotropic, nematic and smectic phases were observed, and the isotropic-nematic transition was found to be more strongly first order than for the original Gay-Berne parameterisation. A noticeable shift, of a few percent, in the isotropic-nematic transition temperature temperature was observed between systems of $N = 512$ and $N = 1000$.

Recently more comprehensive studies of the phase diagram using the original Gay-Berne parameterisation and systematic perturbations from it have been conducted.

These have concentrated upon the effect that changes in the well depth parameters [86] and molecular elongation [87] have upon the overall phase behaviour of the system. Particular attention was paid to the vapour-isotropic region (as observed by de Miguel *at al* [80]) and the effect of different parameterisations upon this.

Considering changes to the original parameterisation, it was found that the well depth anisotropy parameter $\epsilon_{ss}/\epsilon_{ee}$ has a significant effect upon the phase behaviour. Increasing values destabilise the nematic phase with respect to the smectic phase at a given temperature, and shift the density at which the smectic phase occurs down slightly. This is because $\epsilon_{ss}/\epsilon_{ee}$ governs the relative strength of the side-by-side and end-to-end well depths, which controls the degree of layering in orientationally ordered systems. Concentrating on low values of $\epsilon_{ss}/\epsilon_{ee}$ it was found that decreasing values shift the isotropic-vapour coexistence region upwards. This is to be expected since lower values involve stronger overall attractive interactions, due to the increasing end-to-end well depth. Combined with a stabilisation of the nematic phase, this leads to a region of stable vapour-nematic coexistence for $1.25 \geq \epsilon_{ss}/\epsilon_{ee} \geq 1.0$. The well depths for $\epsilon_{ss}/\epsilon_{ee} = 1$ are shown in Fig. 4.4.

The molecular elongation parameter σ_{ee}/σ_{ss} was also found to have a significant effect. It was found that with increasing values, the vapour-isotropic region disappears since the smectic phase is stabilised and thus is preferred to the isotropic region (illustrated in Fig. 4.5). The nematic phase still occurs at too high a temperature for any vapour-nematic coexistence to occur, although it too is shifted to lower densities. It was also found that with increasing elongation a smectic A phase enters
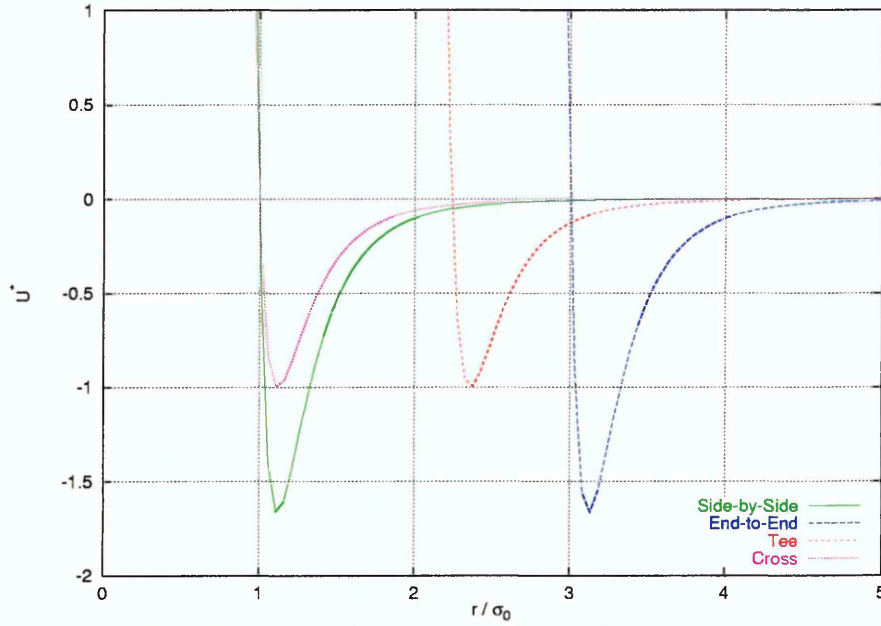
Figure 4.4: Gay-Berne well depths; $\sigma_{ee}/\sigma_{ss} = 3.0$, $\epsilon_{ss}/\epsilon_{ee} = 1.0$, $\mu = 2.0$ and $\nu = 1.0$

the phase diagram, for $\sigma_{ee}/\sigma_{ss} \geq 3.6$, with the density and temperature range at which this phase exists being enlarged with increasing elongation. This stabilisation of the ordered phases is to be expected since increasing σ_{ee}/σ_{ss} results in deeper well depths for parallel configurations of molecules (illustrated in Fig. 4.6), making them energetically more favourable.

Another recent study [88] has been undertaken to examine the nature of the vapour coexistence regions via the Gibbs Ensemble Monte Carlo method and by direct simulation using a single simulation box, the latter allowing properties of the liquid crystal-vapour interface to be examined. Rather than using the original parameterisation, the *stronger* exponents ($\mu = 1.0$ and $\nu = 2.0$) of Ref. [79] were employed, however the shape anisotropy was reduced to $\sigma_{ee}/\sigma_{ss} = 2.0$. This reduces the well depth of the side-by-side configuration, such that it is comparable to that of the
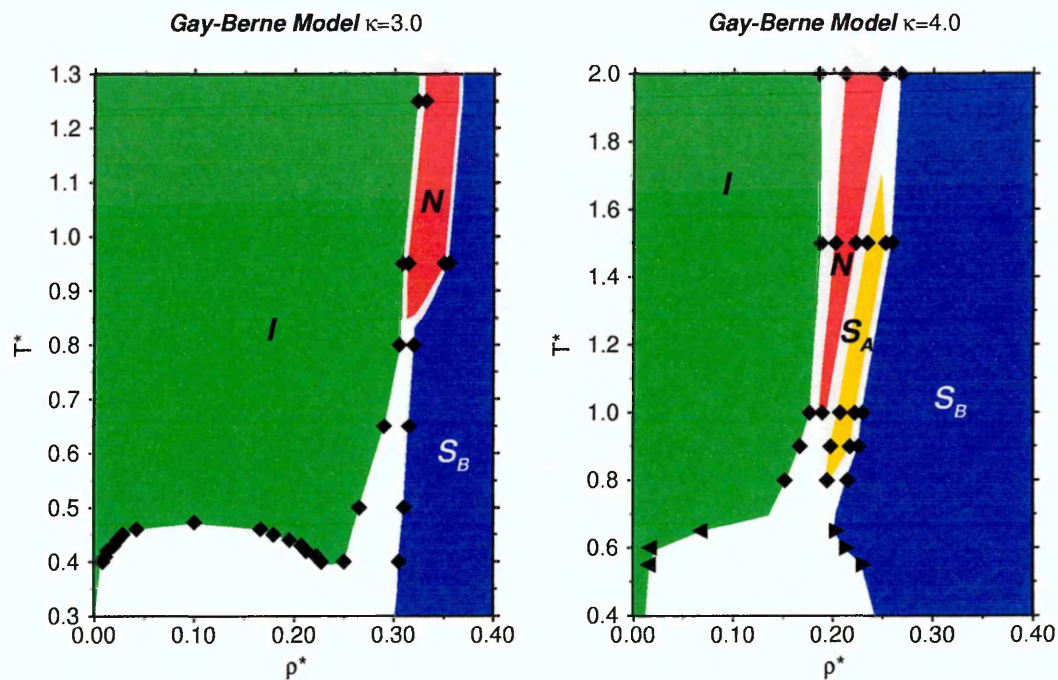
Figure 4.5: Temperature-density phase diagrams for Gay-Berne fluids [87] ($\kappa = \sigma_{ee}/\sigma_{ss}$)
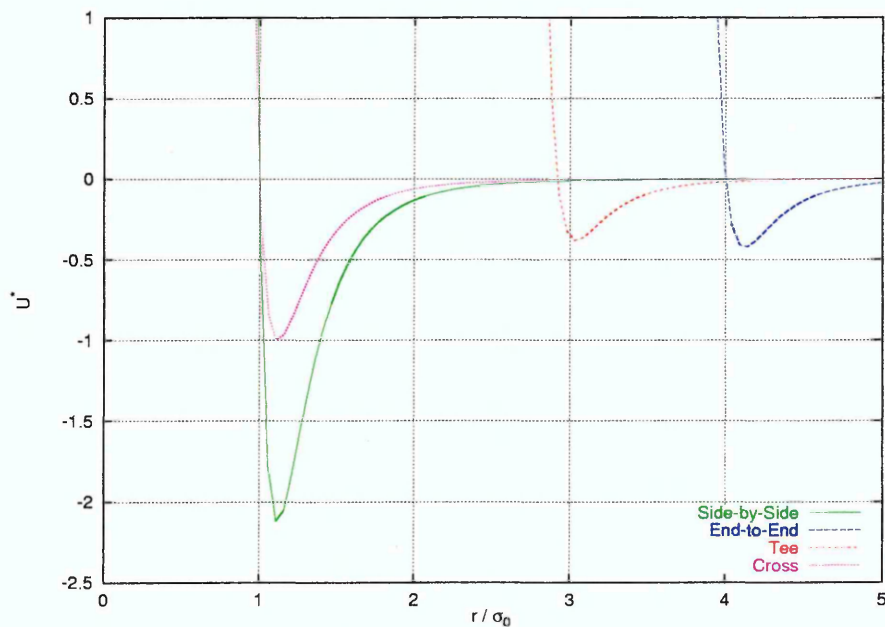

Figure 4.6: Gay-Berne well depths; $\sigma_{ee}/\sigma_{ss} = 4.0$, $\epsilon_{ss}/\epsilon_{ee} = 5.0$, $\mu = 2.0$ and $\nu = 1.0$

original Gay-Berne parameterisation, allowing the vapour-isotropic, -nematic and -crystal coexistence regions to be observed.

Unfortunately the GB potential does not capture the fine detail inherent in real molecules and thus cannot display some of the more subtle liquid crystal features, such as conformational changes within the molecules themselves or bulk tilt ordering. Two limitations of the potential, namely that it is uniaxial and the fact that it applies to identical molecules, have been overcome by generalisation of the potential to biaxial particles [89] (where the effective shape of the molecule is that of a biaxial spherocylinder), dissimilar particles [90] and dissimilar biaxial particles [91].

As with the hard-particle models already mentioned, the effect upon the phase behaviour of the GB model of the inclusion of multipole interactions has been considered by a number of groups, each using a different parameterisation as a reference system. It should be noted, that whilst here only studies considering calamitic systems are discussed, simulations have also been undertaken upon discotic systems with multipole interactions [92, 93].

Satoh et al [94,95] have conducted a series of simulations upon particles interacting via the GB potential ($\sigma_{ee}/\sigma_{ss} = 3.0$, $\epsilon_{ss}/\epsilon_{ee} = 5.0$, $\mu = 1.0$ and $\nu = 2.0$, following Ref. [79]) with a longitudinal point dipole located at the centre and near the end of the molecule within the NVT ensemble. For a central dipole moment the isotropic-nematic transition is independent of the dipole moment, whereas the temperature of the nematic-smectic transition is dependent upon the strength of the dipole, with the nematic region being destabilised with increasing dipole strength. The converse

was found for the terminal dipole, with isotropic-nematic transition being shifted to higher temperatures and the nematic phase being stabilised with increasing dipole strength.

The structure of a system with a longitudinal point dipoles located at the centre or near the end of the molecules, has been investigated by Berardi *et al* [96] using the parameterisation of Ref. [85] as a reference. Simulations were performed at three temperatures, within the isotropic, nematic and smectic A phases to examine the molecular dipole organisation. It was found that for a central point dipole the smectic A phase is replaced by a smectic B phase with random anti-parallel orientational order, whereas for a terminal point dipole the smectic A structure remains, with local polar domains being formed with the net polarisation being zero due to neighbouring domains being orientated in the opposing directions.

Returning to the original Gay-Berne parameterisation, Houssa *et al* [97] have conducted a study, within the constant NPT ensemble to examine the effect of a central point dipole upon the phase behaviour of a non-polar isotherm displaying isotropic, nematic and smectic B phases. These results show that, for a sufficiently strong dipole moment, the nematic phase is destabilised completely with only isotropic and smectic B phases being observed.

A single study [41] has been undertaken to examine the effect of a quadrupole-quadrupole interaction upon the formation of the smectic phase, using molecular dynamics techniques within the NPT ensemble. Here a system of GB molecules, with parameterisation of $\sigma_{ee}/\sigma_{ss} = 4.0$, $\epsilon_{ss}/\epsilon_{ee} = 5.0$, $\mu = 2.0$ and $\nu = 1.0$ (following

83

Ref. [87]), was considered, with an initial configuration taken within the nematic phase with a quadrupole of magnitude $|Q^*| = 1.0$. With decreasing quadrupole strength a smectic A phase was formed for $|Q^*| \leq 0.675$. With further reduction of $|Q^*|$ further transitions were observed, smectic C for $|Q^*| = 0.6$, smectic B for $0.55 \leq |Q^*| \leq 0.4$ and crystal below that. Whilst these observations support the theoretical models developed to explain the formation of the S_C phase based upon a quadrupole-quadrupole interaction, it should be noted that the smectic C phase appears to be formed within a very small range of phase space, and further simulations are necessary to allow further analysis of the phase behaviour of this system.

A molecular dynamics study has also been undertaken to investigate a steric multipole model of liquid crystal geometry [98]. Following a generalised molecular asymmetry model [99], the first three multipoles (monopole, dipole and quadrupole) moments of the molecule are considered to provide molecular asymmetry, and the second and third to describe steric asymmetry. Therefore a longitudinal steric dipole is assigned to molecules having cone-like asymmetry with respect to the cylindrical shape, a transverse steric dipole is assigned to molecules having a banana-like asymmetry. Quadrupoles are represented by antiparallel combinations of dipoles, producing hourglass and zig-zag-like asymmetries for longitudinal and transverse steric quadrupoles respectively.

Simulations were performed upon a system with three Gay-Berne sites per molecule, rigidly constrained into triangle and zig-zag conformations, thus representing longitudinal steric dipole and transverse steric quadrupole interactions. Initial simu-

lations performed within the constant *NVE* ensemble showed that the steric dipole does not effect the temperature of the isotropic-nematic transition, whereas the steric quadrupole suppresses the transition to a lower temperature. Further studies were undertaken within the constant *NPT* ensemble, along an isotherm displaying isotropic, smectic B and crystal phases. The transitions for steric quadrupole were found to occur at lower temperatures than for the steric dipole, indicating that the zig-zag shape frustrates local packing. The smectic B phase for the steric dipole forms well defined layers with an antiparallel molecular arrangement. For the steric quadrupole the layers form a rippled structure, with the ripple becoming more more marked with a greater wavelength as temperature is decreased such that along the wave, particles are tilted with respect to the overall director. This observation does provide some support to the Wulf model [42] where the driving force to tilt the molecules is associated with molecules having a rigid zig-zag structure.

4.2.2.3   Conclusions

Whilst the development of soft potentials has been a significant step forwards, there still remains the problem of relating these model interactions to real molecules where there are many different factors which are known to have dramatic effects upon the observed phase behaviour, for example molecular flexibility is ignored in all the models described above.

Strictly speaking, these soft particle models do not have a hard core, but they have a central region which is very difficult for other molecules to penetrate, and as

such are comparable to a hard core with attractive interactions. The computational simplicity and large parameter space of the Gay-Berne potential make it particularly attractive to the simulator, since it can access the time and length scales required for mesophase ordering.

However, the criticism that such single-site potentials cannot capture the fine detail inherent in real molecules has lead to the development of realistic models, which will now be briefly discussed.

4.2.3 Atomistic Models

Due to the increases in computer power over the last decade it is now possible to create liquid crystal models based upon individual atomic sites. By nature, these models are computationally expensive to simulate, with the large number of interactions needing to be considered restricting the type and size of systems that can be studied. Despite these restrictions good progress has been made, with a number of studies of bulk phases being undertaken over recent years (for a review of current progress see Ref. [100]) for relatively small system sizes and short simulation times. As a result of these limitations, all the conclusions drawn from these studies should be considered as preliminary until larger systems (thus reducing the system size effects) can be simulated for longer periods of time.

The choice of molecules which may be simulated in a realistic manner is also somewhat limited. Ideal candidates for such simulations are molecules which lack strong

polar regions, thus eliminating the need for handling of long range interactions, which would be prohibitively computationally expensive.

Two examples of atomistic simulations which are worthy of note here are the study of DOBAMBC [101] and TBBA [102], which both have strong polar groups and exhibit the S_C^* and S_C phases respectively. These studies only consider the bonded (bond stretching, bond bending and torsional potential energy contributions) and non-bonded (van der Waals) interactions, without the inclusion of any electrostatic interactions. Whilst these studies do not manage to replicate the real phase behaviour of these materials with any great success, which is not surprising due to the lack of electrostatic interactions, they do simulate tilted smectic phases with long-range bond orientational order, thus suggesting that steric packing effects may be sufficient to produce S_C ordering.

Whilst the results from these studies is encouraging, the predictions of the mesophase structure the transition temperatures are somewhat disappointing, and, at present, these atomistic models can only be expected to provide qualitative data at certain state points, rather than quantitative predictions of phase transition temperatures. Such predictions will, hopefully, be possible once larger systems may be considered using refined force fields with the intermolecular potentials carefully tuned to accurately replicate the component atoms.

4.2.4 Conclusions

Clearly the simulation of realistic anisotropic systems is still at a relatively early stage with a great deal of progress to be made. Whilst the development of analytical expressions for the interactions between mesogens has been a significant step forward, there still remains the problem of relating these model interactions to real molecules.

Where computer simulation has been successful is in examining the effects of small perturbations away from ideal behaviour, such as the addition of attractive interactions to a hard particle. The immediate future of simulation is in investigating the effects of changes in these models systematically as the scope of soft particle anisotropic systems is huge, with many different aspects still to be studied.

With respect to the development of models to simulate the S_C phase, the models described here are still relatively undeveloped, with various studies tending to support different theoretical models of the S_C phase. There is still much to be understood about the cause of molecular tilting within the smectic layers. The work presented in the next chapter has focussed upon the development and simulation of a biaxial variant of the Gay-Berne potential formulated to offer a single-site approximation of a molecule in a *zig-zag* conformation in an attempt to contribute further to this understanding.

Chapter 5

Simulation of Rigid *Zig-Zag*

Shaped Molecules

In this chapter, the phase behaviour of a biaxial variant of the Gay-Berne potential, known as the Internally-Rotated Gay-Berne (IRGB) potential, is presented. This variant of the GB potential offers a single-site approximation to a rigid molecule in a *zig-zag* conformation, thereby offering a computationally less expensive model with which to examine the phase behaviour of a system of *zig-zag* shaped molecules than has been considered previously [98].

This chapter is arranged as follows. Firstly the Internally-Rotated Gay-Berne potential is introduced. The results of simulations using Monte Carlo methods within the constant *NVT* and *NPT* ensembles for systems of uniaxial GB particles and biaxial IRGB particles, with varying degrees of biaxiality, are then presented. Thus the

effect of introducing this type of biaxiality upon the phase behaviour is determined for a single reference system. Perturbations away from this initial parameterisation are then examined, with the effect of changing shape anisotropy being considered. Finally, the results of molecular dynamics simulations are presented, from which the dynamic behaviour of the observed phases is determined.

5.1 The Internally-Rotated Gay-Berne Potential

As was discussed in the previous chapter, the Gay-Berne model has been shown to display a wide variety of liquid crystalline phases, and, in two cases [41,98] has been used to test theoretical models proposed to explain the mechanism of tilting within the smectic C phase, with varying degrees of success. One of these studies [98] considered a rigid multi-site model in which each molecule was represented by three Gay-Berne particles, arranged such that the repulsive core regions overlapped. Along with other shapes, a *zig-zag* shaped molecule was considered, thus allowing a comparison to be made with the Wulf model [42] of smectic C formation. Whilst the results from these simulations did not yield a smectic C phase, a rippled smectic B structure was observed such that particles were tilted with respect to the overall director, thus indicating that such a *zig-zag* structure does frustrate the local packing and could induce a tilted smectic phase. Due to the increased number of interactions considered when simulating this type of system, the computational overhead necessary to perform these simulations is relatively high. It is, therefore, desirable to simplify the interaction potential to a single-site, thus allowing a more thorough

examination of the parameter space of this type of system to be undertaken.

In order to make such a simplification, it is necessary to consider the effect of a *zig-zag* conformation upon the interaction between a pair of molecules for the multi-site case. The geometry of such a molecule is shown in Fig. 5.1. Three Gay-Berne particles are joined rigidly at a distance $(\sigma_{ee}/\sigma_{ss})/2$ along each particles long axis and are twisted by an angle δ, within a single plane (the xy plane), to give an overall *zig-zag* shape. The molecular long axis is defined as as the axis upon which all three centres of mass are located.
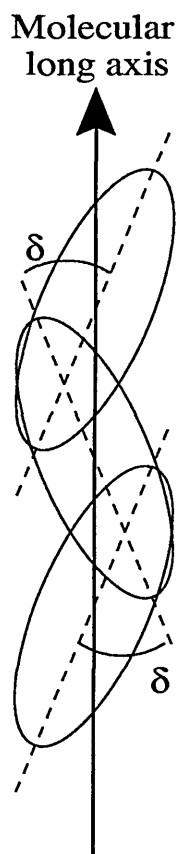

Figure 5.1: Schematic representation of the geometry of a multi-site *zig-zag* model.

Figure 5.2 shows the potential energy contours of two parallel molecules interacting

via this multi-site potential as a function of their intermolecular vector for various values of δ. The parameterisation of the Gay-Berne potential used to generate these charts was $\sigma_{ee}/\sigma_{ss} = 2.0$, $\epsilon_{ss}/\epsilon_{ee} = 5.0$, $\mu = 1.0$ and $\nu = 2.0$. This choice was made since short particles with deep well depths accentuate the behaviour shown by these types of molecules.

The most striking feature of these contour plots is that the shape of the molecules, defined as the contour corresponding to the change in potential energy from positive to negative, becomes more asymmetric with increasing δ. It should, however, be noted that the shapes of these molecules remain approximately symmetric for small y displacements. Therefore, a model which only considers the packing effects of this type of model would not be expected to display a smectic phase in which the molecular long axes (as defined here) were tilted with respect to the layer normal.

The shape asymmetry is, however, not the only effect that the *zig-zag* conformation has upon the interaction between two molecules. As the angle between the constituent particles is increased, the location of the most favourable side-to-side interaction in the xy plane is shifted around the molecule such that the most favourable configuration no longer occurs when intermolecular vector is perpendicular to the molecular long axis. When the interaction between two parallel linear molecules is considered within the xz plane however, the potential contours maintain mirror symmetry about the molecular long axis, with the most favourable arrangement being side-by-side for all values of δ. Thus, the region where the potential energy is at a minimum may be considered as a *doughnut* shape which is perpendicular to
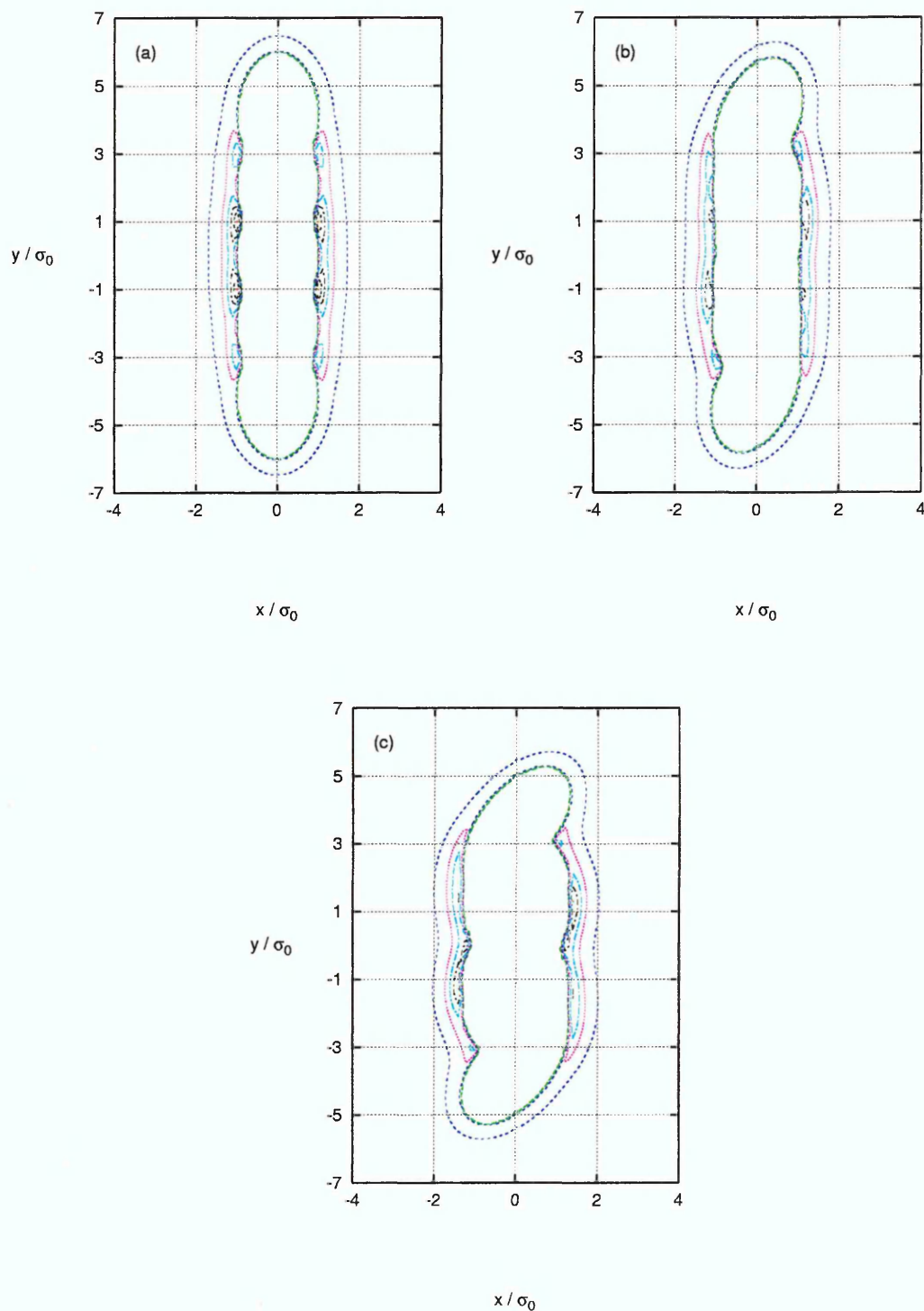
Figure 5.2: Potential energy contours calculated for parallel molecules interacting via the Gay-Berne potential in a three site *zig-zag* conformation as a function of their separation and orientation with respect to the intermolecular vector for (a) $\delta = 0$, (b) $\delta = 30$ and (c) $\delta = 60$. The molecular long axis for each case is orientated along the y axis.

the molecular long axis in the uniaxial case, and is rotated about the z axis with increasing δ.

Since the aim here is to mimic this behaviour using a single-site potential, where the shape function is defined as that of the Gay-Berne potential, we now examine the molecular well depth anisotropy function $\epsilon(\hat{\mathbf{r}}_{ij}, \hat{\mathbf{U}}_i, \hat{\mathbf{U}}_j, \delta)$ given by the summation of the nine $\epsilon(\hat{\mathbf{r}}_{ij}, \hat{\mathbf{u}}_i, \hat{\mathbf{u}}_j)$ terms involved in Neal et al's multi-site particle-particle interaction. Here $\hat{\mathbf{U}}_i$ and $\hat{\mathbf{U}}_j$ are unit vectors giving the orientations of the molecular long axes. Therefore the potential energy between molecules may be expressed as,

$$U(\hat{\mathbf{r}}_{ij}, \hat{\mathbf{U}}_i, \hat{\mathbf{U}}_j, \delta) = 4\epsilon(\hat{\mathbf{r}}_{ij}, \hat{\mathbf{U}}_i, \hat{\mathbf{U}}_j, \delta) \left[\left(\frac{\sigma_0}{r_{ij} - \sigma(\hat{\mathbf{r}}_{ij}, \hat{\mathbf{U}}_i, \hat{\mathbf{U}}_j) + \sigma_0} \right)^{12} \right.$$
$$\left. - \left(\frac{\sigma_0}{r_{ij} - \sigma(\hat{\mathbf{r}}_{ij}, \hat{\mathbf{U}}_i, \hat{\mathbf{U}}_j) + \sigma_0} \right)^6 \right] \qquad (5.1)$$

where,

$$\epsilon(\hat{\mathbf{r}}_{ij}, \hat{\mathbf{U}}_i, \hat{\mathbf{U}}_j, \delta) = \lim_{r_{ij} \to \infty} \sum_{k=1}^{3} \sum_{l=1}^{3} \epsilon(\hat{\mathbf{r}}_{kl}, \hat{\mathbf{u}}_k, \hat{\mathbf{u}}_l) \qquad (5.2)$$

The summation process in eqn. 5.2 is taken with the limit that intermolecular vector $\mathbf{r}_{ij}$ is very large such that the centres of mass of the constituent Gay-Berne sites are coincidental, thus removing the complex relationship that this function will have for small $\mathbf{r}_{ij}$.

Figure 5.3 shows the effect of varying δ upon the molecular well depth anisotropy
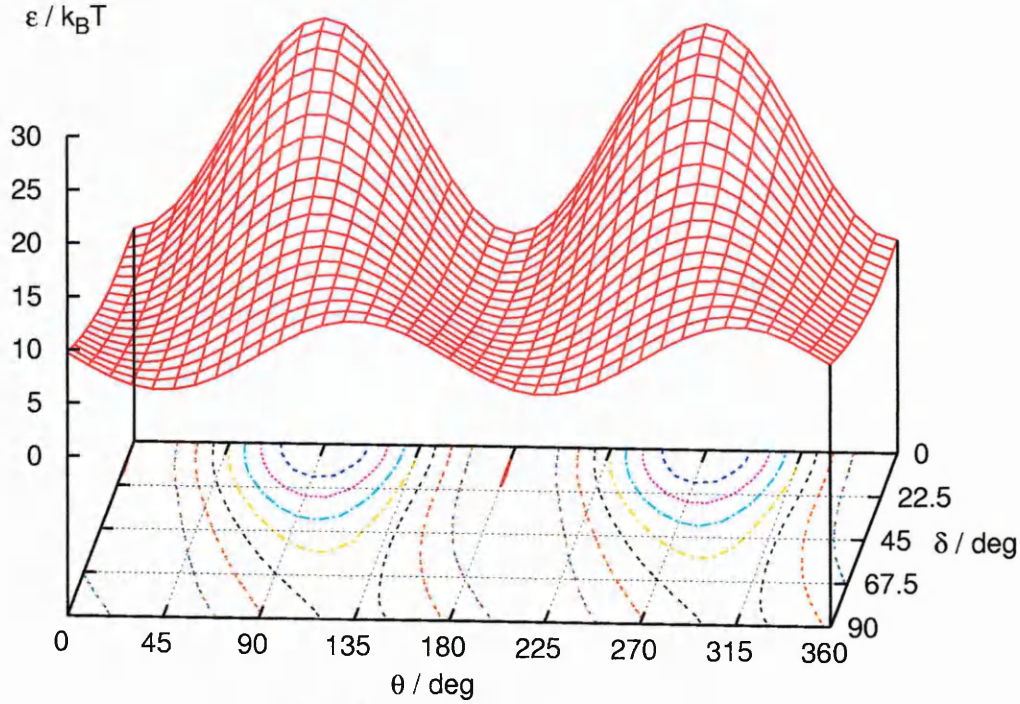
94

Figure 5.3: $\epsilon(\hat{\mathbf{r}}_{ij}, \hat{\mathbf{U}}_i, \hat{\mathbf{U}}_j, \delta)$ for two parallel molecules interacting via a multi-site Gay-Berne potential in a three site *zig-zag* conformation as a function of the angle between the intermolecular vector and the molecular long axis in the *xy* plane $(\cos\theta = \hat{\mathbf{r}}_{ij} \cdot \hat{\mathbf{U}}_i)$, and the angle between constituent Gay-Berne particles (δ).

function for two parallel molecules in the *xy* plane. The locations of the maxima of this function, when combined with the shape function in eqn. 5.1, provide the locations of the potential minima. For the uniaxial case, the largest values of $\epsilon(\hat{\mathbf{r}}_{ij}, \hat{\mathbf{U}}_i, \hat{\mathbf{U}}_j, \delta)$ occur for $\cos\theta = 0$, which leads to the side-by-side configuration becoming the most favoured. As the angle between the constituent molecules is increased, the locations of the maxima of $\epsilon(\hat{\mathbf{r}}_{ij}, \hat{\mathbf{U}}_i, \hat{\mathbf{U}}_j, \delta)$ are rotated about the molecule away from those of the uniaxial case, thus making a tilted phase the energetically most favourable arrangement. Both the non-linear relationship between δ and the locations of the maxima of $\epsilon(\hat{\mathbf{r}}_{ij}, \hat{\mathbf{U}}_i, \hat{\mathbf{U}}_j, \delta)$, and the corresponding reduction

of well depth anisotropy results from the summation process of eqn. 5.2.

Whilst eqn. 5.1 offers a single-site approximation to molecules in a *zig-zag* conformation, the computational effort required to simulate such a model is still considerably greater than that of the single-site Gay-Berne potential. It is, however, possible to rotate the *doughnut* of potential minima associated with a single-site Gay-Berne particle in a similar manner, thus eliminating the need for the computationally costly summation term in eqn. 5.2. This is achieved by decoupling the axes used to define the anisotropic shape and well depth functions. The Internally-Rotated Gay-Berne potential is, thus, defined as

$$
U(\hat{\mathbf{r}}_{ij}, \hat{\mathbf{u}}_i, \hat{\mathbf{u}}_j, \hat{\mathbf{v}}_i, \hat{\mathbf{v}}_j) = 4\epsilon(\hat{\mathbf{r}}_{ij}, \hat{\mathbf{u}}_i, \hat{\mathbf{u}}_j, \hat{\mathbf{v}}_i, \hat{\mathbf{v}}_j) \left[\left(\frac{\sigma_0}{r_{ij} - \sigma(\hat{\mathbf{r}}_{ij}, \hat{\mathbf{u}}_i, \hat{\mathbf{u}}_j) + \sigma_0} \right)^{12} - \left(\frac{\sigma_0}{r_{ij} - \sigma(\hat{\mathbf{r}}_{ij}, \hat{\mathbf{u}}_i, \hat{\mathbf{u}}_j) + \sigma_0} \right)^{6} \right] \quad (5.3)
$$

where,

$$
\epsilon(\hat{\mathbf{r}}_{ij}, \hat{\mathbf{u}}_i, \hat{\mathbf{u}}_j, \hat{\mathbf{v}}_i, \hat{\mathbf{v}}_j) = \epsilon_0 \epsilon_1^{\nu}(\hat{\mathbf{u}}_i, \hat{\mathbf{u}}_j) \epsilon_2^{\mu}(\hat{\mathbf{r}}_{ij}, \hat{\mathbf{v}}_i, \hat{\mathbf{v}}_j) \quad (5.4)
$$

and all other variables have the same meaning as for the Gay-Berne potential. Here $\hat{\mathbf{u}}$ denotes a unit vector defining the shape of the molecule and $\hat{\mathbf{v}}$ denotes a unit vector defining the location of the potential minima, such that the *doughnut* of potential minima occupies a plane perpendicular to $\hat{\mathbf{v}}$. The variable δ is now redefined as the angle between $\hat{\mathbf{u}}$ and $\hat{\mathbf{v}}$ is referred to as the *angle of internal rotation*. Fig-

ure 5.4 shows the potential energy contours for parallel molecules interacting via the Internally-Rotated Gay-Berne potential (with parameterisation $\sigma_{ee}/\sigma_{ss} = 3.0$, $\epsilon_{ss}/\epsilon_{ee} = 5.0$, $\mu = 1.0$ and $\nu = 2.0$) as a function of their separation and orientation with respect to the intermolecular vector for various values of δ. It is clear from eqn. 5.4 that when $\hat{\mathbf{u}} = \hat{\mathbf{v}}$, the Internally-Rotated Gay-Berne potential reduces to the Gay-Berne potential.

It should be noted that the ϵ_1 term in eqn. 5.4 must remain a function of $\hat{\mathbf{u}}$ to promote the tendency of the molecular long axes to align. Without this dependence, the well depth anisotropy will have the unrealistic characteristic that the lowest possible interaction energy is for a configuration where the axes used to define the well depth anisotropy align, with the two $\hat{\mathbf{u}}$ vectors free to lie in any configuration on the cone $\hat{\mathbf{u}} \cdot \hat{\mathbf{v}} = \cos \delta$. This method of calculating ϵ does not include any reduction in the well depth anisotropy with increasing δ as was found with the multi-site model. This feature may be introduced into the Internally-Rotated Gay-Berne potential by reducing the value of $\epsilon_{ss}/\epsilon_{ee}$ as δ is increased. However for the purpose of examining the effect of this type of biaxiality upon the phase behaviour presented in the next section, $\epsilon_{ss}/\epsilon_{ee}$ has been kept constant.
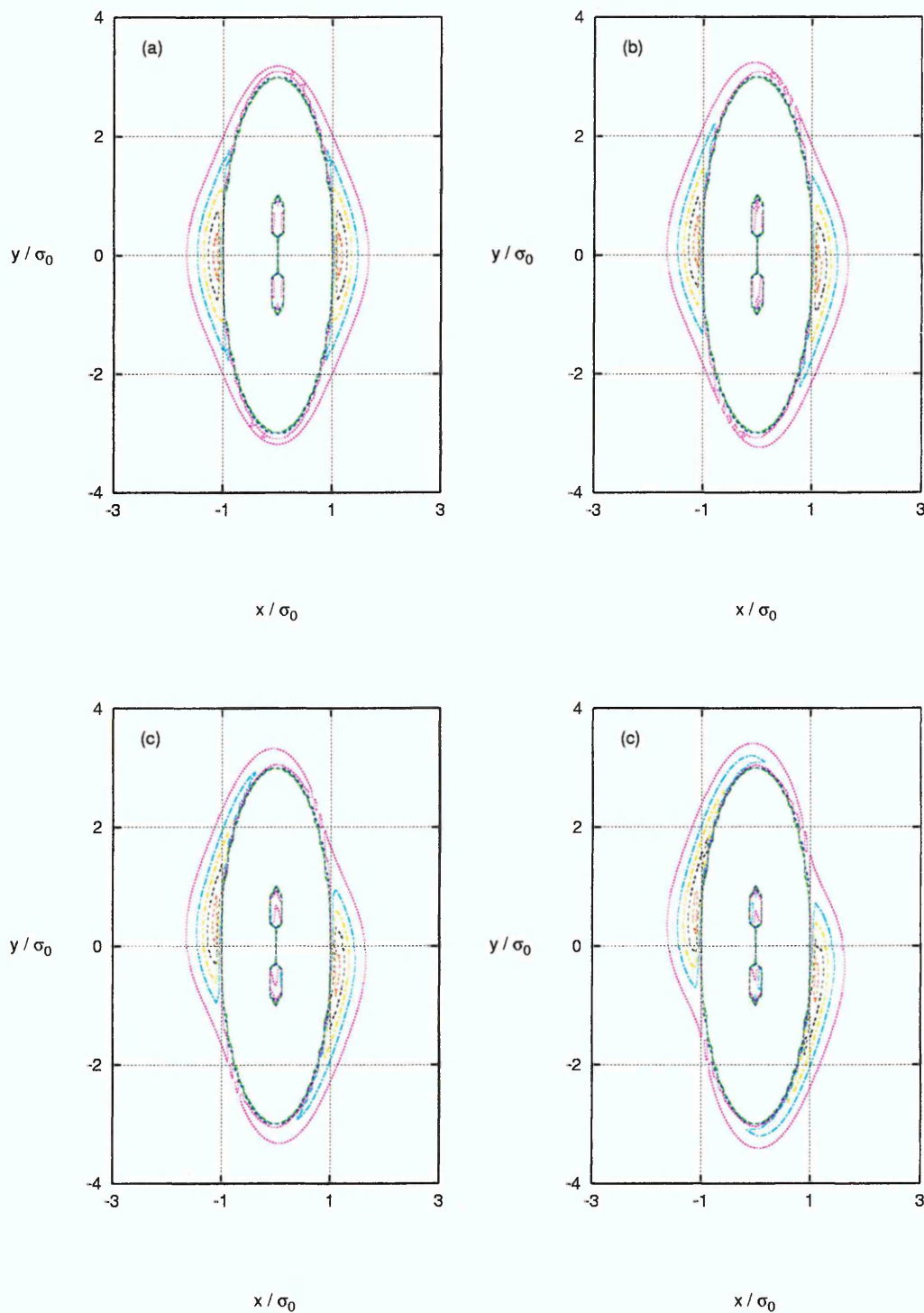
Figure 5.4: Potential energy contours calculated for parallel molecules interacting via the Internally-Rotated Gay-Berne potential as a function of their separation and orientation with respect to the intermolecular vector for (a) $\delta = 0$, (b) $\delta = 10$, (c) $\delta = 20$ and (d) $\delta = 30$. $\hat{\mathbf{u}}$ for each case is orientated along the y axis and $\hat{\mathbf{v}}$ is defined by $(\sin\delta, \cos\delta, 0)$.

5.2 Phase Behaviour of Bulk Internally-Rotated Gay-Berne Fluids

Approximate phase diagrams of fluids interacting via the Internally Rotated Gay-Berne fluid were constructed from Monte Carlo simulation in using the constant NVT and NPT ensembles, for various values of the angle of internal rotation δ.

The ultimate aim of these simulations has been to attempt to obtain a smectic C phase. Since the smectic C phase may be considered as a tilted analogue of the smectic A phase, the parameterisation used here has been chosen so a smectic A phase is observed for the uniaxial case. The phase behaviour of the standard Gay-Berne potential, $\sigma_{ee}/\sigma_{ss} = 3.0$, $\epsilon_{ss}/\epsilon_{ee} = 5.0$, $\mu = 2.0$ and $\nu = 1.0$, has been well classified [80–83], with no smectic A phase being observed. Systematic investigations into perturbations away from this initial parameterisation have shown that increasing the shape anisotropy [87], leads to a smectic A phase being observed. It is believed that the increasing strength of the side-by-side interaction with increasing molecular elongation is responsible for this behaviour. The smectic A phase has, however, been reported using alternative version of the Gay-Berne potential, where the exponents have the alternative values $\mu = 1.0$, $\nu = 2.0$ [79]. For a given σ_{ee}/σ_{ss} and $\epsilon_{ss}/\epsilon_{ee}$ these give much stronger well depths for parallel configurations, which are thought to stabilise mesophase formation. For this reason, the parameterisation of $\sigma_{ee}/\sigma_{ss} = 3.0$, $\epsilon_{ss}/\epsilon_{ee} = 5.0$, $\mu = 1.0$ and $\nu = 2.0$, following Ref. [79], has been chosen for these preliminary simulations of the IRGB.

For all the simulations described here, the intermolecular potential is truncated at a distance $r_{cut} = (\sigma_{ee}/\sigma_{ss}+1)\sigma_0$. When defining a cut off distance, care should be taken that the interaction energy at distances greater than r_{cut} is very small compared with the maximum well depth. Such use of truncated potentials is of great importance within computer simulations; only interactions between molecules with $r_{ij} < r_{cut}$ need be considered, thus eliminating the need to calculate interactions between molecules which are not significant due to their large separation. However, the truncation of the intermolecular potential at a cut-off introduces some difficulties in defining a consistent potential, which is of particular importance in the MD method. The function $U(\mathbf{r}_{ij}, \hat{\mathbf{u}}_i, \hat{\mathbf{u}}_j, \hat{\mathbf{v}}_i, \hat{\mathbf{v}}_j)$ used now contains a discontinuity at $r_{ij} = r_{cut}$ and whenever a pair of molecules crosses this boundary, the total energy will not be conserved. This has been avoided by shifting the potential function by an amount $U_c = U(\mathbf{r}_{cut}, \hat{\mathbf{u}}_i, \hat{\mathbf{u}}_j, \hat{\mathbf{v}}_i, \hat{\mathbf{v}}_j)$; i.e. redefining the pair potential as,

$$
U^s(\mathbf{r}_{ij}, \hat{\mathbf{u}}_i, \hat{\mathbf{u}}_j, \hat{\mathbf{v}}_i, \hat{\mathbf{v}}_j) = \begin{cases} U(\mathbf{r}_{ij}, \hat{\mathbf{u}}_i, \hat{\mathbf{u}}_j, \hat{\mathbf{v}}_i, \hat{\mathbf{v}}_j) - U_c & r_{ij} \leq r_{cut} \\ 0 & r_{ij} > r_{cut} \end{cases} \tag{5.5}
$$

Initially simulations in the constant NVT ensemble were performed, with each system being initiated from a lattice generated at $T^* = 2.5$, a temperature which should be within the isotropic phase. As is usual for computer simulations [7], the starting configuration was equilibrated for a sufficient length of time for all of the observables to adopt stable values. The average values were then calculated over production runs of length such that the averages and their errors were stable. The final configuration from one production run was then used as the starting one at the next state point

being simulated.

5.2.1 Constant NVT Ensemble

Simulations within the constant NVT ensemble have been undertaken for $N = 512$

particles interacting via the Internally Rotated Gay-Berne potential for $\delta = 0$, 20,

30 and 40 with periodic boundary conditions. A single series of simulations was

undertaken for each value of δ at a reduced density of $\rho^* = 0.30$ with reducing

temperature, following Ref. [79], in discrete steps of $\Delta T^* = 0.05$.

Two modifications to the general Monte Carlo scheme, described in section 4.1.1,

have been made. Firstly, due to the biaxiality of the constituent molecules, the

method used to generate the orientation of the molecules within a new configura-

tion consists firstly of a random rotation of the molecule about one of the three

space-fixes axes (the Barker-Watts algorithm [45]), followed by a random rotation

of the molecule about its new $\hat{u}$ axis, thus enabling phase space to be sampled more

efficiently. The second modification has been implemented due to the possibility

that natural structure may not fit the dimensions of the simulation box within the

constant NVT ensemble, with possibility of deformation of translationally ordered

phases arising due to the rigidity of the simulation box [83]. To overcome the pos-

sibility of such deformation the shape of the simulation box is allowed to vary. To

implement this, each MC cycle consists of N attempted particle displacement and

orientational moves, and one attempt to change the shape of the box. The latter

move is attempted by randomly changing the length of one of the box sides (chosen

at random), with the other two lengths also also being changed such that the total volume is kept constant. The translational coordinates of the system may then be scaled such that all particles lie within the new simulation box and, since the volume is being kept constant, the move is accepted or rejected with the usual constant *NVT* acceptance criterion.

Since the stronger version of Gay-Berne potential [79], which is being used as a reference system to study the effect of increasing δ, has only been the subject of a brief study, the behaviour of the uniaxial $\delta = 0$ case will be considered initially.

5.2.1.1 $\delta = 0$

As has already been stated, these simulations were initiated from a lattice at $T^* = 2.50$. The internal energy and order parameter evolutions as the system equilibrates are shown in Fig. 5.5 and 5.6 respectively.

As can be seen, the values are reasonably stable after 40,000 MC sweeps, and thus equilibration periods were typically taken to be 5×10^4 sweeps, increasing to $(1 - 2) \times 10^5$ sweeps in the vicinity of phase transitions. Average values were then measured for various observables over production runs of 5×10^4 sweeps, the errors on these averages being estimated by a block averaging technique, with 100 blocks of 500 sweeps each.

The variation of internal energy as the system was cooled is shown in Fig. 5.7 and the corresponding variation in the nematic order parameter, Q_{00}^2, is shown in Fig. 5.8.
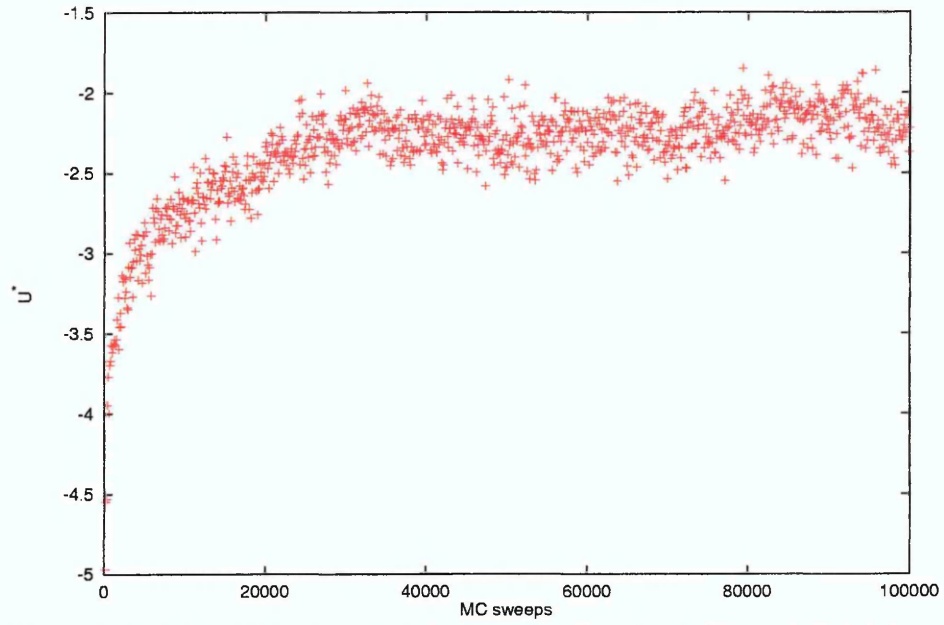
Figure 5.5: Internal energy evolution for $\delta = 0$ at $T^* = 2.5$ initiated from a lattice configuration.
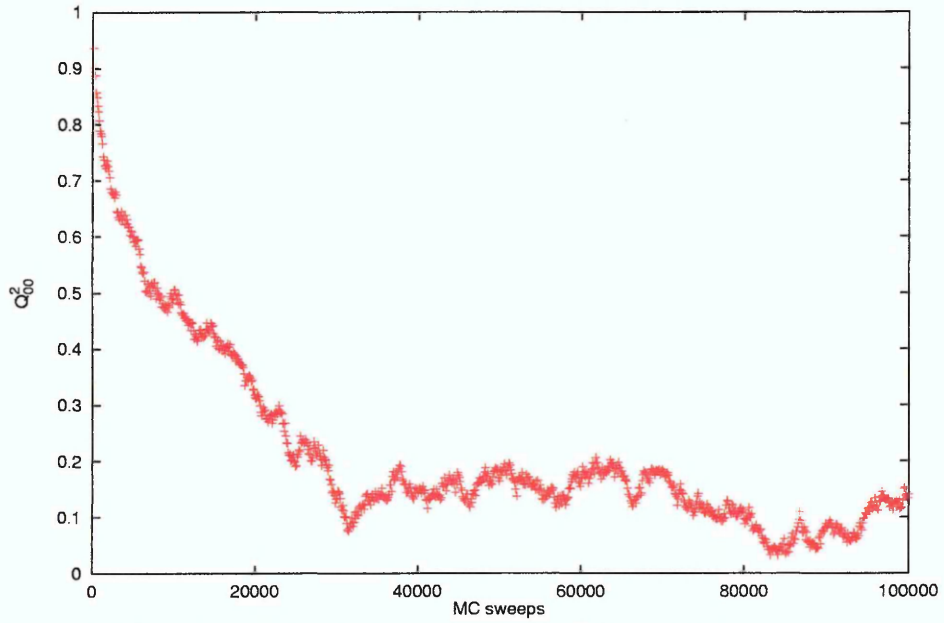

Figure 5.6: Nematic order parameter (Q_{00}^2) evolution for $\delta = 0$ at $T^* = 2.5$ initiated from a lattice configuration.

103

Observation of the nematic order parameter in the region $2.50 \geq T^* \geq 2.20$ suggests the absence of orientational order, indicative of the isotropic phase. However, as the system is cooled, a marked pre-transition fluctuation is observed in the nematic order parameter. This phenomenon has also been observed in the constant NPT ensemble [85,98], with such fluctuations being ascribed to the first-order nature of the transition. At $T^* = 2.15$ a marked discontinuous fall in the average energy is observed, with a corresponding increase in the nematic order parameter. Considering the lack of structure in the pair correlation functions (shown in figures 5.9 and 5.10) this indicates a phase transition from isotropic to nematic.

As the temperature is further reduced, additional discontinuous falls in the average internal energy are observed between $1.40 > T^* > 1.35$ and $1.25 > T^* > 1.20$, with corresponding increases in the nematic order parameter. Examination of the radial distribution function resolved parallel to the layer normal (Fig. 5.9) shows that at $T^* = 1.40$ a weakly layered structure is formed, with the amplitude of the density wave increasing with decreasing temperature. The radial distribution function resolved within the layer (Fig. 5.10) displays only short range structure for $T^* \geq 1.25$, thus indicating a smectic A phase. For $T^* \leq 1.20$ the radial distribution function within the layer displays long range ordering characteristic of a smectic B phase.

When these results are compared with the initial study of this parameterisation of the Gay-Berne potential [79], it should be noted that the nematic phase was reported at $T^* = 2.49$ and the smectic A phase at $T^* = 1.49$. These early simulations
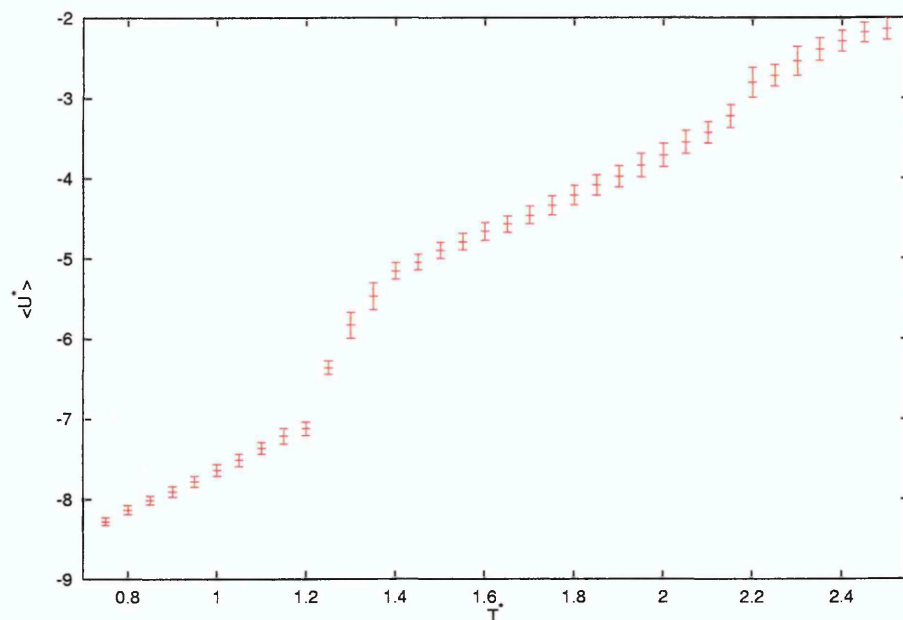
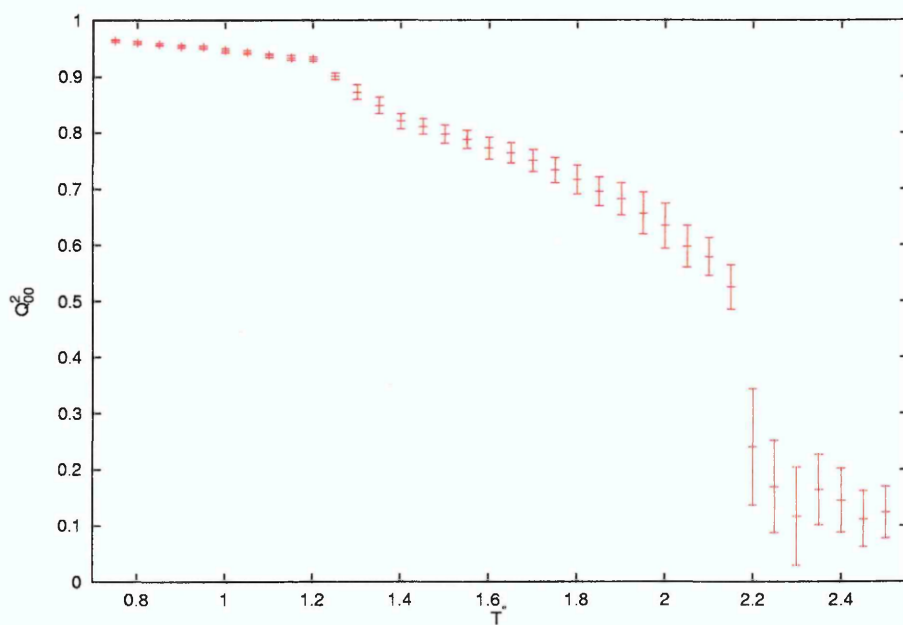Figure 5.7: Average internal energy, $\langle U^* \rangle$, for $\delta = 0$.

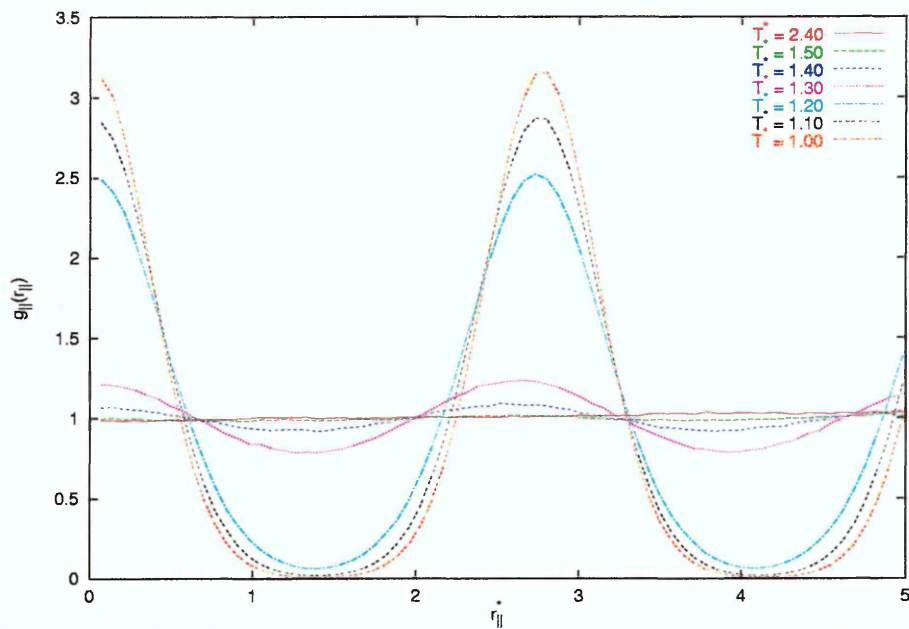Figure 5.8: Average nematic order parameter, Q_{00}^2, for $\delta = 0$.

Figure 5.9: Radial distribution function resolved parallel to the layer normal for $\delta = 0$.
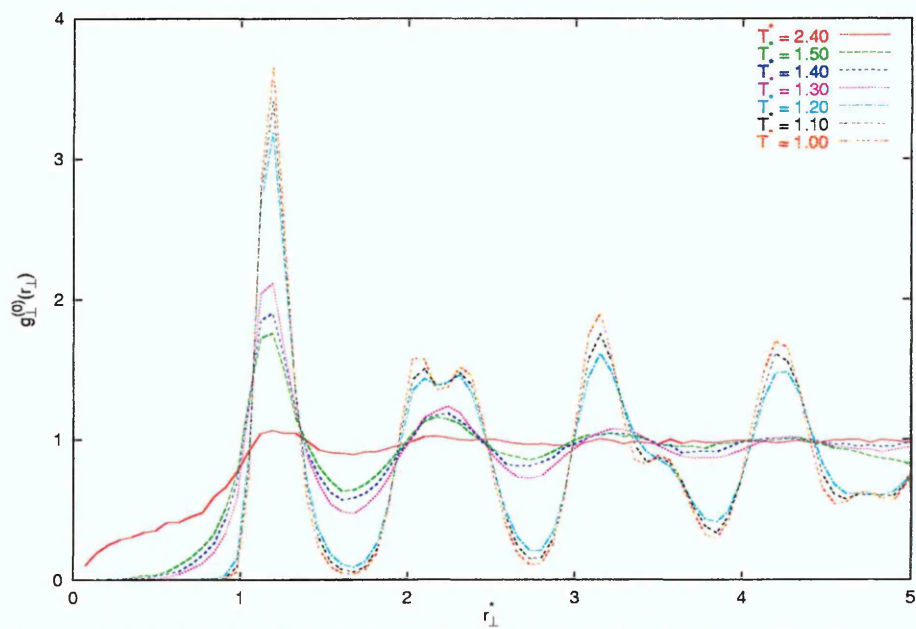

Figure 5.10: Radial distribution function resolved perpendicular to the layer normal for $\delta = 0$.

106

were, however, performed using an un-shifted potential with a shorter cut-off distance, with very large temperature steps between points, $\Delta T \geq 0.5$, and relatively short equilibration times. The results presented here are, however, in much closer agreement with the more recent studies of Satoh et al [94,95] who also considered the un-shifted version of this potential with $\Delta T = 0.2$ in the region of the phase transitions.

Having now defined the behaviour of the uniaxial $\delta = 0$ case as a reference system, the effect of increasing δ may be considered, initially for $\delta = 20$.

5.2.1.2 $\delta = 20$

The variation of the internal energy and orientational order parameters as the system was cooled are shown in Fig. 5.11 and 5.12 respectively. With reducing temperature, the nematic order parameter shows no indication of orientational order in the region $2.50 \geq T^* \geq 2.15$, once again with pre-transition fluctuations being observed in Q_{00}^2. At $T^* = 2.10$ a marked discontinuous fall in the average energy is observed, with a corresponding increase in the nematic order parameter. However, the error bars calculated at this point are rather large. Examination of the evolution of the nematic order parameter over a much longer simulation period (shown in Fig. 5.13) shows that the order parameter fluctuates over a large number of MC sweeps, indicating that the system cannot reach an equilibrium value. Since these fluctuations are much larger than those observed in the isotropic phase, it appears that at this temperature the system is in a coexistence region, between isotropic and nematic, with no single
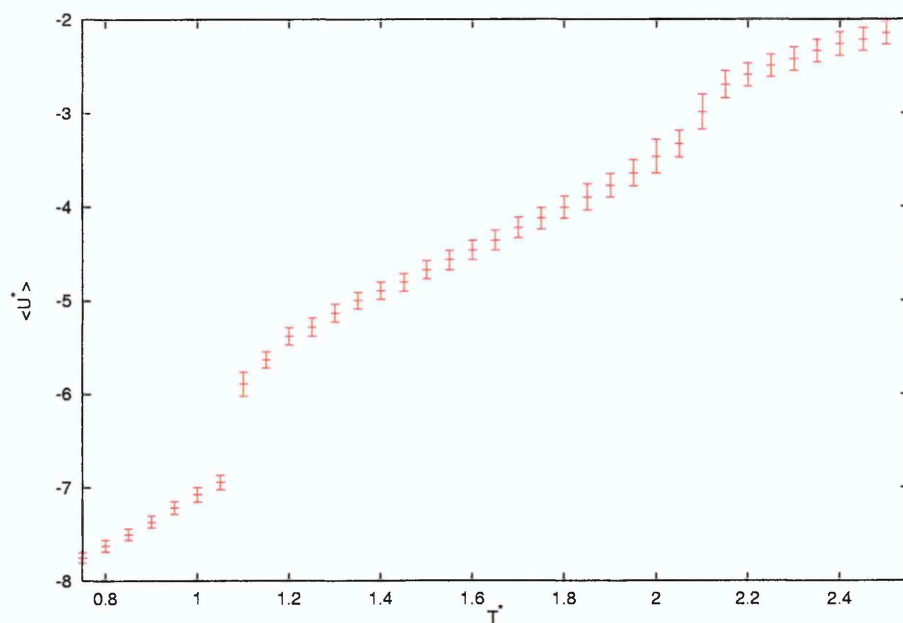
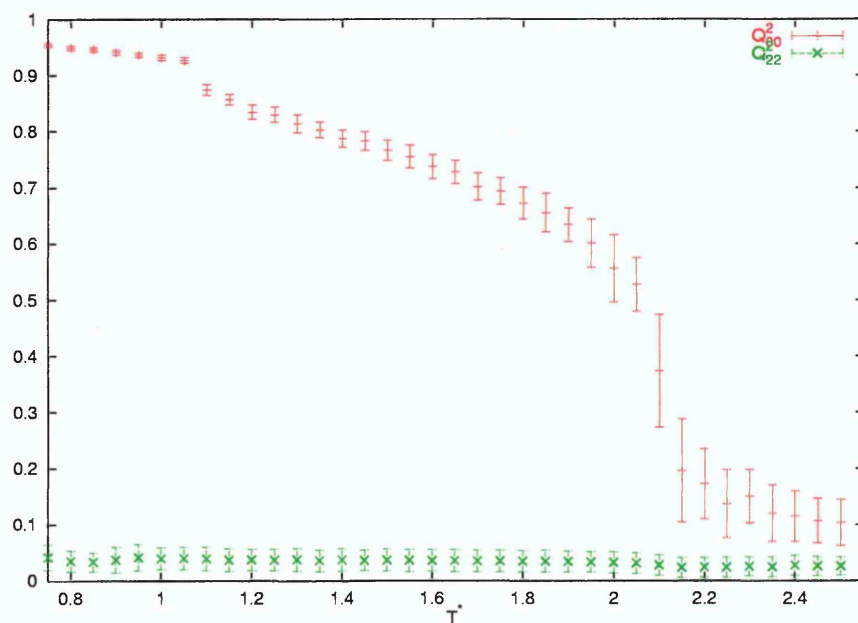Figure 5.11: Average internal energy, $\langle U^* \rangle$, for $\delta = 20$.

Figure 5.12: Average nematic, Q_{00}^2, and biaxial, Q_{22}^2, order parameters for $\delta = 20$.

phase being stable within the constant NVT ensemble. At $T^* = 2.05$, the size of the error bars of the nematic order parameter are much reduced, and, since a lack of structure is observed in the pair correlation functions (Fig. 5.14 and 5.15), it appears that a stable nematic phase is present at this temperature.
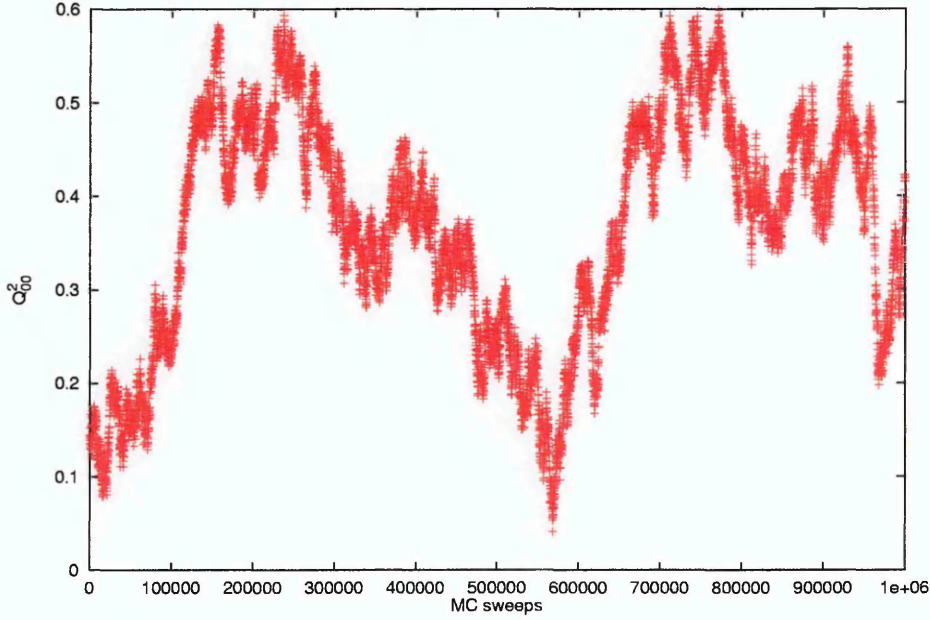
Figure 5.13: Nematic order parameter (Q_{00}^2) evolution for $\delta = 20$ at $T^* = 2.10$.

As with the $\delta = 0$ case, two further discontinuities are observed in the average energy and nematic order parameter for $1.20 < T^* < 1.15$ and $1.10 < T^* < 1.05$, with no increase in the biaxial order being observed. Examination of the radial distribution functions shows that these phases are smectic A and smectic B respectively.

Therefore, the increase in δ from 0 to 20 has caused the same sequence of phases to be observed, with all transitions being shifted to lower temperatures, indicating that the introduction of this type of biaxiality does indeed frustrate ordering.

Figure 5.14: Radial distribution function resolved parallel to the layer normal for $\delta = 20$.

Figure 5.15: Radial distribution function resolved perpendicular to the layer normal for $\delta = 20$.

110

5.2.1.3 $\delta = 30$

The behaviour of the average internal energy and orientational order parameters for a further increase of δ to 30 are shown in Figs. 5.16 and 5.17. Once again an isotropic region is observed over the range $2.50 \geq T^* \geq 2.15$, with pre-transitional fluctuations being ob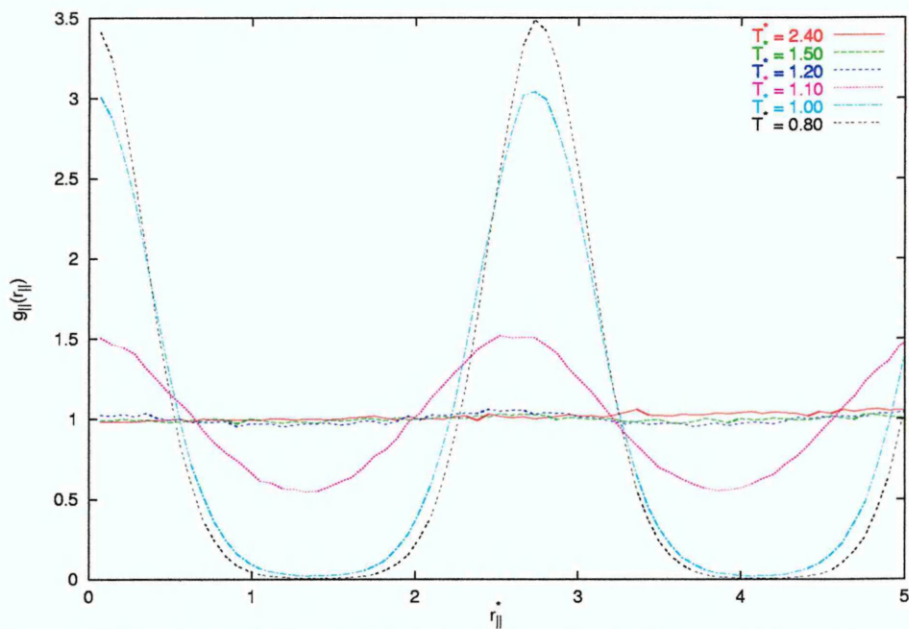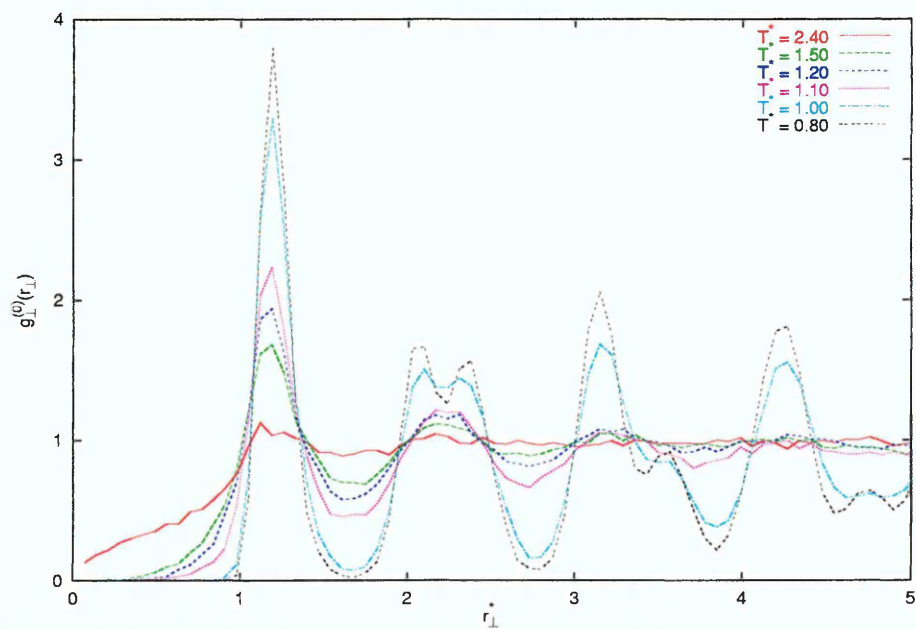served in Q_{00}^2. At temperatures of $T^* = 2.15$ and 2.10 large error bars are once again calculated for Q_{00}^2, and examination of the evolution of Q_{00}^2 over long equilibration periods (not illustrated) shows that the order parameter fluctuates over a large range of values at both of these temperatures, in a manner similar to $\delta = 20$ at $T^* = 2.15$.

With reducing temperature, only one further discontinuity is observed in the average internal energy, over the range $0.95 < T^* < 0.90$, with corresponding continuous increases in both the nematic and biaxial order parameters being observed. Although it should be noted that for $T^* \leq 1.00$ a weak density wave is observed in $g_{\parallel}(r_{\parallel}^*)$ (Fig. 5.18), the amplitude of this is considerably less than any formed for the $\delta = 0$ and 20 cases considered thus far. Examination of the radial distribution function resolved parallel to the layer normal (Fig. 5.18) at lower temperatures shows that this phase has a well defined layered structure, with the distribution function resolved within the layer (Fig. 5.19) displaying characteristic long-range hexatic ordering. Since the biaxial order parameter, Q_{22}^2, takes a non-zero value within this hexatic phase a tilted structure is expected. This is confirmed by the use of visualisation techniques, with a example configuration at $T^* = 0.75$ being illustrated in Fig. 5.20. Further details of this structure are given in the next section.

Figure 5.16: Average internal energy, $\langle U^* \rangle$, for $\delta = 30$.

Figure 5.17: Average nematic, Q_{00}^2, and biaxial, Q_{22}^2, order parameters for $\delta = 30$.

Figure 5.18: Radial distribution function resolved parallel to the layer normal for $\delta = 30$.

Figure 5.19: Radial distribution function resolved perpendicular to the layer normal for $\delta = 30$.
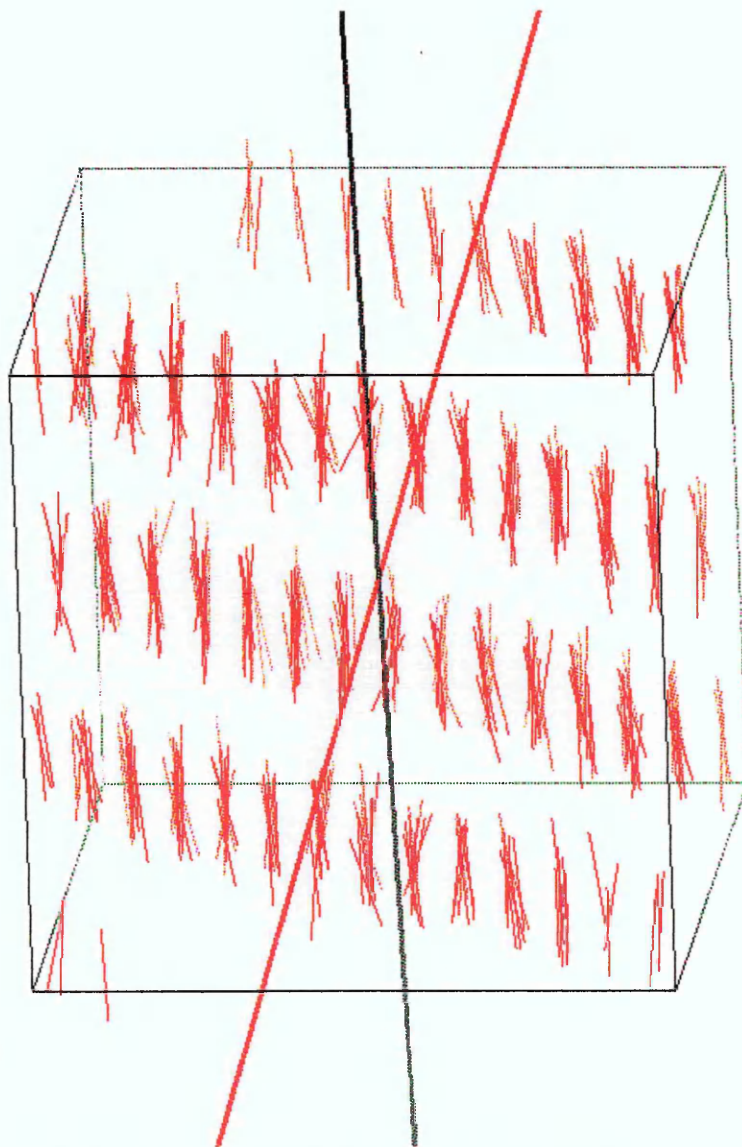
Figure 5.20: Typical configuration for $\delta = 30$ at $T^* = 0.75$. The black vector represents the average director $\hat{\mathbf{n}}$ and the red vector represents the layer normal $\hat{\mathbf{l}}$.

5.2.1.4 $\delta = 40$

For the $\delta = 40$ system, the behaviour of the average internal energy (Fig. 5.21) and orientational order parameters (Fig. 5.22) are similar to those of the $\delta = 30$ system. The isotropic phase is observed over the region $2.50 \geq T^* \geq 2.10$, with the points at $T^* = 2.05$ and 2.00 having large fluctuations in their nematic order parameter, indicating a region of phase coexistence. The range of the nematic phase has been broadened further, with the second transition being observed in the region $0.80 < T^* < 0.85$. As with the $\delta = 30$ case, this low temperature phase displays well defined layering of the constituent molecules (Fig. 5.23) and long range hexatic ordering within the layer (Fig. 5.24).

In addition to the further reduction of the transition temperatures, the nature of the phase transition from nematic to tilted hexatic phase is different from that of the $\delta = 30$ system. The transition here appears to be first-order in nature rather than continuous, with a discrete jump being seen in all of the observed variables in the region of the phase transition. The behaviour of the average tilt angle, $\langle \theta \rangle = \left\langle \cos^{-1}(\hat{\mathbf{l}} \cdot \hat{\mathbf{n}}) \right\rangle$ (shown in Table 5.1), displays first-order characteristics for both $\delta = 30$ and 40, with a large tilt angle (which increases with increasing δ) being observed at the transition temperature which increases only slightly with decreasing temperature. Whilst a smectic C phase is not observed here, this type of temperature dependence of the average tilt has been observed experimentally for the nematic to smectic C transition. For the $\delta = 20$ case no average tilt is found, confirming that only un-tilted phases are observed in this case. The distance between neighbouring
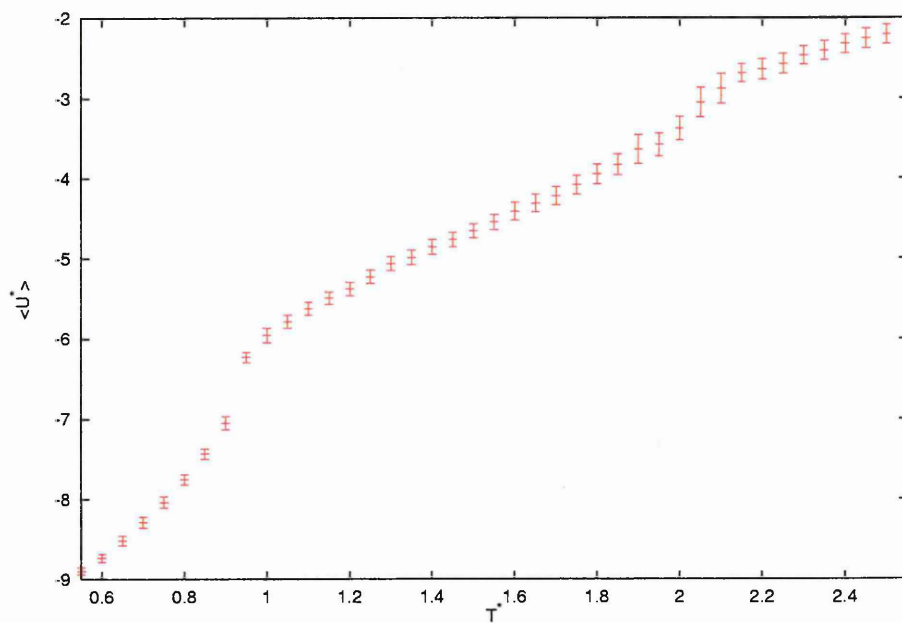
115

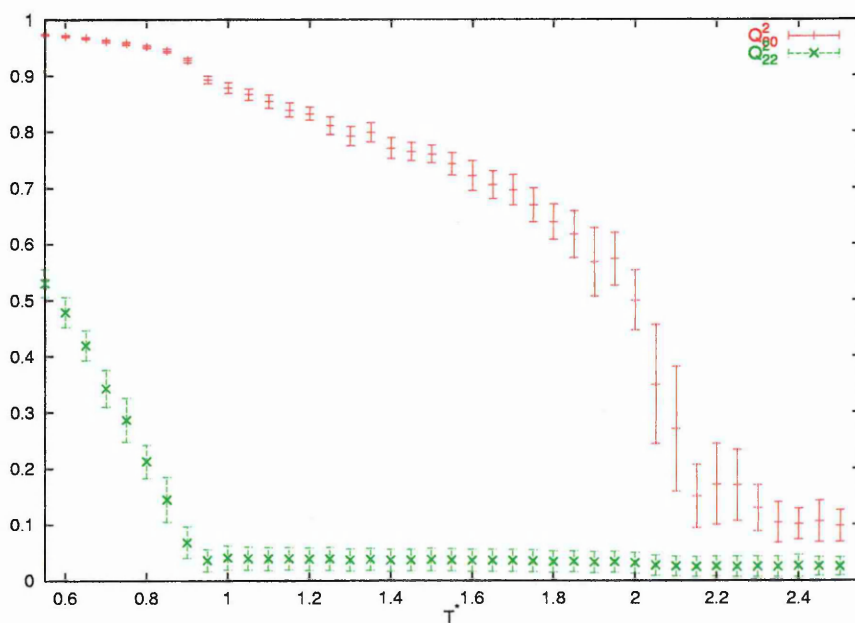Figure 5.21: Average internal energy, $\langle U^* \rangle$, for $\delta = 40$.

Figure 5.22: Average nematic, Q_{00}^2, and biaxial, Q_{22}^2, order parameters for $\delta = 40$.
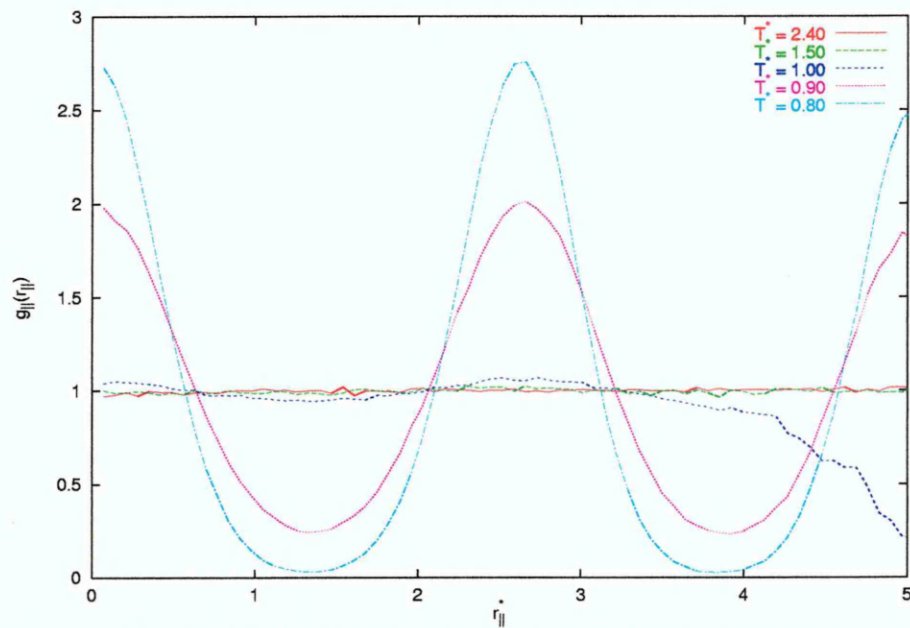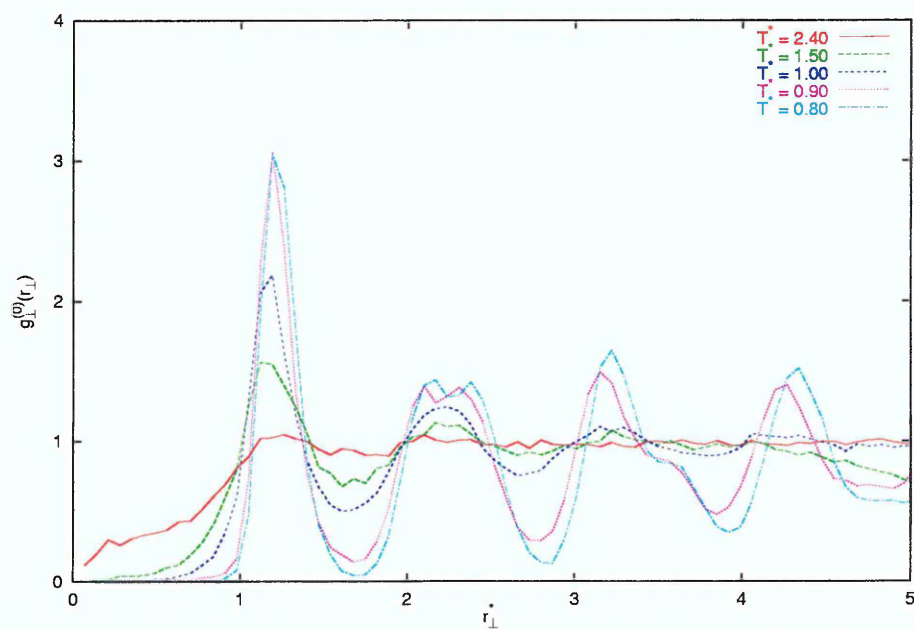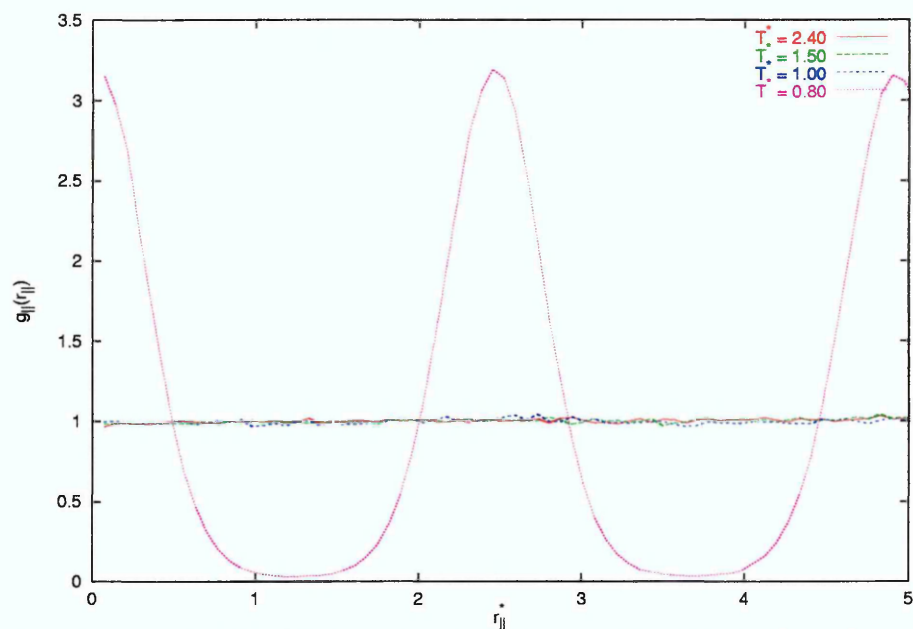
Figure 5.23: Radial distribution function resolved parallel to the layer normal for $\delta = 40$.
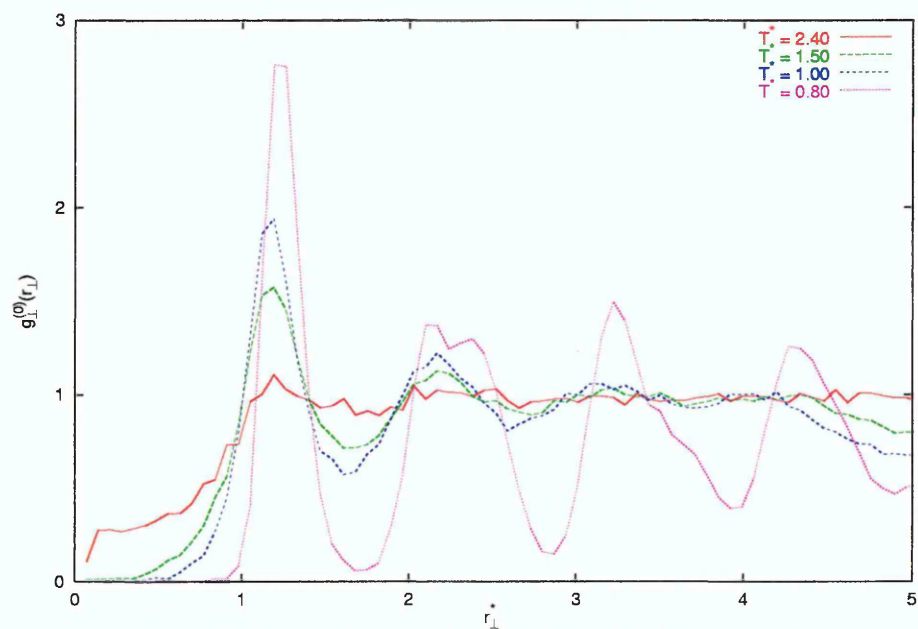
Figure 5.24: Radial distribution function resolved perpendicular to the layer normal for $\delta = 40$.
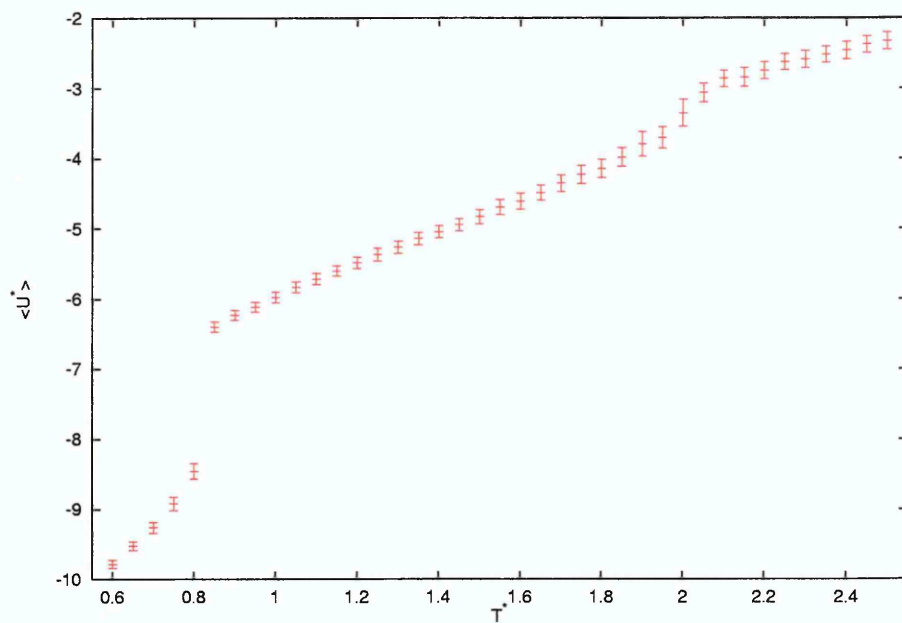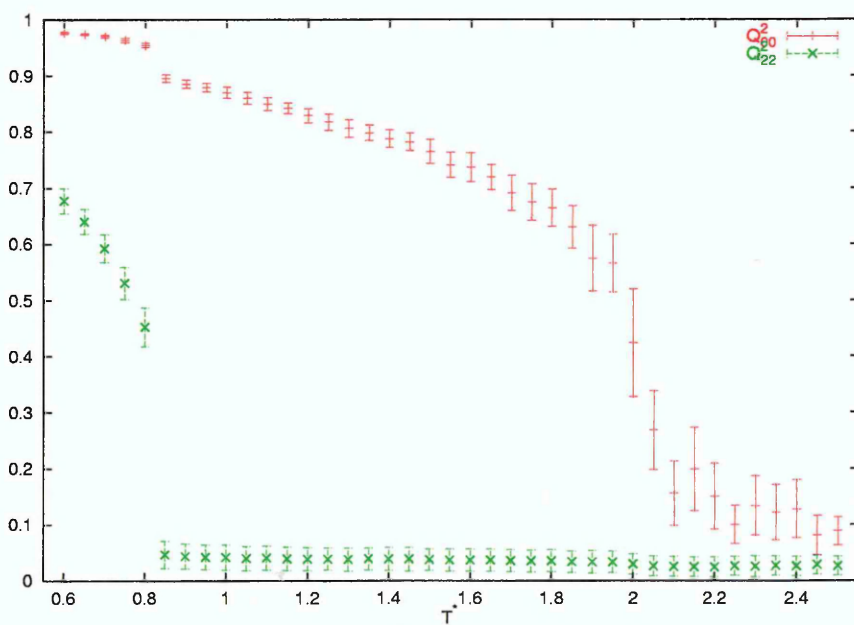
T^*	$\delta = 20$		$\delta = 30$		$\delta = 40$	
	$\langle\theta\rangle$	$r_\parallel^*$	$\langle\theta\rangle$	$r_\parallel^*$	$\langle\theta\rangle$	$r_\parallel^*$
0.95	none	2.72	none	–	none	–
0.90	none	2.74	21.41(1.08)	2.55	none	–
0.85	none	2.74	21.62(1.33)	2.53	none	–
0.80	none	2.76	21.71(0.67)	2.54	31.05(1.66)	2.44
0.75	none	2.75	22.86(0.29)	2.55	32.40(1.46)	2.43
0.70	none	2.76	23.74(0.48)	2.56	34.23(1.46)	2.41
0.65	none	2.77	23.74(0.46)	2.57	34.59(0.41)	2.40
0.60	none	2.77	24.15(0.28)	2.58	35.68(0.74)	2.40

Table 5.1: Average tilt angles, $\langle\theta\rangle$, and distance between adjacent peaks of $g_\parallel(r_\parallel^*)$.

layers, calculated from the distance between adjacent peaks in the radial distribution function resolved parallel to the layer normal (also shown in Table 5.1), is reduced with increasing δ, and, therefore, large increases of $\langle\theta\rangle$. That said, only the $\delta = 40$ case displays the expected decrease of layer separation with increasing $\langle\theta\rangle$. However, for such small changes in the tilt angle, experimental techniques which calculate the tilt angle from the layer spacing and molecular length, with a simple cosine relationship [11], have been shown to be crude and inaccurate [103]. For the results presented here, there is no simple relationship between the average tilt angle and the layer spacing. The layer spacing for the $\delta = 20$ case is less than the length of the molecule indicating interdigitation of molecules into neighbouring layers. For the tilted phases, the lamellar spacing may not be predicted from the average tilt angle and the un-tilted layer spacing, or molecular length, using a simple cosine relation, indicating that the degree of interdigitation is altered by the tilting process.

Since the in-layer radial distribution functions shown in Figs. 5.19 and 5.24 do not allow the type of tilted hexatic phase to be classified, the in-plane distribution

functions resolved parallel and perpendicular to the direction of tilt are employed. For the $\delta = 30$ system these distribution functions within the layer are shown in Fig. 5.25(a). These profiles clearly display long range periodic translational order, which is expected within these hexatic phases, with the period of the density wave being $\approx 0.6\sigma_0$ and $\approx 1.05\sigma_0$ along the components parallel and perpendicular to the direction of tilt respectively. By considering the type of structure which would exhibit this behaviour, it is concluded that the structure of this phase is that of a hexagonal close-packed unit cell with the direction of tilt being towards the apex of the hexagonal net. The tilt has also distorted the hexagonal net in the direction of tilt, such that nearest neighbour bonds which have a component which lies along the direction of tilt are greater than for a undistorted hexatic unit cell, as is expected from experimental observations [12]. These observations, along with the high degree of correlation of these distribution functions between adjacent layers (Figs. 5.25(b) and (c)), identifies this phase as smectic J.

For the $\delta = 40$ case, different behaviour is observed, however. The identities of the in-plane radial distribution functions (Fig. 5.26(a)) are reversed compared with those observed for $\delta = 30$. Such an observation is to be expected for a structure where the direction of tilt is towards the side of the hexagonal net. Once again the hexagonal net is distorted within this tilted phase, with the period of the density wave along the direction of tilt being greater than observed for the undistorted profile perpendicular to the direction of tilt for $\delta = 30$. The inter-layer correlation functions (Figs. 5.26(b) and (c)) show correlation between adjacent layers, thus identifying this phase as smectic G.

119
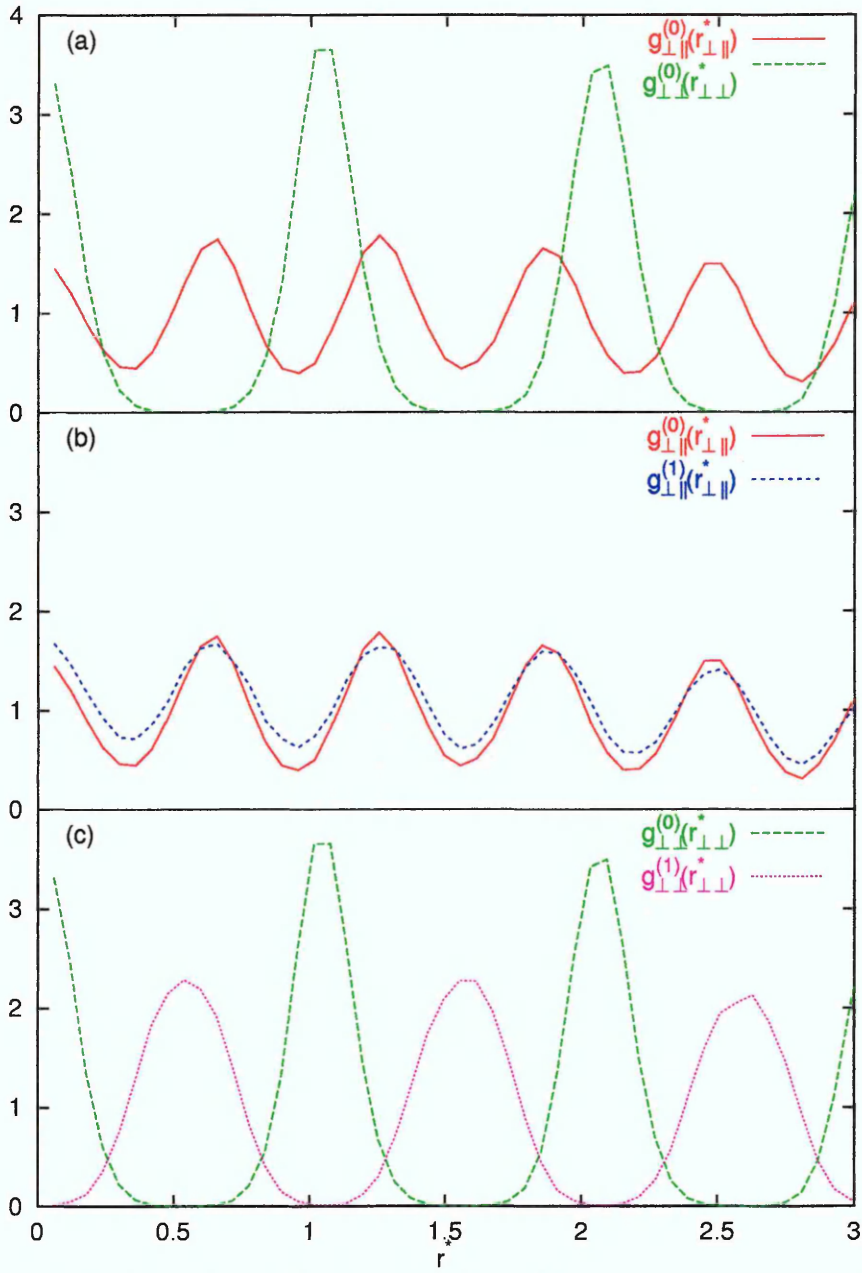
Figure 5.25: Radial distribution functions (a) resolved within the layer parallel, $g_{\perp\parallel}^{(0)}(r_{\perp\parallel}^*)$, and perpendicular, $g_{\perp\perp}^{(0)}(r_{\perp\perp}^*)$, to the direction of tilt and between adjacent layers resolved (b) parallel to the direction of tilt and (c) perpendicular to the direction of tilt for $\delta = 30$ and $T^* = 0.60$.
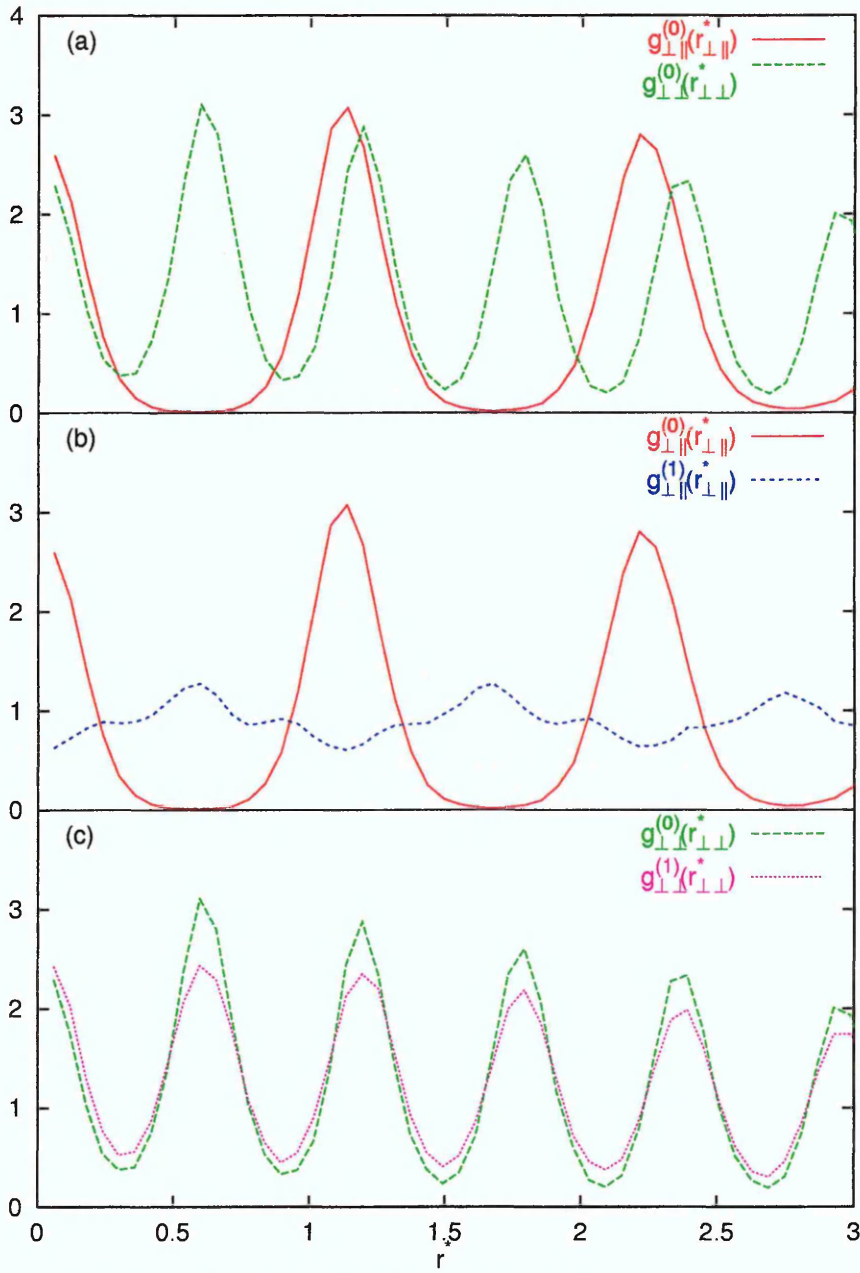
Figure 5.26: Radial distribution functions (a) resolved within the layer parallel, $g^{(0)}_{\perp\|}(r^*_{\perp\|})$, and perpendicular, $g^{(0)}_{\perp\perp}(r^*_{\perp\perp})$, to the direction of tilt and between adjacent layers resolved (b) parallel to the direction of tilt and (c) perpendicular to the direction of tilt for $\delta = 40$ and $T^* = 0.60$.

5.2.1.5 Summary

This first attempt at determining the phase behaviour of the Internally-Rotated Gay-Berne potential has proved to be reasonably successful. As is to be expected increasing the angle of internal rotation, thus representing a molecule with a more pronounced *zig-zag* conformation, frustrates formation of orientationally ordered phases, confirmed by the observation that all the phase transitions are destabilised to lower temperatures with increasing δ. The temperature range of the smectic A region observed for the uniaxial case is also reduced with increasing δ, to a point where no translationally disordered layered structure is observed. The differing phase behaviour of the low temperature tilted hexatic phases with different values of δ indicates a non-trivial ordering mechanism. In-depth analysis of this behaviour will be deferred to the next section.

As has been illustrated for the isotropic-nematic region, simulations performed within the constant NVT ensemble are prone to accessing areas of phase space where the system would like to phase separate into two bulk phases of different density but is prevented from doing so by finite-size effects. Since all previous simulations performed upon this parameterisation of the Gay-Berne potential have also used the constant NVT ensemble [79, 94, 95], at the density used here the nature of any phase coexistence regions remains unexplored. In order to resolve this, details of simulations performed within the constant NPT ensemble will now be presented.

5.2.2 Constant *NPT* Ensemble

In order for approximate phase diagrams to be constructed, the constant *NVT* simulations described above have been complemented by constant *NPT* simulations in which the box size and shape are allowed to vary. Here, each MC cycle consists of *N* attempted particle displacement and orientational moves, and one attempt to change the box volume. The latter move is attempted by sampling the box sides independently, thus allowing the aspect ratio of the box to vary.

5.2.2.1 Results at High Temperature

Initially, the results of simulations along isotherms of high temperature will be presented. The temperature of each isotherm has been chosen to intersect the nematic and smectic phases observed within the constant *NVT* simulations and to be above the critical temperature, thus avoiding the liquid-vapour coexistence region. This process has been undertaken for $\delta = 0$, 30 and 40; the $\delta = 20$ case has not been considered since the sequence of phases observed previously were identical to those observed for $\delta = 0$, with no evidence of biaxial ordering being found within the constant *NVT* study.

The sequences of simulations were initiated from a lattice configuration at low pressures, such as to obtain an isotropic phase. As with the constant *NVT* simulations, the system size was $N = 512$. Equilibration periods were typically taken to be 5×10^4 sweeps, increasing to $(1 - 2) \times 10^5$ sweeps in the vicinity of phase transi-

tions. Average values were then measured over a further 5×10^4 sweeps.

5.2.2.1.1 $\delta = 0$

Two isotherms have been considered for the uniaxial $\delta = 0$ case, at $T^* = 1.50$ and 1.35, such as to intersect the nematic and smectic A regions observed in the constant NVT simulations. Attempts were also made to perform simulations along isotherms with $T^* \leq 1.30$. Equilibration at these lower temperatures proved to be very difficult at low pressures, suggesting that these temperature are below the liquid-vapour critical point. In order to examine this area of phase space other simulation methods, such as the Gibbs Ensemble Monte Carlo method, should be used.

The equations of state obtained from these simulations are shown in Fig. 5.27, with other observables being tabulated in Table 5.2. Increasing pressure or density is accompanied by a phase transition, indicated by a discontinuity in the equation of state and a marked increase in orientational order. The first ordered phase, for both isotherms, is nematic phase, confirmed by the non-zero value adopted by the nematic order parameter and the liquid-like behaviour of the radial distribution functions (Figs. 5.28 and 5.29). At higher densities, both isotherms undergo a second transition into a smectic phase which is identified as smectic B since it displays the characteristic long range in-layer ordering. As is expected, the transition densities and pressures are increased with increasing temperature.
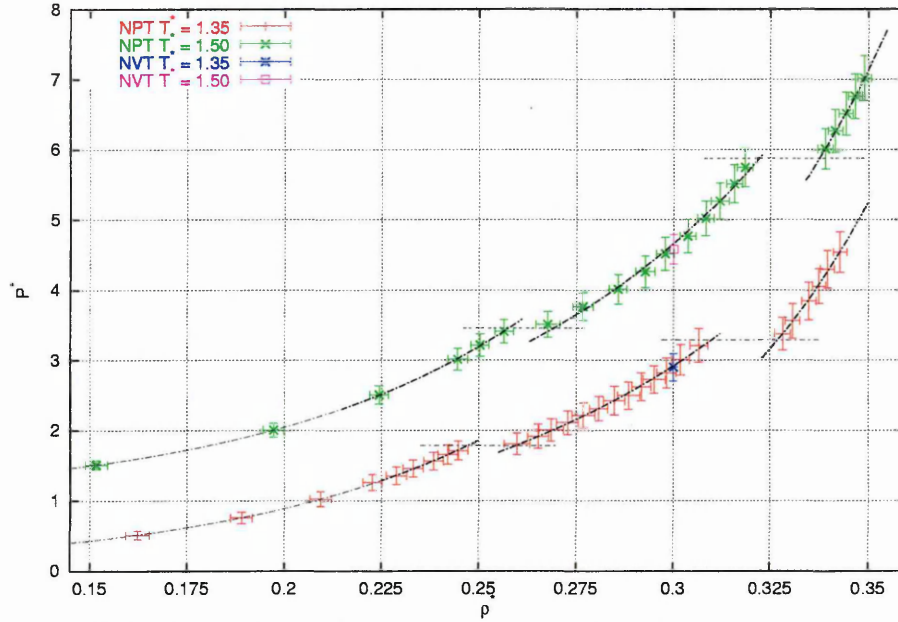
Figure 5.27: Equations of state (pressure P^* vs density ρ^*) with $\delta = 0$ at $T^* = 1.35$ and $T^* = 1.50$; for clarity the latter is displaced upwards by one unit. Lines are drawn to guide the eye, horizontal lines indicate estimates of the transition pressures.

For the lower temperature isotherm, a weak density wave is observed in $g_{\parallel}(r_{\parallel}^*)$ before the smectic B phase is entered. These oscillations are initially observed for pressures greater than 2.70 ($\rho^* \geq 0.295$) with the structure, surprisingly, not being enhanced with increasing pressure. Examination of the equation of state and the other observables does not show any discontinuity with increasing pressure, suggesting that the phase transition is very weak. It should be noted that pre-smectic ordering has been observed previously [104] for a bi-disperse liquid crystalline mixture, attributing this behaviour to the competition between the the differing lengths of the molecular species. This explanation is not valid for the mono-disperse system here. It should, however, be noted that thermodynamic and structural properties near $\rho^* = 0.30$ agree with the quantities calculated for the constant NVT simulation

125

$T^* = 1.35$			$T^* = 1.50$		
P^*	$\langle U^* \rangle$	Q_{00}^2	P^*	$\langle U^* \rangle$	Q_{00}^2
0.50	-1.88(0.06)	0.044(0.017)	0.50	-1.67(0.06)	0.050(0.019)
0.75	-2.26(0.06)	0.058(0.016)	1.00	-2.27(0.07)	0.064(0.022)
1.00	-2.56(0.07)	0.079(0.026)	1.50	-2.66(0.07)	0.095(0.036)
1.25	-2.77(0.07)	0.082(0.027)	2.00	-3.00(0.09)	0.123(0.047)
1.35	-2.90(0.08)	0.117(0.037)	2.20	-3.05(0.08)	0.142(0.047)
1.45	-2.96(0.08)	0.109(0.042)	2.40	-3.16(0.09)	0.153(0.063)
1.55	-3.09(0.09)	0.171(0.050)	2.50	-3.82(0.17)	0.557(0.068)
1.65	-3.14(0.09)	0.160(0.043)	2.75	-4.12(0.13)	0.638(0.039)
1.75	-3.20(0.10)	0.210(0.042)	3.00	-4.48(0.11)	0.734(0.020)
1.80	-3.99(0.16)	0.621(0.037)	3.50	-4.73(0.14)	0.774(0.024)
1.90	-4.20(0.11)	0.674(0.025)	3.75	-5.05(0.11)	0.817(0.011)
2.00	-4.26(0.16)	0.662(0.050)	4.00	-5.18(0.12)	0.830(0.011)
2.10	-4.40(0.13)	0.704(0.031)	4.25	-5.24(0.12)	0.836(0.015)
2.20	-4.55(0.15)	0.736(0.029)	4.50	-5.32(0.12)	0.839(0.014)
2.30	-4.69(0.11)	0.757(0.019)	4.75	-5.36(0.12)	0.839(0.014)
2.40	-4.85(0.15)	0.777(0.023)	5.00	-7.40(0.12)	0.940(0.008)
2.50	-5.00(0.17)	0.801(0.025)	5.25	-7.53(0.11)	0.944(0.004)
2.60	-5.11(0.13)	0.812(0.019)	5.50	-7.60(0.11)	0.945(0.004)
2.70	-5.29(0.20)	0.826(0.021)	5.75	-7.64(0.11)	0.948(0.004)
2.80	-5.43(0.15)	0.843(0.011)	6.00	-7.69(0.11)	0.949(0.004)
3.00	-5.47(0.12)	0.843(0.013)			
3.20	-5.68(0.14)	0.867(0.011)			
3.30	-7.61(0.11)	0.945(0.004)			
3.50	-7.66(0.11)	0.946(0.004)			
3.75	-7.80(0.11)	0.950(0.004)			
4.00	-7.87(0.10)	0.952(0.004)			
4.25	-7.90(0.11)	0.953(0.004)			
4.50	-8.00(0.11)	0.957(0.003)			

Table 5.2: Observable averages at various pressures for $\delta = 0$.
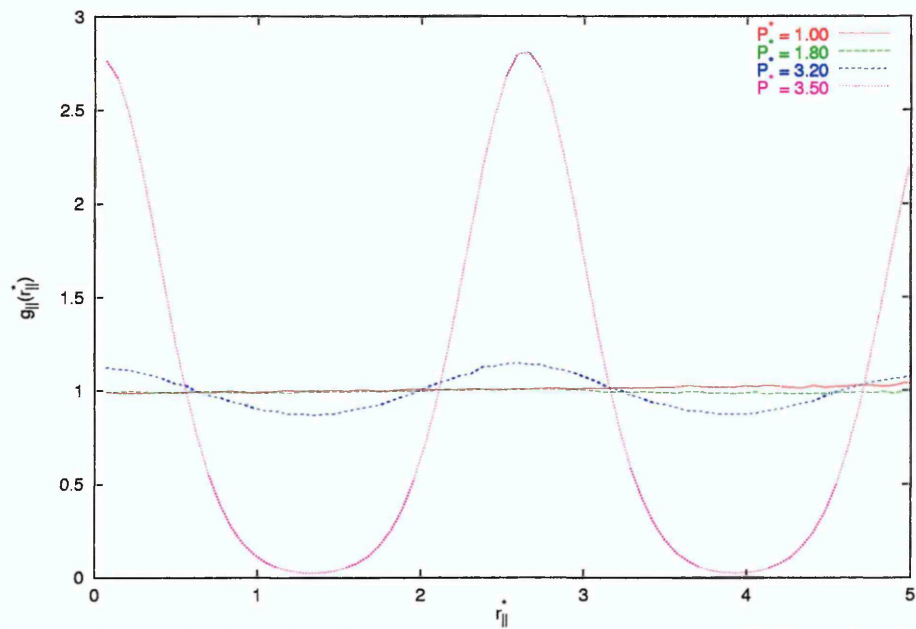
Figure 5.28: Radial distribution function resolved parallel to the layer normal for $\delta = 0$ and $T^* = 1.35$.
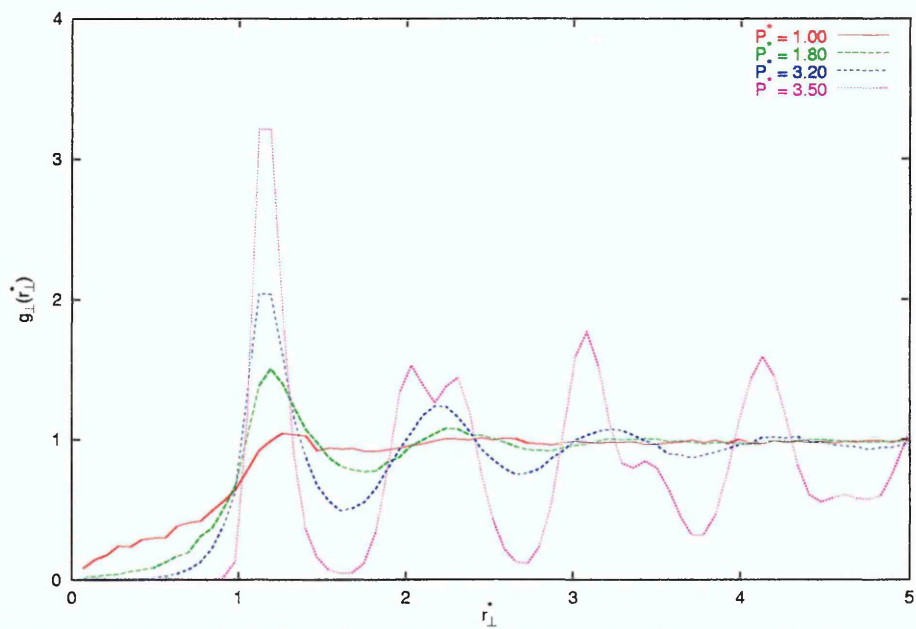
Figure 5.29: Radial distribution function resolved perpendicular to the layer normal for $\delta = 0$ and $T^* = 1.35$.

at this temperature. It would therefore appear that the increased strength of the side-to-side and end-to-end interactions of this parameterisation of the Gay-Berne potential does indeed stabilise mesophase formation although only to a point where a very weak density wave parallel to the layer normal is observed for the smectic A phase.

As has been mentioned above, the observed thermodynamic and structural properties calculated along both isotherms at a density of $\rho \approx 0.30$ agree with the corresponding quantities calculated at the same temperatures within the constant NVT simulations (illustrated upon the equation of state in Fig. 5.27). This would indicate that the modified constant NVT simulation method of allowing the shape of the box to be varied during the course of the simulation does sample phase space correctly.

5.2.2.1.2 $\delta = 30$

For $\delta = 30$ two isotherms have been considered at $T^* = 1.50$ and 1.00. The initial observation that the simulation of the lower temperature isotherm has been possible using the method described above indicates that the liquid-vapour coexistence region of this biaxial model, if existent at all, occurs at a lower temperature than for the uniaxial case. Beyond this, no further comment may be made regarding the nature of this biphasic region since such investigations require the use of the Gibbs Ensemble Monte Carlo methods which have not been implemented during this study.

The equations of state obtained from these simulations are shown in Fig. 5.30, with

128

the other observables being tabulated in Table 5.3. For the $T^* = 1.50$ isotherm only one discontinuity is observed in the equation of state. The marked increase in the orientational order parameter and liquid-like structure in the radial distribution functions (not shown) indicates an isotropic to nematic transition. The transition density is increased compared with that found using the uniaxial model. This observation, along with the absence of a hexatic phase at higher densities, provides more evidence that this type of biaxiality does frustrate orientationally ordered phase formation.
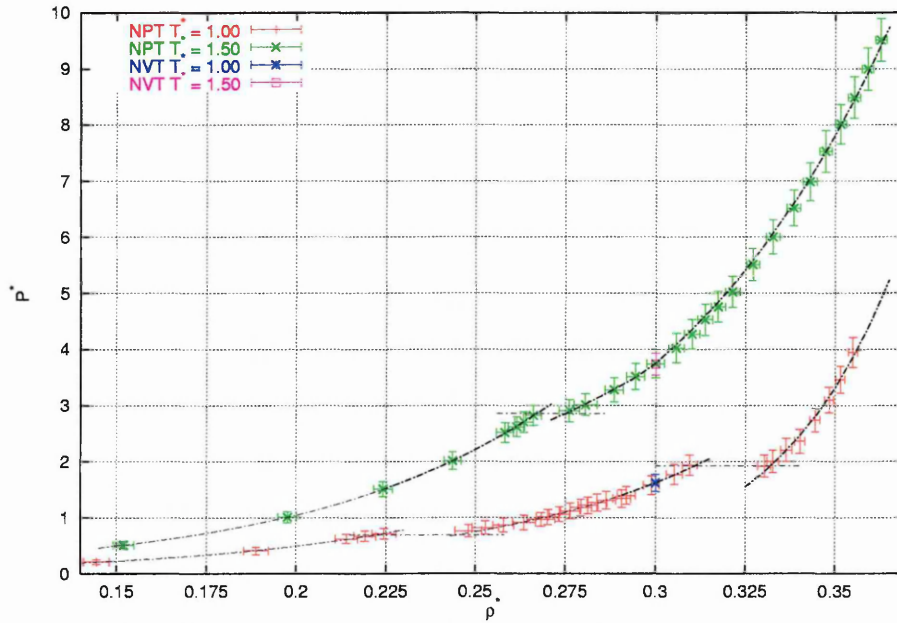
Figure 5.30: Equations of state (pressure P^* vs density ρ^*) with $\delta = 30$ at $T^* = 1.00$ and $T^* = 1.50$. Lines are drawn to guide the eye, horizontal lines indicate estimates of the transition pressures.

For the lower temperature isotherm, an isotropic to nematic transition is observed at a lower density than for $T^* = 1.50$. Once again smectic ordering is observed at higher densities, with a very weak density wave being observed in $g_{\parallel}(r^*_{\parallel})$ (Fig. 5.31) for $P^* \geq 1.30$, corresponding to $\rho^* \geq 0.286$, indicating a very weakly layered smectic

$T^* = 1.00$				$T^* = 1.50$			
P^*	$\langle U^* \rangle$	Q_{00}^2	Q_{22}^2	P^*	$\langle U^* \rangle$	Q_{00}^2	Q_{22}^2
0.20	-1.88(06)	0.058(17)	0.028(14)	0.50	-1.72(05)	0.054(15)	0.027(14)
0.40	-2.58(07)	0.081(27)	0.028(17)	1.00	-2.32(06)	0.062(17)	0.028(15)
0.60	-3.02(08)	0.124(39)	0.025(22)	1.50	-2.68(07)	0.073(23)	0.029(15)
0.65	-3.14(09)	0.137(45)	0.024(19)	2.00	-2.96(07)	0.103(40)	0.029(18)
0.70	-3.26(11)	0.200(76)	0.021(18)	2.50	-3.14(08)	0.100(27)	0.027(20)
0.75	-4.22(13)	0.664(35)	0.034(20)	2.60	-3.22(09)	0.160(68)	0.026(17)
0.80	-4.37(14)	0.694(35)	0.035(19)	2.70	-3.23(12)	0.149(74)	0.024(17)
0.85	-4.53(10)	0.727(21)	0.037(20)	2.80	-3.27(08)	0.153(40)	0.021(16)
0.90	-4.72(12)	0.754(23)	0.037(20)	2.90	-3.85(15)	0.537(51)	0.031(19)
0.95	-4.89(17)	0.779(28)	0.037(20)	3.00	-4.03(18)	0.598(65)	0.032(19)
1.00	-4.91(11)	0.784(16)	0.036(20)	3.25	-4.30(13)	0.679(38)	0.036(19)
1.05	-5.03(11)	0.798(19)	0.037(20)	3.50	-4.46(12)	0.712(29)	0.037(20)
1.10	-5.10(10)	0.810(15)	0.037(19)	3.75	-4.63(11)	0.747(19)	0.037(19)
1.15	-5.20(13)	0.811(16)	0.037(20)	4.00	-4.80(11)	0.778(20)	0.035(19)
1.20	-5.24(09)	0.816(12)	0.038(21)	4.25	-4.91(10)	0.793(19)	0.036(20)
1.25	-5.34(10)	0.831(14)	0.039(20)	4.50	-4.96(10)	0.804(15)	0.037(19)
1.30	-5.42(10)	0.833(14)	0.038(20)	4.75	-5.03(11)	0.805(16)	0.037(20)
1.35	-5.65(11)	0.859(12)	0.039(20)	5.00	-5.14(10)	0.828(10)	0.038(20)
1.40	-5.67(12)	0.858(15)	0.039(21)	5.50	-5.22(09)	0.834(13)	0.036(20)
1.60	-5.90(11)	0.879(11)	0.039(22)	6.00	-5.31(10)	0.850(10)	0.040(21)
1.80	-6.12(12)	0.888(10)	0.038(20)	6.50	-5.41(10)	0.863(10)	0.038(20)
2.00	-6.24(10)	0.898(07)	0.041(21)	7.00	-5.45(11)	0.868(12)	0.038(20)
2.10	-8.04(11)	0.958(03)	0.111(36)	7.50	-5.50(10)	0.875(08)	0.038(20)
2.20	-8.14(11)	0.961(03)	0.129(37)	8.00	-5.53(10)	0.882(08)	0.038(20)
2.50	-8.41(10)	0.969(02)	0.137(39)	8.50	-5.57(11)	0.890(08)	0.037(20)
3.00	-8.49(10)	0.971(02)	0.143(36)	9.00	-5.61(11)	0.897(07)	0.039(20)
3.50	-8.55(10)	0.973(02)	0.164(35)	9.50	-5.63(11)	0.900(06)	0.038(20)
4.00	-8.65(09)	0.975(02)	0.177(38)				
4.50	-8.67(09)	0.977(02)	0.198(39)				
5.00	-8.68(09)	0.976(02)	0.198(41)				

Table 5.3: Observable averages at various pressures for $\delta = 30$.
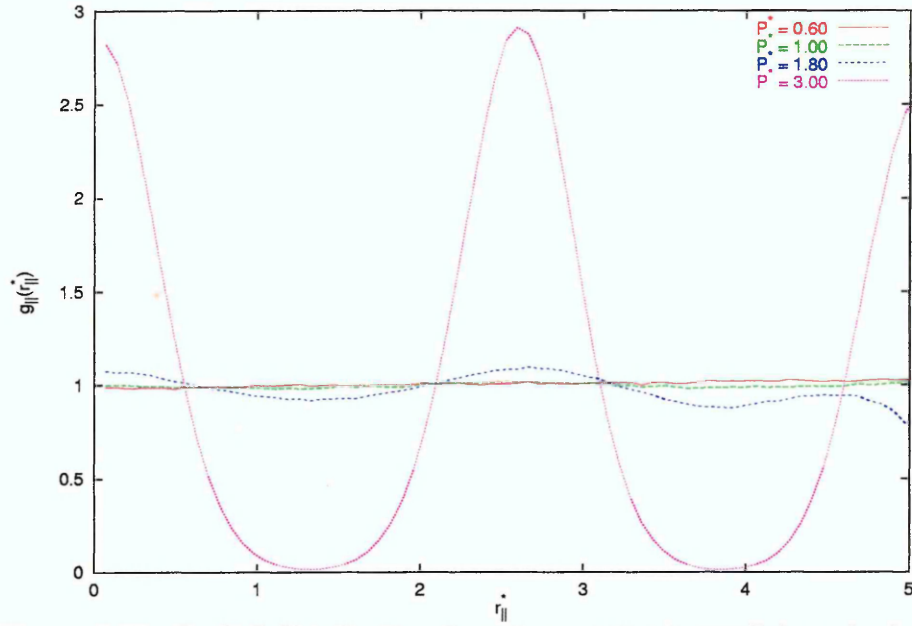
130

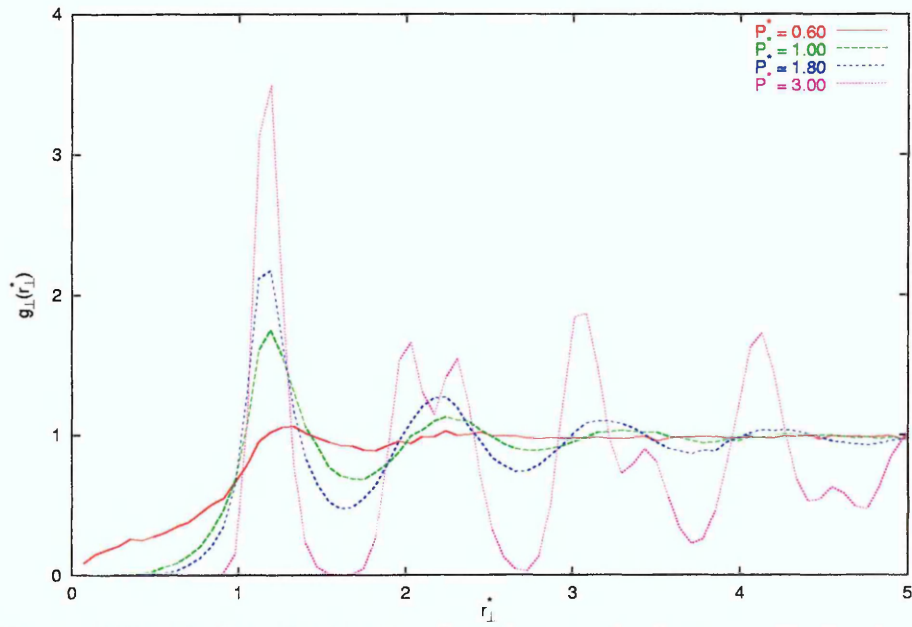Figure 5.31: Radial distribution function resolved parallel to the layer normal for $\delta = 30$ and $T^* = 1.00$.

Figure 5.32: Radial distribution function resolved perpendicular to the layer normal for $\delta = 30$ and $T^* = 1.00$.

131

phase. As with the $\delta = 0$ case, there is no evidence, from examination of the equation of state or any of the other observables, that a phase transition from nematic to smectic A occurs. Recall that a weakly layered structure has been observed at $T^* = 1.00$ in the constant NVT simulations. With further increase in density a second discontinuity is observed in the equation of state, with a corresponding increase in both nematic and biaxial order parameters. Examination of the radial distribution functions (Fig. 5.31 and 5.32) confirms that this low temperature, high density phase has a well defined layered structure and long range hexatic ordering within the layer. Visualisation techniques confirm that a tilted hexatic phase, similar to that illustrated in Fig. 5.20, is being formed. In order to classify the type of tilted phase, the in-plane radial distribution function resolved parallel and perpendicular to the direction of tilt is once again employed. These profiles, shown in Fig. 5.33, show that the direction of tilt is towards to apex of the hexagonal net with correlation between adjacent layers, thus identifying this phase as smectic J.

5.2.2.1.3 $\delta = 40$

For the $\delta = 40$ case only one isotherm at $T^* = 1.00$ has been considered. The higher temperature isotherm has not been considered here, since only isotropic and nematic phases were observed for the $T^* = 1.50$ isotherm with $\delta = 30$, and therefore only these two phases would be expected. The equation of state obtained for this isotherm is shown in Fig. 5.34 with the other observables being tabulated in Table 5.4. Once again an isotropic to nematic transition is observed, at approximately

132

Figure 5.33: Radial distribution functions (a) resolved within the layer parallel, $g_{\perp\|}^{(0)}(r_{\perp\|}^*)$, and perpendicular, $g_{\perp\perp}^{(0)}(r_{\perp\perp}^*)$, to the direction of tilt and between adjacent layers resolved (b) parallel to the direction of tilt and (c) perpendicular to the direction of tilt for $\delta = 30$ and $P^* = 3.00$.

the same pressure as for $\delta = 30$, although the coexistence region extends over a larger range of densities. With increasing density, there is no evidence of any smectic ordering before the second discontinuity in the equation of state, which occurs at a considerably higher density than for $\delta = 30$, as expected given the increase in δ. The radial distribution functions (Figs. 5.35 and 5.36) along with the non-zero value of the biaxial order parameter show that, once again, a tilted hexatic phase is formed. Examination of the in-plane radial distribution function resolved parallel and perpendicular to the direction of tilt (Fig. 5.37) show that this phase is also a smectic J, rather than the smectic F indicated by the constant NVT results.
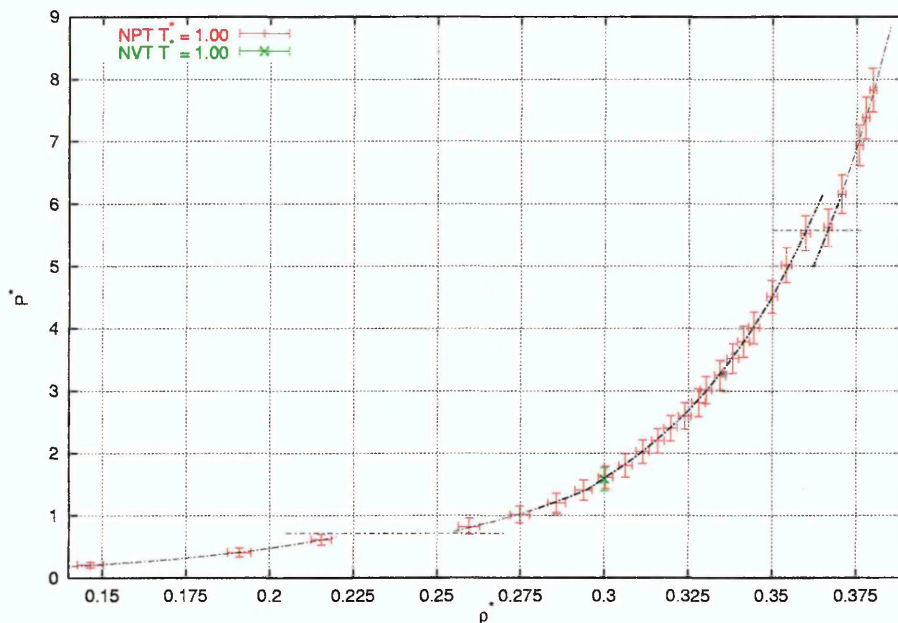
Figure 5.34: Equation of state (pressure P^* vs density ρ^*) with $\delta = 40$ at $T^* = 1.00$. Lines are drawn to guide the eye, horizontal lines indicate estimates of the transition pressures.

The nature of the transition into the smectic J phase is identical for both $\delta = 30$ and 40, with the biaxial order parameter and average tilt angle (shown in Table 5.5) displaying first-order characteristics with values increasing with increasing pressure.

P^*	$\langle U^* \rangle$	Q^2_{00}	Q^2_{22}
0.20	-1.97(0.07)	0.062(0.018)	0.029(0.015)
0.40	-2.67(0.07)	0.081(0.029)	0.028(0.015)
0.60	-3.13(0.07)	0.119(0.040)	0.027(0.019)
0.80	-4.73(0.12)	0.743(0.028)	0.037(0.020)
1.00	-5.21(0.10)	0.808(0.016)	0.039(0.021)
1.20	-5.55(0.11)	0.839(0.012)	0.039(0.020)
1.40	-5.79(0.11)	0.858(0.013)	0.041(0.022)
1.60	-5.99(0.09)	0.870(0.010)	0.042(0.024)
1.80	-6.15(0.09)	0.883(0.008)	0.043(0.023)
2.00	-6.30(0.09)	0.889(0.007)	0.040(0.022)
2.20	-6.43(0.08)	0.894(0.007)	0.043(0.022)
2.40	-6.51(0.09)	0.896(0.006)	0.042(0.021)
2.60	-6.62(0.08)	0.904(0.006)	0.042(0.022)
2.80	-6.80(0.10)	0.910(0.006)	0.045(0.023)
3.00	-6.79(0.09)	0.910(0.006)	0.045(0.025)
3.25	-6.90(0.10)	0.917(0.004)	0.044(0.023)
3.50	-7.02(0.10)	0.920(0.006)	0.045(0.023)
3.75	-7.08(0.09)	0.923(0.005)	0.048(0.025)
4.00	-7.15(0.09)	0.927(0.005)	0.050(0.026)
4.50	-7.24(0.08)	0.929(0.005)	0.055(0.030)
5.00	-7.32(0.08)	0.931(0.003)	0.054(0.028)
5.50	-7.39(0.08)	0.935(0.003)	0.050(0.024)
6.00	-9.22(0.10)	0.973(0.002)	0.316(0.041)
6.50	-9.42(0.09)	0.974(0.002)	0.350(0.037)
7.00	-9.57(0.09)	0.982(0.001)	0.373(0.034)
7.50	-9.51(0.10)	0.980(0.001)	0.363(0.037)
8.00	-9.50(0.10)	0.981(0.001)	0.362(0.037)

Table 5.4: Observable averages at various pressures for $\delta = 40$.
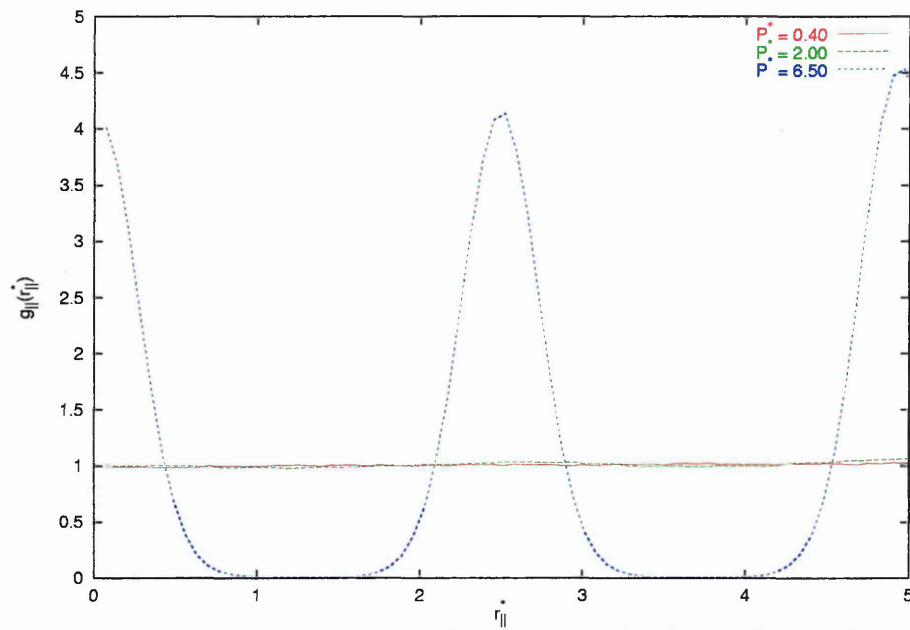
Figure 5.35: Radial distribution function resolved parallel to the layer normal for $\delta = 40$ and $T^* = 1.00$.
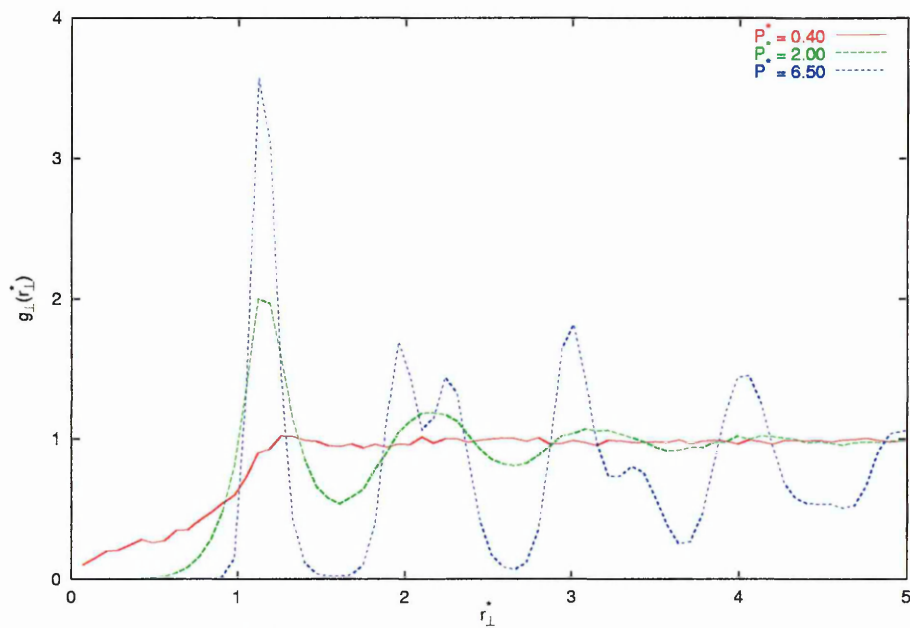
Figure 5.36: Radial distribution function resolved perpendicular to the layer normal for $\delta = 40$ and $T^* = 1.00$.
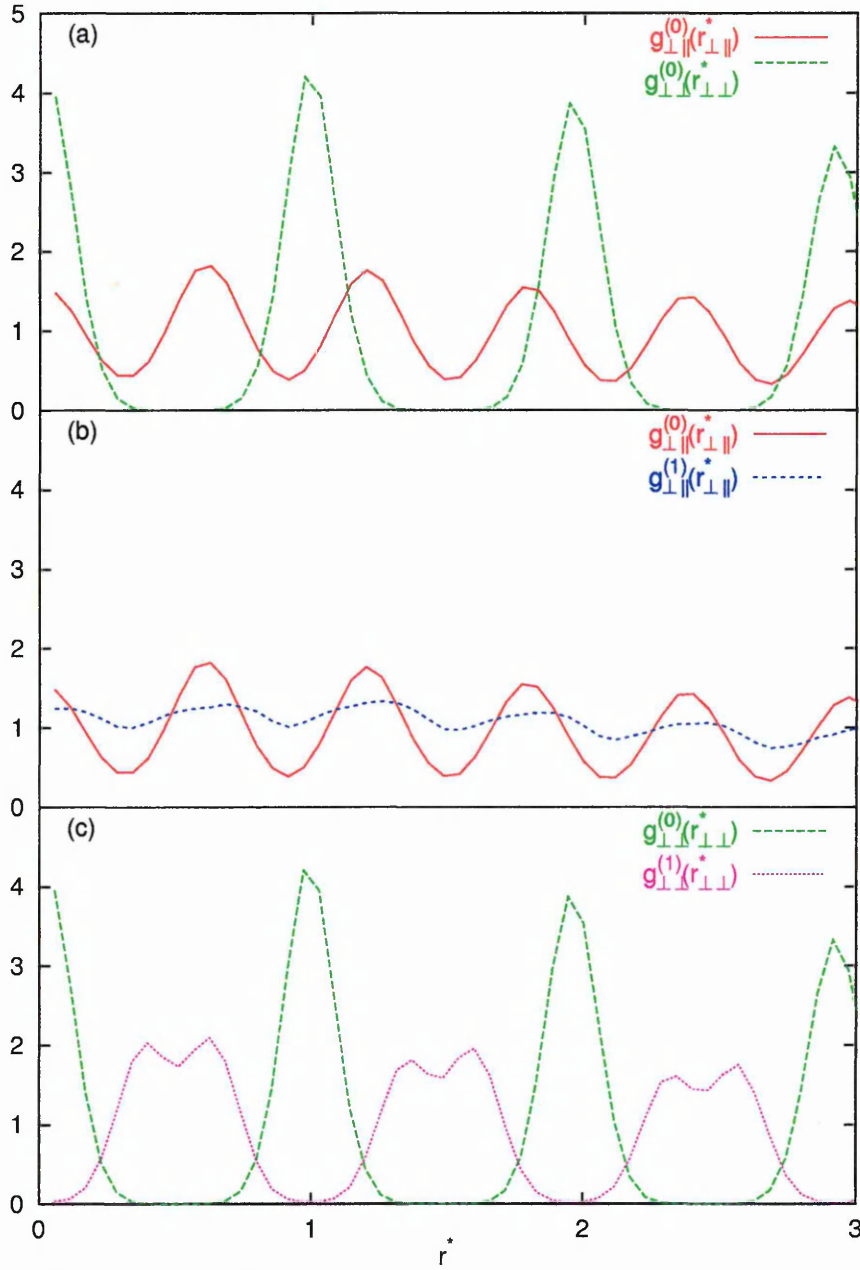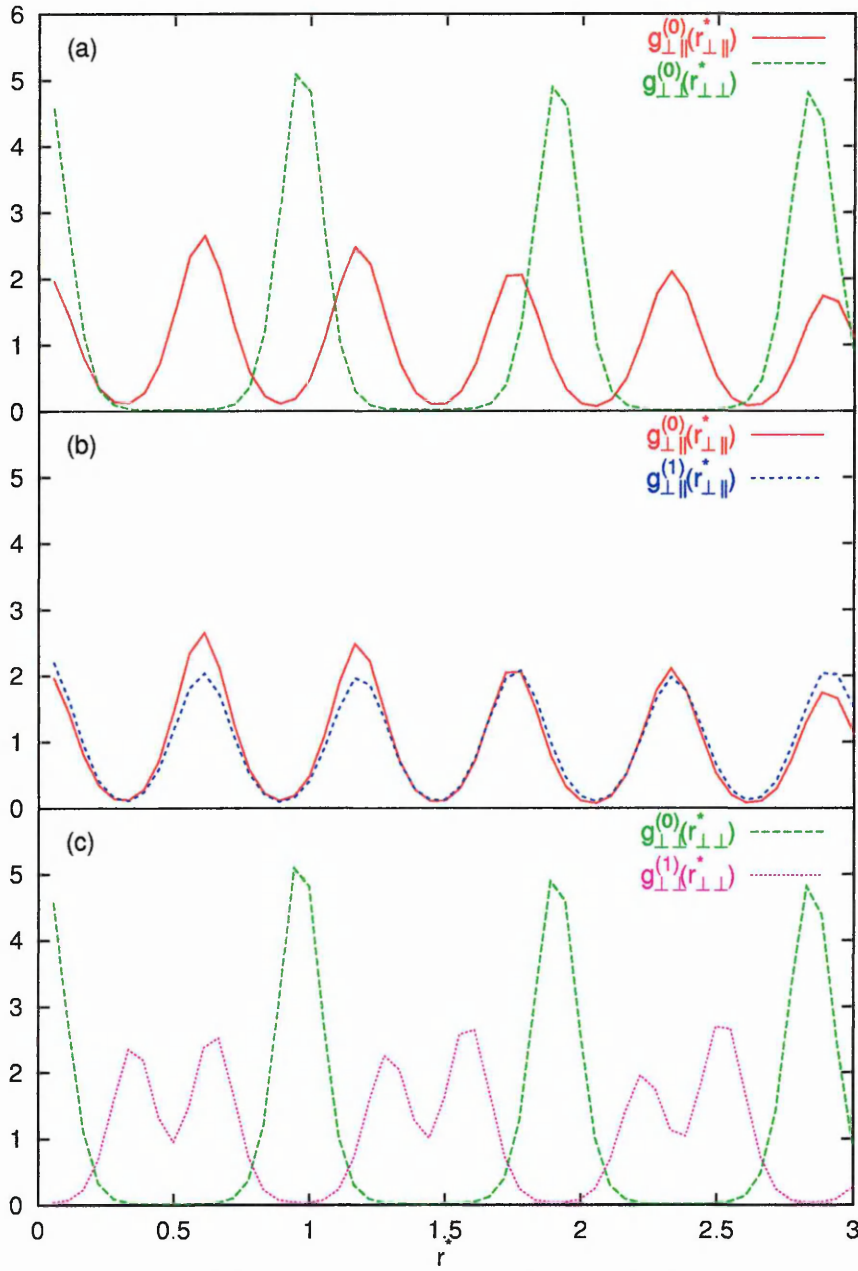
Figure 5.37: Radial distribution functions (a) resolved within the layer parallel, $g_{\perp\|}^{(0)}(r_{\perp\|}^*)$, and perpendicular, $g_{\perp\perp}^{(0)}(r_{\perp\perp}^*)$, to the direction of tilt and between adjacent layers resolved (b) parallel to the direction of tilt and (c) perpendicular to the direction of tilt for $\delta = 40$ and $P^* = 7.00$.

The $\delta = 40$ system, once again, displays a higher biaxial order parameter than that found for $\delta = 30$, whereas the average tilt angle is approximately equal for both cases. The distances between neighbouring layers are also almost identical, with the $\delta = 40$ system displaying a slightly smaller layer spacing. It is also interesting to note that the weak smectic ordering observed within the smectic A phase, over the pressure range $1.30 \le P^* \le 2.00$, for the $\delta = 30$ system has the same period as the smectic J phase, rather than being larger as would be expected for an untilted smectic A phase.

$\delta = 30$			$\delta = 40$		
P^*	$\langle \theta \rangle$	$r_\parallel$	P^*	$\langle \theta \rangle$	$r_\parallel$
2.10	16.55(0.68)	2.54	6.00	16.43(0.40)	2.49
2.20	17.45(0.71)	2.53	6.50	20.08(0.46)	2.47
2.50	21.51(0.57)	2.55	7.00	20.52(0.44)	2.48
3.00	21.74(0.56)	2.53	7.50	20.39(0.42)	2.47
3.50	21.64(0.55)	2.53	8.00	20.38(0.40)	2.47
4.00	21.71(0.36)	2.53			
4.50	21.68(0.44)	2.54			
5.00	20.33(1.13)	2.53			

Table 5.5: Average tilt angles, $\langle \theta \rangle$, and distance between adjacent peaks of $g_\parallel(r_\parallel^*)$.

5.2.2.2 Results at Low Temperature

Whilst the simulations presented in the previous section have allowed the phase behaviour at temperatures above the critical point to be evaluated, the behaviour at low temperatures needs to be treated in a different manner. Since the effect of increasing δ has been to shift the location of the hexagonally close packed phase to lower temperatures and higher densities, a series of cooling runs, at $P^* = 0$,

have been undertaken. The value of this type of simulation has been recognised previously [87] due to the very low (practically indistinguishable from zero) vapour-hexatic phase coexistence pressure. Thus, at a particular temperature, standard constant NPT simulation techniques will allow the system to equilibrate to the density of the coexistence region-hexatic phase transition.

To initiate these sequences of runs, the highest temperature configurations exhibiting a hexatic phase for each value of δ (considered in the previous section) from the constant NVT simulations were equilibrated with $P^* = 0$. However, for all systems this temperature is above the vapour coexistence region, thus a rapid reduction in density and complete loss of translation and rotation order were observed during the equilibration process. This process was therefore repeated for each next lowest temperature, until a translationally and rotationally ordered phase was found to be stable, at $T^* = 0.90$, 0.80 and 0.70 for $\delta = 0$, 30 and 40 respectively. Each of these configurations was then used as a starting point for a sequence of simulations with the temperature being reduced in discrete steps of $\Delta T^* = 0.05$. Equilibration and production periods were both taken to be 5×10^4.

The results of these simulations are shown in Table 5.6. No discontinuity is seen in any of these observables, with the radial distribution functions resolved parallel and perpendicular to the direction of tilt (not shown) identifying all of these points as being a hexatic smectic phase. The in-plane radial distribution functions for the $\delta = 30$ and 40 cases (not shown) both display profiles similar to those shown in Figs. 5.33 and 5.37, indicating that the smectic J phase is observed for all values of

139

T^*	$\langle U^* \rangle$	Q_{00}^2	Q_{22}^2	ρ^*	$\langle \theta \rangle$	$r_\parallel^*$
$\delta = 0$						
0.90	-7.33(16)	0.942(05)	-	0.283(04)	none	2.78
0.85	-7.93(11)	0.957(03)	-	0.297(03)	none	2.75
0.80	-8.31(09)	0.964(03)	-	0.306(02)	none	2.69
0.75	-8.72(09)	0.971(02)	-	0.314(02)	none	2.65
0.70	-9.01(07)	0.975(02)	-	0.320(02)	none	2.63
0.65	-9.29(06)	0.979(01)	-	0.326(02)	none	2.60
0.60	-9.53(05)	0.982(01)	-	0.331(02)	none	2.58
0.55	-9.79(05)	0.985(01)	-	0.337(02)	none	2.55
0.50	-9.97(04)	0.987(01)	-	0.340(01)	none	2.54
$\delta = 30$						
0.80	-8.21(12)	0.961(03)	0.268(38)	0.309(02)	22.48(56)	2.55
0.75	-8.68(09)	0.969(02)	0.344(36)	0.315(02)	22.82(48)	2.54
0.70	-9.09(08)	0.975(02)	0.425(36)	0.320(02)	22.88(47)	2.54
0.65	-9.42(07)	0.979(01)	0.482(33)	0.324(01)	23.04(34)	2.55
0.60	-9.70(06)	0.982(01)	0.548(31)	0.327(01)	23.11(33)	2.55
0.55	-9.94(05)	0.985(01)	0.602(25)	0.330(01)	23.16(25)	2.55
0.50	-10.17(04)	0.987(01)	0.653(25)	0.332(01)	23.36(21)	2.56
0.45	-10.37(04)	0.989(01)	0.698(20)	0.335(01)	23.38(25)	2.56
0.40	-10.56(04)	0.990(01)	0.741(22)	0.337(01)	23.54(27)	2.56
0.35	-10.75(03)	0.992(01)	0.783(16)	0.339(01)	23.57(24)	2.56
0.30	-10.91(02)	0.993(01)	0.818(14)	0.341(01)	23.72(21)	2.57
0.25	-11.08(02)	0.994(01)	0.855(11)	0.343(01)	23.79(18)	2.57
$\delta = 40$						
0.70	-10.24(09)	0.982(01)	0.661(23)	0.334(02)	34.45(26)	2.31
0.65	-10.58(07)	0.985(01)	0.702(20)	0.338(01)	34.59(22)	2.30
0.60	-10.87(07)	0.987(01)	0.736(20)	0.342(01)	34.55(29)	2.29
0.55	-11.18(06)	0.989(01)	0.774(15)	0.346(01)	34.64(20)	2.28
0.50	-11.44(05)	0.991(01)	0.804(14)	0.349(01)	34.64(20)	2.27
0.45	-11.68(04)	0.992(01)	0.830(12)	0.352(01)	34.71(19)	2.26
0.40	-11.89(04)	0.993(01)	0.852(10)	0.355(01)	34.75(17)	2.25
0.35	-12.09(04)	0.993(01)	0.870(09)	0.357(01)	34.77(18)	2.25
0.30	-12.27(03)	0.994(01)	0.884(07)	0.359(01)	34.80(21)	2.24
0.25	-12.43(03)	0.994(01)	0.894(06)	0.361(01)	34.79(16)	2.23

Table 5.6: Observable averages at various temperatures and angles of internal rotation at $P^* = 0.00$.

140

δ where a tilted hexatic phase is observed using this parameterisation, rather than a smectic G phase being formed for larger values of δ as indicated by the constant NVT results. It should, however, be noted that the observed density (with the exception of $T^* = 0.90$ and 0.85 for $\delta = 0$) is greater than the density used for the constant NVT simulations. As a result of this the simulations at low temperatures within the constant NVT simulations have been performed within a region of phase coexistence. Therefore, the observation of differing behaviour between these sets of results indicates that, whilst the modified constant NVT method has been shown to correctly simulate points of phase space where phase separation does not occur, results from areas of phase space where the system would like to phase separate are inaccurate due to finite-size effects associated with the fixed volume of the system. That said though, the constant NVT results exhibit the same general trends as these results, with larger values of the biaxial order parameter, larger tilt angles and smaller layer spacing being found with increasing δ.

It is also interesting to note that as the temperature is reduced for the $\delta = 0$ case, the layer spacing is substantially reduced, whereas no such behaviour is noted for the $\delta = 30$ and 40 cases. As with the constant NVT results, the layer spacing may not be calculated with the simple relation $\frac{\sigma_{ee}}{\sigma_{ss}} \cos \langle \theta \rangle$, although such a calculation becomes more accurate as the average tilt angle increases. This is due to the degree of interdigitation being reduced as the tilt angle is increased, an observation which may be confirmed by considering the packing of hard elipsiods into adjacent layers with increasing tilt angle.

In order to understand why the smectic J phase is being formed, rather than the smectic G, the form of the potential energy as a function of intermolecular vector will be considered, for both types of tilted hexatic phase, along the two directions of bond order, r_1 and r_2 (as defined in the inset of Fig. 5.38), for a perfectly orientated hexagonal unit cell within a single smectic layer. Only these two functions need be considered since the symmetry of the unit cell allows the total potential energy of a single unit cell to be given in terms of only these two functions,
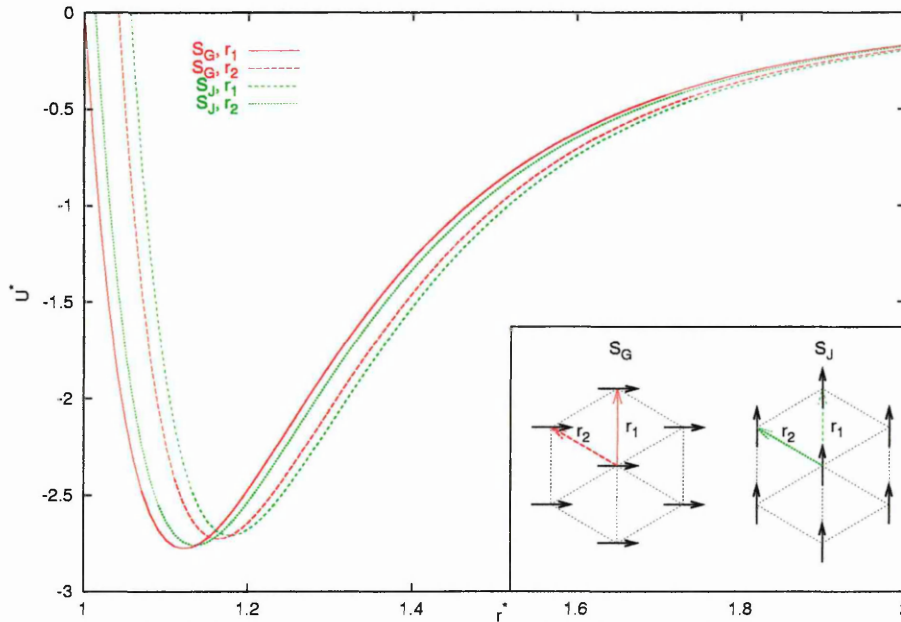
Figure 5.38: Well depths of two particles interacting via the IRGB potential along the two directions of bond order, r_1 and r_2, exhibited by a perfectly orientated hexagonal close-packed unit cell for the smectic G and J phases with $\delta = 30$ and $\theta = 20$. Inset shows definition of r_1 and r_2 within the hexagonal net.

$$U_{tot} = U_{r_1}(r_{1_1}) + U_{r_1}(r_{1_2}) + U_{r_2}(r_{2_1}) + U_{r_2}(r_{2_2}) + U_{r_2}(r_{2_3}) + U_{r_2}(r_{2_4}) \qquad (5.6)$$

where U_{r_1} gives the potential energy associated with the molecules located along the r_1 direction at distances of r_{1_1} and r_{1_2}, and, similarly, U_{r_2} gives the potential energy

142

associated with the molecules along the r_2 directions at distances of r_{2_1}, r_{2_1}, etc. The angle between r_1 and r_2 is not equal to 60^0 since the hexagonal net is distorted due to the tilting process and has been calculated such that undistorted hexagonal close packing is observed when then system is viewed along the molecular long axes [12].

The well depths calculated as a function of distance along the directions of bond ordering (Fig. 5.38) show that, for a system where the angle between the molecular long axes and the layer normal (θ) is less than δ, the energetically most favourable configuration is that of the side-by-side configuration of the smectic G phase, whereas the energetically least favourable configuration is in the smectic J phase. When the total potential energy for the unit cell is calculated using eqn. 5.6, for values of r_1 and r_2 which minimise the potential energy along each bond direction, it may be shown that the minimum energy configuration in the smectic G phase gives a lower potential energy than the smectic J phase. Therefore the smectic G phase would be expected to be observed following consideration purely in-layer interactions.

However, the area of the layer which each unit cell occupies at the minimum energy configuration is larger for the smectic J phase. Since the volume of the unit cell occupied by the molecules is identical for both the smectic G and J phases, the unoccupied volume of the unit cell within the smectic J phase will be larger than that of the smectic G phase. Thus a greater degree of interdigitation may be expected for the smectic J phase. It would therefore appear that the smectic J phase is energetically more favourable for systems where the reduction in potential energy achieved by the reducing the layer spacing is greater than the increase in potential

energy associated with the formation the smectic J phase rather than the smectic G phase.

5.2.2.3 Summary

These extended simulations of the Internally-Rotated Gay-Berne potential within the constant *NPT* ensemble have shown a rich phase behaviour. The results of these simulations are summarised in the schematic phase diagrams shown in Fig. 5.39. The results clearly show that the introduction of biaxiality destabilises all of the ordered phases, such that the observed phase transitions are shifted to lower temperatures and higher densities, with the tilted smectic J phase replacing the smectic B phase for sufficiently large values of δ. As δ is increased, the nematic phase dominates the phase diagram at high densities, with the hexatic smectic phase being suppressed to lower temperatures and higher densities. The smectic A phase is destabilised completely for sufficiently large δ, with neither a smectic A or C phase being observed for large values of δ. That said, the smectic A phase observed for the uniaxial $\delta = 0$ case occupies only a very small temperature and density range, with weakly defined smectic layers being observed. Due to this, the details of simulations which have been undertaken upon systems with parameterisations which have been chosen to stabilise the smectic A phase will now be presented.
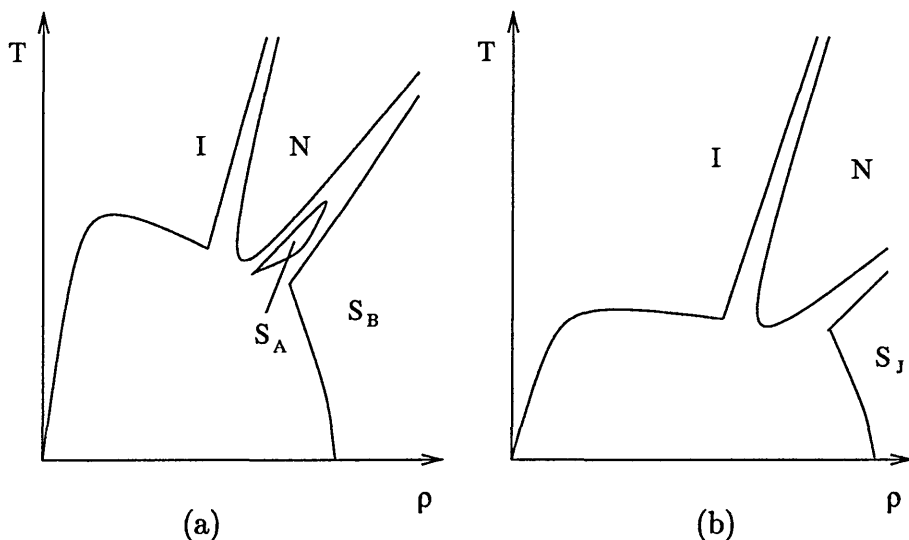
Figure 5.39: Schematic phase diagrams in the $\rho-T$ plane. (a) Topology deduced from simulation for $\delta = 0$, and (b) topology deduced from simulation for $\delta = 40$.

5.3   The Effect of Elongation upon the Phase Behaviour

Having now considered the phase behaviour of Internally-Rotated Gay-Berne fluids for various angles of internal rotation, the effect upon the phase behaviour of increasing molecular elongation will now be considered. Following the simulation study of Brown *et al* [87], which demonstrated that the smectic phases are stabilised with increasing particle elongation, it is to be expected that increasing elongation will stabilise the smectic A phase, and increase the density and temperature range over which the phase exists for the alternative parameterisation used here.

In order to test this prediction, constant NPT simulations along isotherms have been undertaken for $\sigma_{ee}/\sigma_{ss} = 3.5$ and 4.0, with the other parameters held con-

145

stant ($\epsilon_{ss}/\epsilon_{ee} = 5.0$, $\mu = 1$, $\nu = 2$) using the simulation techniques described in section 5.2.2.1. Since the results presented in the previous section show that the $\delta = 30$ case gives a tilted hexatic phase along with a smectic A phase, albeit with a weak density wave parallel to the layer normal, the $\delta = 30$ case will be considered here. These simulations were performed at $T^* = 1.50$ thus allowing direct comparison with the equation of state obtain for the $\sigma_{ee}/\sigma_{ss} = 3.0$ system (Fig. 5.30), for which only isotropic and nematic phases were observed. Simulations were also attempted for the lower temperature isotherm ($T^* = 1.00$), with a tilted hexatic phase being observed for very low pressures for both elongations, indicating that there is indeed a dramatic effect upon the phase behaviour, with the increased stabilisation of the smectic phases increasing the temperature range of the coexistence region, as is expected following the results of Brown *et al* [87].

5.3.1 $\sigma_{ee}/\sigma_{ss} = 3.5$

The equation of state obtained for the $\sigma_{ee}/\sigma_{ss} = 3.5$ case is shown in Fig. 5.40 with the other observables being tabulated in Table 5.7. Upon compression from the initial isotropic configuration, an isotropic to nematic transition was observed. Smectic ordering once again sets in at higher densities, as indicated by the density wave seen in $g_{\parallel}(r^*_{\parallel})$ (Fig. 5.41), with oscillations being initially observed at $P^* = 2.50$, corresponding to $\rho^* = 0.254$, as the smectic region develops, with the structure being greatly enhanced with further increasing density. The liquid-like structure within each layer (Fig. 5.42) over the range $2.50 \geq P^* \geq 3.50$, considered in conjunction

with the fact that the smectic layers are formed perpendicular to the layer normal and the lack of biaxial ordering indicates that this is a smectic A phase.
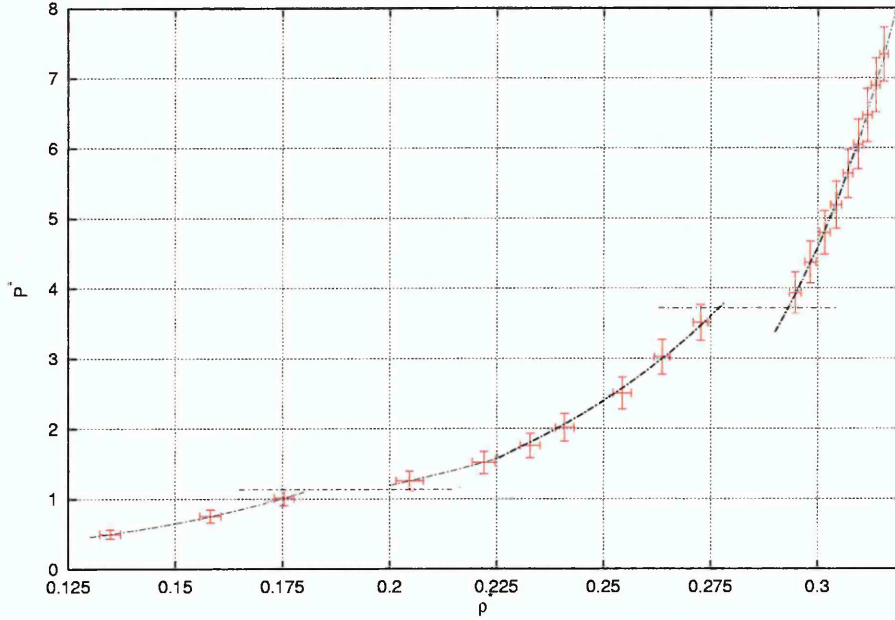

Figure 5.40: Equation of state (pressure P^* vs density ρ^*) of the IRGB fluid with $\sigma_{ee}/\sigma_{ss} = 3.5$ at $T^* = 1.50$. Lines are drawn to guide the eye, horizontal lines indicate estimates of the transition pressures.

A third transition is also observed as the density is increased further, with a corresponding discontinuity being clearly observed in the nematic order parameter, with only a very slight increase being observed for the biaxial order parameter. The radial distributions functions (Figs. 5.41 and 5.42) show that this highest density phase displays well defined smectic ordering, with long range hexatic ordering within the layers. Whilst there is no evidence of biaxial ordering, examination of the average tilt angle shows that a tilted hexatic phase is being formed. A discontinuous increase in the average tilt angle being observed at the transition from smectic A, which increases slightly with increasing density with a corresponding decrease being observed in the lamellar spacing.

P^*	$\langle U^* \rangle$	Q^2_{00}	Q^2_{22}	$\langle \theta \rangle$	$r^*_\parallel$
0.50	-2.08(0.07)	0.062(0.019)	0.028(0.015)	none	-
0.75	-2.54(0.08)	0.076(0.026)	0.028(0.016)	none	-
1.00	-2.94(0.09)	0.091(0.032)	0.027(0.019)	none	-
1.25	-4.36(0.18)	0.652(0.048)	0.034(0.019)	none	-
1.50	-5.16(0.15)	0.786(0.023)	0.038(0.019)	none	-
1.75	-5.63(0.12)	0.834(0.012)	0.037(0.020)	none	-
2.00	-5.93(0.13)	0.855(0.012)	0.039(0.021)	none	-
2.50	-6.61(0.15)	0.889(0.009)	0.040(0.020)	none	3.01
3.00	-6.91(0.13)	0.903(0.007)	0.042(0.021)	none	2.90
3.50	-7.51(0.13)	0.923(0.005)	0.041(0.021)	none	2.97
4.00	-9.98(0.13)	0.973(0.002)	0.063(0.028)	13.29(0.57)	3.05
4.50	-10.12(0.12)	0.974(0.002)	0.068(0.032)	13.25(0.53)	3.03
5.00	-10.23(0.13)	0.976(0.002)	0.073(0.031)	13.60(0.51)	3.01
5.50	-10.29(0.12)	0.977(0.002)	0.073(0.031)	13.75(0.49)	3.01
6.00	-10.39(0.14)	0.978(0.002)	0.075(0.033)	14.02(0.53)	2.99
6.50	-10.43(0.14)	0.979(0.002)	0.082(0.032)	14.25(0.54)	2.98
7.00	-10.45(0.13)	0.979(0.002)	0.085(0.035)	14.23(0.51)	2.97
7.50	-10.47(0.13)	0.980(0.001)	0.081(0.034)	14.45(0.53)	2.96
8.00	-10.53(0.13)	0.981(0.001)	0.094(0.033)	14.45(0.41)	2.96

Table 5.7: Observable averages at various pressures for $\sigma_{ee}/\sigma_{ss} = 3.5$.

Classification of this tilted hexatic phase is once again attempted by use of the in-plane radial distribution functions resolved parallel and perpendicular to the direction of tilt, shown in Fig. 5.43 for $P^* = 4.50$, with similar profiles being obtained for all the pressures within the tilted hexatic phase. Since the profile is almost identical when resolved perpendicular and parallel to the direction of tilt, the phase may not be classified by mapping of these profiles onto an ideal hexagonal lattice as has been done in the previous section. However, since these profiles are accumulated for all particles over all configurations (where a configuration is taken every 1,000 sweeps), these types of profile may be expected if the direction of tilt within the hexagonal close-packed unit cell changes during the course of the simulation. This phenomena

is confirmed by use of visualisation techniques (illustrated in Fig. 5.44), showing that the direction of tilt, resolved to the nearest set of intermolecular bonds, within a layer does change during the course of the simulation. This type of behaviour is not observed experimentally, since the smectic F, G, I and J phases have been shown to be distinct mesophases which are not miscible [11].

Since this isotherm has been undertaken at a relatively high temperature, a series of simulations have been undertaken to determine whether this phenomenon is temperature dependent. To achieve this, a series of simulations have been undertaken at $P^* = 4.50$ with the temperature being reduced in discrete steps of $\Delta T^* = 0.05$. The values of the key observables are presented in Table 5.8. All the observed values vary continuously with decreasing temperature, with the biaxial order parameter rapidly adopting non-zero values showing that the reduction in temperature results in improved orientational ordering. Examination of the in-layer radial distribution functions (Fig. 5.45) shows that, as the temperature is reduced, a regular periodic structure of a type expected for a tilted hexatic phase is observed. The direction of tilt is preferentially towards the side of the hexagonal net, indicating that the smectic G phase is dominant at low temperatures. For the lowest temperature considered here, however, these profiles show (particularly noticeable in $g_{\perp\parallel}(r^*_{\perp\parallel})$) that the direction of tilt is still changing during the course of the simulation.

Returning to the explanation presented in section 5.2.2.2 as to origin of the type of tilted hexatic phase which will be observed; this *switching* between the two phases may be expected if the reduction in potential energy achieved by reducing the layer
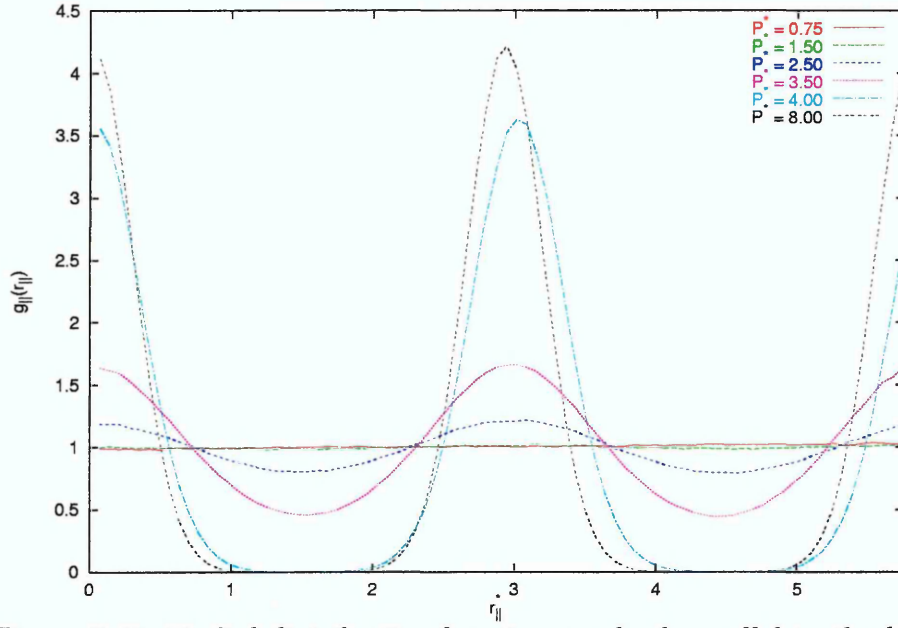
Figure 5.41: Radial distribution function resolved parallel to the layer normal for $\sigma_{ee}/\sigma_{ss} = 3.5$ and $T^* = 1.50$.
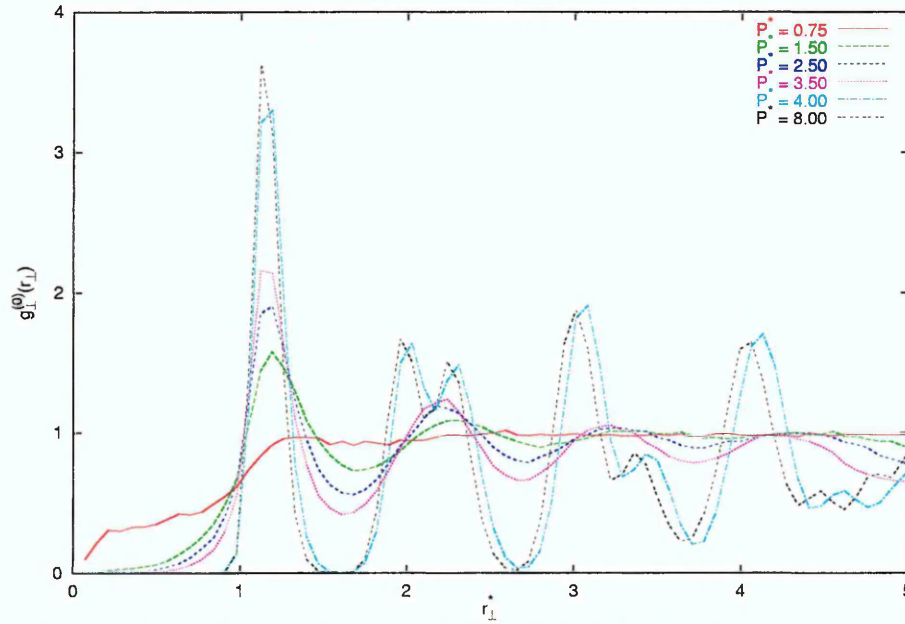
Figure 5.42: Radial distribution function resolved perpendicular to the layer normal for $\sigma_{ee}/\sigma_{ss} = 3.5$ and $T^* = 1.50$.

Figure 5.43: Radial distribution functions (a) resolved within the layer parallel, $g_{\perp\parallel}^{(0)}(r_{\perp\parallel}^*)$, and perpendicular, $g_{\perp\perp}^{(0)}(r_{\perp\perp}^*)$, to the direction 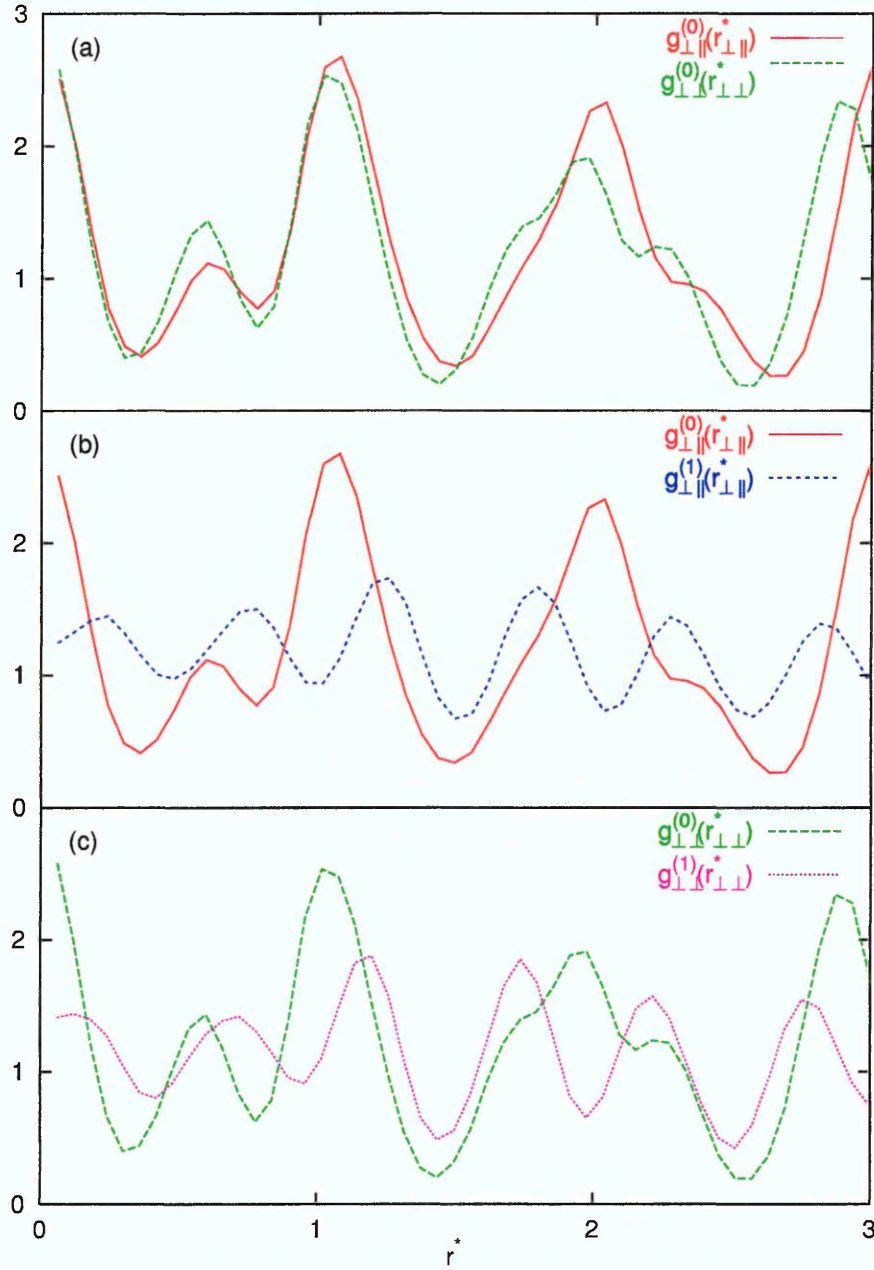of tilt and between adjacent layers resolved (b) parallel to the direction of tilt and (c) perpendicular to the direction of tilt for $\sigma_{ee}/\sigma_{ss} = 3.5$ and $P^* = 4.50$.

(a)

(b)

(c)
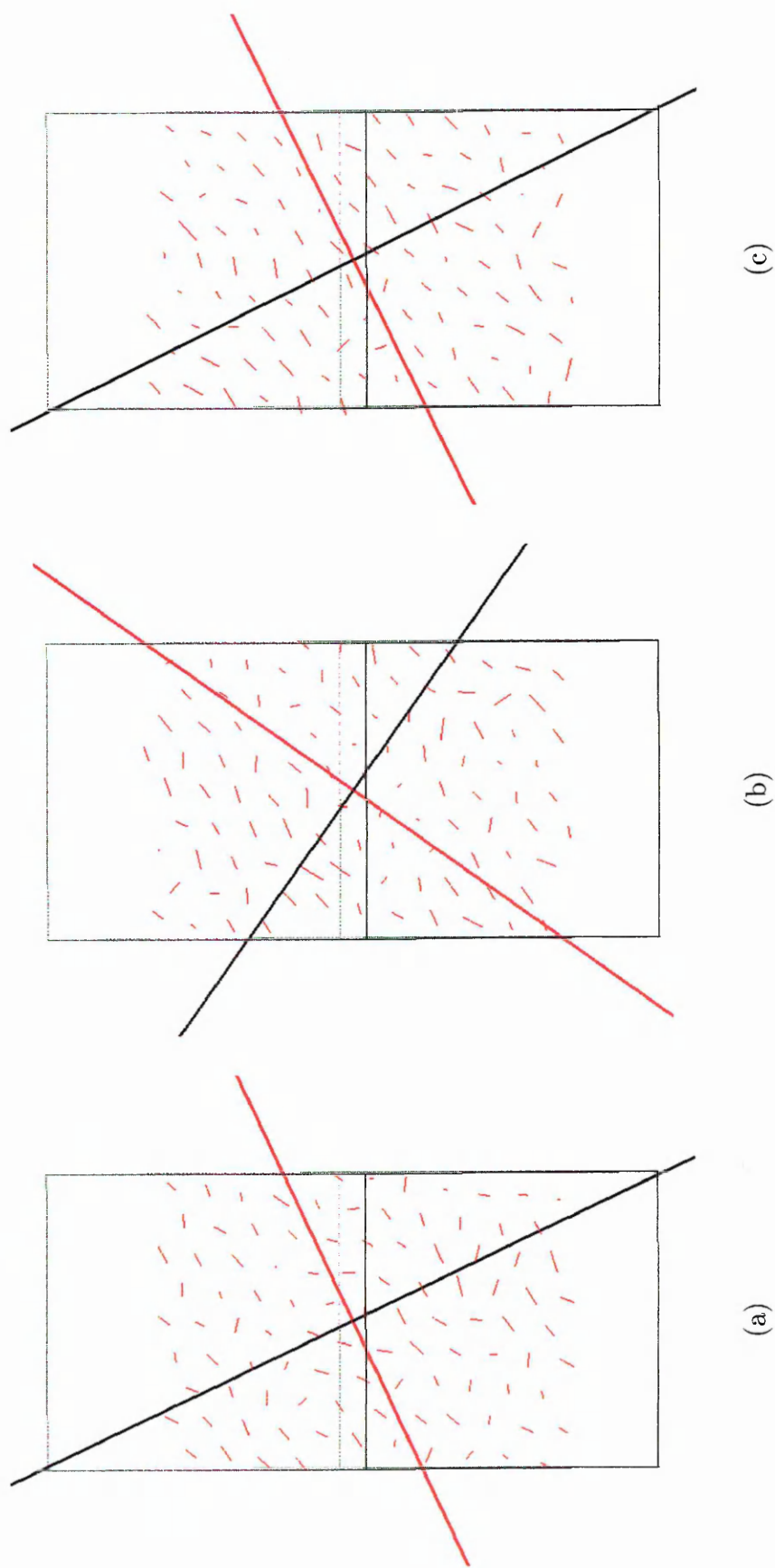
Figure 5.44: Molecular organisation of the molecules with the layer for $\sigma_{ee}/\sigma_{ss} = 3.5$ at $P^* = 4.50$ during the course of the production period of the simulation after (a) 3,000 sweeps, (b) 6,000 sweeps and (c) 9,000 sweeps. The red and black vectors are parallel and perpendicular to the direction of tilt within the layer respectively. The view is set such that the layer normal is perpendicular to the page.

Figure 5.45: Radial distribution functions resolved within the layer parallel (a) parallel and (b) perpendicular to the direction of tilt for $P^* = 4.50$.

153

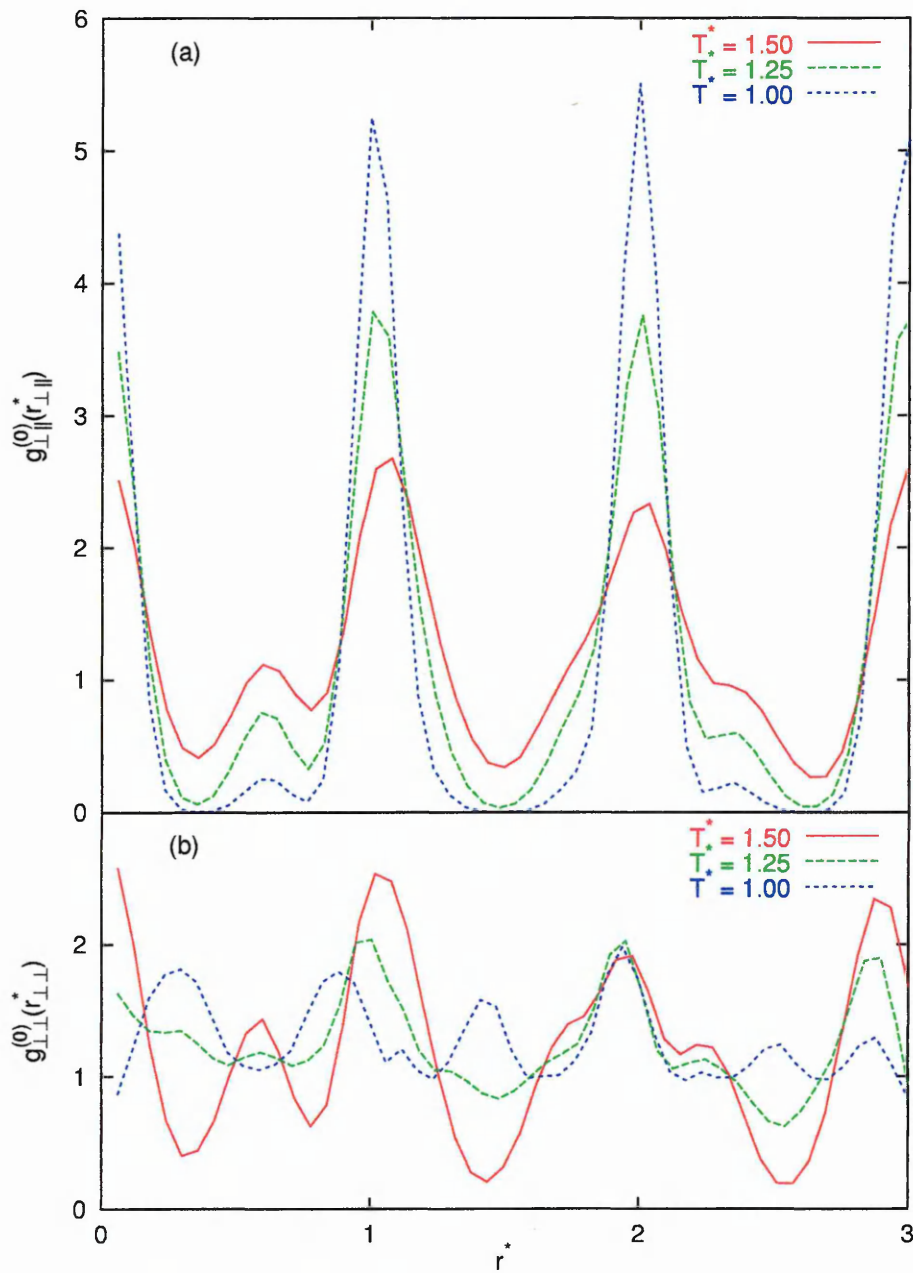| T^*	$\langle U^* \rangle$	Q_{00}^2	Q_{22}^2	$\langle \rho^* \rangle$	$\langle \theta \rangle$	$r_\parallel$
1.50	-10.12(12)	0.974(02)	0.068(32)	0.302(01)	13.25(57)	3.03
1.45	-10.48(12)	0.978(02)	0.086(35)	0.303(01)	13.91(59)	3.02
1.40	-10.70(12)	0.980(01)	0.109(36)	0.305(01)	14.03(48)	3.00
1.35	-10.94(13)	0.981(01)	0.135(41)	0.306(01)	14.18(59)	3.00
1.30	-11.23(12)	0.983(01)	0.174(36)	0.308(01)	14.48(35)	2.99
1.25	-11.40(12)	0.984(01)	0.183(40)	0.309(01)	14.49(51)	2.98
1.20	-11.70(10)	0.985(01)	0.236(36)	0.310(01)	14.74(39)	2.97
1.15	-11.95(10)	0.987(01)	0.274(39)	0.312(01)	14.74(40)	2.97
1.10	-12.21(10)	0.988(01)	0.329(36)	0.313(01)	14.88(33)	2.97
1.05	-12.46(10)	0.989(01)	0.378(33)	0.314(01)	14.96(37)	2.97
1.00	-12.70(09)	0.990(01)	0.414(34)	0.315(01)	14.98(33)	2.96

Table 5.8: Observable averages at various temperatures for $\sigma_{ee}/\sigma_{ss} = 3.5$ at $P^* = 4.50$.

spacing (which will be less here than for the previous case due to the increased length of the molecule) being equal to the increase in potential energy resulting from the smectic J phase being formed rather than the smectic G. This will result in each phase being as energetically favourable as the other. Whilst at low temperatures, the smectic G phase is the more favourable here, thermal effects will allow the direction of tilt to vary with increasing temperature, if the reduction in potential energy associated with the system adopting the smectic J phase is small.

5.3.2 $\quad \sigma_{ee}/\sigma_{ss} = 4.0$

Finally, the $\sigma_{ee}/\sigma_{ss} = 4.0$ case is considered, with the equation of state being shown in Fig. 5.46 with the other observables being tabulated in Table 5.9. Once again, simulation along the isotherm was initiated at low pressure within the isotropic phase. Upon compression no nematic phase is observed, with a layered structure

being formed at $P^* = 0.60$ (shown in Fig. 5.47), this transition density being lower than that of the isotropic-nematic transition observed for the $\sigma_{ee}/\sigma_{ss} = 3.5$ system. Since this phase displays liquid-like structure within each layer (shown in Fig. 5.48), and the layers are formed perpendicular to the direction of tilt, with no evidence of biaxial ordering, this phase is classified as smectic A.
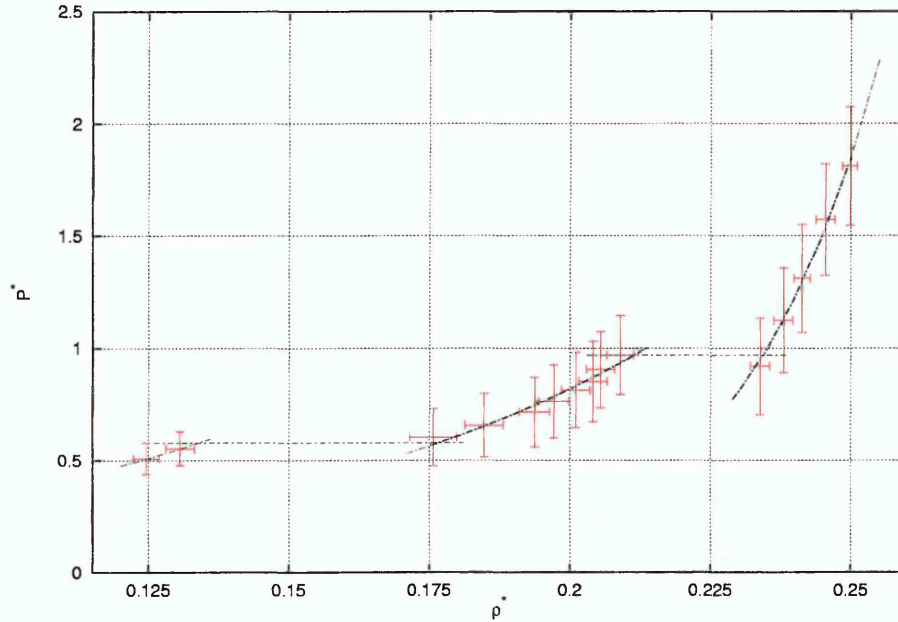
Figure 5.46: Equation of state (pressure P^* vs density ρ^*) of the IRGB fluid with $\sigma_{ee}/\sigma_{ss} = 4.0$ at $T^* = 1.50$. Lines are drawn to guide the eye, horizontal lines indicate estimates of the transition pressures.

As the pressure is increased further, a second transition is observed into a phase which, once again, displays a well defined layered structure with long range hexatic ordering within the layer (shown in Figs. 5.47 and 5.48). Both the biaxial order parameter and average tilt angle display first-order characteristics on entering the hexatic phase, assuming non-zero values which increase with increasing density. It is interesting to note that the lamellar spacing reduces continuously with increasing density in both the smectic A and hexatic phases.

P^*	$\langle U^* \rangle$	Q_{00}^2	Q_{22}^2	$\langle \theta \rangle$	$r_{\parallel}^*$
0.50	-2.78(0.11)	0.111(0.041)	0.026(0.018)	none	–
0.55	-3.02(0.15)	0.130(0.043)	0.024(0.019)	none	–
0.60	-6.28(0.34)	0.847(0.021)	0.037(0.020)	none	3.75
0.65	-6.95(0.29)	0.887(0.013)	0.039(0.021)	none	3.75
0.70	-7.71(0.22)	0.912(0.008)	0.041(0.021)	none	3.64
0.75	-7.95(0.25)	0.917(0.009)	0.041(0.021)	none	3.67
0.80	-8.27(0.21)	0.925(0.007)	0.041(0.021)	none	3.65
0.85	-8.54(0.22)	0.930(0.006)	0.039(0.020)	none	3.68
0.90	-8.56(0.21)	0.932(0.006)	0.041(0.021)	none	3.61
0.95	-8.87(0.23)	0.937(0.006)	0.042(0.022)	none	3.60
1.00	-12.06(0.20)	0.974(0.002)	0.186(0.038)	21.83(0.71)	3.49
1.25	-12.41(0.20)	0.977(0.002)	0.204(0.038)	22.05(0.57)	3.45
1.50	-12.70(0.19)	0.978(0.002)	0.225(0.037)	22.46(0.40)	3.43
1.75	-13.05(0.21)	0.980(0.002)	0.248(0.040)	24.00(0.82)	3.39
2.00	-13.45(0.17)	0.983(0.001)	0.276(0.036)	24.74(0.40)	3.36

Table 5.9: Observable averages at various pressures for $\sigma_{ee}/\sigma_{ss} = 4.0$.

Once again classification of this tilted hexatic phase is achieved by use of the in-plane radial distribution functions resolved parallel and perpendicular to the direction of tilt, shown in Fig. 5.49 for $P^* = 1.50$. These profiles clearly show that the direction of tilt is towards to the side of the hexagonal net, with a clear correlation between adjacent layers, indicating a smectic G phase.

5.3.3 Summary

These results have confirmed that increasing elongation has a dramatic effect upon the phase behaviour of the Internally-Rotated Gay-Berne fluid. As was expected, following Brown et al [87], increasing elongation has stabilised the smectic phases, such that the temperature range of the coexistence region is increased and, for the
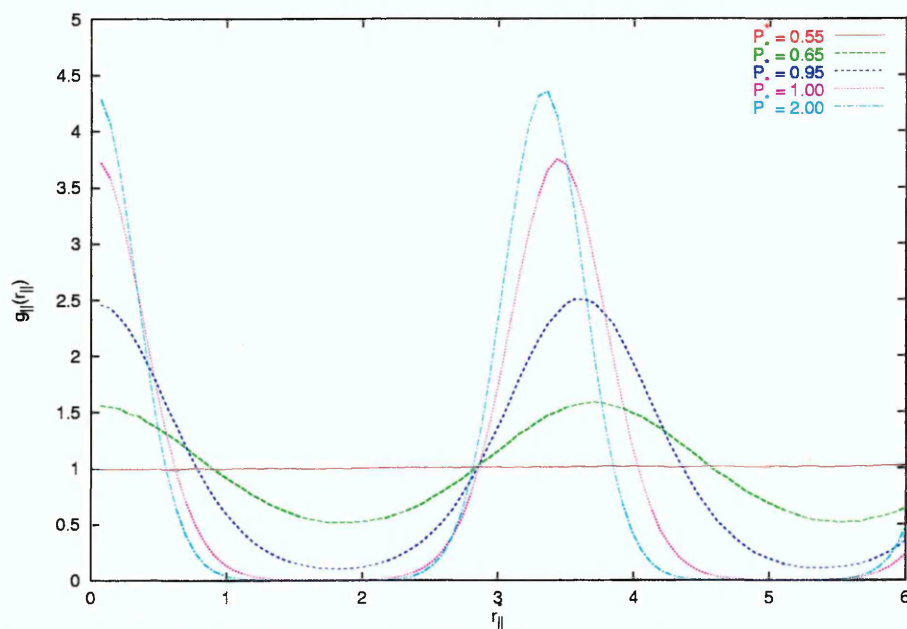
Figure 5.47: Radial distribution function resolved parallel to the layer normal for $\sigma_{ee}/\sigma_{ss} = 4.0$ and $T^* = 1.50$.
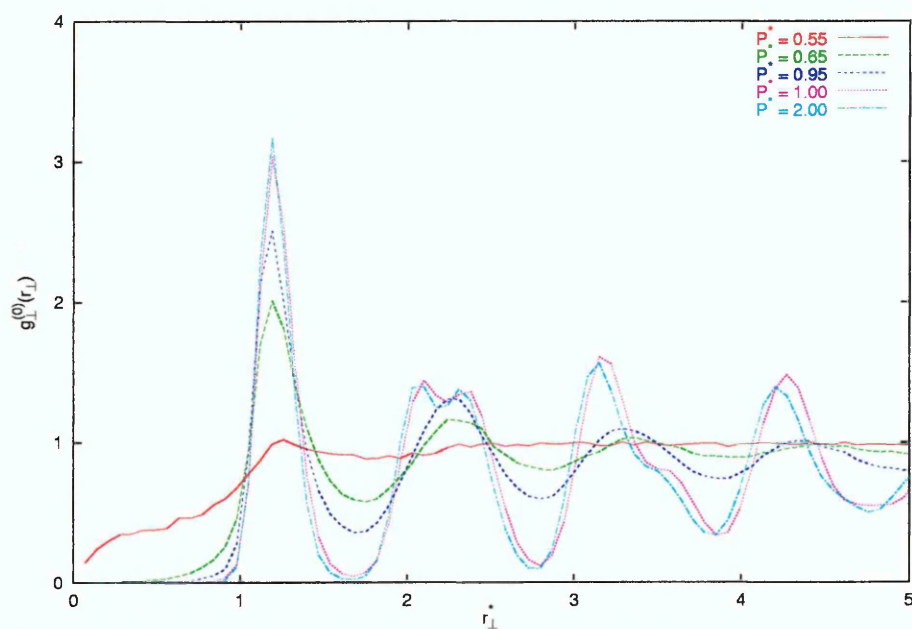
Figure 5.48: Radial distribution function resolved perpendicular to the layer normal for $\sigma_{ee}/\sigma_{ss} = 4.0$ and $T^* = 1.50$.

Figure 5.49: Radial distribution functions (a) resolved within the layer parallel, $g_{\perp\|}^{(0)}(r_{\perp\|}^*)$, and perpendicular, $g_{\perp\perp}^{(0)}(r_{\perp\perp}^*)$, to the direction of tilt and between adjacent layers resolved (b) parallel to the direction of tilt and (c) perpendicular to the direction of tilt for $\sigma_{ee}/\sigma_{ss} = 4.0$ and $P^* = 1.50$.

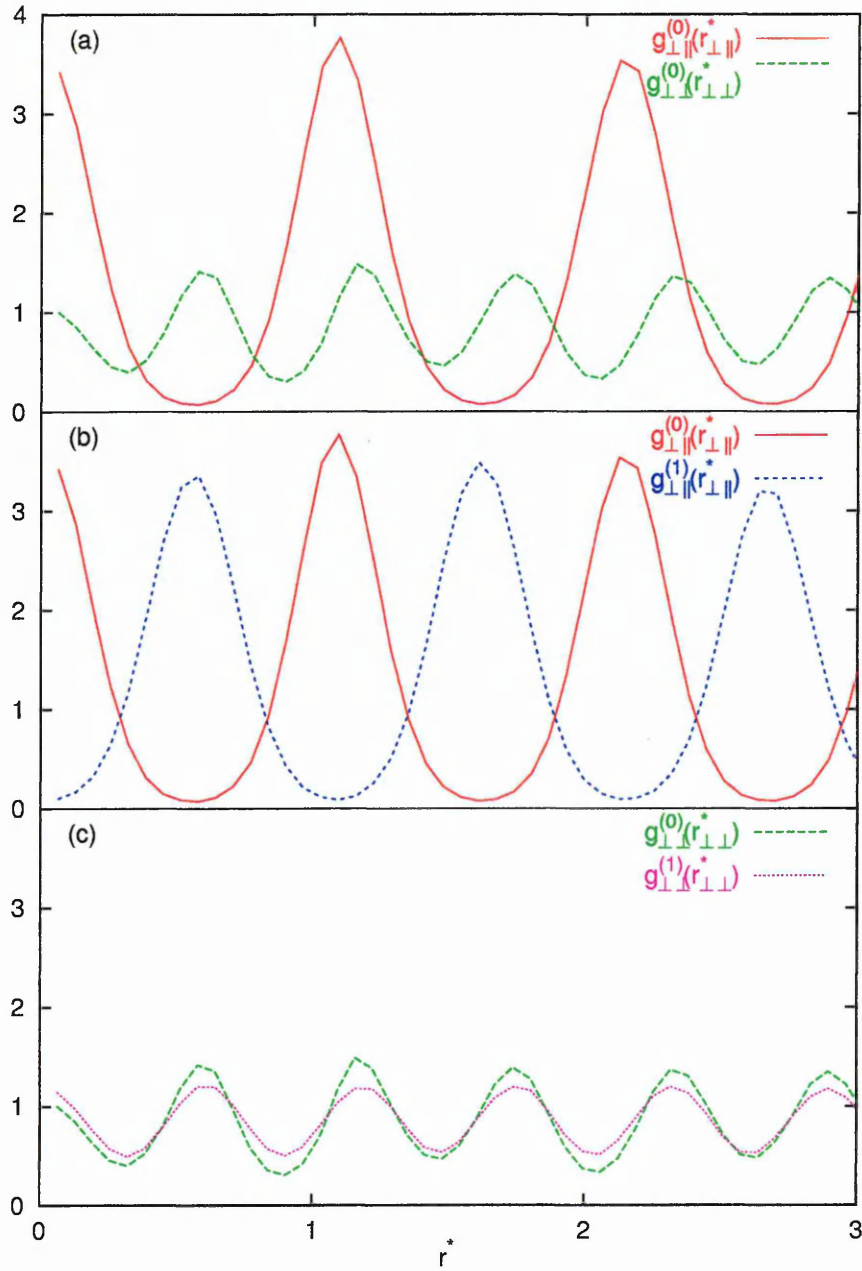single isotherm considered here, the nematic phase is replaced by the smectic A phase as the aspect ratio of the molecules is increased from 3:1 to 4:1. The type of tilted hexatic phase observed at high densities is also dependent upon the molecular length, apparently being controlled through a subtle relationship between the inter- and intra-layer interactions. Since the only types of tilted phase which have been observed during the course of these simulations have been hexatic phases, it would appear that models which consider the steric effects associated with molecules which are constrained into a *zig zag* conformation are a poor route to obtain the smectic C phase. That said though, the Gay-Berne potential has a large range of parameter space, and it may be that a smectic C phase could be obtained using this type of model with alternative parameterisations.

It should also be noted that at no point during these simulations has a phase transition from a hexatic smectic phase to crystal been observed, with the radial distribution functions indicating strong positional correlations within each layer and between layers for all the simulations attempted within these hexatic phases. It is, however, almost impossible in our finite-size simulations to draw a distinction between quasi-long-ranged and true long-ranged order [79, 87] and therefore the question as to whether these are smectic or crystal phases arises. Calculation of the shear modulus for a Gay-Berne fluid [87] gave low values as is expected in the smectic B phase, however no phase transition is observed as the temperature is reduced to very low values, and it may be equally termed a solid phase. Experimental classification of these types of highly correlated phase makes the distinction between them and the solid phase by considering the free, or nearly-free, rotation of the molecules

159

about their molecular long axes. Following this lead, the dynamics of the systems considered thus far will now be examined.

5.4 Dynamics of the Internally-Rotated Gay-Berne Fluid

In order to further characterise the behaviour of the tilted hexatic phases a series of simulations have been undertaken using molecular dynamics techniques within the constant NVE ensemble, thus allowing the dynamical behaviour of the IRGB fluid to be determined. Similar studies have been undertaken for the Gay-Berne fluid [83, 105] within the isotropic and nematic phase, with comparisons being made with various theoretical models. Since the aim here is simply to determine the type of motion which the hexatic phases exhibit, these theoretical models (which within the nematic phase do not represent the observed behaviour with any great [105] success) will not be considered here.

The translational motion and molecular reorientation have been analysed in terms of the time autocorrelation functions (ACF's) [106], defined as

$$\phi_A(t) = \frac{\langle \mathbf{A}_i(t_0) \cdot \mathbf{A}_i(t_0 + t) \rangle}{\langle \mathbf{A}_i(t_0) \cdot \mathbf{A}_i(t_0) \rangle} \tag{5.7}$$

where $\mathbf{A}_i(t)$ is a classical dynamical property of molecule i evaluated at time t. In these calculations $\mathbf{A}$ has been taken to be the linear velocities, $\mathbf{v}$, and the angular

velocities, $\boldsymbol{\omega}$, resolved parallel and perpendicular to the molecular long axes,

$$
\begin{aligned}
\mathbf{A}_{\|_i} &= (\mathbf{A}_i \cdot \hat{\mathbf{u}}_i)\hat{\mathbf{u}}_i \\
\mathbf{A}_{\perp_i} &= \mathbf{A}_i - (\mathbf{A}_i \cdot \hat{\mathbf{u}}_i)\hat{\mathbf{u}}_i.
\end{aligned}
\tag{5.8}
$$

Therefore, for example, $\phi_{\omega_\perp}(t)$ relates to the rotation of the molecule about the molecular short axes, associated with the tumbling motion of the molecules, and $\phi_{\omega_\|}(t)$ corresponds to rotation of the molecule about the molecular long axis, associated with the spinning motion of the molecule. In eqn. 5.7, the angular brackets imply an average over all particles as well as over time origins. According to these definitions, the correlation functions are all normalised to unity.

These simulations were initiated from final configuration obtained from the Monte Carlo simulations described in the previous sections. Initial velocities were taken to be in the same direction as the initial forces and torques, with the magnitudes conforming to the required temperature and corrected such that there was no overall momentum. It has been shown [107] that for calamitic molecules, such as those represented by the IRGB potential, the moment of inertia about the long axis of a linear molecule is approximately an order of magnitude less than that about the short axes. Since the short-axis moment of inertia is usually taken to be unity for the Gay-Berne potential, the moments of inertia have been chosen to be $I_{xx} = I_{yy}$ = 1.0 and $I_{zz} = 0.1$. In order to determine the time step, δt, to be used, a brief series of simulations were undertaken to study energy conservation as a function of the time step for run lengths whose total time is $N\delta t$. The energy conservation is

defined as

$$\Delta E(\delta t) = \frac{1}{N} \sum_{k=1}^{N} \left| \frac{E(k\delta t) - E(0)}{E(0)} \right|. \tag{5.9}$$

The value of $N\delta t = 10.0$ was chosen and kept constant for all such simulations. Thus, the equations of motion may be solved for a fixed period of time and the energy conservation may be measured as a function of time step, as shown in Fig. 5.50. For $\delta t = 0.0015$, which has typically been used in the past for molecular dynamics simulations of the Gay-Berne potential, the total energy is not conserved with a large drift being observed in the energy evolution with time. This behaviour is expected, since the introduction of biaxiality introduces a rapid rotation of the molecules about their long axes which is not present for the standard Gay-Berne potential. For a time step an order of magnitude less than this no drift is observed. As a result of this, a time step of $\delta t = 1 \times 10^{-5}$ has been employed here, for which energy fluctuations are less than 1 part in 10^{-4}.

The trajectories of the particles were followed for a total of 1×10^{6} time steps after an initial equilibration period of 5×10^{5} steps. For the evaluation of the ACF's, the spacing between consecutive time origins was 100 time steps.

5.4.1 Translational Dynamics

The velocity autocorrelation functions calculated for 3:1 molecules at $\delta = 30$ within the nematic ($P^* = 1.00$, $T^* = 1.00$), smectic A ($P^* = 1.00$, $T^* = 1.80$) and smectic
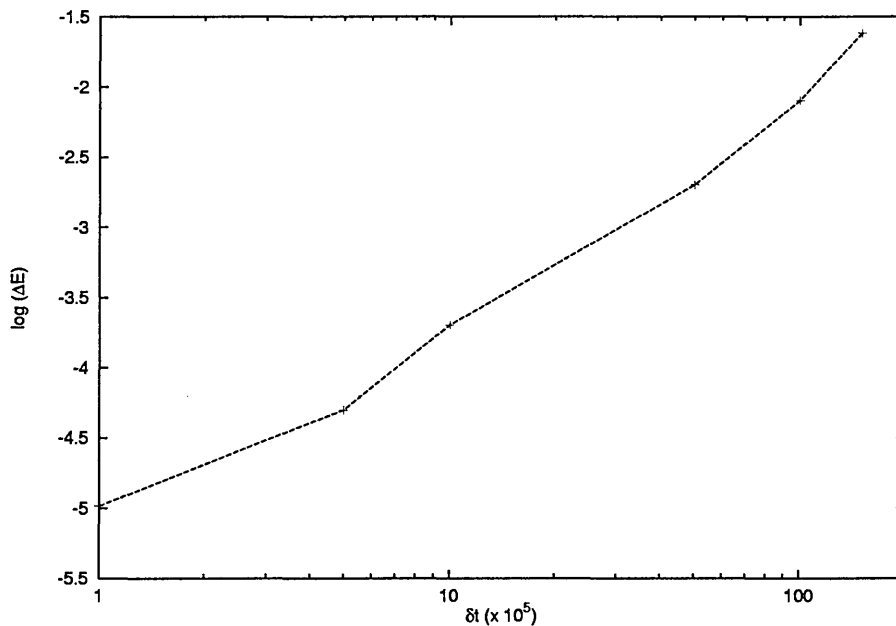
162

Figure 5.50: Energy conservation dependence as a function of time step.

J ($P^* = 0.00$) phases are shown in Fig. 5.51. For the nematic and smectic A phase it is apparent that the onset of orientational ordering causes $\phi_{v_\parallel}(t)$ to relax more slowly than $\phi_{v_\perp}(t)$, with a more pronounced negative region being observed with increasing density. This type of behaviour has been reported previously [83, 105] and is attributed to the cage effect, described as if the individual molecules are diffusing along cylindrical cages. Thus, the rapid relaxation and reversal of the perpendicular component are ascribed to successive collisions with the molecules forming this cage, while the parallel component undergoes a diffusive motion along the cylindrical cage.

Within the more ordered smectic J phase, these functions have a more pronounced negative region with clear oscillatory behaviour, with greater amplitudes and higher frequencies being observed with decreasing temperature. Since a negative region for these functions is ascribed to a reversal of the velocities with respect to the initial
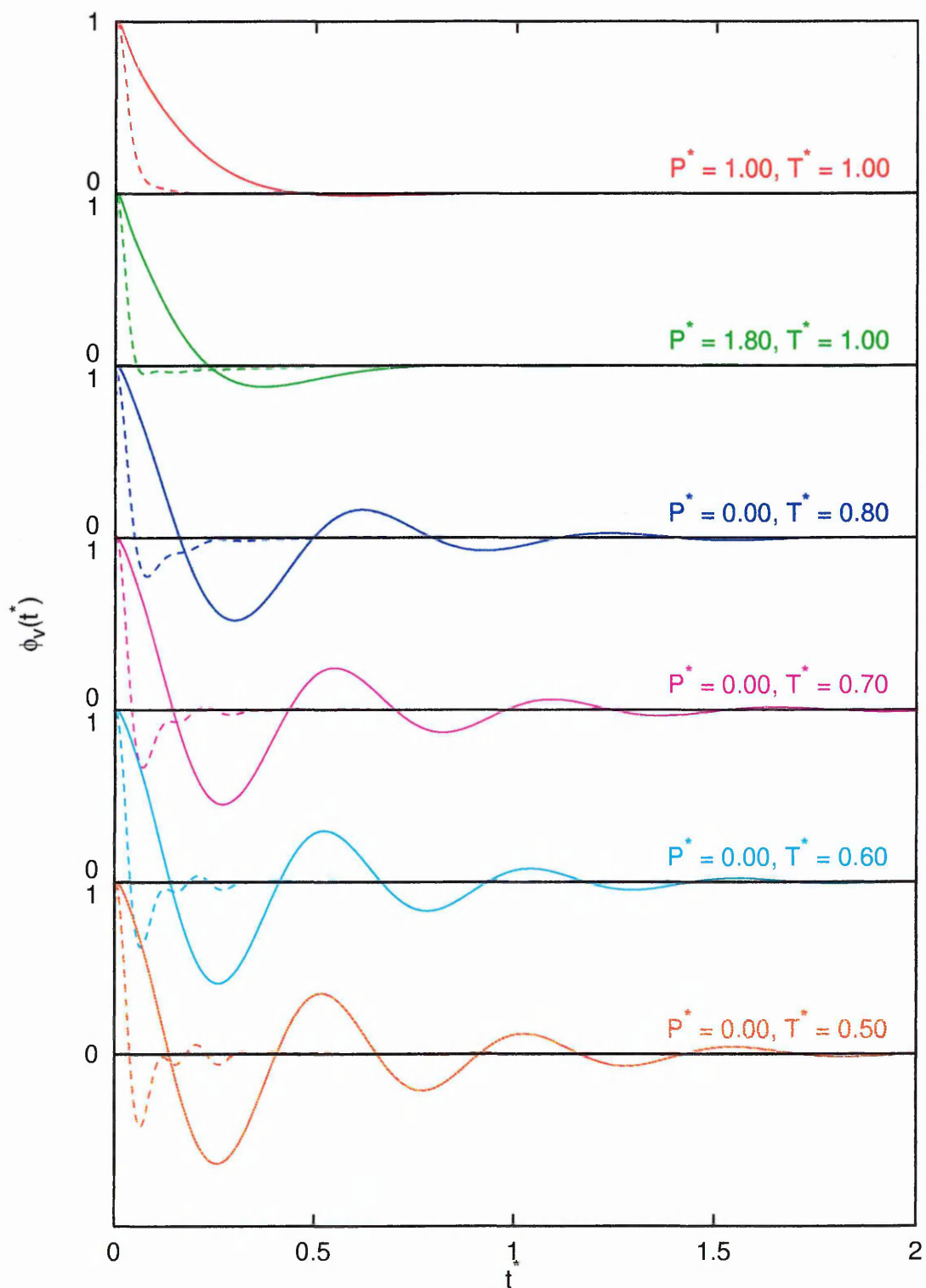
163

Figure 5.51: Velocity autocorrelation functions resolved parallel, $\phi_{v_\parallel}(t)$ (solid line), and perpendicular, $\phi_{v_\perp}(t)$ (dashed line), to molecular axes for 3:1 molecules at $\delta = 30$.

velocity after a time lapse, it appears that within the smectic J phase the cage effect not only constrains the molecules' perpendicular motion but also controls that in the parallel direction. Numerical integration of these functions (which yields the correlation time which may be used to calculate the diffusion coefficient) within the smectic J phase leads to almost zero values whereas non-zero values are obtained for the nematic and smectic A phases. This suggests that there is no diffusive process occuring within the smectic J phase. Similar behaviour is also seen for the smectic G phase observed for the 4:1 molecules and the bi-stable smectic G/J phase observed for the 3.5:1 molecules.

5.4.2 Rotational Dynamics

The angular velocity autocorrelation functions calculated for 3:1 molecules at $\delta = 30$, at the same temperatures and pressures as were used in the previous section, are shown in Fig. 5.52. Within all of these orientationally ordered phases $\phi_{\omega_\perp}(t)$ (associated with the tumbling motion of the molecules) decays rapidly towards zero, with a clear negative lobe being observed for all cases. Within the smectic J phase, oscillatory behaviour is observed, with greater amplitudes and higher frequencies being observed with decreasing temperature. This type of behaviour is to be expected since the tumbling motion should be restricted due to the presence of orientational ordering, with the rapid decay and negative regions resulting due to rapid collisions of molecules with their nearest neighbours. Numerical integration of each of these functions gives almost zero values.
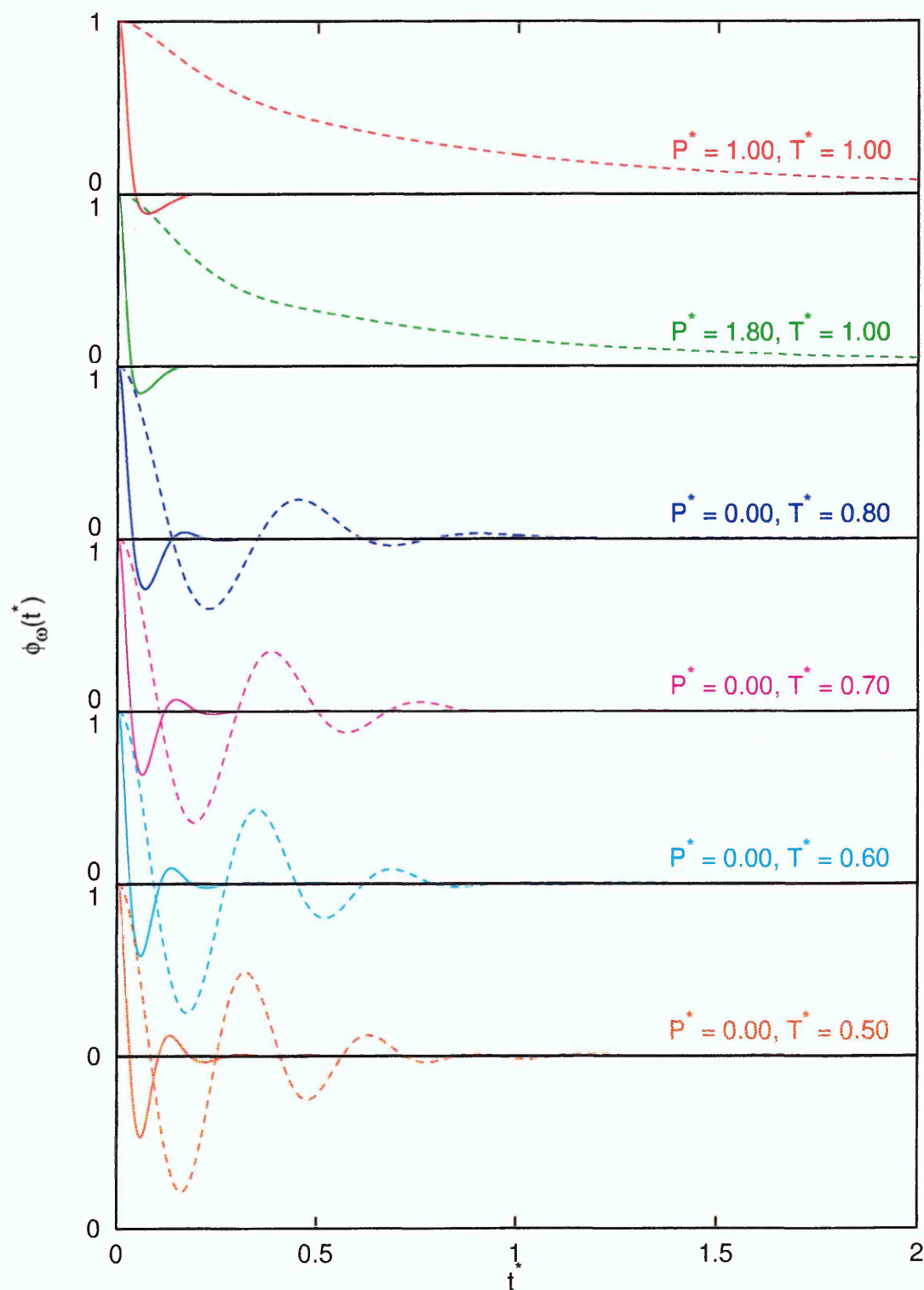
165

Figure 5.52: Angular velocity autocorrelation functions resolved parallel, $\phi_{\omega_\parallel}(t)$ (dashed line), and perpendicular, $\phi_{\omega_\perp}(t)$ (solid line), to molecular axes for 3:1 molecules at $\delta = 30$.

166

The spinning motion of the molecules about their long axes (given by $\phi_{\omega_\parallel}(t)$) relaxes much more slowly, with a gradual decay to zero and negative regions being observed within the nematic and smectic A phases. This behaviour is to be expected for systems where free rotation about the molecular long axes is permitted. Within the smectic J phase, $\phi_{\omega_\parallel}$ decays much more rapidly and displays oscillatory behaviour, which leads to almost zero values of the correlation time being calculated. Since a negative region corresponds to a reversal in the direction of the angular momentum with respect to its initial value, it would appear that free rotation of the molecules about their long axes is not permitted, with the angular velocity oscillating rapidly. That said, large oscillatory motions which are much larger than conventional thermal rotations within a crystal phase, termed nearly-free rotation, have been observed experimentally within smectic mesophases. Since no phase transition into a crystal phase is observed, distinction between nearly-free behaviour and the constrained motion expected for the crystal phase cannot be made from these results.

For the other two types of hexatic phases reported for longer molecules, similar behaviour is observed for the smectic G phase formed by 4:1 molecules, whereas the bi-stable smectic G/J phase formed by 3.5:1 molecules (shown in Fig. 5.53 within the nematic ($P^* = 1.50$), smectic A ($P^* = 2.00$) and smectic G/J ($P^* = 4.50$ and 7.50) phases) displays similar behaviour for $\phi_{\omega_\perp}(t)$ but not for $\phi_{\omega_\parallel}(t)$. The latter ACF within the hexatic phase, whilst decaying more rapidly than in the nematic and smectic A phases, does not oscillate about zero and calculation of the correlation times gives non-zero values. Whilst these observations confirm that free rotation about the molecular long axes is permitted, further discussion regarding this phase

will not be entered into since experimental evidence suggests this to be an unrealistic feature of this model.

5.5 Conclusions

This chapter has considered the simulation of a novel biaxial variant of the Gay-Berne potential which has been developed to offer a single-site representation of a multi-site model constrained into a *zig-zag* conformation. The Gay-Berne potential has been extensively studied and provides a rich body of previous work for comparison.

Since the time step required to perform simulations using this biaxial potential with molecular dynamics methods is an order of magnitude less than that typically used for the simulation of the uniaxial Gay-Berne potential, Monte Carlo methods have been employed to perform extensive simulations within the constant NVT and NPT ensembles, allowing approximate phase diagrams to be constructed. The equilibration periods used here are similar to those used for the Gay-Berne potential, and therefore the use of these slightly modified Monte Carlo methods provides a more efficient method with which to construct such phase diagrams. The modified constant NVT method, in which the aspect ratio of the simulation box is allowed to vary and so removes the possibility of distortion of the translationally ordered phases, has been shown to agree with the results obtained from the more realistic constant NPT method, provided that the system is not is a region of phase coexistence.
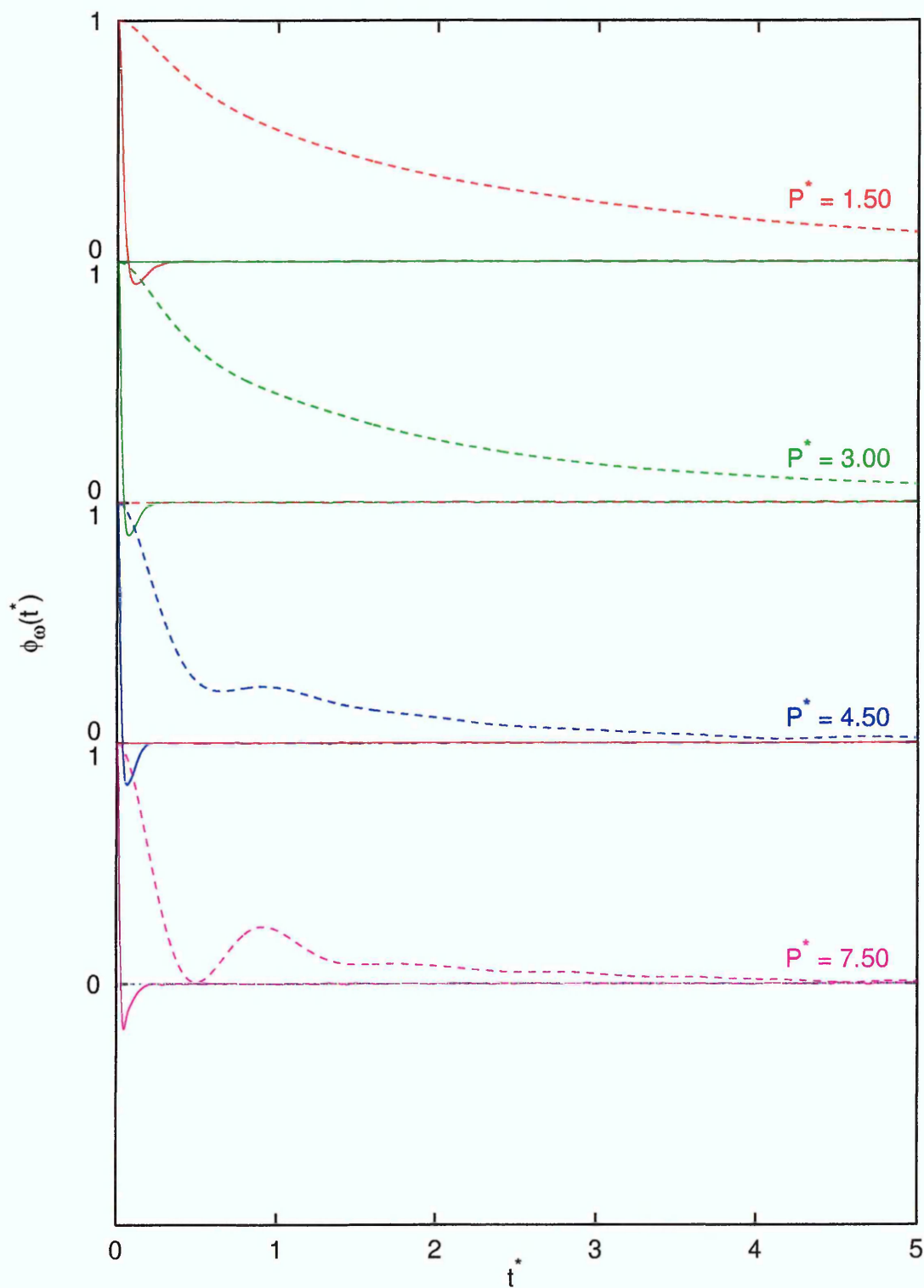
Figure 5.53: Angular velocity autocorrelation functions resolved parallel, $\phi_{\omega_{\parallel}}(t)$ (dashed line), and perpendicular, $\phi_{\omega_{\perp}}(t)$ (solid line), to molecular axes for 3.5:1 molecules at $\delta = 30$.

That said, care should still be taken when using the constant NVT ensemble since simulations performed within a region of phase space where the system wishes to phase separate can give erroneous results, leading to the incorrect classification of phases being made.

Firstly, the variation of phase behaviour with increasing angle of internal rotation, corresponding to a molecule with a more pronounced *zig-zag* conformation, will be considered. For uniaxial molecules with a 3:1 aspect ratio with the stronger ($\nu = 2$ and $\mu = 1$) parameterisation, an approximate phase diagram has been constructed which includes the nematic, smectic A (albeit with a very weak density wave parallel to the molecular long axes) and smectic B phases. Increasing values of the angle of internal rotation frustrates the local packing, which results in the destabilisation of the more ordered mesophases such that all of the observed phase transitions are shifted to higher densities and lower temperatures, and the temperature range of the vapour coexistence region also appears to be reduced. For sufficiently large angles of internal rotation, the smectic B phase is replaced by the tilted smectic J phase, with the smectic A phase being totally destabilised.

Since the smectic A phase has only been observed for a small range of temperatures and densities, with only a weakly defined layered structure being formed for this initial parameterisation, the effect of increasing the elongation of the constituent molecules has been considered since simulations considering perturbations away from the original Gay-Berne parameterisation [87] have shown that increasing molecular elongation stabilises the smectic mesophases. The phase behaviour of

the Internally-Rotated Gay-Berne potential at $\delta = 30$ using the alternative exponents has been studied for molecules with aspect ratios of 3.5:1 and 4:1. The results obtained agree well with the expected trends; namely that the observed phase transitions are shifted to lower densities and pressures, with the temperature range of the vapour coexistence region being extended. The smectic A phase is stabilised with respect to the nematic phase such that for 4:1 molecules no nematic phase is observed at the temperature considered here. The nature of the tilted hexatic phase is also found to be dependent upon the length of the constituent molecules, with short molecules displaying the smectic J phase while longer molecules display the smectic G phase. Molecules of an intermediate length display an unrealistic bi-stable smectic G/J phase. Whilst there are very few studies which consider the effect of molecular structure upon the type of tilted hexatic phase which is observed, it does not appear that the behaviour of these phases is governed purely due to the molecular length [11]. That said, the results presented here show that the degree of interdigitation and the subtle relationship between inter- and intra-layer interactions is of considerable importance and should not be overlooked; worryingly, exactly this has been done in some previous theoretical [29,30] and simulation [101,102] studies.

At no point during the course of this simulation study has a tilted phase displaying smectic C like properties been observed, with the only tilted phases being observed having long range translational order with free rotation of the molecules about their long axes not being permitted. It would therefore appear that models which only consider steric biaxiality of the constituent molecules (i.e. the Wulf model [42]) represents a poor route to obtaining a smectic C phase. It should, however, be

noted that the Gay-Berne potential offers the computer simulator a wide range of parameter space, and the possibility that the smectic C phase may be observed using this model with an alternative parameterisation should not be completely ruled out. However, since for sufficiently long molecules a smectic A phase is observed it seems likely that a smectic C phase will only be formed for parameterisations where the side-to-side well depth is greater than that considered here.

Chapter 6

Investigation into the Effect of Molecular Flexibility

6.1 Introduction

In this chapter, results are reported obtained from a version of the Internally-Rotated Gay-Berne potential, modified to include a degree of molecular flexibility.

The motivation for this work derives from the conclusion of the previous chapter that the Internally-Rotated Gay-Berne model, arrived at as to represent a molecule rigidly constrained into a *zig-zag* conformation, offers a poor route to obtaining a smectic C phase. In practice, molecules which form the smectic C phase are not rigid structures [6], but have flexible terminal chains attached to a rigid central core. Such flexibility is considered important for the formation of the liquid crystalline phases,

since it both promotes reasonably low melting points and is thought to stabilise the molecular alignment within the mesophase structures.

Since molecules which exhibit the smectic C phase usually have two terminal chains, rather than one terminal chain and a small polar substituent, the representation of a molecule by three Gay-Berne units may be interpreted such that the central Gay-Berne unit represents the central core of the molecule, with the two outboard Gay-Berne units representing the terminal chains. Given this interpretation, a degree of molecular flexibility may be introduced into the model by allowing the angle between the constituent Gay-Berne units to vary during the course of the simulation. In order for this modification to be introduced into the single-site Internally-Rotated Gay-Berne potential, constraints upon the location of the constituent units within the multi-site model must be imposed (shown schematically in Fig. 6.1(a)); firstly, the Gay-Berne units representing the terminal chains must always lie in the same plane, and, secondly, the two terminal units must be mutually parallel.

Recall, from section 5.1, that the effect of this type of molecular flexibility upon the interaction between a pair of molecules is to rotate the *doughnut* of potential minima about one of the molecular short axes. Thus, this type of molecular flexibility may be represented using the Internally-Rotated Gay-Berne potential where the angle between $\hat{u}$ (defining the shape of the molecule) and $\hat{v}$ (defining the location of the potential minima) is no longer fixed during the course of the simulation. The angle between $\hat{u}$ and $\hat{v}$, whilst being allowed to vary, may be linked harmonically to an ideal value, such that the energetically most favourable configuration is that of a
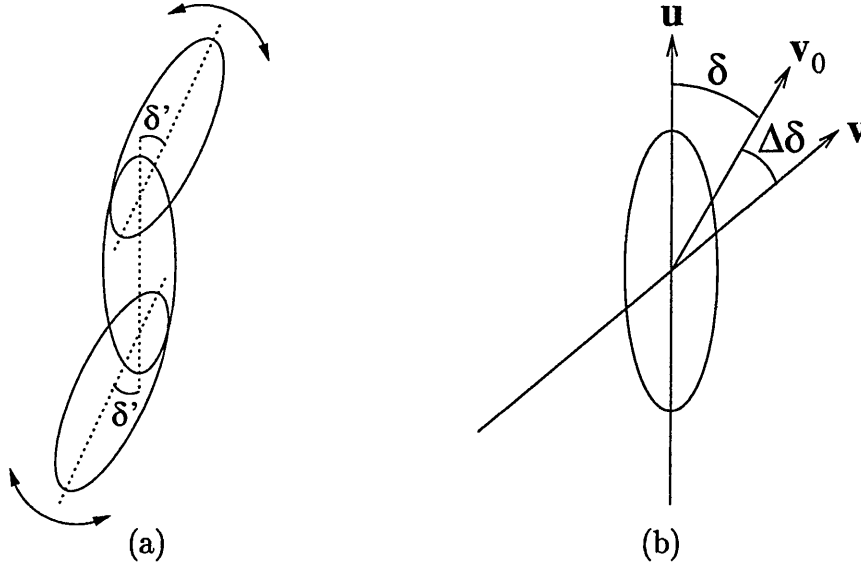
Figure 6.1: Schematic representation of a flexible molecule, (a) in terms of the multi-site model and (b) definition of axes for the flexible Internally-Rotated Gay-Berne potential.

known angle of internal rotation. A schematic representation of the vectors used to define the molecule is shown in Fig. 6.1(b). The variable δ is now redefined as the angle between $\hat{u}$ and the ideal orientation of $\hat{v}$ ($\hat{v}_0$) and is referred to as the *ideal angle of internal rotation*. $\Delta\delta$ gives the angle between the ideal and actual orientation of $\hat{v}$, i.e. $\cos\Delta\delta = \hat{v} \cdot \hat{v}_0$. Thus, the potential energy of molecule i is given by,

$$U_i = \sum_{i \neq j}^{N} U(\mathbf{r}_{ij}, \hat{u}_i, \hat{u}_j, \hat{v}_i, \hat{v}_j) + k\left[1 - \cos^2\Delta\delta_i\right] \qquad (6.1)$$

where the first term gives the potential energy between molecule i and all the other molecules (within a cutoff distance), and the second term represents the energetic cost associated with $\hat{v}$ moving away from its ideal orientation with respect to $\hat{u}$. As a result of this definition, the parameter k may be considered as a spring constant

175

linking the orientation of $\hat{\mathbf{v}}$ to its ideal orientation.

As with the simulations performed upon the rigid molecules, the intermolecular potential is truncated at a distance $r_{cut} = (\sigma_{ee}/\sigma_{ss} + 1)\sigma_0$, with a shifted potential being used to eliminate the discontinuity in the potential energy as a pair of molecules crosses this boundary. Since the energetic cost associated with moving $\hat{\mathbf{v}}$ away from its ideal orientation is a intramolecular property, the second term in eqn. 6.1 is not considered when the shifting the potential.

Most of the simulations performed using this model have employed Monte Carlo methods within the constant NPT ensemble, with each MC cycle consisting of N attempted particle displacements and orientational moves, and one attempt to change the box volume. The orientational moves were attempted by independent random rotations of both $\hat{\mathbf{u}}$ and $\hat{\mathbf{v}}$, via the Barker-Watts algorithm [45]. The ideal location of $\hat{\mathbf{v}}$ was then calculated from the condition that $\hat{\mathbf{v}}_0$ is at an angle δ from $\hat{\mathbf{u}}$ and lies within the same plane as $\hat{\mathbf{u}}$ and $\hat{\mathbf{v}}$ on the same side of the molecule as $\hat{\mathbf{v}}$. Further simulations were then performed using molecular dynamics techniques, thus allowing the dynamic behaviour of the system to be determined.

Each sequence of simulations was initiated from a lattice configuration equilibrated at low pressure, such as to obtain an isotropic phase. Once again the system size was $N = 512$. Equilibration periods were typically taken to be 5×10^4 sweeps, increasing to $(1-2) \times 10^5$ sweeps in the vicinity of phase transitions. Average values were then measured over a further 5×10^4 sweeps.

The simulations were performed upon systems with the stronger well depth parameterisation ($\epsilon_{ss}/\epsilon_{ee} = 5.0$, $\mu = 1.0$ and $\nu = 2.0$) for two values of the shape anisotropy ($\sigma_{ee}/\sigma_{ss} = 3.0$ and 4.0) and various values of the spring constant, k. A single isotherm was considered for each system, at $T^* = 1.00$ and 1.50 for the 3:1 and 4:1 molecules respectively. The ideal angle of internal rotation was set at 30^0. This choice of parameterisation has been chosen to enable comparison to be made with the results presented in the preceding chapter, which will be referred to as $k = \infty$ (since this value in eqn. 6.1 gives a rigid molecule).

Since simulations of this type have not been attempted previously, it is initially necessary to determine the values of the spring constant k to be used. To achieve this a brief series of simulations were undertaken, initiated from the final configuration of the lowest density which exhibited the smectic J phase observed for the rigid 3:1 IRGB molecules at $\delta = 30$ ($P^* = 2.20$ and $T^* = 1.00$), with reducing k. Examination of the orientational order parameters and radial distributions from these runs (not shown) indicates that the smectic J phase persists for $100 \geq k \geq \infty$, with a nematic phase being observed for $k \leq 10$. The corresponding averaged probability distributions of the angles of internal rotation is shown in Fig. 6.2, normalised such that the area under these profiles is equal to unity.

It is clear from these distributions, that there is no molecular flexibility present for large values of k ($\geq 1 \times 10^4$). As k is further reduced, flexibility is introduced into the model, with a broader peaks centred upon 30^0 (the ideal angle of internal rotation) being observed. The width of the peak is increased and the height of the
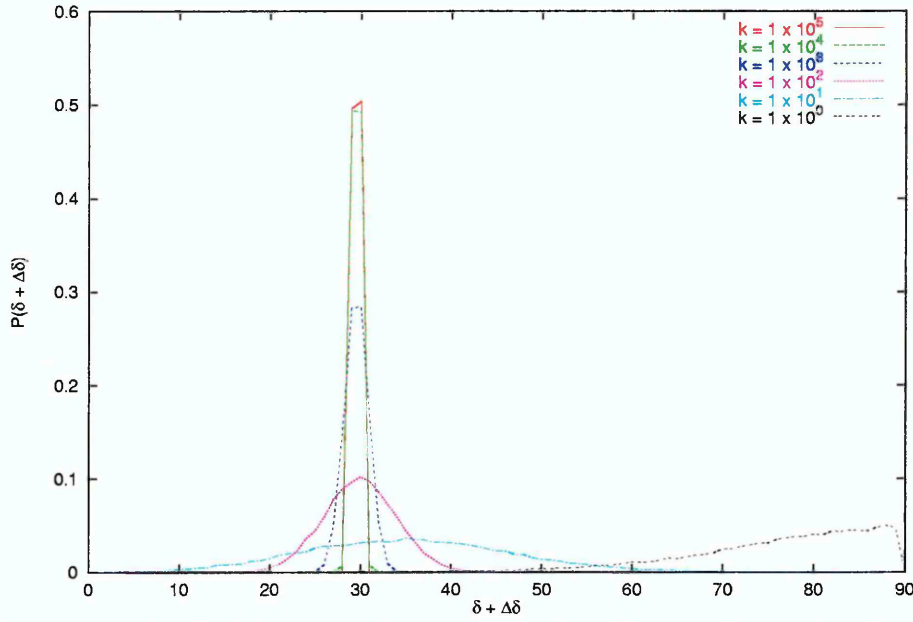
Figure 6.2: Probability distribution of angles of internal rotation $\delta + \Delta\delta$ for 3:1 molecules at $P^* = 2.20$ and $T^* = 1.00$.

peak is reduced with decreasing k. For $k = 10$ and 1, where the nematic phase is observed, the peak is no longer centred about the ideal angle of internal rotation, but $\approx 35^0$ and 90^0 respectively. This behaviour seems likely to be due to low values of k providing too weak a coupling between the observed angle of internal rotation and its ideal value to constrain molecules within a translationally ordered phase. The distribution of angles of internal rotation is, therefore, shifted to higher values since a larger surface area of each molecule is associated with the *doughnut* of potential minima, thus giving a greater number of pair interactions access to the potential minima within these translationally disordered phases.

Since the aim here is to attempt to obtain a smectic C phase, intermediate values of the spring constant from $k = 100$, at which flexibility is introduced into the model without the translationally ordered phase being destabilised, to $k = 10$, where the

translationally ordered phase is destabilised for the state point considered above, will be employed. Initially the phase behaviour for the shorter 3:1 molecules will be considered.

6.2 Short Molecules

The equations of state obtained from the simulations of particles interacting via the flexible Internally-Rotated Gay-Berne potential with an aspect ratio of 3:1 at $T^* = 1.00$ for $k = \infty$, 100 and 10 are shown in Fig. 6.3. The $k = \infty$ case is redrawn from Fig. 5.30, and provides a rigid molecule reference system, with the sequence of phases being isotropic ($\rho^* \lesssim 0.225$, $P^* \lesssim 0.70$), nematic ($0.248 \lesssim \rho^* \lesssim 0.286$, $0.75 \lesssim P^* \lesssim 1.25$), smectic A ($0.286 \lesssim \rho^* \lesssim 0.310$, $1.25 \lesssim P^* \lesssim 2.00$) and smectic J ($\rho^* \gtrsim 0.330$, $P^* \gtrsim 2.20$). The other observables calculated for the $k = 100$ and 10 cases are tabulated in Table 6.1.

Initially the stronger $k = 100$ case will be discussed. As is expected the first ordered phase is nematic, confirmed by the non-zero value adopted by the nematic order parameter and the liquid like behaviour of the radial distribution functions (Figs. 6.4 and 6.5). Whilst this transition is observed over the same pressure range as for the $k = \infty$ case, with the uppermost density in the isotropic phase being observed at the same point, the coexistence region extends over a slightly smaller range of densities for the flexible model. With further increasing density, a weak density wave is once again observed in $g_{\parallel}(r_{\parallel}^*)$ (Fig. 6.4) for $P^* \geq 1.30$, corresponding to $\rho^* \geq 0.287$,
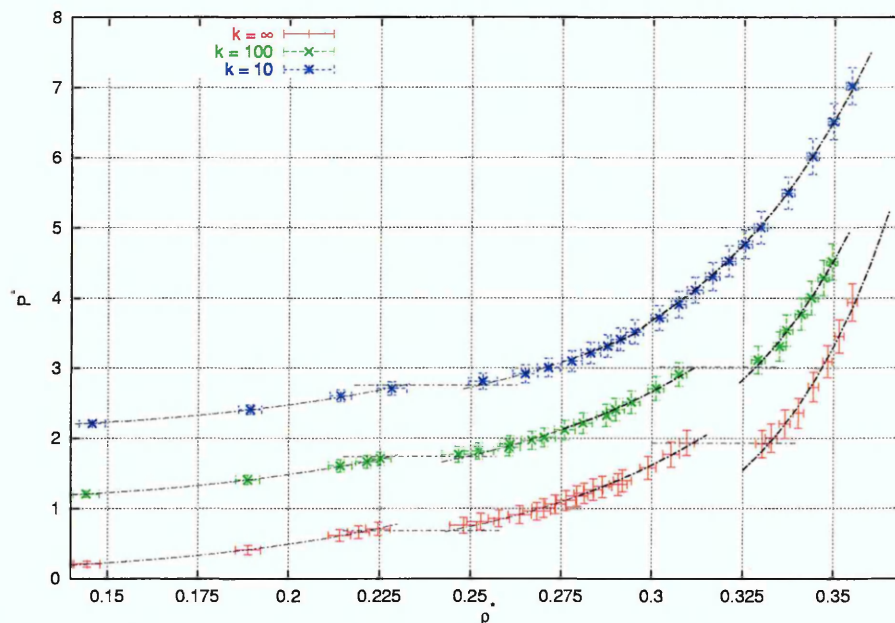
Figure 6.3: Equations of state (pressure P^* vs density ρ^*) for 3:1 molecules with various values of k at $T^* = 1.00$; for clarity these results are successively displaced upwards by one unit. Lines are drawn to guide the eye, horizontal lines indicate estimates of the transition pressures.

indicating the onset of smectic ordering at the same pressure and density as is observed for the $k = \infty$ case. Since this phase displays liquid like ordering within each layer (Fig. 6.5), with no evidence biaxial ordering or molecular tilting, this phase is classified as smectic A. It is worth noting that the amplitude of the oscillation of the density wave in $g_\parallel(r_\parallel^*)$ is greater than for the rigid molecule.

A second discontinuity is observed in the equation of state with increasing density, with a corresponding increase in the nematic order parameter, and a very slight increase in the biaxial order parameter being observed. Examination of the radial distribution functions (Figs. 6.4 and 6.5) shows that this phase has a well defined layered structure with long range hexatic ordering within each layer. This phase transitions also occurs over the same pressure range as for the $k = \infty$ case, although

180

Table 6.1: Observable averages calculated for 3:1 molecules for $k = 100.0$ and 10.0 at $T^* = 1.00$.

P^*	$\langle U^* \rangle$	Q_{00}^2	Q_{22}^2	$\langle \theta \rangle$	$r_{\parallel}$
		$k = 100$			
0.20	-1.38(0.07)	0.060(0.016)	0.029(0.015)	none	-
0.40	-2.06(0.09)	0.074(0.022)	0.029(0.018)	none	-
0.60	-2.53(0.09)	0.086(0.043)	0.026(0.019)	none	-
0.65	-2.75(0.10)	0.107(0.063)	0.023(0.017)	none	-
0.70	-2.79(0.09)	0.108(0.048)	0.023(0.017)	none	-
0.75	-3.67(0.19)	0.647(0.059)	0.033(0.019)	none	-
0.80	-3.83(0.16)	0.688(0.039)	0.036(0.020)	none	-
0.85	-4.16(0.11)	0.760(0.018)	0.038(0.020)	none	-
0.90	-4.09(0.11)	0.722(0.023)	0.036(0.020)	none	-
0.95	-4.31(0.11)	0.773(0.017)	0.035(0.019)	none	-
1.00	-4.42(0.12)	0.785(0.023)	0.037(0.020)	none	-
1.10	-4.58(0.12)	0.804(0.020)	0.036(0.020)	none	-
1.20	-4.73(0.11)	0.819(0.012)	0.038(0.020)	none	-
1.30	-4.97(0.11)	0.847(0.012)	0.039(0.021)	none	2.57
1.40	-5.00(0.11)	0.843(0.013)	0.036(0.019)	none	2.58
1.50	-5.15(0.11)	0.856(0.011)	0.037(0.020)	none	2.56
1.70	-5.39(0.11)	0.864(0.012)	0.039(0.020)	none	2.58
1.90	-5.60(0.12)	0.881(0.010)	0.039(0.020)	none	2.57
2.10	-7.18(0.10)	0.946(0.004)	0.042(0.022)	5.60(1.82)	2.59
2.30	-7.52(0.10)	0.959(0.003)	0.063(0.030)	9.98(0.69)	2.60
2.50	-7.52(0.10)	0.960(0.003)	0.054(0.026)	9.71(0.70)	2.59
2.75	-7.69(0.10)	0.963(0.003)	0.060(0.030)	10.03(0.57)	2.59
3.00	-7.70(0.10)	0.964(0.003)	0.055(0.027)	9.40(0.57)	2.58
3.25	-7.85(0.10)	0.966(0.002)	0.077(0.036)	10.01(0.63)	2.58
3.50	-7.90(0.10)	0.968(0.002)	0.079(0.032)	9.98(0.58)	2.57
		$k = 10$			
0.20	-1.34(0.07)	0.059(0.016)	0.028(0.014)	none	-
0.40	-2.04(0.08)	0.075(0.022)	0.030(0.016)	none	-
0.60	-2.49(0.09)	0.097(0.029)	0.025(0.018)	none	-
0.70	-2.87(0.15)	0.107(0.075)	0.023(0.018)	none	-
0.80	-3.82(0.16)	0.691(0.038)	0.036(0.020)	none	-
0.90	-4.22(0.13)	0.762(0.026)	0.038(0.020)	none	-
1.00	-4.39(0.13)	0.784(0.022)	0.037(0.020)	none	-
1.10	-4.61(0.11)	0.805(0.015)	0.038(0.021)	none	-
1.20	-4.73(0.10)	0.821(0.014)	0.038(0.020)	none	-
1.30	-4.90(0.11)	0.838(0.014)	0.041(0.021)	none	-
1.40	-4.98(0.11)	0.841(0.013)	0.037(0.020)	none	-
1.50	-5.08(0.10)	0.845(0.011)	0.040(0.020)	none	-
1.70	-5.29(0.10)	0.869(0.010)	0.041(0.021)	none	-

continued from previous page					
P^*	$\langle U^* \rangle$	Q^2_{00}	Q^2_{22}	$\langle \theta \rangle$	$r_{\parallel}$
1.90	-5.42(0.10)	0.878(0.009)	0.039(0.020)	none	-
2.10	-5.52(0.10)	0.881(0.010)	0.038(0.021)	none	-
2.30	-5.67(0.10)	0.890(0.008)	0.038(0.020)	none	-
2.50	-5.79(0.10)	0.896(0.006)	0.041(0.020)	none	-
2.75	-5.92(0.10)	0.901(0.007)	0.040(0.018)	none	-
3.00	-6.00(0.10)	0.906(0.006)	0.039(0.020)	none	-
3.50	-6.19(0.10)	0.914(0.006)	0.044(0.022)	none	-
4.00	-6.36(0.10)	0.924(0.005)	0.042(0.023)	none	-
4.50	-6.53(0.08)	0.928(0.004)	0.046(0.024)	none	2.33
5.00	-6.47(0.10)	0.929(0.006)	0.045(0.024)	none	2.34

at lower densities. Whilst the biaxial order parameter is very small within this highest density phase, the layer normal $\hat{l}$ and the average director $\hat{n}$ are not coincident, giving an average tilt angle approximately half that observed for the rigid molecule. Examination of the radial distribution function resolved parallel and perpendicular to the direction of tilt, shown in Fig. 6.6, shows that this phase is smectic J.

These results show that, for a moderately large value of k, that the same sequence of phases is observed as for the rigid case. The observation that the transitions are shifted to lower densities for the flexible model confirms that a certain degree of molecular flexibility does stabilise mesophase formation. That said, flexibility also appears to destabilise the tilted hexatic phase; the significant reduction in the values found for the biaxial order parameter and average tilt angles suggests that the molecular flexibility is not frozen out within the hexatic phase. This inference is confirmed by examination of the probability distributions of the angle of internal rotation (shown in Fig. 6.7), which takes the form of a symmetric distribution centred upon the ideal angle of internal rotation within each of the observed phases. Somewhat surprisingly, the width and height of the peak remain unchanged with
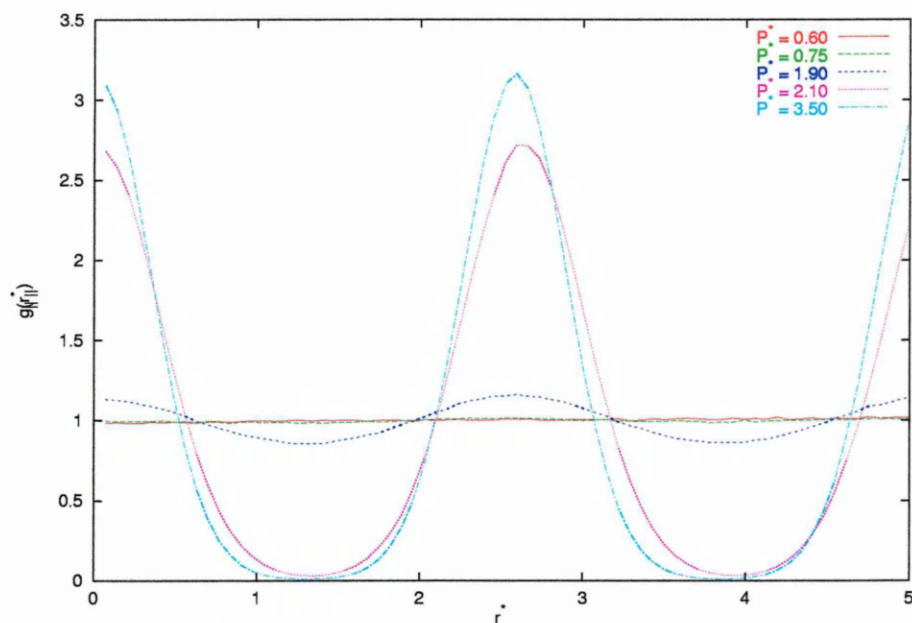
182

Figure 6.4: Radial distribution function resolved parallel to the layer normal for 3:1 molecules at $k = 100$ and $T^* = 1.00$.
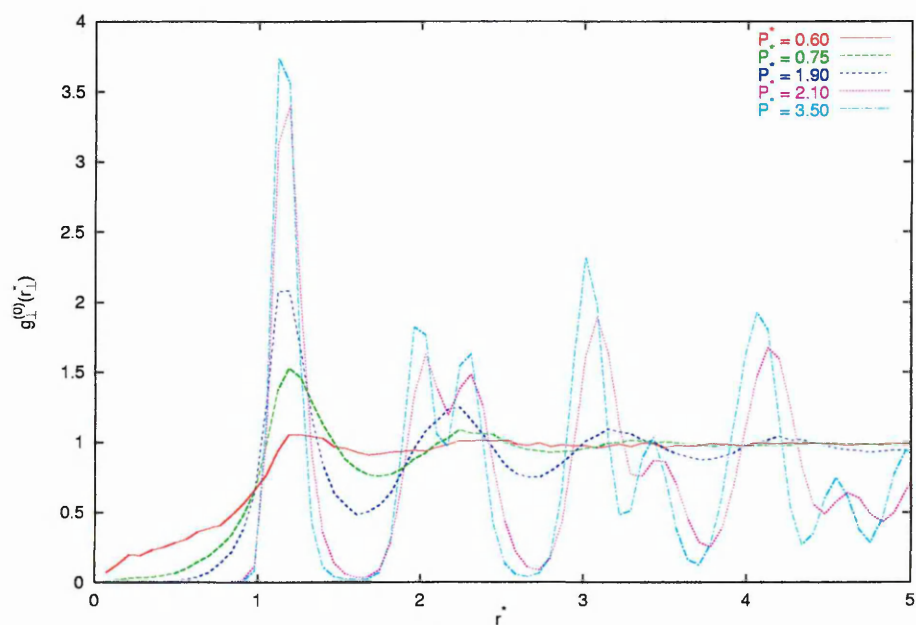

Figure 6.5: Radial distribution function resolved perpendicular to the layer normal for 3:1 molecules at $k = 100$ and $T^* = 1.00$.
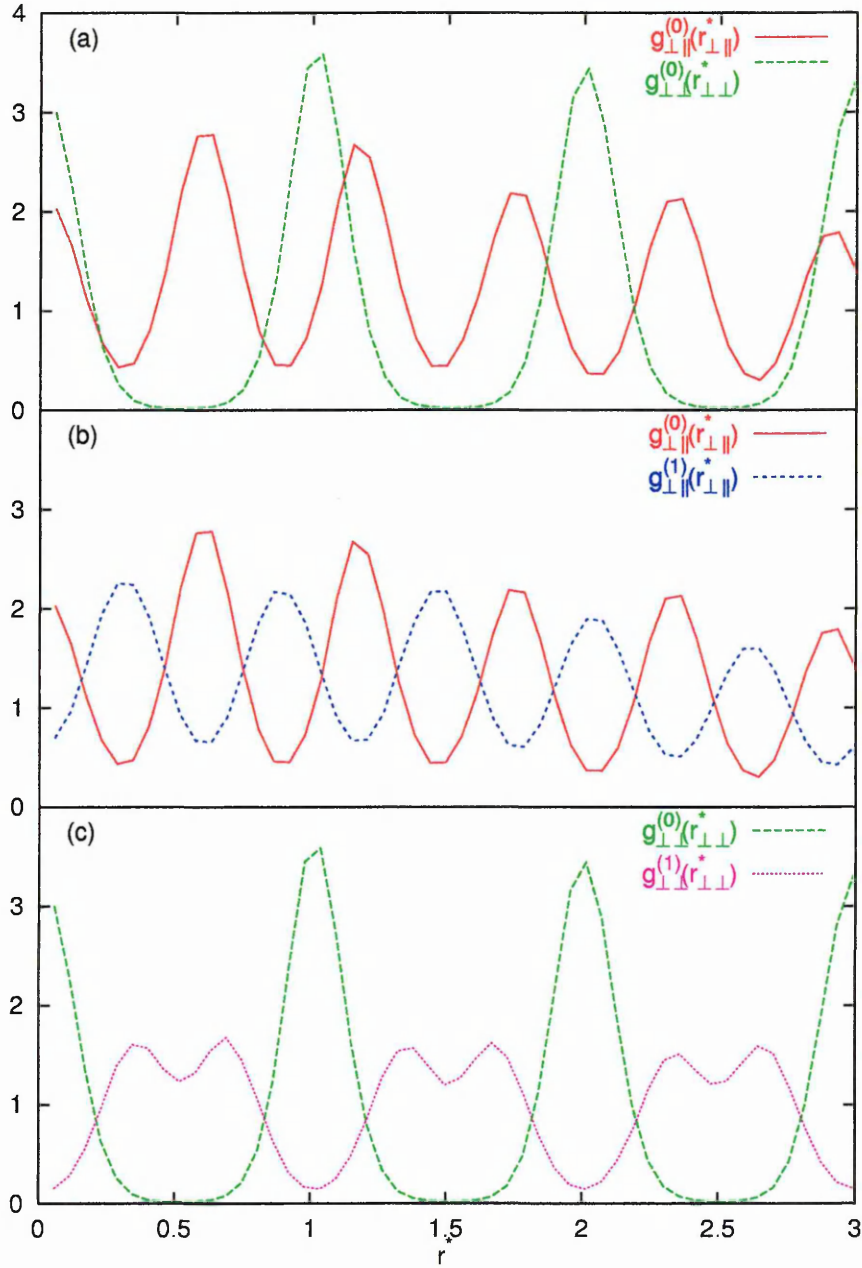
183

Figure 6.6: Radial distribution functions (a) resolved within the layer parallel, $g_{\perp\|}^{(0)}(r_{\perp\|}^*)$, and perpendicular, $g_{\perp\perp}^{(0)}(r_{\perp\perp}^*)$, to the direction of tilt and between adjacent layers resolved (b) parallel to the direction of tilt and (c) perpendicular to the direction of tilt for 3:1 molecules at $k = 100$, $T^* = 1.00$ and $P^* = 1.50$.

increasing density. Further discussion relating to this behaviour will be deferred to Section 6.4; the weaker $k = 10$ case will now being considered.
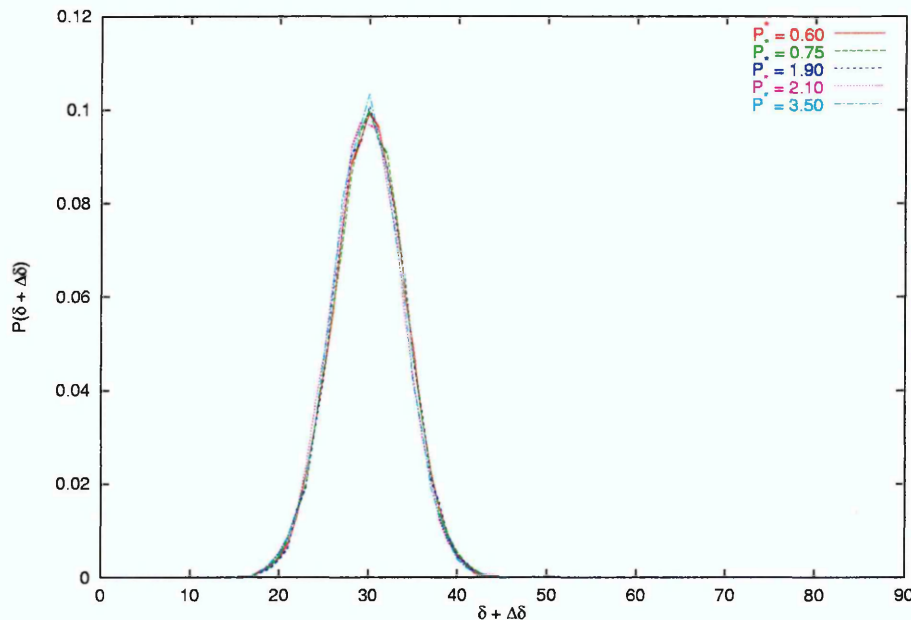

Figure 6.7: Probability distribution of molecular tilt angles $\delta + \Delta\delta$ for 3:1 molecules at $k = 100$ and $T^* = 1.00$.

Only one discontinuity is observed in the equation of state for the $k = 10$ case. The marked increase in the orientational order parameter and the liquid like structure in the radial distribution functions (Figs. 6.8 and 6.9) indicates an isotropic to nematic transition. The transition density is increased compared with that observed for the $k = 100$ and ∞ cases. As the density is further increased, a weak density wave is once again observed in $g_{\parallel}(r_{\parallel}^*)$ (Fig. 6.8) for $P^* \geq 4.50$, corresponding to $\rho^* \geq 0.350$. The liquid-like structure observed within each layer (Fig. 6.9) and lack of biaxial ordering indicates a smectic A phase.

As is expected, the probability distribution of angles of internal rotation (Fig. 6.10), shows that a wider range of $\delta + \Delta\delta$ values are adopted for this smaller spring constant.
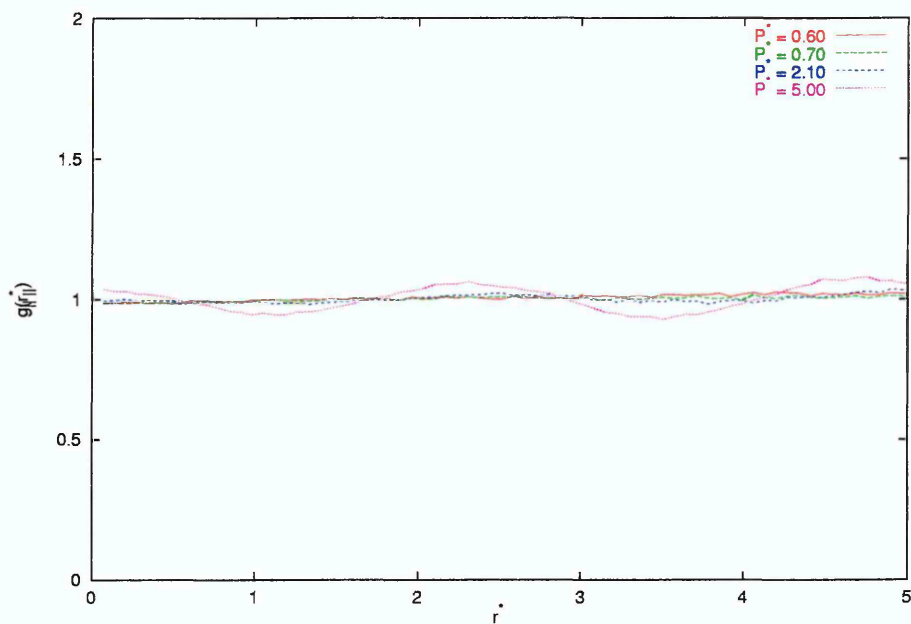
185

Figure 6.8: Radial distribution function resolved parallel to the layer normal for 3:1 molecules at $k = 10$ and $T^* = 1.00$.
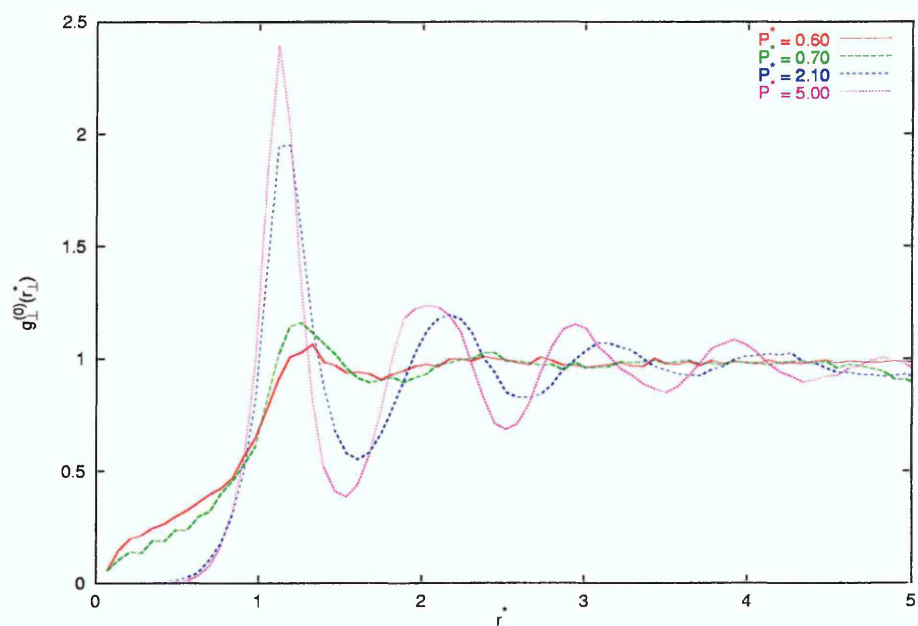

Figure 6.9: Radial distribution function resolved perpendicular to the layer normal for 3:1 molecules at $k = 10$ and $T^* = 1.00$.

186

As with the $k = 100$ case, the widths and heights of the peaks remain unchanged with increasing density. However, the centres of the peaks are shifted to higher values as the density is increased. This observation, along with the shifting of the transition densities to higher values and absence of a hexatic phase, indicates that at this low value of k the coupling between the observed angle of internal rotation and its ideal value is subject to domination by intermolecular effects. This tendency to undergo molecular deformation appears to restrict the range of mesophases available.

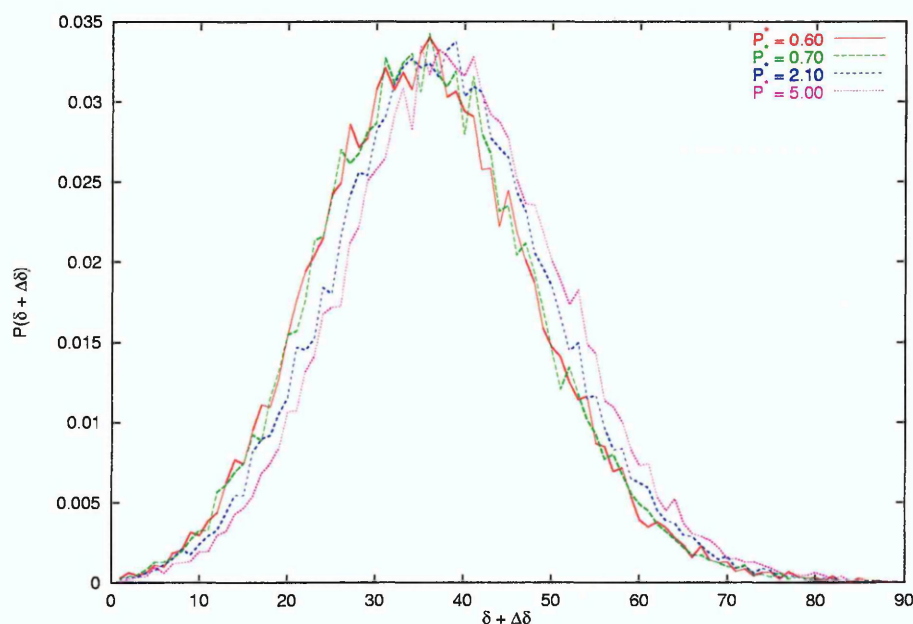Figure 6.10: Probability distribution of molecular tilt angles $\delta + \Delta\delta$ for 3:1 molecules at $k = 10$ and $T^* = 1.00$.

6.3 Long Molecules

The equations of state obtained from the simulations of particles interacting via the flexible Internally-Rotated Gay-Berne potential with an aspect ratio of 4:1 at $T^* = 1.50$ for $k = \infty$, 100, 50 and 10 are shown in Fig. 6.11. The $k = \infty$ case is

redrawn from Fig. 5.34, and represents a rigid reference system, with the sequence of phases being isotropic ($\rho^* \lesssim 0.131$, $P^* \lesssim 0.55$), smectic A ($0.176 \lesssim \rho^* \lesssim 0.209$, $0.60 \lesssim P^* \lesssim 0.95$) and smectic G ($\rho^* \gtrsim 0.234$, $P^* \gtrsim 1.00$). The other observables calculated for the $k = 100$, 50 and 10 cases are tabulated in Table 6.2.
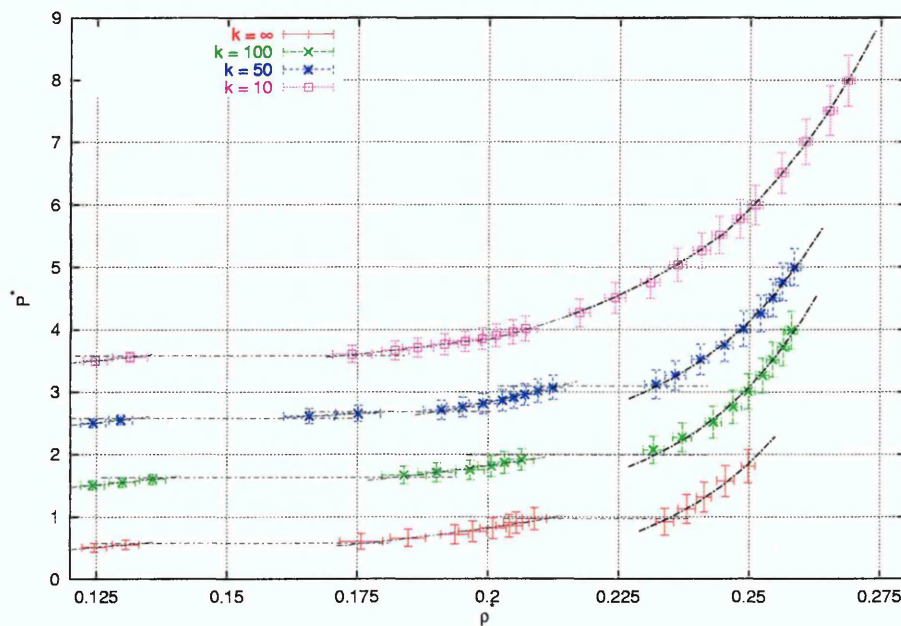

Figure 6.11: Equations of state (pressure P^* vs density ρ^*) for 4:1 molecules with various values of k at $T^* = 1.50$; for clarity these results are displaced upwards by one unit. Lines are drawn to guide the eye, horizontal lines indicate estimates of the transition pressures.

For the $k = 100$ case, the first phase transition observed upon compression is at a higher pressure and density than that found in the rigid case, with a layered structure being formed (shown in Fig. 6.12). Since no evidence of biaxial ordering is found, and the layers are formed perpendicular to the average director $\hat{\mathbf{n}}$, with liquid-like structure being observed within each layer (Fig. 6.13), this phase is classified as smectic A. It is interesting to note that for this value of k, which for 3:1 molecules stabilised the nematic phase, the smectic A phase is destabilised here.

Table 6.2: Observable averages calculated for 4:1 molecules for $k = 100.0$, 50.0 and 10.0 at $T^* = 1.50$.

P^*	$\langle U^* \rangle$	Q_{00}^2	Q_{22}^2	$\langle \theta \rangle$	$r_{\parallel}$
$k = 100$					
0.50	-2.01(0.13)	0.083(0.039)	0.029(0.020)	none	-
0.55	-2.20(0.15)	0.086(0.041)	0.024(0.018)	none	-
0.60	-2.46(0.15)	0.104(0.057)	0.023(0.022)	none	-
0.65	-6.09(0.37)	0.882(0.018)	0.039(0.020)	none	3.66
0.70	-6.59(0.34)	0.899(0.013)	0.039(0.021)	none	3.70
0.75	-7.14(0.24)	0.917(0.008)	0.040(0.021)	none	3.68
0.80	-7.48(0.22)	0.925(0.006)	0.040(0.020)	none	3.68
0.85	-7.62(0.26)	0.928(0.007)	0.039(0.020)	none	3.65
0.90	-7.92(0.21)	0.934(0.006)	0.042(0.021)	none	3.63
1.00	-10.75(0.22)	0.969(0.002)	0.108(0.036)	15.77(1.37)	3.55
1.25	-11.27(0.20)	0.973(0.003)	0.140(0.036)	16.67(1.20)	3.55
1.50	-11.96(0.20)	0.976(0.002)	0.217(0.034)	22.86(0.62)	3.50
1.75	-12.36(0.19)	0.978(0.002)	0.263(0.043)	24.64(0.81)	3.41
2.00	-12.54(0.16)	0.978(0.002)	0.263(0.040)	24.25(0.99)	3.37
2.25	-12.84(0.18)	0.979(0.002)	0.303(0.037)	25.51(0.62)	3.36
2.50	-12.90(0.16)	0.980(0.002)	0.291(0.033)	26.19(0.77)	3.34
2.75	-13.09(0.16)	0.981(0.001)	0.310(0.035)	27.37(0.89)	3.33
3.00	-13.14(0.16)	0.981(0.001)	0.304(0.039)	28.75(0.93)	3.34
$k = 50$					
0.50	-2.01(0.14)	0.086(0.045)	0.026(0.016)	none	-
0.55	-2.18(0.13)	0.107(0.060)	0.024(0.018)	none	-
0.60	-4.66(0.34)	0.785(0.033)	0.037(0.020)	none	-
0.65	-5.24(0.33)	0.835(0.030)	0.038(0.019)	none	-
0.70	-6.65(0.32)	0.904(0.012)	0.039(0.021)	none	3.69
0.75	-6.95(0.28)	0.910(0.009)	0.042(0.022)	none	3.65
0.80	-7.25(0.25)	0.920(0.008)	0.042(0.021)	none	3.66
0.85	-7.56(0.24)	0.927(0.006)	0.041(0.021)	none	3.64
0.90	-7.71(0.19)	0.930(0.006)	0.039(0.020)	none	3.64
0.95	-7.85(0.26)	0.932(0.007)	0.041(0.021)	none	3.62
1.00	-8.04(0.21)	0.936(0.006)	0.042(0.021)	none	3.61
1.05	-8.29(0.22)	0.941(0.005)	0.041(0.022)	none	3.61
1.10	-10.64(0.25)	0.970(0.003)	0.071(0.036)	10.44(2.20)	3.58
1.25	-10.96(0.23)	0.973(0.002)	0.085(0.036)	11.33(2.29)	3.55
1.50	-11.42(0.19)	0.975(0.002)	0.117(0.036)	13.29(1.66)	3.53
1.75	-11.86(0.22)	0.978(0.002)	0.148(0.039)	14.61(1.61)	3.49
2.00	-12.11(0.17)	0.979(0.001)	0.160(0.040)	15.39(1.29)	3.50
2.25	-12.46(0.71)	0.981(0.001)	0.203(0.041)	17.07(1.44)	3.45
2.50	-12.64(0.18)	0.982(0.001)	0.221(0.037)	17.09(1.38)	3.45
2.75	-12.76(0.17)	0.983(0.001)	0.219(0.038)	17.10(1.09)	3.44

continued from previous page					
P^*	$\langle U^* \rangle$	Q^2_{00}	Q^2_{22}	$\langle \theta \rangle$	$r_{\parallel}$
3.00	-12.90(0.16)	0.983(0.001)	0.220(0.036)	17.15(1.29)	3.44
$k = 10$					
0.50	-1.87(0.12)	0.081(0.032)	0.027(0.020)	none	-
0.55	-2.14(0.20)	0.103(0.079)	0.026(0.017)	none	-
0.60	-4.93(0.23)	0.832(0.023)	0.039(0.021)	none	-
0.65	-5.44(0.18)	0.866(0.011)	0.039(0.020)	none	-
0.70	-5.67(0.19)	0.874(0.011)	0.038(0.020)	none	-
0.75	-5.97(0.17)	0.892(0.008)	0.039(0.021)	none	-
0.80	-6.22(0.22)	0.898(0.010)	0.039(0.020)	none	-
0.85	-6.42(0.20)	0.904(0.007)	0.039(0.021)	none	-
0.80	-6.55(0.17)	0.909(0.007)	0.038(0.020)	none	-
0.95	-6.72(0.20)	0.914(0.008)	0.038(0.020)	none	-
1.00	-6.89(0.18)	0.916(0.008)	0.040(0.021)	none	-
1.25	-7.49(0.17)	0.933(0.005)	0.041(0.020)	none	-
1.50	-7.87(0.16)	0.938(0.005)	0.039(0.021)	none	-
1.75	-8.35(0.31)	0.946(0.004)	0.042(0.022)	none	-
2.00	-8.66(0.31)	0.949(0.003)	0.042(0.023)	none	-
2.25	-8.92(0.33)	0.955(0.003)	0.040(0.021)	none	-
2.50	-9.13(0.43)	0.955(0.002)	0.044(0.024)	none	-
2.75	-9.37(0.53)	0.959(0.003)	0.044(0.022)	none	-
3.00	-9.62(0.12)	0.961(0.002)	0.040(0.022)	none	-
3.50	-10.08(0.47)	0.964(0.002)	0.057(0.029)	none	-
4.00	-10.23(0.58)	0.967(0.002)	0.046(0.023)	none	-
4.50	-10.59(0.17)	0.970(0.002)	0.048(0.026)	none	-
5.00	-10.75(0.12)	0.970(0.002)	0.046(0.023)	none	-

Upon further compression a second phase transition is observed, at approximately the same pressure as for the rigid case, although, as with the 3:1 molecules, at a lower density. A corresponding increase in both the nematic and biaxial order parameters is observed at this transition. Examination of the radial distribution functions (Figs. 6.12, 6.13 and 6.14) shows that this highest density phase has a well defined layered structure, long range ordering within each layer with the direction of tilt being towards the side of the hexagonal net, indicating a smectic G phase. Unlike the 3:1 molecules already considered, the biaxial order parameter and average tilt angles calculated within this highly order phase are comparable with those found in

the rigid case, providing further evidence that increasing molecular elongation does dramatically stabilise mesophase formation.

The probability distribution functions of the angle of internal rotation (Fig. 6.15) display behaviour similar to that observed for the 3:1 molecules with this value of k; the maximum value is coincident with the ideal angle of internal rotation, with no noticeable change in the widths and heights of the distributions with increasing density. It is, however, interesting to note that the profile has an increased width, with a lower peak height being observed, compared with the 3:1 case, and that the distribution is no longer symmetric, with values of the angle of internal rotation greater than the ideal value being more favourable. These observations indicate that a greater degree of flexibility is introduced into the model, possibly due to the temperature being greater here than was the case for the 3:1 molecules.

For the $k = 50$ system, the first phase transition observed upon compression occurs at the same pressure as for the $k = \infty$ case, lower than that observed for the $k = 100$ case, with the density range of the coexistence region being less than for both cases previously considered. The radial distribution functions (Figs. 6.16 and 6.17) within this first ordered phase display liquid-like behaviour, indicative of the nematic phase. Upon further compression a second phase transition is observed, with a layered structure (Fig. 6.16) being formed at a density and pressure greater than for both the $k = \infty$ and 100 cases. The lack of structure within each layer (Fig. 6.17), along with no evidence of biaxial ordering and absence of molecular tilt within the layers, identifies this phase as smectic A.
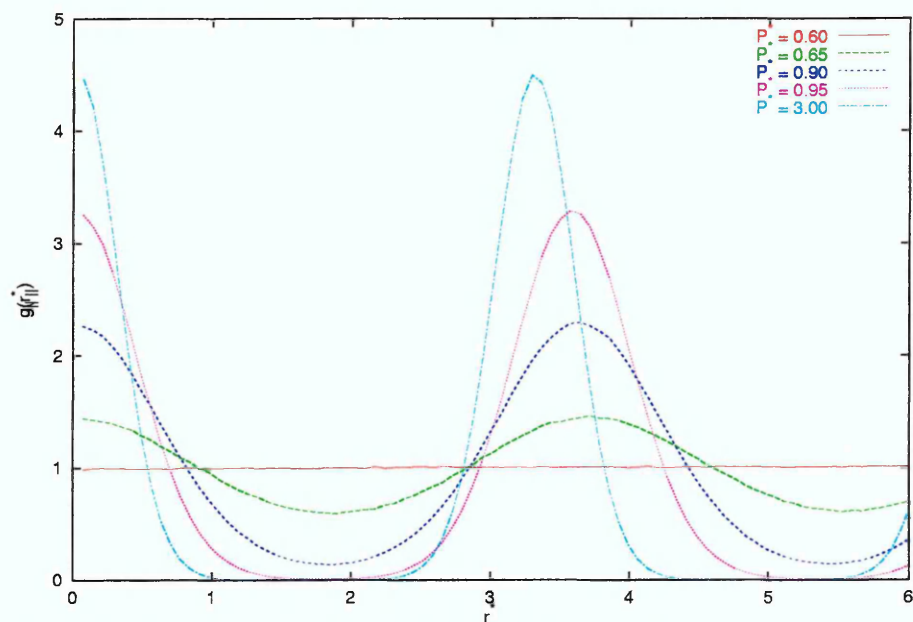
Figure 6.12: Radial distribution function resolved parallel to the layer normal for 4:1 molecules at $k = 100$ and $T^* = 1.50$.
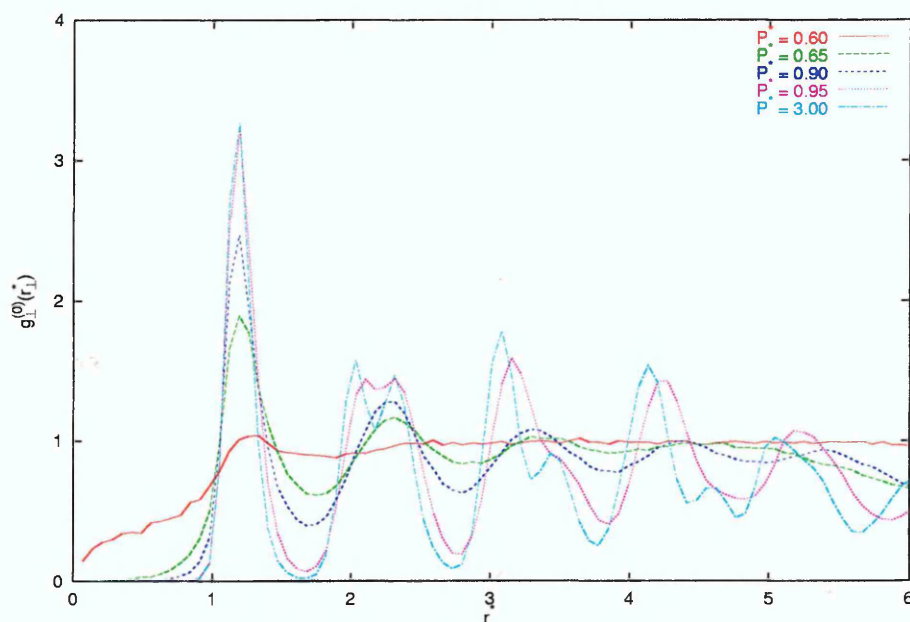

Figure 6.13: Radial distribution function resolved perpendicular to the layer normal for 4:1 molecules at $k = 100$ and $T^* = 1.50$.
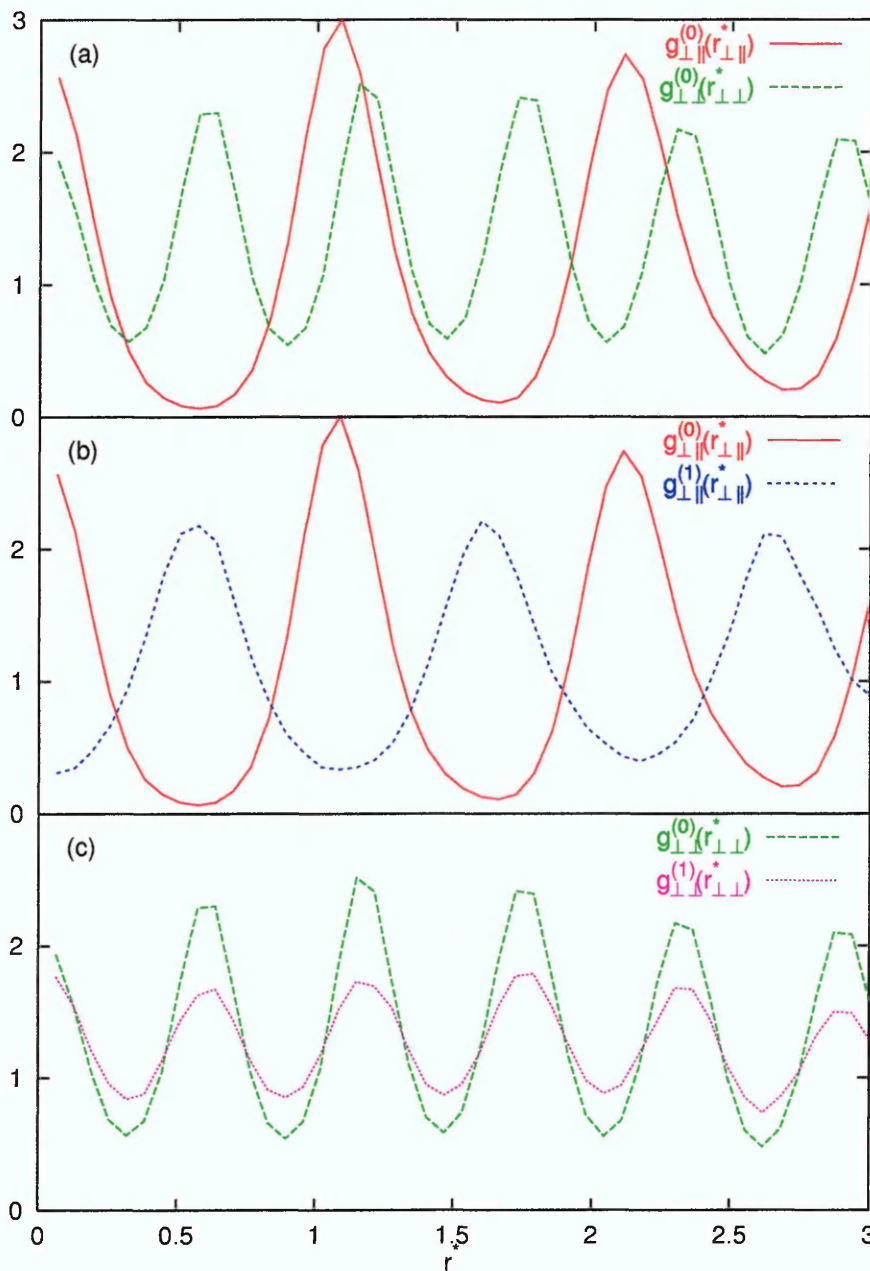
192

Figure 6.14: Radial distribution functions (a) resolved within the layer parallel, $g_{\perp\|}^{(0)}(r_{\perp\|}^*)$, and perpendicular, $g_{\perp\perp}^{(0)}(r_{\perp\perp}^*)$, to the direction of tilt and between adjacent layers resolved (b) parallel to the direction of tilt and (c) perpendicular to the direction of tilt for 4:1 molecules at $k = 100$, $T^* = 1.50$ and $P^* = 1.50$.
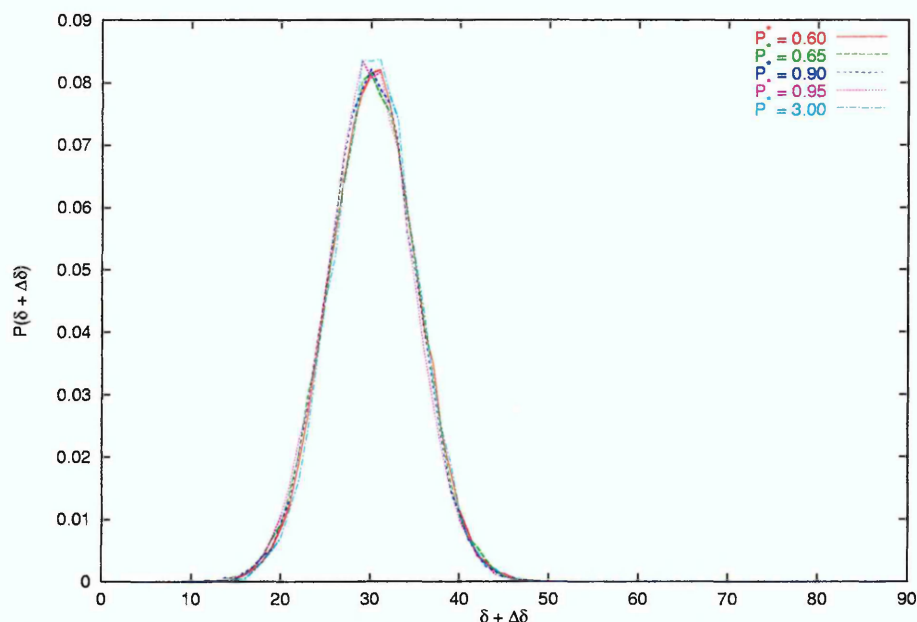
Figure 6.15: Probability distribution of molecular tilt angles $\delta + \Delta\delta$ for 4:1 molecules at $k = 100$ and $T^* = 1.50$.

A third phase transition is also observed along this isotherm, at a higher pressure and density than for the $k = \infty$ and 100 cases, with a corresponding increase in both the nematic and biaxial order parameters being observed. Examination of the radial distribution functions (Figs. 6.16, 6.17 and 6.18) shows that this phase has a well defined layered structure, displaying long range ordering within each layer, with the direction of tilt being towards the side of the hexagonal net, thus identifying this phase as smectic G. As with the 3:1 molecules for $k = 100$, the values calculated for the biaxial order parameters and average tilt angles within the smectic G phase, are considerably less than for the $k = \infty$ and 100 cases.

The probability distribution functions of the internal angles of rotation (Fig. 6.19), as expected, are broader, with lower peak heights, than were those observed for the $k = 100$ case. As with the other cases where the tilted hexatic phases are observed,
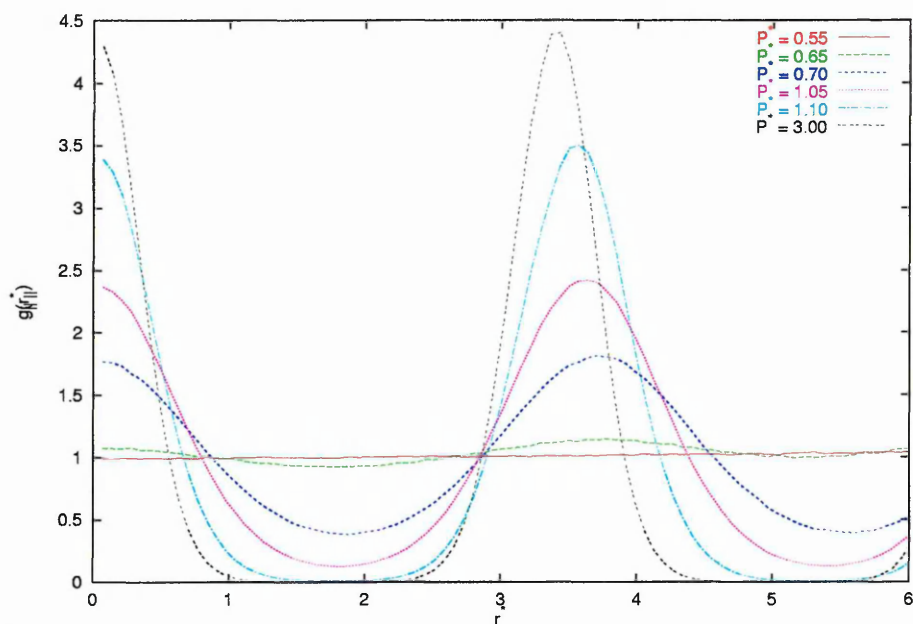
194

Figure 6.16: Radial distribution function resolved parallel to the layer normal for 4:1 molecules at $k = 50$ and $T^* = 1.50$.
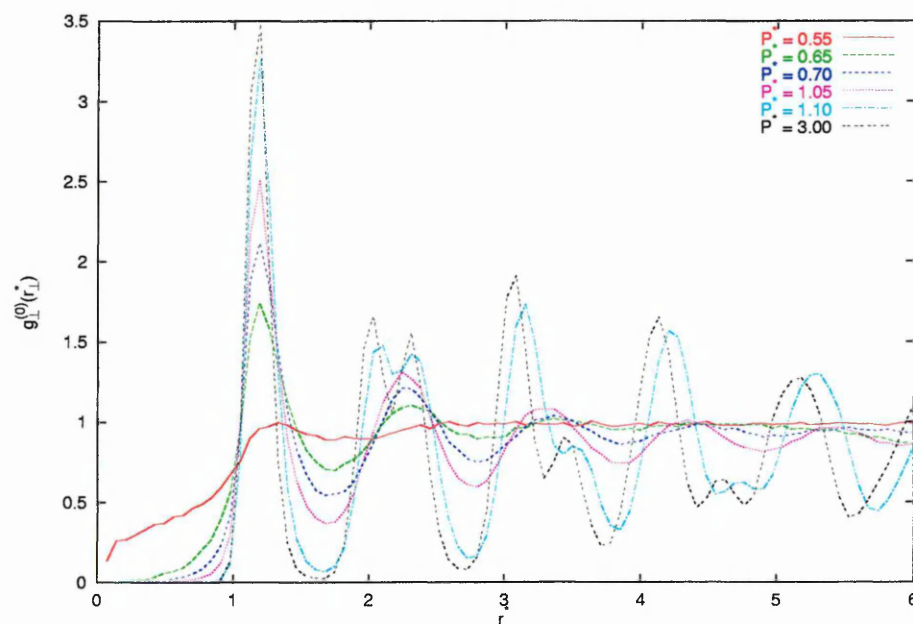

Figure 6.17: Radial distribution function resolved perpendicular to the layer normal for 4:1 molecules at $k = 50$ and $T^* = 1.50$.

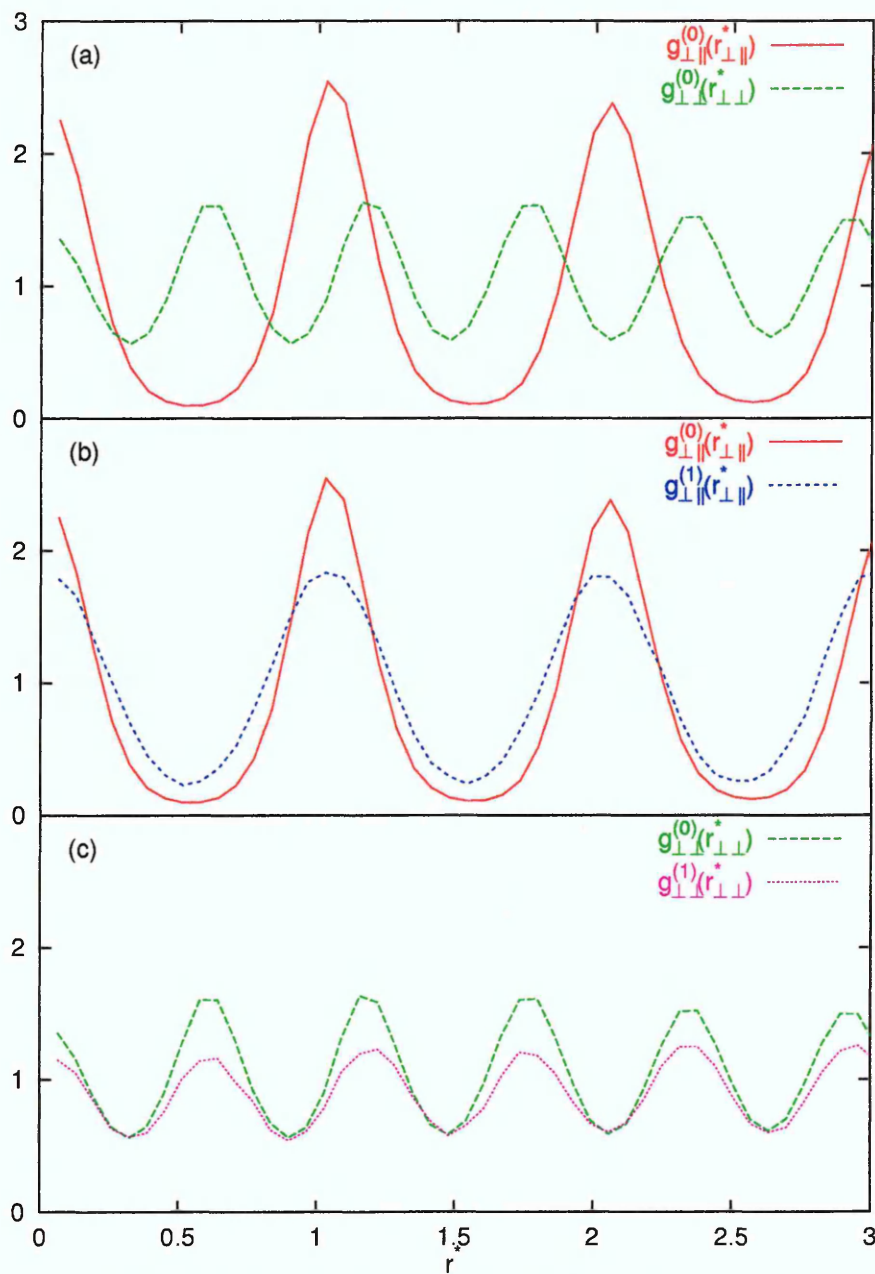Figure 6.18: Radial distribution functions (a) resolved within the layer parallel, $g^{(0)}_{\perp\parallel}(r^*_{\perp\parallel})$, and perpendicular, $g^{(0)}_{\perp\perp}(r^*_{\perp\perp})$, to the direction of tilt and between adjacent layers resolved (b) parallel to the direction of tilt and (c) perpendicular to the direction of tilt for 4:1 molecules at $k = 50$, $T^* = 1.50$ and $P^* = 1.50$.

the heights, widths and locations of the peaks remain unchanged with increasing density. Once again, the peaks are not symmetric about their maxima, with angles of internal rotation greater than the ideal value being more favourable. It is also interesting to note that the maximum value is not coincident with the ideal angle of internal rotation, occuring instead at a slightly larger value. These observations show that whilst the further reduction of k has resulted in a weaker coupling between the angle of internal rotation and its ideal value, the translationally ordered phases are still observed, although they are shifted to higher densities. This weaker coupling has, however, injected the nematic phase into the observed sequence of phases.
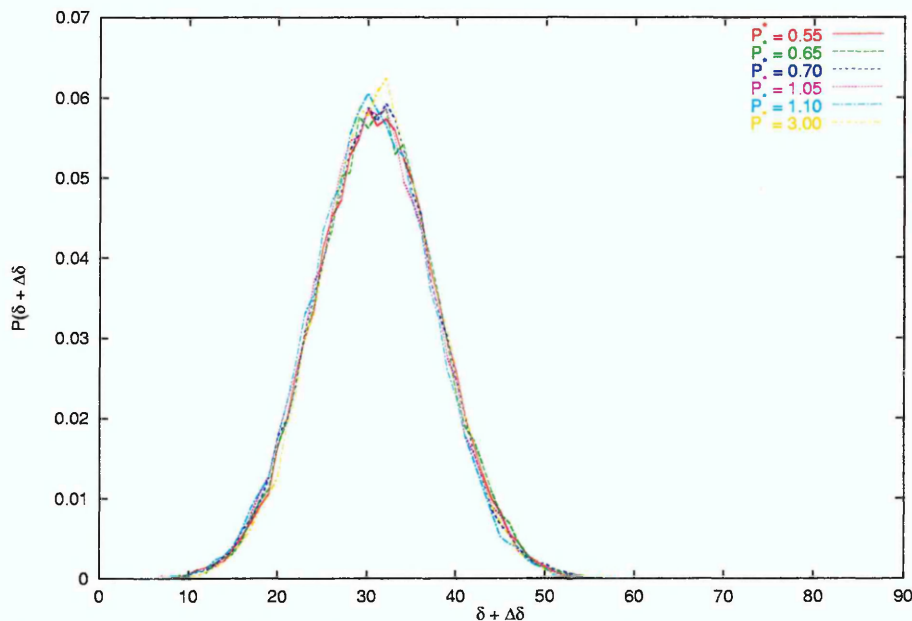
Figure 6.19: Probability distribution of molecular tilt angles $\delta + \Delta\delta$ for 4:1 molecules at $k = 50$ and $T^* = 1.50$.

As with the 3:1 molecules already considered, only one discontinuity is observed in the equation of state for the $k = 10$ case. The non-zero value adopted by the nematic order parameter and the liquid-like structure observed in the radial distribution functions (Figs. 6.20 and 6.21) identifies this transition as being from isotropic to

nematic. The density range of the coexistence region is extended compared with the $k = 50$ case. Unlike the results obtained for the 3:1 molecules for this value of k, no layered structure is observed with increasing density (Fig. 6.20). This absence of a layered structure is not surprising when the probability distribution function of the angles of internal rotation (Fig. 6.22) is examined. These distributions clearly show that as the density is increased, the average angle of internal rotation is shifted to much larger values than were observed for the 3:1 molecules, once again illustrating that there is a greater degree of flexibility along this isotherm.

Having examined the phase behaviour of this type of flexible molecule, the dynamics of the system will now be considered, in an attempt to determine the effects of this type of flexibility upon the molecular motion.

6.4 Dynamic Behaviour

In order to determine the dynamic behaviour of the flexible variant of the Internally-Rotated Gay-Berne fluid, a series of simulations were undertaken using molecular dynamics techniques within the constant NVE ensemble. As with the simulations performed upon the rigid Internally-Rotated Gay-Berne fluid, described in section 5.4, the aim here was simply to determine the type of molecular motion, and comparison with theoretical models will not be made.

In order to simulate the flexible Internally-Rotated Gay-Berne potential the molecular dynamics technique was modified from that used in the previous chapter: $\hat{u}$

198

Figure 6.20: Radial distribution function resolved parallel to the layer normal for 4:1 molecules at $k = 10$ and $T^* = 1.50$.

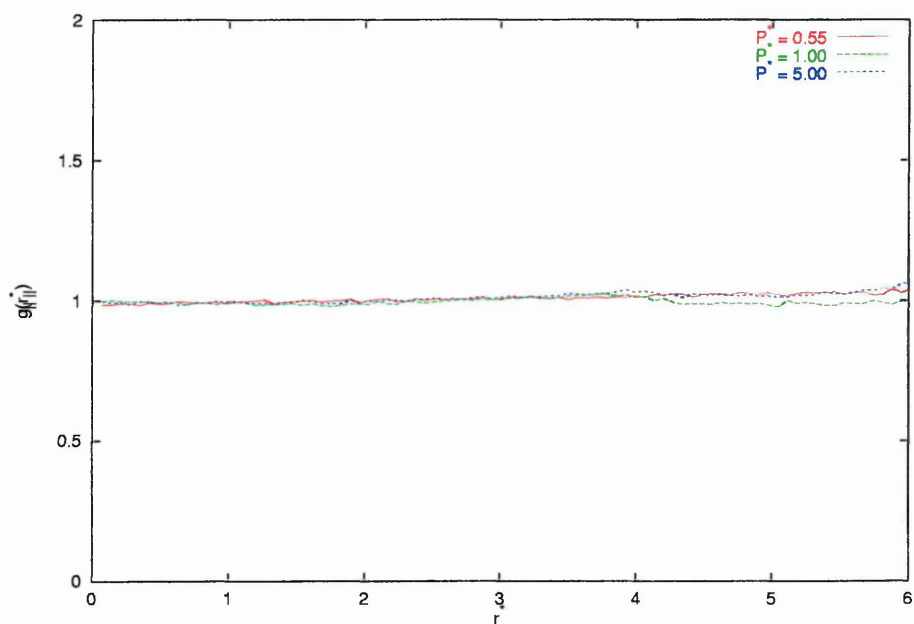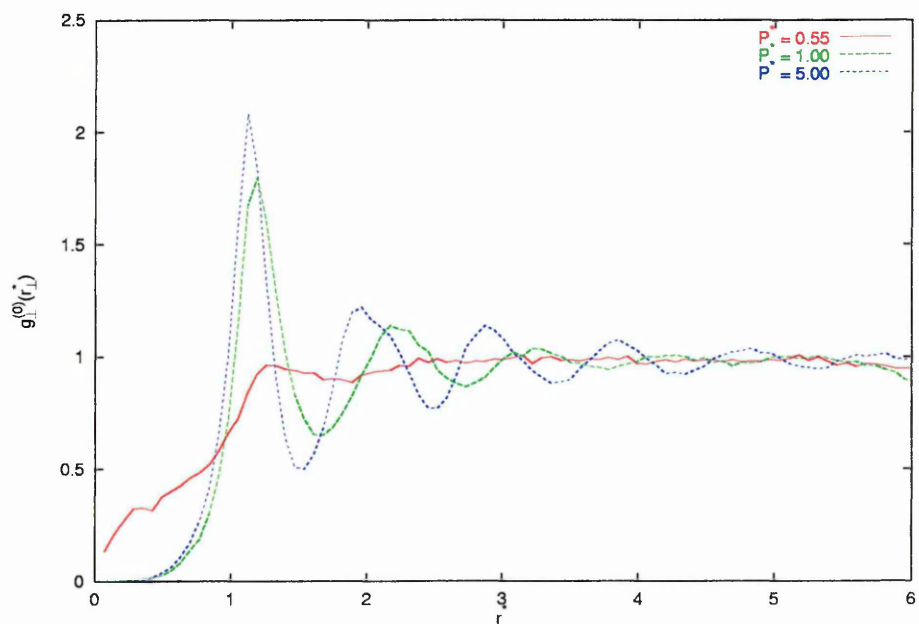Figure 6.21: Radial distribution function resolved perpendicular to the layer normal for 4:1 molecules at $k = 10$ and $T^* = 1.50$.
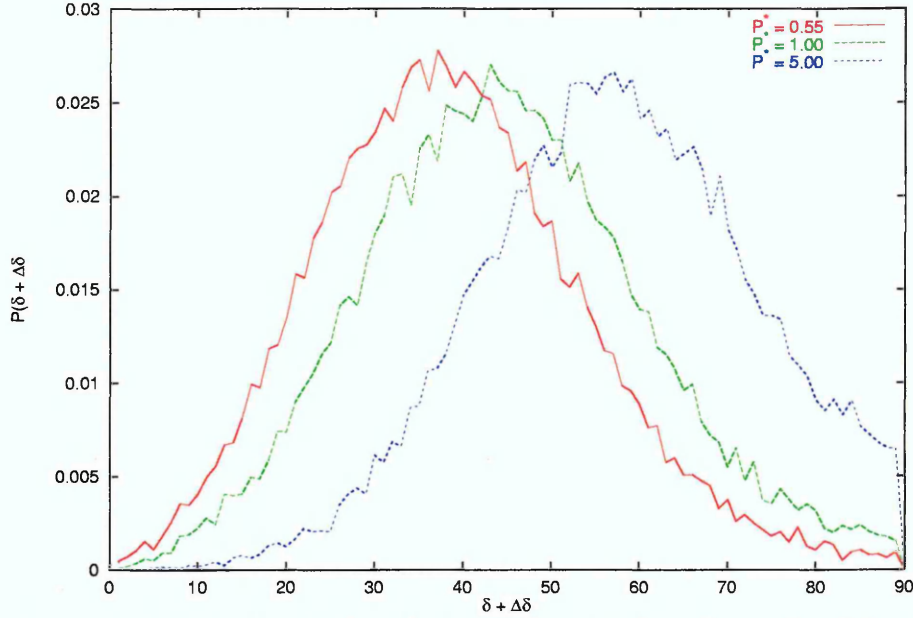
Figure 6.22: Probability distribution of molecular tilt angles θ for 4:1 molecules at $k = 10$ and $T^* = 1.50$.

and $\hat{\mathbf{v}}$ were treated as separate linear objects able to rotate independently about the centre of mass of the molecule. Details of how this was achieved are given in Appendix A.2.3. Given this approach, based on linear objects, both $\hat{\mathbf{u}}$ and $\hat{\mathbf{v}}$ require a single moment of inertia (since $I_{xx} = I_{yy}$ and $I_{zz} = 0$ for linear objects). As the moment inertia is usually taken to be unity for the Gay-Berne potential, the moment of inertia associated with the shape of the molecule, I_u, was also taken to be unity. In order to determine the moment of inertia associated with location of the potential minima about the molecule, I_v, a series of simulations have been performed with a very small time step, $\delta t = 1 \times 10^{-7}$, with the value of I_v being varied until perfect energy conservation was achieved. From the results of these runs, the moment of inertia associated with $\hat{\mathbf{v}}$ was chosen to be 0.005. The observation that I_v is much smaller than I_u is to be expected, since the intramolecular and spinning motion of the molecule is expected to occur much more rapidly than the tumbling motion of

200

the molecule as a whole.

In order to determine the time step, δt, to be used, a series of simulations were undertaken to study the energy conservation as a function of time step, similar to those described in section 5.4. As is to be expected, since the moment of inertia associated with $\hat{v}$ is much smaller than the moment of inertia associated with the spinning motion of the rigid molecule, the time step used for the rigid molecule, $\delta t = 1 \times 10^5$, offers poor energy conservation. Reduction of δt by an order of magnitude, however, results in acceptable energy conservation. As a result of this, a time step of $\delta t = 1 \times 10^6$ has been employed here, with energy fluctuations being less than 1 part in 10^{-4}.

The translational motion and molecular reorientation have been analysed in terms of the time autocorrelation functions (ACF's), as defined in eqn. 5.7. Once again the this has been undertaken for the linear velocities, $\mathbf{v}$, and the angular velocities, ω_u (associated with $\hat{u}$) and ω_v (associated with $\hat{v}$), resolved parallel and perpendicular to the molecular long axes (given by eqn. 5.8). That said, only the perpendicular component of ω_u is considered here, since $\hat{u}$ is used to define the molecular long axes. As a result of this definition, the spinning motion of $\hat{u}$, given by $\omega_{u_\parallel}$, is not considered within the molecular dynamics algorithm for linear molecules, since this motion leaves the system invariant.

These simulations were initiated from the final configuration obtained from the Monte Carlo simulations described in the previous section. The initial velocities were taken to be in the same direction as the initial forces and torques, with the

201

magnitudes conforming to the required temperature and corrected such that there was no overall momentum. The trajectories of the particles were followed for a total of 1×10^7 time steps after an initial equilibration period of 5×10^6 steps. For the evaluation of the ACF's, the spacing between consecutive time origins was 1,000 time steps.

6.4.1 Translational Dynamics

The velocity autocorrelation functions calculated for 4:1 molecules with $k = 50$ within the nematic ($P^* = 0.65$), smectic A ($P^* = 0.75$ and 1.00) and smectic G ($P^* = 1.25$ and 2.50) phases are shown in Fig. 6.23. Qualitatively the form of the correlation functions is identical to those obtained for the rigid molecule; namely, the cage effect can be observed for velocities resolved perpendicular to the molecular long axes, within each of the orientationally ordered phases, with a more pronounced negative region being observed with increasing density. Within the nematic and smectic A phases diffusive motion along the cylindrical cage is still possible, whereas within the smectic G phase, a more pronounced negative region with clear oscillatory behaviour is observed, with greater amplitudes and higher frequencies being observed with increasing density. This once again indicates that the cage effect constrains both the parallel and perpendicular motion. Similar behaviour is observed for the other values of k for the 4:1 molecules, and for the 3:1 molecules.

It would therefore appear that the introduction of flexibility into the model does not dramatically effect the translation motion of the system.
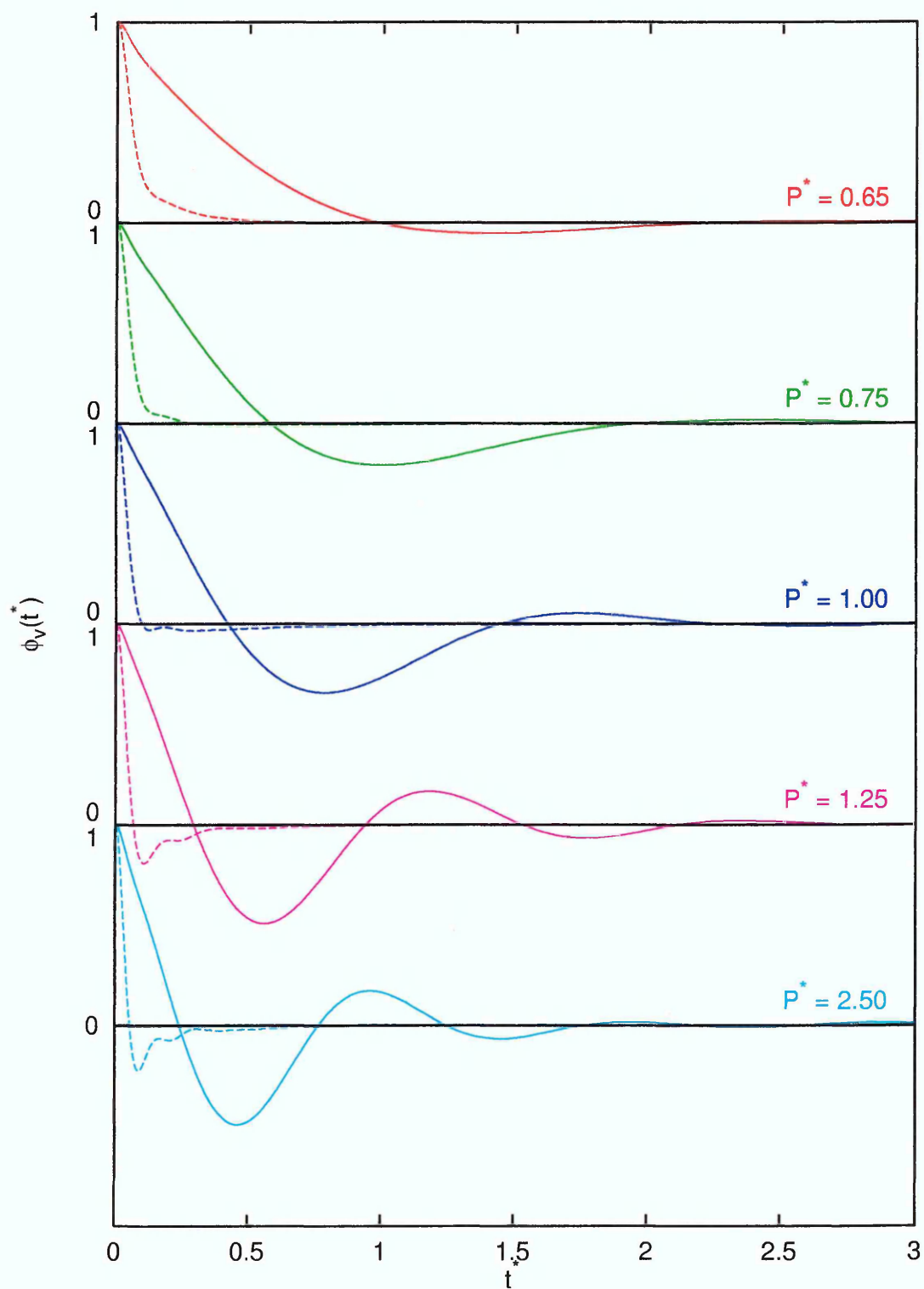
Figure 6.23: Velocity autocorrelation functions resolved parallel, $\phi_{v_\parallel}(t^*)$ (solid line), and perpendicular, $\phi_{v_\perp}(t^*)$ (dashed line), to molecular axes for 4:1 molecules with $k = 50$.

6.4.2 Rotational Dynamics

The angular velocity autocorrelation functions associated with the tumbling motion of the molecular long axes, $\phi_{\omega_{u_\perp}}(t^*)$, for 4:1 molecules with $k = 50$ at the same pressures as were used in the previous section, are shown in Fig. 6.24. As with the rigid case, within all of these orientationally ordered phases, this function decays rapidly towards zero, with a clear negative lobe being observed at all pressures, with the rate of decay and depth of the negative lobe increasing as the density is increased. This is as expected due to the cage effect, with the tumbling motion being restricted due to the presence of orientational ordering, with the rate of decay increasing with increasing density since the molecules will collide more rapidly with their nearest neighbours at higher densities. Similar behaviour is observed for the other values of k for the 4:1 molecules, and for the 3:1 molecules, with similar rates of decay being observed for corresponding densities with differing values of k, indicating that the introduction of flexibility does not dramatically effect the overall tumbling motion of the molecule.

The angular velocity autocorrelation functions associated with the rotation of $\hat{\mathbf{v}}$ for 4:1 molecules with $k = 50$ at the same pressures as considered above, is shown in Fig. 6.25. The spinning motion of the molecules (given by $\phi_{\omega_{v_\parallel}}(t^*)$), within the nematic and smectic A phases displays a slow decay to zero, thus indicating free rotation of the molecules about their long axes. At low pressures within the smectic G phase the decay is much more rapid. Whilst oscillatory behaviour about zero is not observed here, the presence of a local minima confirms that the rotation
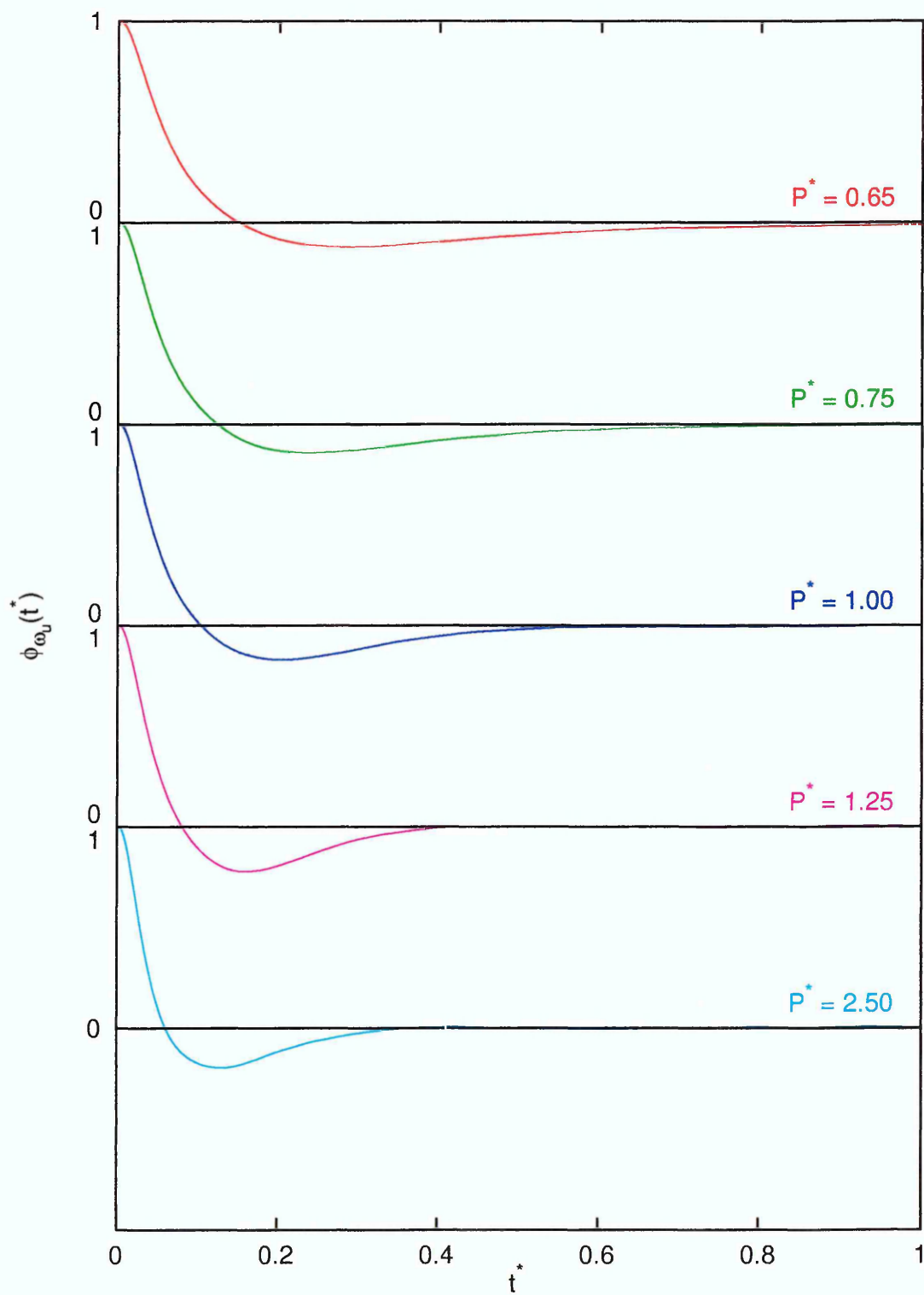
Figure 6.24: Angular velocity autocorrelation function associated with $\hat{\mathbf{u}}$ resolved perpendicular to molecular axes for 4:1 molecules with $k = 50$.

of the molecules about their long axes is being constrained more than within the nematic and smectic A phases. As the pressure is increased, the oscillatory behaviour associated with constrained motion is once again observed. The observation of relatively free rotation indicates that this phase is a smectic or plastic crystal phase, rather than a crystalline solid phase, however since no phase transition is observed here, a true distinction between the two cannot be made.

As is to be expected, due to the cage effect, the tumbling motion of $\hat{v}$ (given by $\phi_{\omega_{v_\perp}}(t^*)$) decays much more rapidly towards zero. This function, however, does not exhibit a smooth decay to a negative minimum followed by a continuous negative decay to zero (as observed in $\phi_{\omega_{u_\perp}}(t^*)$, and for the rigid molecule at low densities), or a slow oscillation about zero (as observed for the rigid molecules at high densities). Instead a rapid oscillation is observed about this caged tumbling motion.

This behaviour originates since the orientation of $\hat{v}$ is linked to an ideal orientation, $\hat{v}_0$, via a spring term within the potential energy calculation. As a result of this, the orientation of $\hat{v}$ may be expected by oscillate about its ideal orientation. Since the orientation of $\hat{v}_0$ is always taken to be in the $\hat{u}\hat{v}$ plane, this oscillation is also expected to only be observed about the molecular short axes, i.e. only within this autocorrelation function. Thus, the underlying cage behaviour arises since the tumbling motion of $\hat{u}$ results in a corresponding tumbling motion of $\hat{v}_0$. Therefore, the angular velocity correlation function of $\hat{v}_0$, which cannot be calculated here, would be expected to display the features of the cage effect observed for the rigid molecules, and provides the underlying form of the functions observed here. The

206

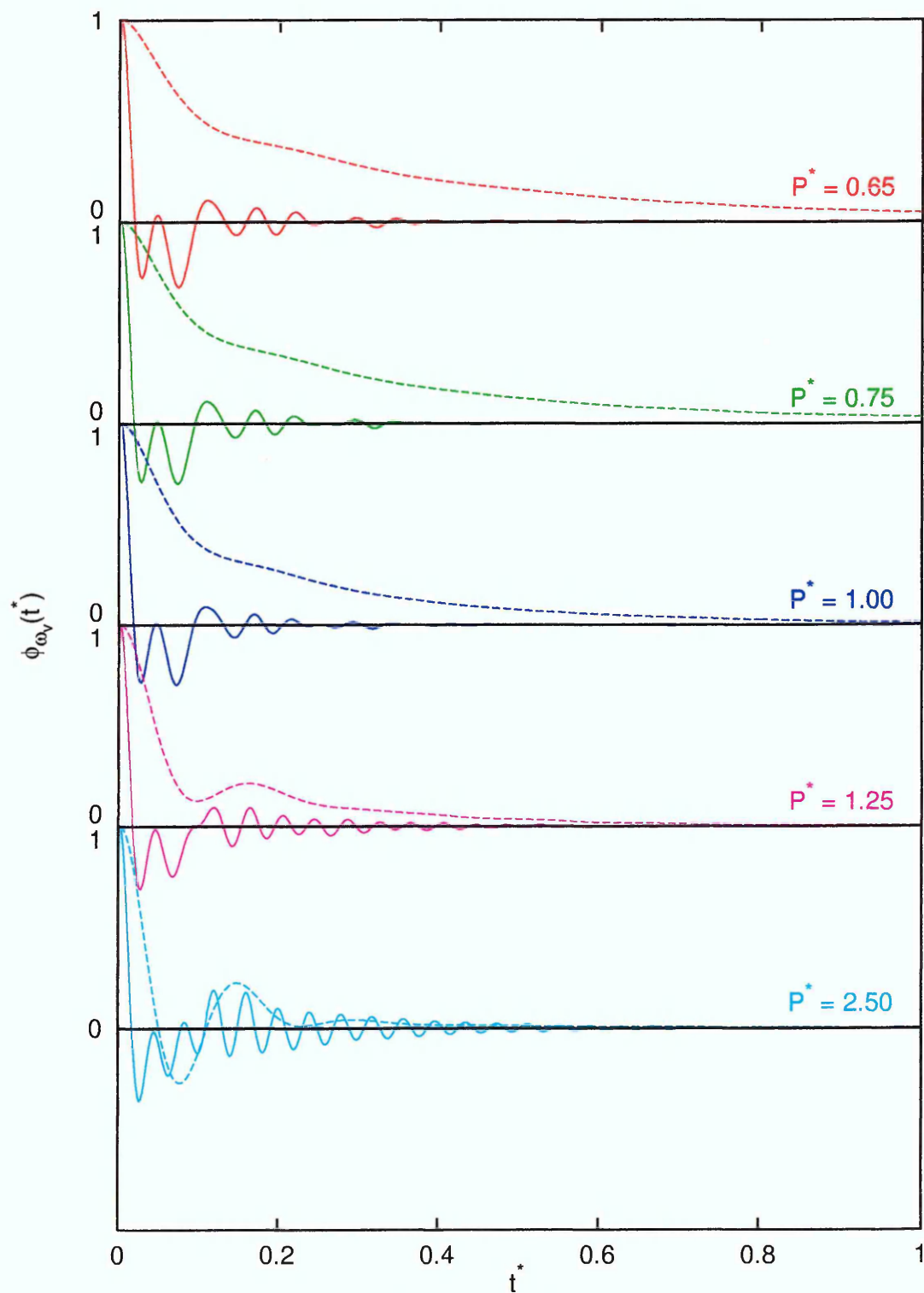Figure 6.25: Angular velocity autocorrelation functions associated with $\hat{\mathbf{v}}$ resolved parallel, $\phi_{\omega_\parallel}(t^*)$ (dashed line), and perpendicular, $\phi_{v_\perp}(t^*)$ (solid line), to molecular axes for 4:1 molecules with $k = 50$.

rapid oscillation arises due to the spring term, with $\hat{v}$ oscillating rapidly about its ideal location. Since a negative region for these functions is ascribed to a reversal of the velocities with respect to the initial velocity, regions where these functions are less than the expected autocorrelation function for $\hat{v}_0$ corresponds to a reversal in the velocities with respect to the velocity of $\hat{v}_0$ due to the presence of spring term within the model.

The observation that the distribution of angles of internal rotation remains unchanged with increasing density suggests that the average amplitude of these oscillations about $\hat{v}_0$ remains unchanged with increasing density. This is not, however, evident from these correlation functions, since the underlying tumbling motion of the molecule is density dependent. That said, it is interesting to note that, with increasing density, the oscillations associated with changing $\Delta\delta$ remain correlated for longer times, while the frequency of the oscillations remains constant. It would, therefore appear that the oscillatory motion of $\hat{v}$ about $\hat{v}_0$ is not dependent upon density, with this behaviour becoming more apparent in $\phi_{\omega_{v_\perp}}(t^*)$ as the tumbling motion of $\hat{v}_0$ becomes more constrained due to the cage effect at higher densities.

For the $k = 100$ case (shown in Fig. 6.26, within the smectic A ($P^* = 0.70$ and 0.85) and smectic G ($P^* = 2.00$ and 3.00) phases), similar behaviour is observed for both types of motion within the smectic A phase, whereas free rotation of the molecules about their long axes is not permitted at any pressure within the smectic G phase, indicating that the free rotation of the molecule about its long axis within this highly ordered phase is only permitted for sufficiently small values of k. It is also

interesting to note that the frequency of the oscillations of $\hat{v}$ about $\hat{v}_0$ has increased with increasing k, as is to be expected due to a stronger spring interaction. For the $k = 10$ case (shown in Fig. 6.27, all within the nematic phase) the spinning motion of the molecules displays the expected unconstrained behaviour. The frequency of the oscillations of $\hat{v}$ about $\hat{v}_0$ has decreased, whilst the amplitude of successive peaks is reduced with increasing density. Since the distribution of angles of internal rotation is shifted to higher values with increasing density, it is not surprising that the angular velocities become rapidly uncorrelated due to the very weak coupling between $\hat{v}$ and $\hat{v}_0$. Similar behaviour is observed for the 3:1 molecules.

6.5   Conclusions

In this chapter, we have considered the simulation of a flexible variant of the Internally-Rotated Gay-Berne potential, and found that the introduction of molecular flexibility does have a significant effect upon the location of the observed phase transitions. The flexibility has been introduced into the model in such a way that the orientation of rigid linear terminal chains are linked to an ideal orientation via a spring term within the potential energy calculation. Whilst the constraints placed upon the type of flexibility allowed are idealised compared with the complex behaviour which a real molecule will exhibit [6], it is know that molecules within the smectic C phase assume a *zig zag* conformation [15] in which the terminal chains adopt a linear conformation.

Figure 6.26: Angular velocity autocorrelation functions associated with $\hat{\mathbf{v}}$ resolved parallel, $\phi_{\omega_\parallel}(t^*)$ (dashed line), and perpendicular, $\phi_{v_\perp}(t^*)$ (solid line), to molecular axes for 4:1 molecules with $k = 100$.
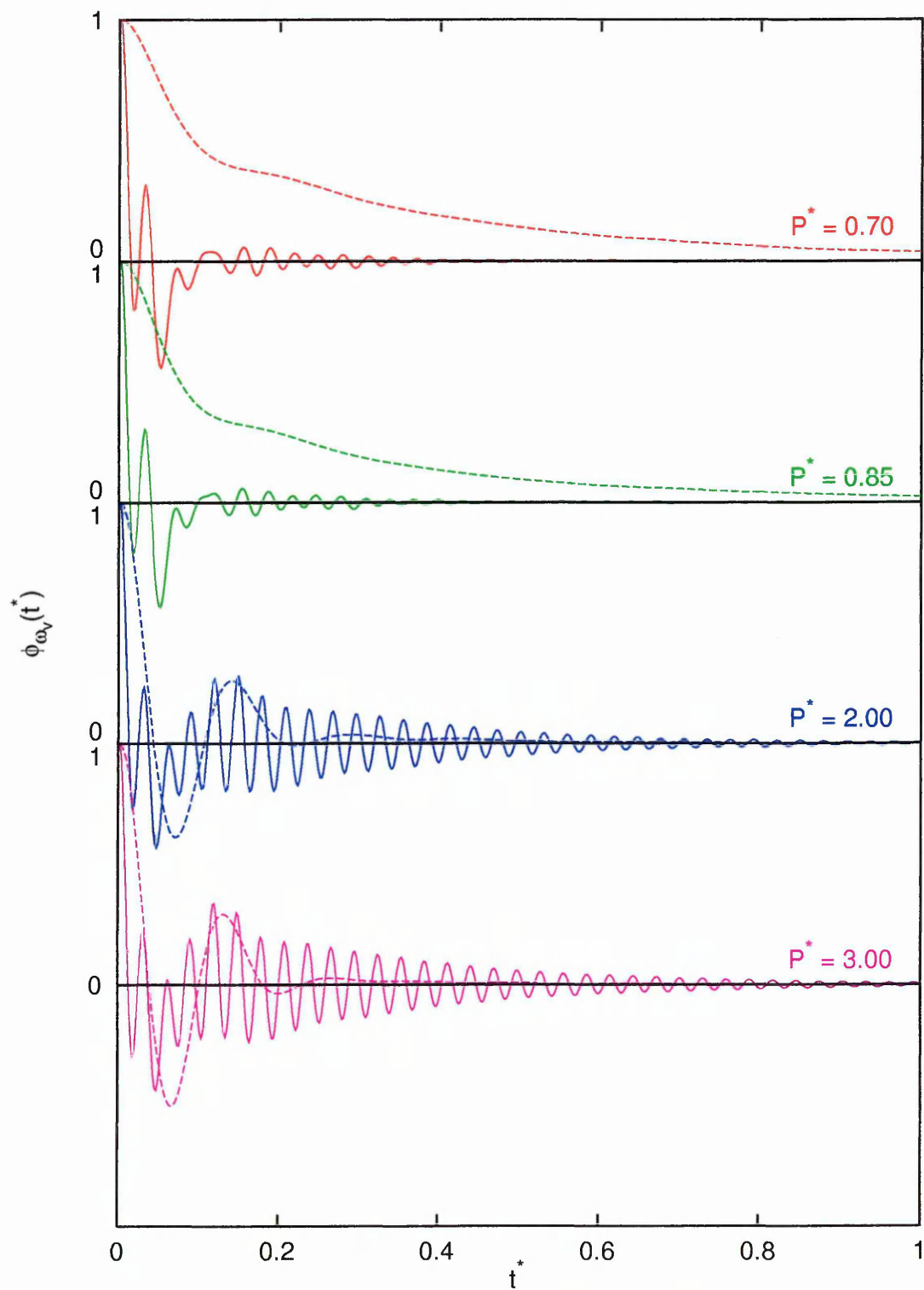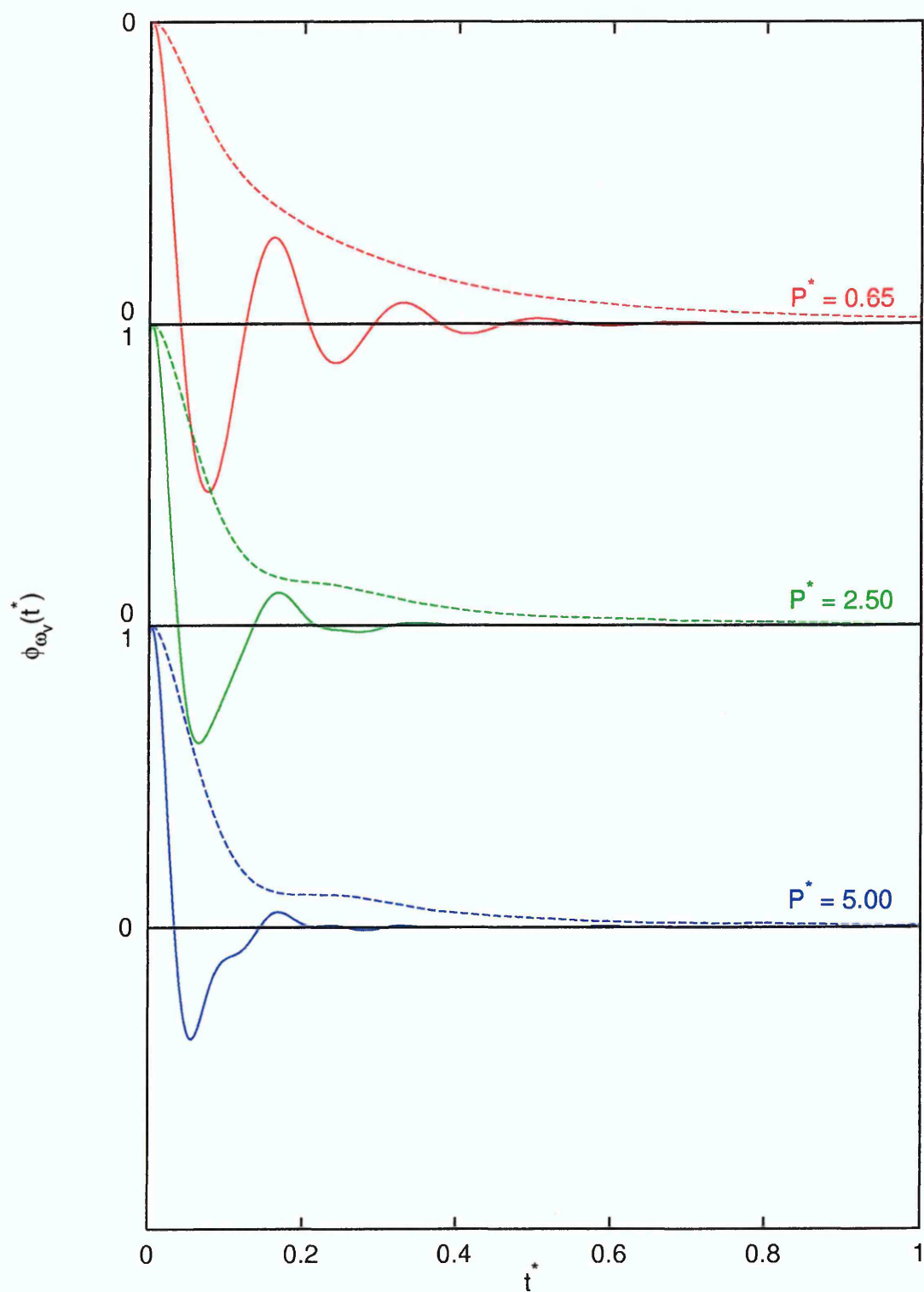
Figure 6.27: Angular velocity autocorrelation functions associated with $\hat{\mathbf{v}}$ resolved parallel, $\phi_{\omega_\parallel}(t^*)$ (dashed line), and perpendicular, $\phi_{v_\perp}(t^*)$ (solid line), to molecular axes for 4:1 molecules with $k = 10$.

The simulations were performed upon systems interacting via the flexible Internally-Rotated Gay-Berne potential with the stronger $(\epsilon_{ss}/\epsilon_{ee} = 5.0, \nu = 2.0$ and $\mu = 1.0)$ parameterisation for two different shape anisotropies $(\sigma_{ee}/\sigma_{ss} = 3.0$ and $4.0)$ at temperatures chosen such that comparison may be made with the phase behaviour already determined within the preceding chapter. The effect upon the observed phase behaviour with reducing values of k, the spring constant linking the orientation of the terminal chains to their ideal orientation, was then determined.

For very large values of k $(\geq 1 \times 10^4)$ no evidence of flexibility being introduced into the model was found. Conversely, for small values of k (< 10) it appears that the molecule is too flexible, with the translationally ordered phases being destabilised and the angles of internal rotation no longer being constrained to their ideal values. As a result of these observations, the sweeps through phase space were restricted to the range $100 \geq k \geq 10$.

For $k = 100$, the observed sequence of phases for both the 3:1 and 4:1 molecules was found to be unchanged compared with the rigid case. For the 3:1 molecules all of the phase transitions occured at approximately the same pressures as were observed for the rigid molecules, with the lowest density at which the nematic and smectic J phases are formed being shifted to lower values, whilst the density at which the smectic A phase is stabilised remains unchanged. The amplitude of the density wave perpendicular to the layer within the smectic A phase was greater than that observed for the rigid case. These observations indicate that molecular flexibility does help stabilise mesophase formation. For the longer 4:1 molecules, the transition

from smectic A to smectic G occured at the same pressure and lower density than for the rigid case, whereas the isotropic to smectic A transition was shifted to higher densities and pressures, indicating that the smectic A phase is destabilised by the introduction of flexibility. Whilst it is generally accepted that molecular flexibility helps to stabilise mesophase formation [6], studies into the effect of the introduction of double bonds into the terminal chains [108] have shown that this more rigid structure stabilises the smectic C phase. As a consequence of this observation, the introduction of molecular flexibility may also be expected to destabilise the smectic A phase, as is observed here. That said, experimental studies into the phase behaviour usually consider the temperature dependence, which has not been investigated here. To allow further comparison with experimental observations, further simulations must be performed.

The $k = 50$ case has only been considered for the longer 4:1 molecules, with both the smectic A and G phases being destabilised compared with the $k = 100$ case. The nematic phase is, however, injected into the phase sequence between the isotropic and smectic A phases, occuring for densities lower than the smectic A for both the $k = 100$ and rigid cases.

For $k = 10$, the onset of nematic ordering is suppressed to higher densities for both 3:1 and 4:1 molecules. At higher densities the smectic A phase is only observed for the 3:1 molecules. No hexatic phase is observed for either. These observations indicate that the spring is too weak, with the translationally ordered mesophases being completely destabilised or shifter to high densities. However, the observation

of the smectic A phase for the 3:1 molecules, along with a broader distribution of angles of internal rotation for the 4:1 molecules, for both $k = 100$ and 10, which deviates from the ideal angle by a greater amount, for $k = 10$, implies that a greater degree of molecular flexibility is present for the longer molecules. This observation seems likely since a higher temperature is employed for the 4:1 molecules.

The results obtained from the molecular dynamics simulations show that the orientation of $\hat{v}$ oscillates rapidly about its ideal orientation, as is to be expected since the coupling is provided by a spring term. Somewhat surprisingly, the amplitude and frequency of these oscillations remains unchanged with increasing density. This indicates that the flexibility of the constituent molecules is not frozen out as the density is increased. However, for this idealised model, this oscillatory motion is governed purely by the presence of the spring term within the potential energy calculation, with no steric hindrance to this type of motion being considered. As a consequence of this assumption, the amplitude and frequency of these oscillations will be governed purely by the thermal effects, and thus be density independent.

At no point during the course of these simulations has a smectic C phase been observed. As with the rigid molecules, the only tilted phases observed have long range translational order, with free rotation of the molecules about their long axes being permitted for sufficiently small values of k, where no such free rotation was observed for more rigid molecules. These observations, whilst avoiding the criticism of the freezing out of the free rotation of the molecules about their long axes, still suggests that theoretical models which consider steric biaxiality (i.e. the Wulf model [42])

Chapter 7

Investigation into the Effects of the Inclusion of a Quadrupole Moment

7.1 Introduction

In this chapter, the results of computer simulations performed upon systems of rigid Internally-Rotated Gay-Berne particles with longitudinal linear quadrupoles attached to each particle, are reported, together with appropriate analysis and comparison with existing results in the literature.

The motivation for this work comes from the conclusion of the preceding chapters, that a purely steric representation of molecules offers a poor route to obtaining

the smectic C phase. It would, however, appear that electrostatic interactions are necessary for a smectic C phase to be observed. Theoretical models which consider dipole-dipole interactions [29–31, 33] are now not widely accepted, with interest of late being focussed upon the effect of electric quadrupoles [37–40] upon the formation of mesophases. These recent studies have shown that, for uniaxial particles, electric quadrupoles favour the formation of a smectic C phase. Computer simulation studies to date [69–71, 94–97] have shown that dipolar effects may have a marked effect upon transition temperatures and local structure, with no smectic C phase being observed, whereas the inclusion of an axial quadrupole upon a system of Gay-Berne particles [41] has lead to a smectic C phase being observed.

As a consequence of these findings, the effect upon the phase behaviour of Internally-Rotated Gay-Berne fluids with different quadrupole magnitudes has been studied. This has been achieved by modelling the interactions between molecules by the biaxial IRGB potential plus a longitudinal point quadrupole located at the centre of the molecule,

$$U(\hat{\mathbf{r}}_{ij}, \hat{\mathbf{u}}_i, \hat{\mathbf{u}}_j, \hat{\mathbf{v}}_i, \hat{\mathbf{v}}_j) = U_{IRGB}(\hat{\mathbf{r}}_{ij}, \hat{\mathbf{u}}_i, \hat{\mathbf{u}}_j, \hat{\mathbf{v}}_i, \hat{\mathbf{v}}_j) + U_{QQ}(\hat{\mathbf{r}}_{ij}, \hat{\mathbf{u}}_i, \hat{\mathbf{u}}_j) \qquad (7.1)$$

where $U_{IRGB}(\hat{\mathbf{r}}_{ij}, \hat{\mathbf{u}}_i, \hat{\mathbf{u}}_j, \hat{\mathbf{v}}_i, \hat{\mathbf{v}}_j)$ is the contribution to the pair potential from the IRGB potential (given by eqn. 5.3) and the quadrupolar component takes the form [48, 109],

$$U_{QQ}(\hat{\mathbf{r}}_{ij}, \hat{\mathbf{u}}_i, \hat{\mathbf{u}}_j) = \frac{3Q_i^* Q_j^*}{4r^5} \left[1 + 2\left(\hat{\mathbf{u}}_i \cdot \hat{\mathbf{u}}_j\right)^2 - 5\left(\hat{\mathbf{r}}_{ij} \cdot \hat{\mathbf{u}}_i\right)^2 - 5\left(\hat{\mathbf{r}}_{ij} \cdot \hat{\mathbf{u}}_j\right)^2 \right.$$

$$\left. -20\left(\hat{\mathbf{u}}_i \cdot \hat{\mathbf{u}}_j\right)\left(\hat{\mathbf{r}}_{ij} \cdot \hat{\mathbf{u}}_i\right)\left(\hat{\mathbf{r}}_{ij} \cdot \hat{\mathbf{u}}_j\right) + 35\left(\hat{\mathbf{r}}_{ij} \cdot \hat{\mathbf{u}}_i\right)^2 \left(\hat{\mathbf{r}}_{ij} \cdot \hat{\mathbf{u}}_j\right)^2 \right] \tag{7.2}$$

where Q_i^* and Q_j^* are the reduced quadrupole moments of the particles i and j respectively.

As with the simulations described within the preceding chapters, the intermolecular potential is truncated at a distance $r_{cut} = (\sigma_{ee}/\sigma_{ss} + 1)$, with a shifted potential being employed, such that,

$$U^s(\mathbf{r}_{ij}, \hat{\mathbf{u}}_i, \hat{\mathbf{u}}_j, \hat{\mathbf{v}}_i, \hat{\mathbf{v}}_j) = \begin{cases} U(\mathbf{r}_{ij}, \hat{\mathbf{u}}_i, \hat{\mathbf{u}}_j, \hat{\mathbf{v}}_i, \hat{\mathbf{v}}_j) - U_c & r_{ij} \leq r_{cut} \\ 0 & r_{ij} > r_{cut} \end{cases} \tag{7.3}$$

where $U(\mathbf{r}_{ij}, \hat{\mathbf{u}}_i, \hat{\mathbf{u}}_j, \hat{\mathbf{v}}_i, \hat{\mathbf{v}}_j)$ is given by eqn. 7.1, and $U_c = U(\mathbf{r}_{cut}, \hat{\mathbf{u}}_i, \hat{\mathbf{u}}_j, \hat{\mathbf{v}}_i, \hat{\mathbf{v}}_j)$, also given by eqn. 7.1.

These simulations have been performed using Monte Carlo methods within the constant NPT ensemble, with each MC cycle being attempted in the same manner as has been used previously to study the rigid molecules (as described in section 5.2.2). The effect upon the observed phase behaviour of increasing Q^* has been examined via simulations performed along a single isotherm for molecules with two differing values of the shape anisotropy, $\sigma_{ee}/\sigma_{ss} = 3.0$ and 4.0, at $T^* = 1.00$ and 1.50 respectively. The systems used had a δ value of 30^0 (where δ, as with the rigid molecules considered in Chapter 5, refers to the angle between $\hat{\mathbf{u}}$ and $\hat{\mathbf{v}}$, the *angle of internal rotation*), all other variables being set to the values used previously within this

study $(\epsilon_{ss}/\epsilon_{ee} = 5.0, \mu = 1.0$ and $\nu = 2.0)$. As with the simulations performed using the flexible molecule model, this choice of parameterisation allows comparison to be made with the same reference system as was used in the previous chapter, which will be referred to here as $Q^* = 0.00$.

Determination of an appropriate value for the quadrupole moment is difficult since few experimental or theoretical values have been determined and those that have cover an order of magnitude [110, 111]. That said, within the previous simulation study of Neal and Parker [41], an estimate was made for benzene, with a value of Q^* being calculated to be -0.44, whilst the smectic C phase was observed for $|Q^*| = 0.60$. Guided by this, the range $0.00 \leq |Q^*| \leq 0.80$ have been employed in this study, with in incremental steps of 0.20.

Fig. 7.1 shows the potential energy contours for parallel particles interacting via this potential (with $\sigma_{ee}/\sigma_{ss} = 3.0$, $\epsilon_{ss}/\epsilon_{ee} = 5.0$, $\mu = 1.0$ and $\nu = 2.0$) for $\delta = 0$ and 30 with values of $Q^* = 0.00$ and -1.00 as a function of their displacement. Since the quadrupole contribution to the potential energy is dependent upon the separation of the particles, it has its greatest contribution in the side-by-side configuration. For the uniaxial molecule (Fig. 7.1(a) and (b)) it is apparent that the deepest well depth is obtained for $|Q^*| = 0.0$. As $|Q^*|$ is increased, the deepest well depth becomes less deep, but extends further along the sides of the molecule, with the well depths for the end-to-end configuration increasing. For sufficient large quadrupole magnitudes, $|Q^*| \gtrsim 0.5$, two minima occur in the attractive well in the side-by-side configuration. It has been demonstrated [39] that for perfect parallel alignment the
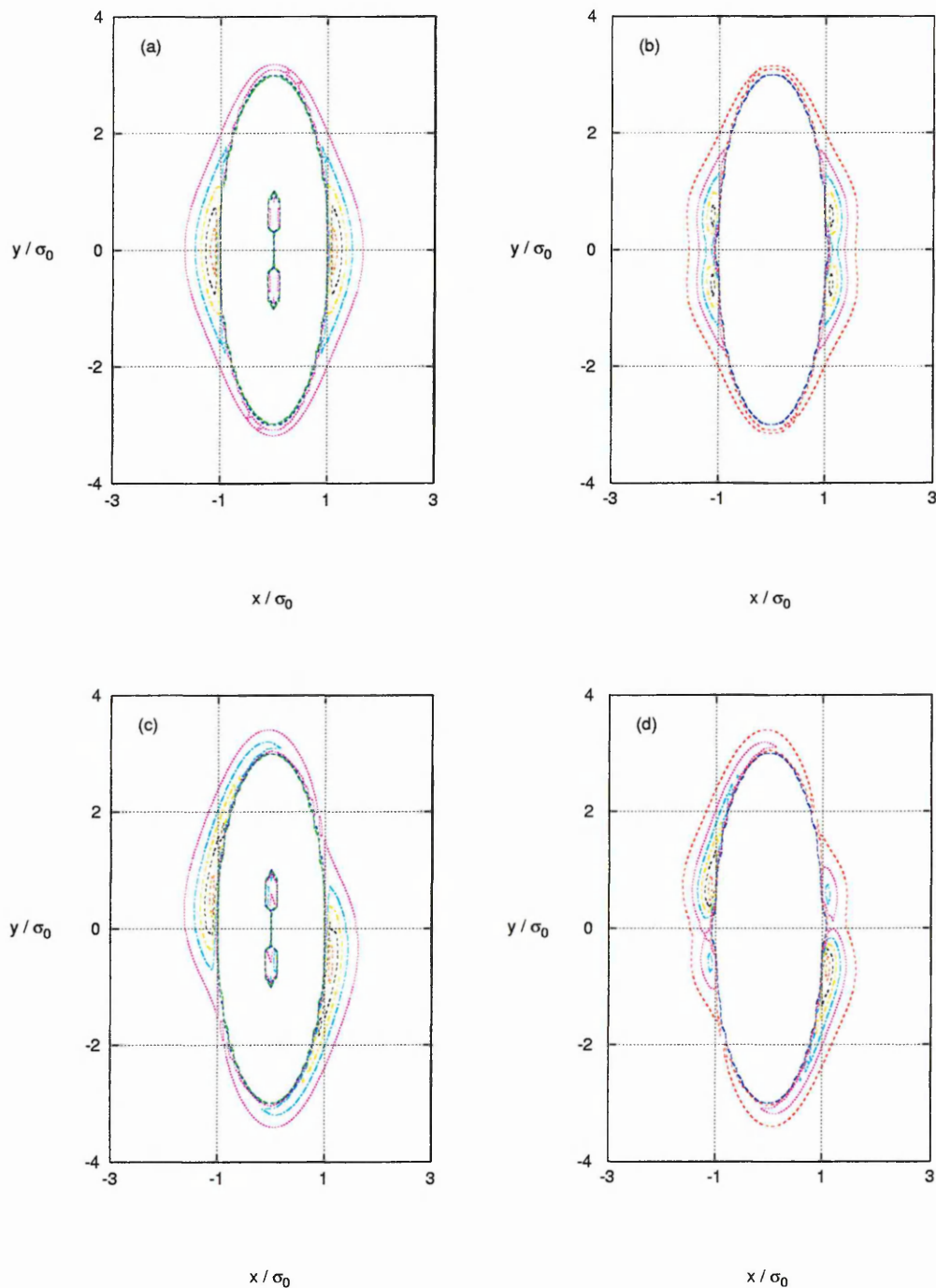
Figure 7.1: Potential energy contours calculated for parallel molecules interacting via the Internally-Rotated Gay-Berne potential plus a longitudinal quadrupole located at the centre of the molecule as a function of their separation and orientation with respect to the intermolecular vector for $\delta = 0$ and (a) $|Q^*| = 0.00$ and (b) $|Q^*| = 1.00$, and for $\delta = 30$ and (c) $|Q^*| = 0.00$ and (d) $|Q^*| = 1.00$. $\hat{\mathbf{u}}$ for each case is orientated along the y axis and $\hat{\mathbf{v}}$ is defined by $(\sin \delta, \cos \delta, 0)$.

220

minimum of quadrupole component of the potential energy occurs for a parallel staggered configuration. Energetically the T configuration, with $\hat{u}_i$ perpendicular to $\hat{u}_j$, is the most favourable configuration for the quadrupole component (as expressed here with only the 224-term being present [39,40]). However, steric hindrance due to the Gay-Berne shape parameter changes this to the side-by-side or parallel staggered configurations. Thus the smectic C phase has been observed [41] for sufficiently large values of $|Q^*|$, where the parallel staggered configuration is the energetically most favourable. Importantly, since the inclusion of a quadrupole moment upon a Gay-Berne particle gives a linear object, free rotation of the molecules about their long axes is permitted.

The incorporation of a quadrupole moment into the Internally-Rotated Gay-Berne potential (Fig. 7.1(c) and (d)) has the same general effect as upon the Gay-Berne potential. However, since the IRGB is a biaxial object the well depth for one parallel staggered configuration is deeper than that of the other. Thus the IRGB with the inclusion of a quadrupole has a prefered direction of tilt, with the linear quadrupole component resulting in free rotation of the molecule being energetically more favourable than for the standard IRGB potential.

The results obtains from these simulations will now be presented, initially considering the shorter 3:1 molecules.

7.2   Short Molecules

The equations of state obtained from the simulations of particles interacting via the Internally-Rotated Gay-Berne potential with a longitudinal point quadrupole for 3:1 molecules at $T^* = 1.00$ for $Q^* = 0.00$, 0.20 and 0.40 are shown in Fig. 7.2. The $Q^* = 0.00$ case is redrawn from Fig. 5.30, and represents a reference system with no quadrupole moment, with the sequence of phases being isotropic ($\rho^* \lesssim 0.225$, $P^* \lesssim 0.70$), nematic ($0.248 \lesssim \rho^* \lesssim 0.286$, $0.75 \lesssim P^* \lesssim 1.25$), smectic A ($0.286 \lesssim \rho^* \lesssim 0.310$, $1.25 \lesssim P^* \lesssim 2.00$) and smectic J ($\rho^* \gtrsim 0.330$, $P^* \gtrsim 2.20$). The other observables calculated for the $Q^* = 0.20$ and 0.40 cases are tabulated in Table 7.1.
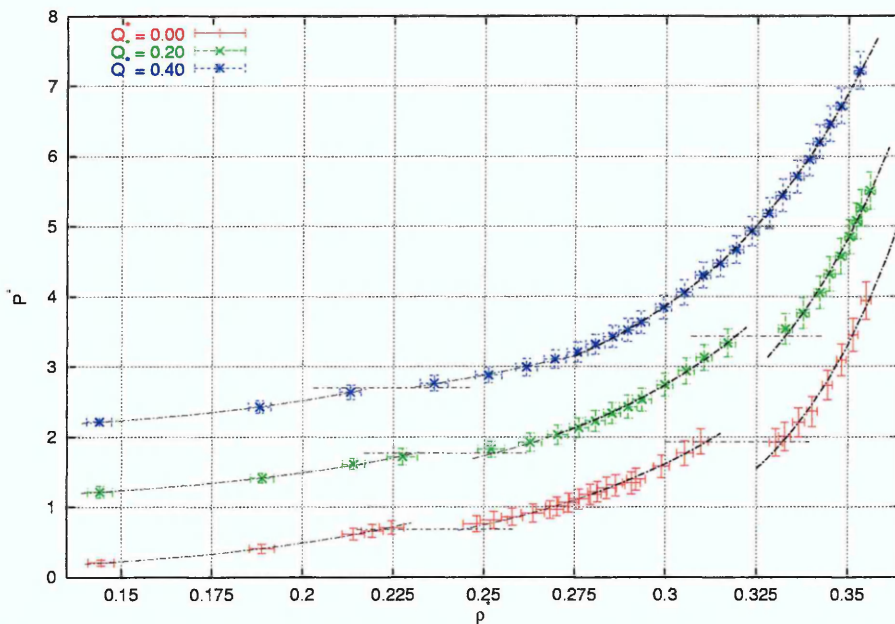

Figure 7.2: Equations of state (pressure P^* vs density ρ^*) for 3:1 molecules with various values of Q^* at $T^* = 1.00$; for clarity successive sets of results are displaced upwards by one unit. Lines are drawn to guide the eye, horizontal lines indicate estimates of the transition pressures.

For the $Q^* = 0.20$ system, the first ordered phase is nematic, confirmed by the non-

Table 7.1: Observable averages calculated for 3:1 molecules for $Q^* = 0.20$ and 0.40 at $T^* = 1.00$.

P^*	$\langle U^* \rangle$	Q_{00}^2	Q_{22}^2	$\langle \theta \rangle$	$r_{\parallel}$
$Q^* = 0.20$
0.20	-1.88(0.06)	0.059(0.016)	0.028(0.015)	none	-
0.40	-2.57(0.07)	0.085(0.026)	0.028(0.017)	none	-
0.60	-3.03(0.09)	0.092(0.046)	0.025(0.019)	none	-
0.70	-3.39(0.16)	0.095(0.107)	0.025(0.017)	none	-
0.80	-4.32(0.14)	0.681(0.044)	0.035(0.020)	none	-
0.90	-4.67(0.11)	0.757(0.023)	0.038(0.020)	none	-
1.00	-4.91(0.11)	0.787(0.021)	0.038(0.021)	none	-
1.10	-5.08(0.10)	0.808(0.015)	0.038(0.021)	none	-
1.20	-5.21(0.10)	0.815(0.017)	0.037(0.020)	none	-
1.30	-5.34(0.09)	0.827(0.011)	0.039(0.019)	none	-
1.40	-5.47(0.09)	0.841(0.011)	0.037(0.020)	none	-
1.50	-5.59(0.10)	0.853(0.011)	0.038(0.020)	none	-
1.70	-5.73(0.09)	0.863(0.011)	0.039(0.021)	none	-
1.90	-5.92(0.10)	0.880(0.009)	0.040(0.021)	none	-
2.10	-6.06(0.10)	0.884(0.008)	0.040(0.021)	none	2.53
2.30	-6.38(0.13)	0.902(0.007)	0.040(0.021)	none	2.52
2.50	-7.60(0.13)	0.946(0.004)	0.155(0.024)	20.23(2.09)	2.59
2.75	-7.98(0.09)	0.954(0.003)	0.204(0.034)	25.14(1.03)	2.54
3.00	-8.23(0.10)	0.957(0.003)	0.250(0.036)	26.92(0.87)	2.50
3.25	-8.31(0.10)	0.958(0.003)	0.275(0.039)	25.24(1.92)	2.46
3.50	-8.45(0.10)	0.960(0.003)	0.270(0.038)	27.41(1.58)	2.43
3.75	-8.47(0.10)	0.961(0.002)	0.271(0.039)	25.97(0.84)	2.43
4.00	-8.51(0.10)	0.963(0.002)	0.273(0.039)	24.93(1.38)	2.44
4.25	-8.42(0.10)	0.963(0.002)	0.259(0.039)	25.78(1.54)	2.50
4.50	-8.51(0.10)	0.963(0.002)	0.286(0.038)	26.49(1.42)	2.46
$Q^* = 0.40$
0.20	-1.87(0.06)	0.059(0.017)	0.029(0.015)	none	-
0.40	-2.55(0.07)	0.077(0.024)	0.028(0.018)	none	-
0.60	-2.98(0.08)	0.099(0.045)	0.024(0.018)	none	-
0.70	-3.77(0.15)	0.543(0.060)	0.032(0.020)	none	-
0.80	-4.27(0.14)	0.673(0.049)	0.033(0.020)	none	-
0.90	-4.60(0.10)	0.739(0.018)	0.035(0.019)	none	-
1.00	-4.83(0.11)	0.777(0.020)	0.037(0.020)	none	-
1.10	-5.03(0.11)	0.803(0.017)	0.039(0.021)	none	-
1.20	-5.15(0.10)	0.814(0.016)	0.039(0.020)	none	-
1.30	-5.29(0.10)	0.826(0.012)	0.038(0.020)	none	-
1.40	-5.41(0.10)	0.837(0.014)	0.037(0.020)	none	-
1.50	-5.50(0.08)	0.845(0.011)	0.039(0.021)	none	-
1.70	-5.65(0.09)	0.856(0.012)	0.037(0.019)	none	-

	continued from previous page				
P^*	$\langle U^* \rangle$	Q^2_{00}	Q^2_{22}	$\langle \theta \rangle$	$r_{\parallel}$
1.90	-5.81(0.09)	0.866(0.011)	0.040(0.021)	none	-
2.10	-5.94(0.08)	0.877(0.009)	0.041(0.021)	none	-
2.30	-6.06(0.08)	0.886(0.009)	0.040(0.021)	none	-
2.50	-6.18(0.09)	0.893(0.008)	0.039(0.021)	none	-
2.75	-6.25(0.08)	0.894(0.008)	0.039(0.020)	none	-
3.00	-6.40(0.07)	0.904(0.005)	0.040(0.022)	none	-
3.25	-6.46(0.09)	0.906(0.007)	0.041(0.021)	none	-
3.50	-6.55(0.08)	0.912(0.005)	0.041(0.021)	none	-
3.75	-6.62(0.08)	0.917(0.005)	0.041(0.021)	none	-
4.00	-6.63(0.07)	0.915(0.006)	0.041(0.021)	none	-
4.25	-6.67(0.09)	0.916(0.007)	0.040(0.021)	none	-
4.50	-6.76(0.07)	0.921(0.005)	0.041(0.021)	none	-
5.00	-6.83(0.08)	0.924(0.005)	0.042(0.021)	none	-

zero value adopted by the nematic order parameter and the liquid like behaviour of the radial distribution functions (Figs. 7.3 and 7.4). Whilst this phase transition is observed over the same pressure range as for the $Q^* = 0.00$ case, the transition density is slightly increased. Upon further compression, a weak density wave is once again observed in $g_{\parallel}(r^*_{\parallel})$ (Fig. 7.3), for $P^* \geq 1.50$, corresponding to $\rho^* \geq 0.294$. This onset of smectic ordering, therefore, occurs at a greater density and pressure than was observed for the $Q^* = 0.00$ case. Since this phase displays liquid like ordering within each layer (Fig. 7.4), with no evidence of biaxial ordering or molecular tilting, this phase is classified as smectic A.

A second discontinuity is observed in the equation of state with increasing density, with a corresponding increasing in the nematic and biaxial order parameters being observed. Examination of the radial distribution functions (Figs. 7.3, 7.4 and 7.5) shows that this phase has a well defined layered structure with long range hexatic ordering within each layer, with the direction of tilt being towards the apex of the
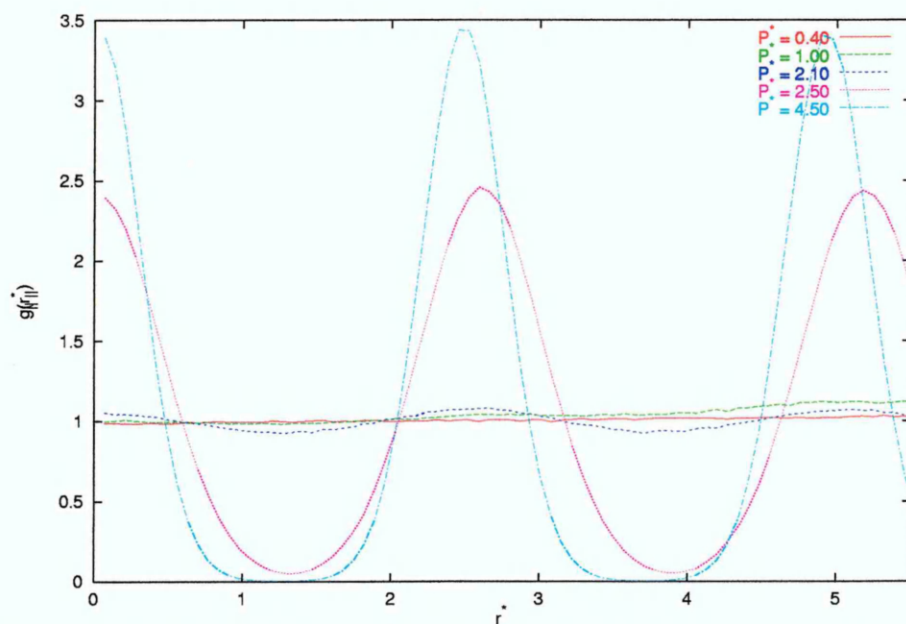
Figure 7.3: Radial distribution function resolved parallel to the layer normal for 3:1 molecules at $Q^* = 0.2$ and $T^* = 1.00$.
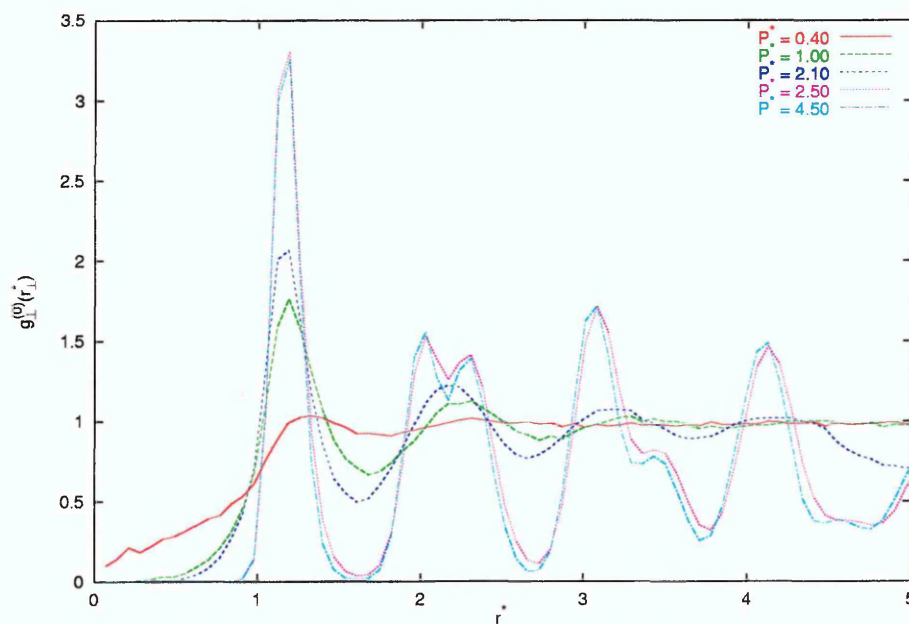

Figure 7.4: Radial distribution function resolved perpendicular to the layer normal for 3:1 molecules at $Q^* = 0.20$ and $T^* = 1.00$.

hexagonal net, indicating a smectic J phase. This phase transition occurs at a higher density and pressure for this system than for the $Q^* = 0.00$ case. It is also interesting to note that the biaxial order parameter and average tilt angle within the smectic J phase are slightly higher than those observed for the $Q^* = 0.00$ case.

These results show that, for this small value of Q^*, the incorporation of a quadrupole moment into the model has resulted in the same sequence of phases being observed, with all of the phase transitions being shifted to higher densities and pressures. It would, therefore, appear that the quadrupole interaction results in the destabilisation of all of the orientationally ordered phases. This is to be expected since theoretical models [39, 40] have also shown that the inclusion of a quadrupole moment results in the destabilisation of the orientationally ordered phases. That said, within the tilted smectic J phase, larger values are calculated for the biaxial order parameter and the average tilt angle, indicating that the inclusion of a quadrupole moment helps stabilise the tilted structure.

For $Q^* = 0.40$, only one discontinuity is observed in the equation of state. The marked increase in the orientational order parameter and the liquid like structure in the radial distribution functions (Figs. 7.6 and 7.7) indicates an isotropic to nematic transition. The transition density and pressure are decreased compared with those observed for the $Q^* = 0.20$ and 0.00 cases. As the density is increased further, no layered structures are observed.

The observation that the nematic phase is stabilised here with respect to the isotropic phase is somewhat surprising since the inclusion of the quadrupole is expected to
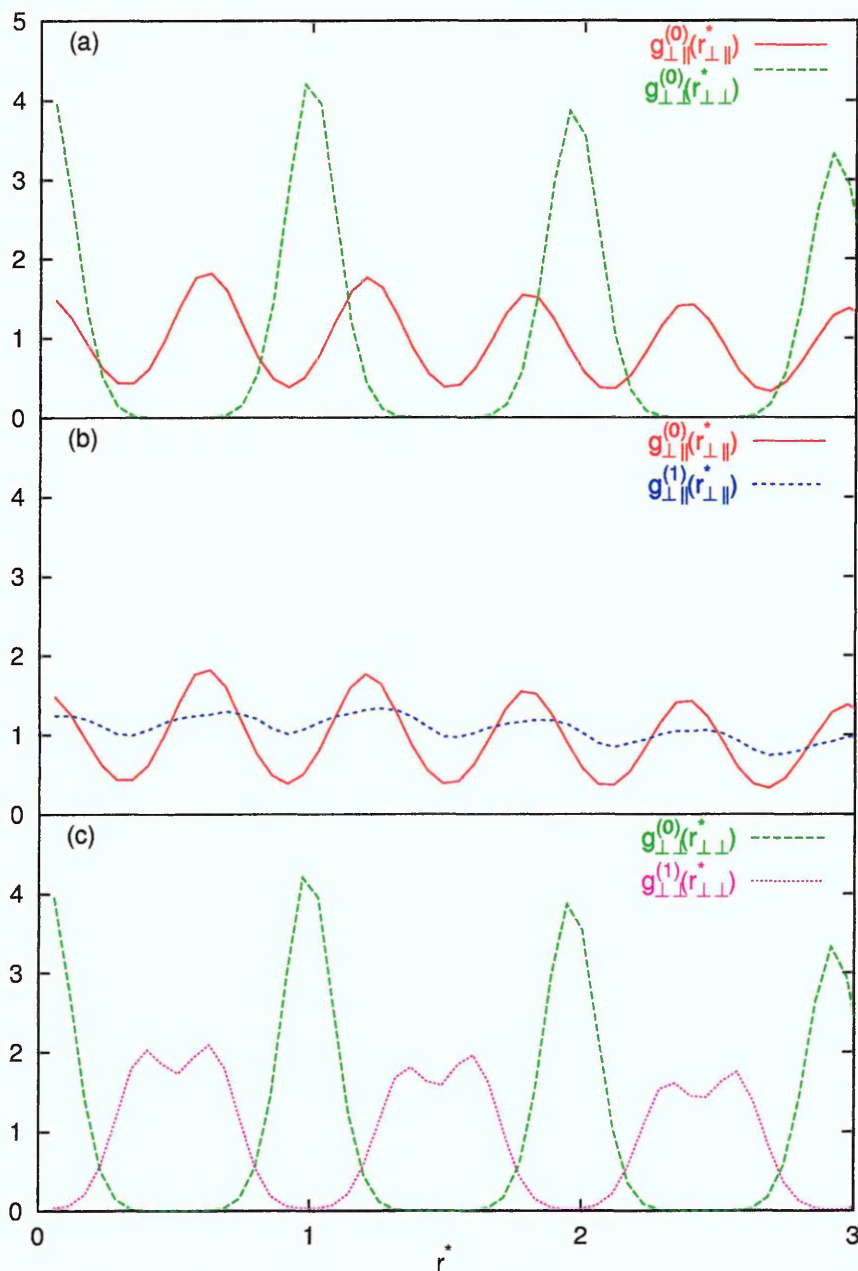
226

Figure 7.5: Radial distribution functions (a) resolved within the layer parallel, $g_{\perp\|}^{(0)}(r_{\perp\|}^*)$, and perpendicular, $g_{\perp\perp}^{(0)}(r_{\perp\perp}^*)$, to the direction of tilt and between adjacent layers resolved (b) parallel to the direction of tilt and (c) perpendicular to the direction of tilt for 3:1 molecules at $Q^* = 0.20$, $T^* = 1.00$ and $P^* = 3.00$.
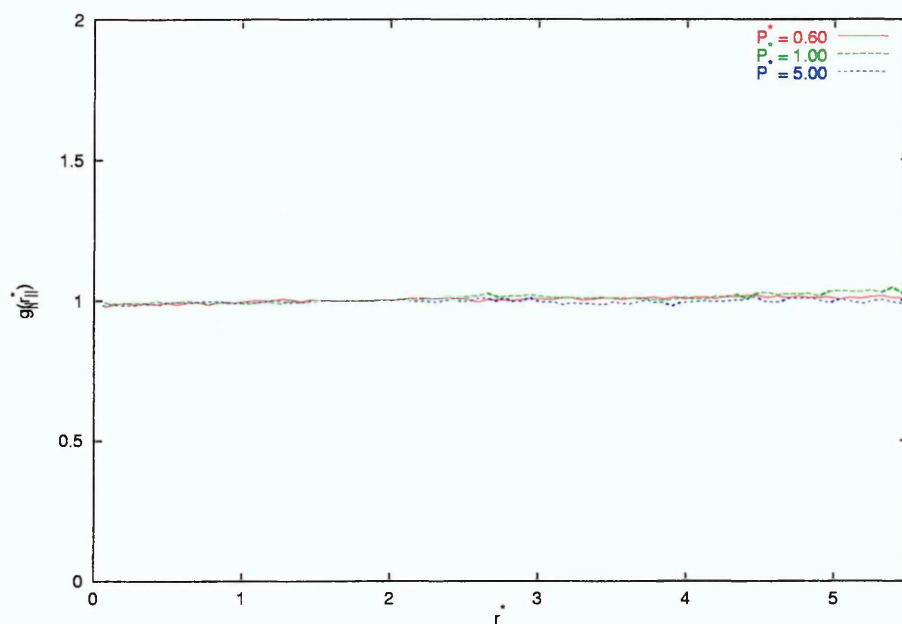
Figure 7.6: Radial distribution function resolved parallel to the layer normal for 3:1 molecules at $Q^* = 0.40$ and $T^* = 1.00$.
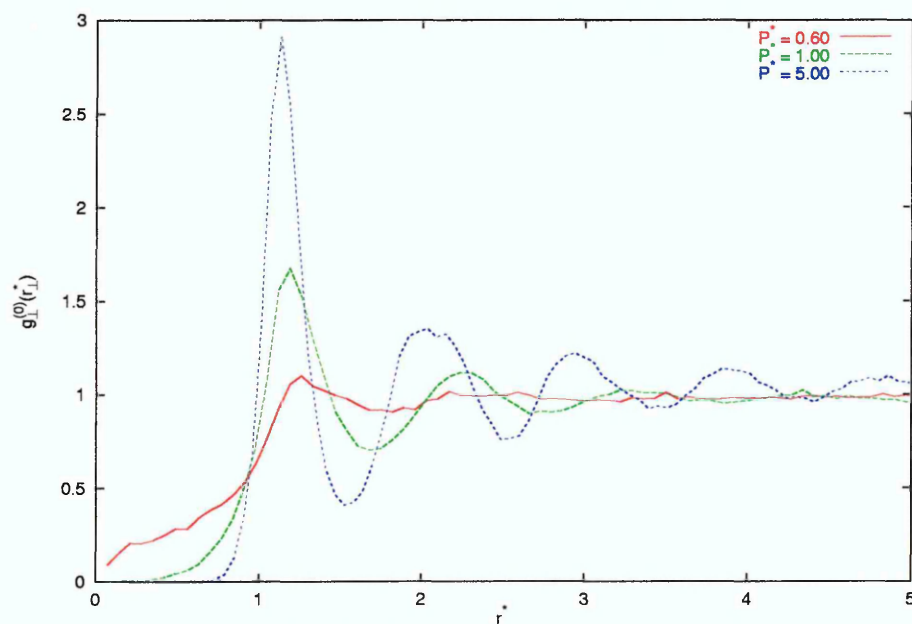

Figure 7.7: Radial distribution function resolved perpendicular to the layer normal for 3:1 molecules at $Q^* = 0.40$ and $T^* = 1.00$.

228

destabilise the orientationally ordered phases. However, as was mentioned in the previous section, increasing the quadrupole magnitude causes the well depth in the side-by-side configuration to extend further along the molecular long axis, before splitting into two minima (for quadrupole magnitudes greater than used here). This stabilisation of the nematic phase may, therefore, result from this broadening of the well depth, which stabilises the side-by-side configuration for these biaxial molecules.

Since a quadrupole magnitude of $Q^* = 0.40$ has resulted in the destabilisation of the translationally ordered phases for these 3:1 molecules, no further simulations have been performed for this system. Attention will now be focussed upon the longer 4:1 molecules.

7.3   Long Molecules

The equations of state obtained from the simulations of particles interacting via the Internally-Rotated Gay-Berne potential plus a longitudinal quadrupole moment with an aspect ratio of 4:1 at $T^* = 1.50$ for $Q^* = 0.00, 0.20, 0.40, 0.60$ and 0.80 are shown in Fig. 7.8. The $Q^* = 0.00$ case is redrawn from Fig. 5.34, thus providing a reference system, with the sequence of phases being isotropic ($\rho^* \lesssim 0.131$, $P^* \lesssim 0.55$), smectic A ($0.176 \lesssim \rho^* \lesssim 0.209$, $0.60 \lesssim P^* \lesssim 0.95$) and smectic G ($\rho^* \gtrsim 0.234$, $P^* \gtrsim 1.00$). The other observables calculated for the $Q^* = 0.20, 0.40, 0.60$ and 0.80 cases are tabulated in Table 7.2.

For $Q^* = 0.20$ the first phase transition is observed over the same pressure range
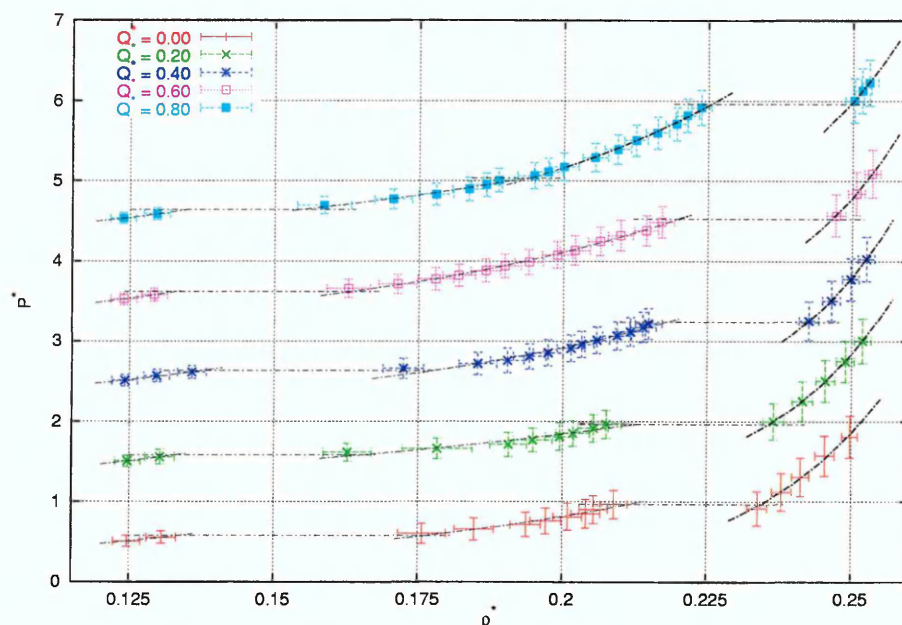
Figure 7.8: Equations of state (pressure P^* vs density ρ^*) for 4:1 molecules with various values of Q^* at $T^* = 1.50$; for clarity these results are displaced upwards by one unit. Lines are drawn to guide the eye, horizontal lines indicate estimates of the transition pressures.

as for $Q^* = 0.00$, with a layered structure (shown in Fig. 7.9) being formed at a lower density than was observed for $Q^* = 0.00$. Since there is no evidence of biaxial ordering, or tilting of the molecules within the layer, with liquid-like structure being observed within each layer (Fig. 7.10), this phase is classified as smectic A.

Upon further compression, a second phase transition is observed, at approximately the same pressure as for $Q^* = 0.00$, although, the coexistence region covers a wider range of densities. A corresponding increase in both the nematic and biaxial order parameters is observed at this transition. Examination of the radial distribution functions (Figs. 7.9, 7.10 and 7.11) shows that this highest density phase has a well defined layered structure, long range ordering within each layer with the direction of tilt being towards the apex of the hexagonal net, indicating a smectic J phase,

Table 7.2: Observable averages calculated for 4:1 molecules for $Q^* = 0.20$, 0.40, 0.60 and 0.80 at $T^* = 1.00$.

P^*	$\langle U^* \rangle$	Q_{00}^2	Q_{22}^2	$\langle \theta \rangle$	$r_{\parallel}$
		$Q^* = 0.20$			
0.50	-2.79(0.10)	0.089(0.038)	0.026(0.019)	none	-
0.55	-3.00(0.15)	0.094(0.064)	0.025(0.018)	none	-
0.60	-5.19(0.27)	0.761(0.031)	0.036(0.019)	none	3.76
0.65	-6.34(0.53)	0.854(0.033)	0.039(0.021)	none	3.70
0.70	-7.39(0.27)	0.902(0.012)	0.039(0.020)	none	3.73
0.75	-7.68(0.31)	0.910(0.011)	0.040(0.021)	none	3.62
0.80	-8.08(0.20)	0.922(0.006)	0.039(0.021)	none	3.64
0.85	-8.23(0.26)	0.926(0.007)	0.042(0.021)	none	3.65
0.90	-8.53(0.24)	0.932(0.006)	0.041(0.021)	none	3.66
0.95	-8.69(0.23)	0.935(0.006)	0.041(0.021)	none	3.65
1.00	-12.16(0.22)	0.976(0.002)	0.207(0.039)	18.50(1.12)	3.51
1.25	-12.62(0.22)	0.979(0.002)	0.253(0.042)	19.20(1.58)	3.49
1.50	-12.97(0.19)	0.981(0.001)	0.256(0.038)	20.08(1.13)	3.47
1.75	-13.22(0.19)	0.983(0.001)	0.259(0.040)	19.66(1.99)	3.46
2.00	-13.50(0.18)	0.984(0.001)	0.262(0.039)	20.17(1.03)	3.45
		$Q^* = 0.40$			
0.50	-2.74(0.10)	0.089(0.033)	0.027(0.019)	none	-
0.55	-2.93(0.12)	0.090(0.035)	0.025(0.019)	none	-
0.60	-3.20(0.15)	0.096(0.052)	0.022(0.022)	none	-
0.65	-5.77(0.24)	0.823(0.022)	0.039(0.020)	none	3.66
0.70	-6.72(0.26)	0.879(0.013)	0.039(0.020)	none	3.69
0.75	-7.08(0.23)	0.893(0.011)	0.039(0.021)	none	3.69
0.80	-7.35(0.23)	0.901(0.010)	0.040(0.021)	none	3.68
0.85	-7.58(0.23)	0.909(0.009)	0.040(0.022)	none	3.67
0.90	-7.90(0.20)	0.917(0.007)	0.042(0.021)	none	3.65
0.95	-7.97(0.18)	0.920(0.007)	0.040(0.021)	none	3.63
1.00	-8.15(0.18)	0.924(0.006)	0.041(0.021)	none	3.60
1.05	-8.52(0.23)	0.932(0.007)	0.041(0.021)	none	3.63
1.10	-8.69(0.24)	0.935(0.006)	0.042(0.021)	none	3.58
1.15	-8.83(0.20)	0.939(0.005)	0.042(0.022)	none	3.59
1.20	-8.88(0.23)	0.938(0.005)	0.041(0.022)	none	3.63
1.25	-12.73(0.20)	0.980(0.002)	0.272(0.042)	25.61(0.50)	3.29
1.50	-13.04(0.18)	0.982(0.001)	0.280(0.041)	25.63(0.38)	3.28
1.75	-13.33(0.18)	0.983(0.001)	0.283(0.041)	25.81(0.38)	3.26
2.00	-13.53(0.18)	0.985(0.001)	0.284(0.036)	25.81(0.30)	3.25
		$Q^* = 0.60$			
0.50	-2.71(0.12)	0.086(0.037)	0.026(0.019)	none	-
0.55	-2.89(0.12)	0.091(0.045)	0.027(0.019)	none	-
0.60	-5.12(0.24)	0.768(0.029)	0.036(0.019)	none	-

231

continued from previous page					
P^*	$\langle U^* \rangle$	Q_{00}^2	Q_{22}^2	$\langle \theta \rangle$	$r_\parallel$
0.65	-5.63(0.21)	0.816(0.020)	0.036(0.020)	none	-
0.70	-6.00(0.22)	0.844(0.016)	0.038(0.020)	none	-
0.75	-6.23(0.19)	0.852(0.015)	0.038(0.020)	none	-
0.80	-6.54(0.19)	0.874(0.012)	0.040(0.020)	none	-
0.85	-6.72(0.21)	0.880(0.013)	0.039(0.020)	none	-
0.90	-7.00(0.20)	0.894(0.010)	0.039(0.020)	none	-
0.95	-7.37(0.21)	0.907(0.008)	0.041(0.020)	none	3.65
1.00	-7.63(0.25)	0.913(0.010)	0.041(0.021)	none	3.62
1.10	-7.93(0.17)	0.921(0.006)	0.040(0.021)	none	3.63
1.20	-8.11(0.21)	0.926(0.006)	0.041(0.021)	none	3.54
1.30	-8.52(0.20)	0.934(0.005)	0.040(0.021)	none	3.57
1.40	-8.68(0.20)	0.936(0.006)	0.041(0.022)	none	3.59
1.50	-13.15(0.18)	0.983(0.001)	0.332(0.033)	33.11(0.46)	3.25
1.75	-13.46(0.18)	0.984(0.001)	0.347(0.034)	33.36(0.32)	3.32
2.00	-13.67(0.17)	0.985(0.001)	0.358(0.034)	33.36(0.33)	3.31
$Q^* = 0.80$					
0.50	-2.70(0.11)	0.083(0.037)	0.026(0.017)	none	-
0.55	-2.94(0.12)	0.095(0.043)	0.026(0.021)	none	-
0.60	-4.82(0.31)	0.719(0.052)	0.036(0.019)	none	-
0.65	-5.54(0.21)	0.805(0.023)	0.037(0.020)	none	-
0.70	-5.98(0.20)	0.838(0.016)	0.038(0.020)	none	-
0.75	-6.33(0.19)	0.860(0.014)	0.038(0.021)	none	-
0.80	-6.48(0.18)	0.869(0.012)	0.039(0.020)	none	-
0.85	-6.56(0.20)	0.872(0.014)	0.039(0.020)	none	-
0.90	-7.00(0.21)	0.894(0.011)	0.040(0.021)	none	-
0.95	-7.15(0.19)	0.898(0.010)	0.040(0.021)	none	-
1.00	-7.31(0.20)	0.902(0.011)	0.039(0.020)	none	-
1.10	-7.69(0.17)	0.916(0.007)	0.040(0.021)	none	-
1.20	-7.92(0.19)	0.919(0.009)	0.041(0.021)	none	-
1.30	-8.09(0.18)	0.926(0.007)	0.043(0.022)	none	-
1.40	-8.35(0.18)	0.933(0.006)	0.042(0.021)	none	-
1.50	-8.60(0.18)	0.939(0.005)	0.043(0.022)	none	-
1.60	-8.67(0.21)	0.938(0.006)	0.040(0.021)	none	-
1.70	-8.82(0.16)	0.941(0.004)	0.042(0.021)	none	-
1.80	-12.96(0.20)	0.980(0.001)	0.064(0.031)	21.68(0.54)	-
1.90	-13.10(0.19)	0.981(0.001)	0.076(0.035)	21.44(0.60)	-
2.00	-13.21(0.19)	0.981(0.001)	0.098(0.038)	20.60(0.62)	-

rather than the smectic G phase observed for $Q^* = 0.00$. Unlike the 3:1 molecules already considered, the biaxial order parameter and average tilt angles calculated within this highly order phase are comparable with the $Q^* = 0.00$ case, indicating that the inclusion of the quadrupole moment with such a small value of Q^* does not help stabilise the tilted structure for these longer molecules.

The observation that the tilted hexatic phase has been destabilised with resect to the smectic A phase is expected following the results of theoretical studies [39, 40], although the observation that the smectic A phase is stabilised with respect to the isotropic is somewhat surprising. However, as was suggested for the 3:1 molecules this may be due to the quadrupole helping to stabilise the side-by-side configuration for these biaxial molecules.

In order to understand why the smectic J phase is being observed for this relatively small quadrupole moment, rather than the smectic G phase, the form of the potential energy as a function of the intermolecular vector, for both types of tilted hexatic phase, along the two directions of bond order, r_1 and r_2, for a perfectly orientated hexagonal unit cell within a single smectic layer is considered. These functions are shown in Fig. 7.12 for $Q^* = 0.00$ and $Q^* = 1.00$, with the potential varying smoothly between these behaviours for intermediate values of Q^*. As was discussed in section 5.2.2 the most favourable pair interaction for $Q^* = 0.0$ is the side-by-side configuration found in the smectic G phase, with the energetically least favourable being along r_1 within the smectic J phase. With increasing Q^*, the depth of the potential well becomes less deep along all of the directions of bond
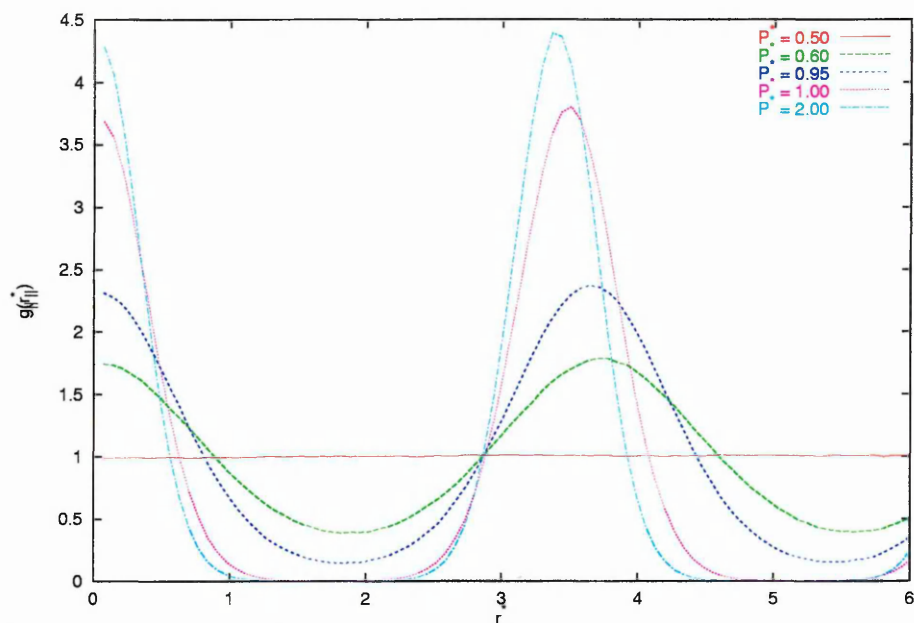
Figure 7.9: Radial distribution function resolved parallel to the layer normal for 4:1 molecules at $Q^* = 0.20$ and $T^* = 1.50$.
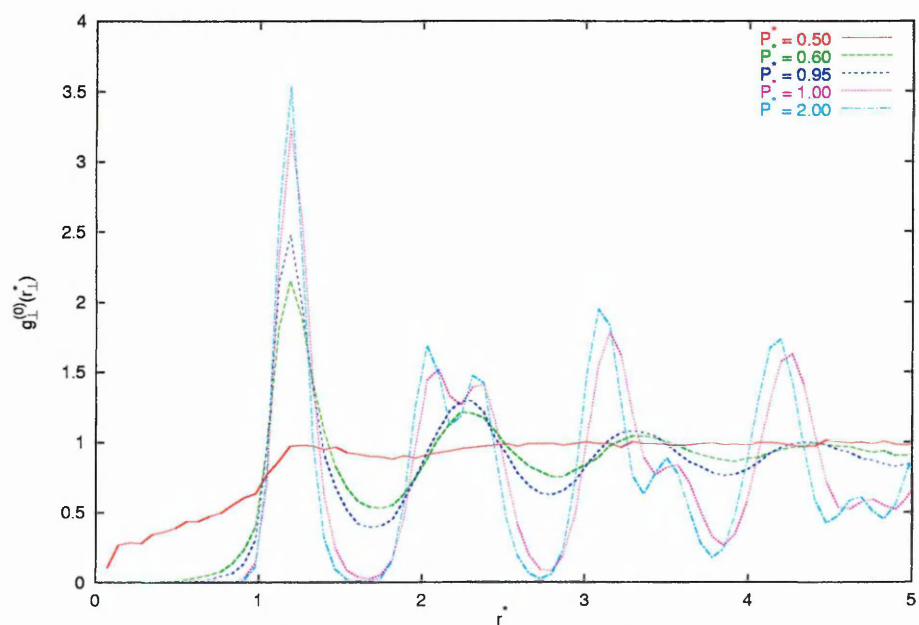

Figure 7.10: Radial distribution function resolved perpendicular to the layer normal for 4:1 molecules at $Q^* = 0.20$ and $T^* = 1.50$.
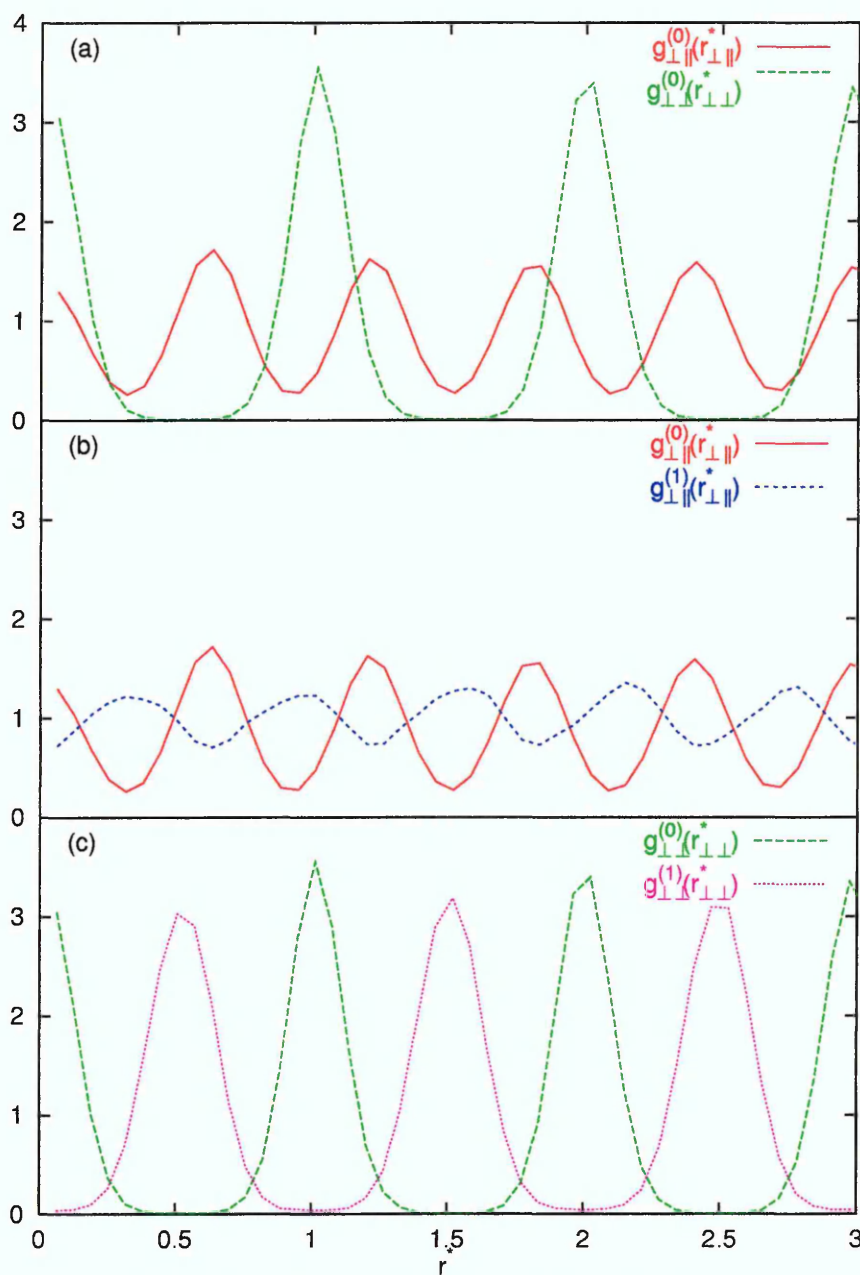
Figure 7.11: Radial distribution functions (a) resolved within the layer parallel, $g_{\perp\parallel}^{(0)}(r_{\perp\parallel}^*)$, and perpendicular, $g_{\perp\perp}^{(0)}(r_{\perp\perp}^*)$, to the direction of tilt and between adjacent layers resolved (b) parallel to the direction of tilt and (c) perpendicular to the direction of tilt for 4:1 molecules at $Q^* = 0.20$, $T^* = 1.50$ and $P^* = 2.00$.

order, with the exception of r_1 within the smectic J phase which remains unchanged. Thus, for sufficiently large values of Q^*, the order in which the well depths occur is reversed, with the side-by-side configuration of the smectic G phase becoming the least favourable, and the r_1 direction within the smectic J phase becoming the most favourable. As a result of this, the smectic J phase provides the energetically most favourable configuration for sufficiently large values of Q^*.

In order to determine the magnitude of the quadrupole moment at which the transition from smectic G to smectic J occurs, a series of simulations were performed, initiated within the smectic G phase ($T^* = 1.50$ and $P^* = 1.50$) observed for $Q^* = 0.00$. The quadrupole magnitude was then increased in incremental steps of $\Delta Q^* = 0.02$. Examination of the observable averages obtained from these simulations (shown in Table 7.3) shows a discontinuity in the internal energy over the range $0.02 \geq Q^* \geq 0.04$, with corresponding increases in the nematic and biaxial order parameters and in the average density. Examination of the radial distribution functions resolved parallel and perpendicular to the direction of tilt (Fig. 7.13) confirms that this corresponds to a phase transition from smectic G to smectic J. It is also pleasing to note that the averages calculated for $Q^* = 0.20$ here agree well with those obtained during the independent series of simulations performed with gradually increased pressure (Table. 7.2).

Returning to the results obtained from the simulations performed upon systems with increasing pressure, the $Q^* = 0.40$ system displays an initial phase transition at a pressure, and over a density range, greater than was observed for $Q^* = 0.20$. This
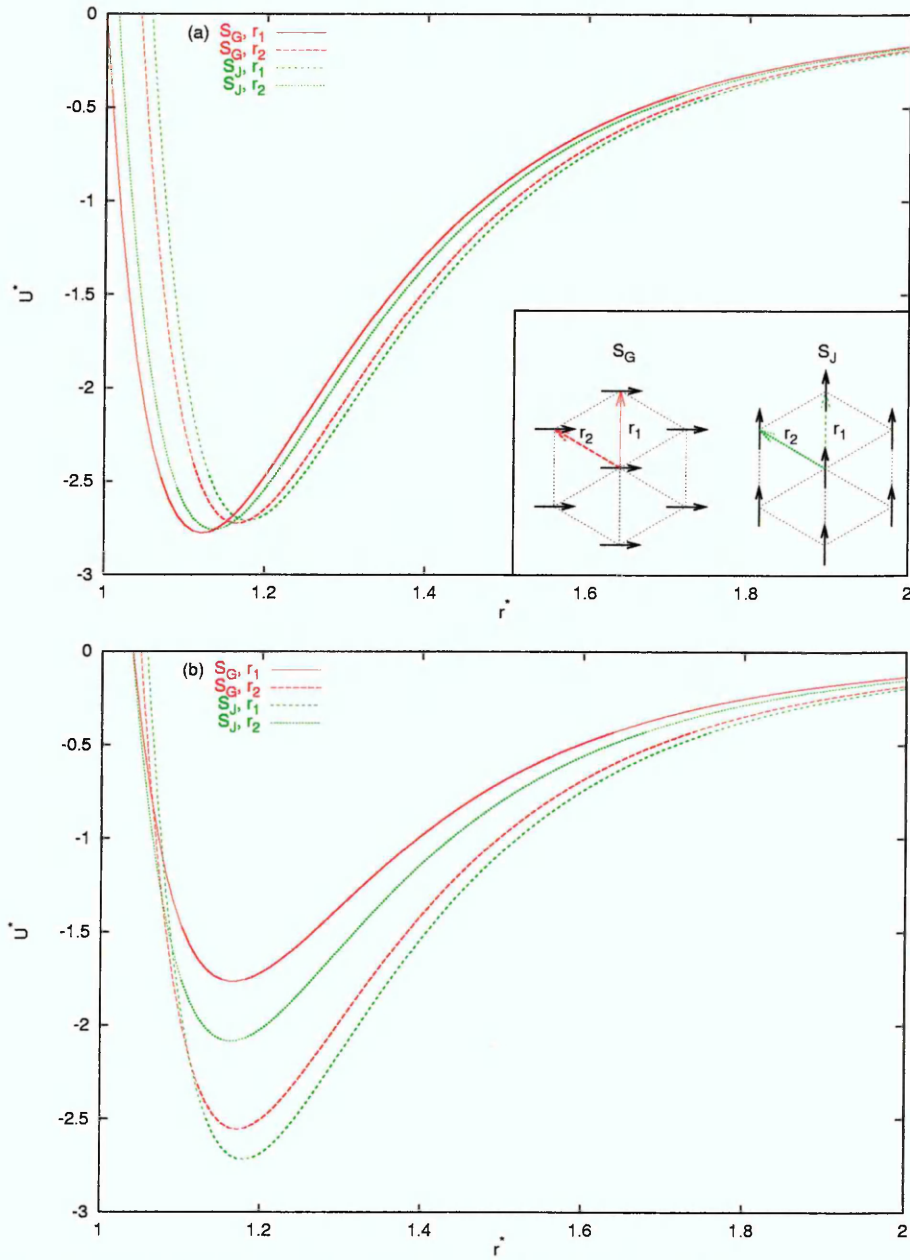
236

Figure 7.12: Well depths of two particles interacting via the IRGB potential plus a longitudinal quadrupole along the two directions of bond order, r_1 and r_2, exhibited by a perfectly orientated hexagonal close-packed unit cell for the smectic G and J phases with $\delta = 30$ and $\theta = 20$ for (a) $Q^* = 0.0$ and (b) $Q^* = 1.0$. Inset of (a) shows definition of r_1 and r_2 within the hexagonal net.
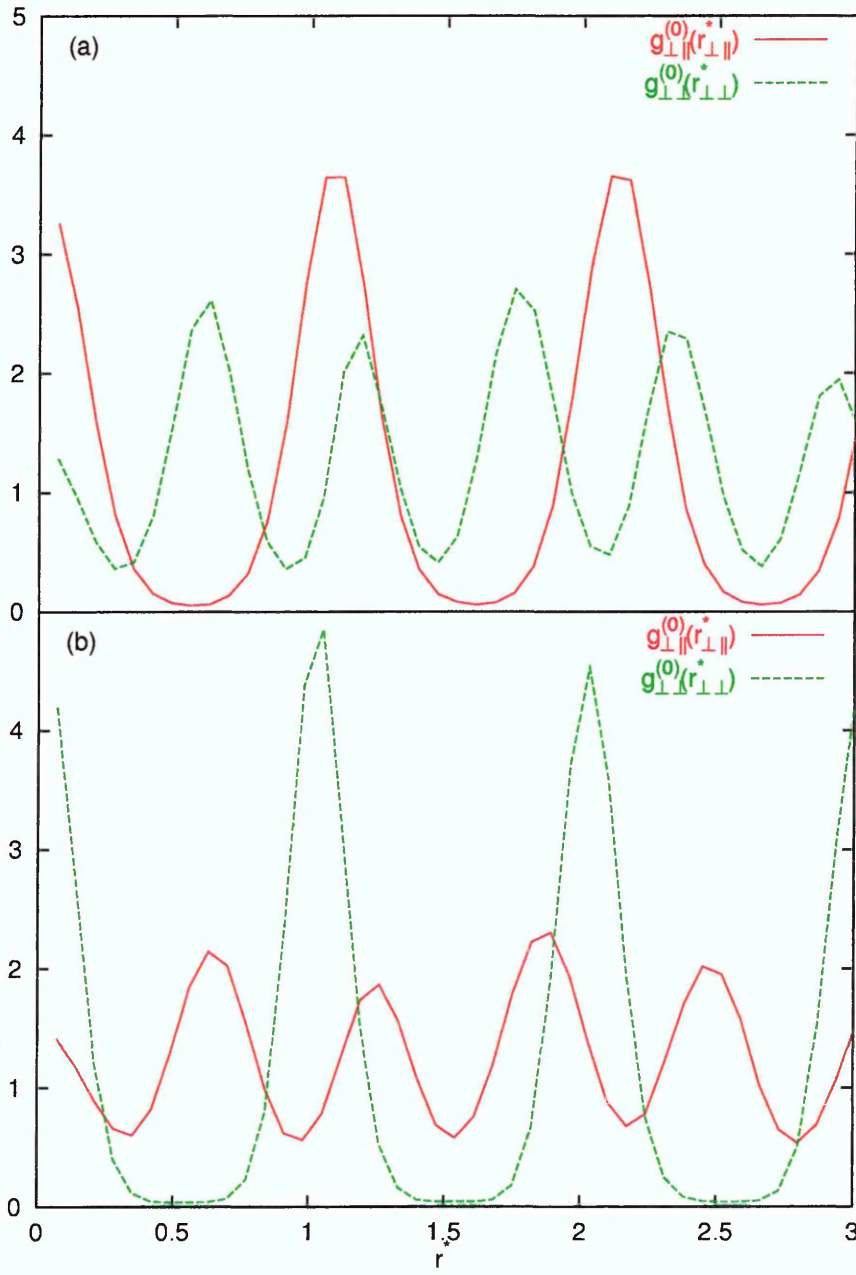
Figure 7.13: Radial distribution functions resolved within the layer parallel, $g_{\perp\parallel}^{(0)}(r_{\perp\parallel}^*)$, and perpendicular, $g_{\perp\perp}^{(0)}(r_{\perp\perp}^*)$, to the direction of tilt for (a) $Q^* = 0.02$ and (b) $Q^* = 0.04$ at $T^* = 1.50$ and $P^* = 1.50$.

Q^*	$\langle U^* \rangle$	Q^2_{00}	Q^2_{22}	$\langle \rho^* \rangle$	$\langle \theta \rangle$	$r_{\parallel}$
0.00	-12.70(19)	0.978(02)	0.225(37)	0.241(01)	22.46(40)	3.43
0.02	-12.72(24)	0.979(02)	0.250(41)	0.242(01)	24.23(38)	3.41
0.04	-13.08(18)	0.981(01)	0.256(34)	0.246(01)	23.33(44)	3.43
0.06	-13.02(17)	0.981(01)	0.248(37)	0.246(01)	23.30(38)	3.42
0.08	-13.05(19)	0.981(01)	0.254(38)	0.246(01)	23.28(46)	3.41
0.10	-13.03(17)	0.981(01)	0.255(36)	0.246(01)	23.30(31)	3.42
0.12	-12.97(18)	0.981(01)	0.250(37)	0.246(01)	23.41(36)	3.41
0.14	-12.99(18)	0.981(01)	0.250(34)	0.246(01)	23.34(44)	3.42
0.16	-12.99(17)	0.981(01)	0.254(37)	0.246(01)	23.41(50)	3.42
0.18	-12.96(18)	0.981(01)	0.248(36)	0.246(01)	23.26(34)	3.42
0.20	-12.97(17)	0.981(01)	0.254(35)	0.246(01)	23.28(46)	3.44

Table 7.3: Observable averages calculated for 4:1 molecules at $T^* = 1.50$ and $P^* = 1.50$ with increasing Q^*.

first orientationally ordered phase also displays a layered structure (Fig. 7.14), with liquid-like structure being observed within each layer (Fig. 7.15). Since there is no evidence of biaxial ordering, or molecular titling within the layers, this phase is also classified as smectic A.

A second phase transition is also observed, at a higher pressure and density range than was observed for $Q^* = 0.20$. The corresponding increase in both the orientational order parameters and the observation that the average director and layer normal are not coincident indicates a transition into a tilted hexatic phase. This is confirmed by examination of the radial distribution functions (Figs. 7.14 and 7.15) with the radial distribution functions resolved parallel and perpendicular to the direction of tilt (Fig. 7.16) showing that a smectic J phase is being formed. It is interesting to note that the biaxial order parameters and average tilt angles calculated here are larger than for the $Q^* = 0.20$ case, indicating that the quadrupole, whilst shifting the phase transitions to higher densities, is stabilising the structure
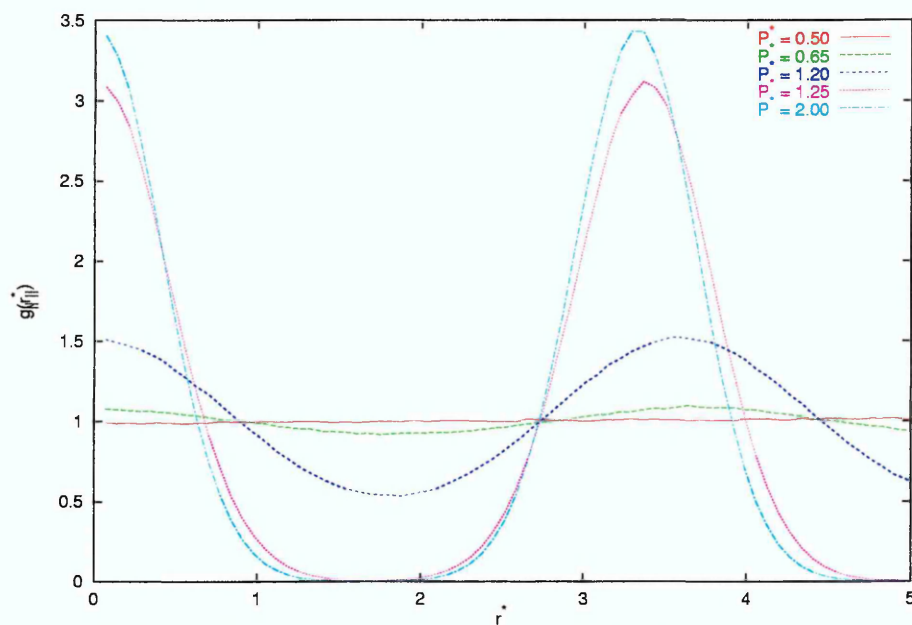
239

Figure 7.14: Radial distribution function resolved parallel to the layer normal for 4:1 molecules at $Q^* = 0.40$ and $T^* = 1.50$.
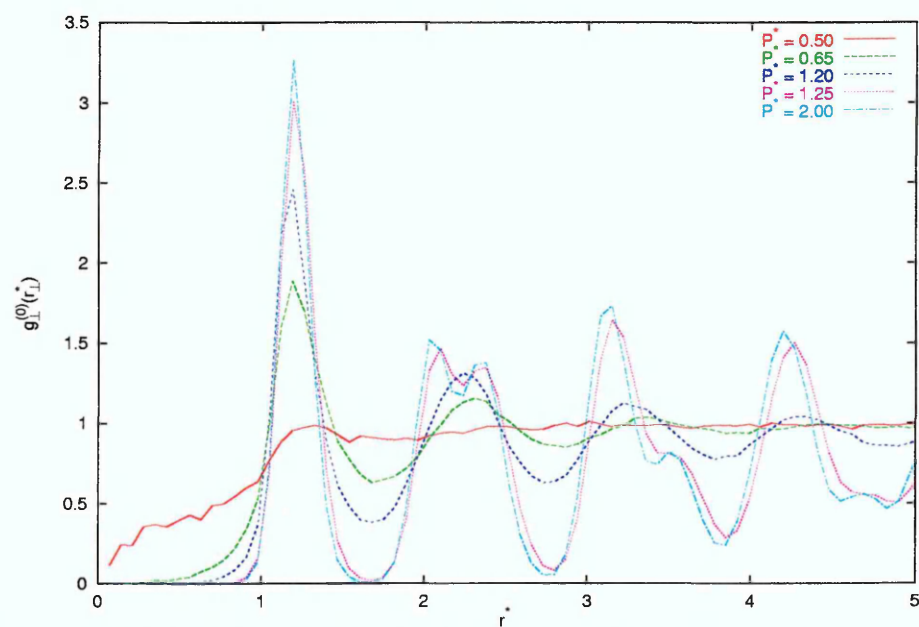

Figure 7.15: Radial distribution function resolved perpendicular to the layer normal for 4:1 molecules at $Q^* = 0.40$ and $T^* = 1.50$.

240

of the tilted hexatic phase.

For the $Q^* = 0.60$ system, an initial phase transition is observed at a lower pressure and over a lower density range than was observed for $Q^* = 0.40$. That said, the radial distribution functions (Figs. 7.17 and 7.18) within this first orientationally ordered phase display liquid-like behaviour, indicative of the nematic phase. Upon further compression, a layered structure is observed for $P^* \geq 0.95$ (Fig. 7.17), corresponding to $\rho^* \geq 0.197$; both of these values are considerable greater than was observed for the onset of smectic ordering for the $Q^* = 0.40$ case. There is, however, no evidence of a discontinuity in the equation of state, or in any of the other observables, indicating a very weak phase transition. The absence of biaxial ordering or molecular tilting with respect to the layer normal, along with the lack of structure within each layer (Fig. 7.18) identifies this phase as smectic A.

A third phase transition is also observed along this isotherm, at a higher pressure and over a wider range of densities than has been observed for the $Q^* < 0.60$ cases, with a corresponding increase in the nematic and biaxial order parameters being observed. The radial distribution functions (Figs. 7.17, 7.18 and 7.19) show that this phase has a well defined layered structure, displaying long range ordering within each layer, with the direction of tilt being towards to apex of the hexagonal net, indicating a smectic J phase. Once again, the biaxial order parameter and average tilt angle are larger than those observed for the $Q^* = 0.40$ case.

For $Q^* = 0.80$ the phase transition into the nematic phase (classified by the liquid-like behaviour observed for the radial distribution functions (Figs. 7.20 and 7.21))
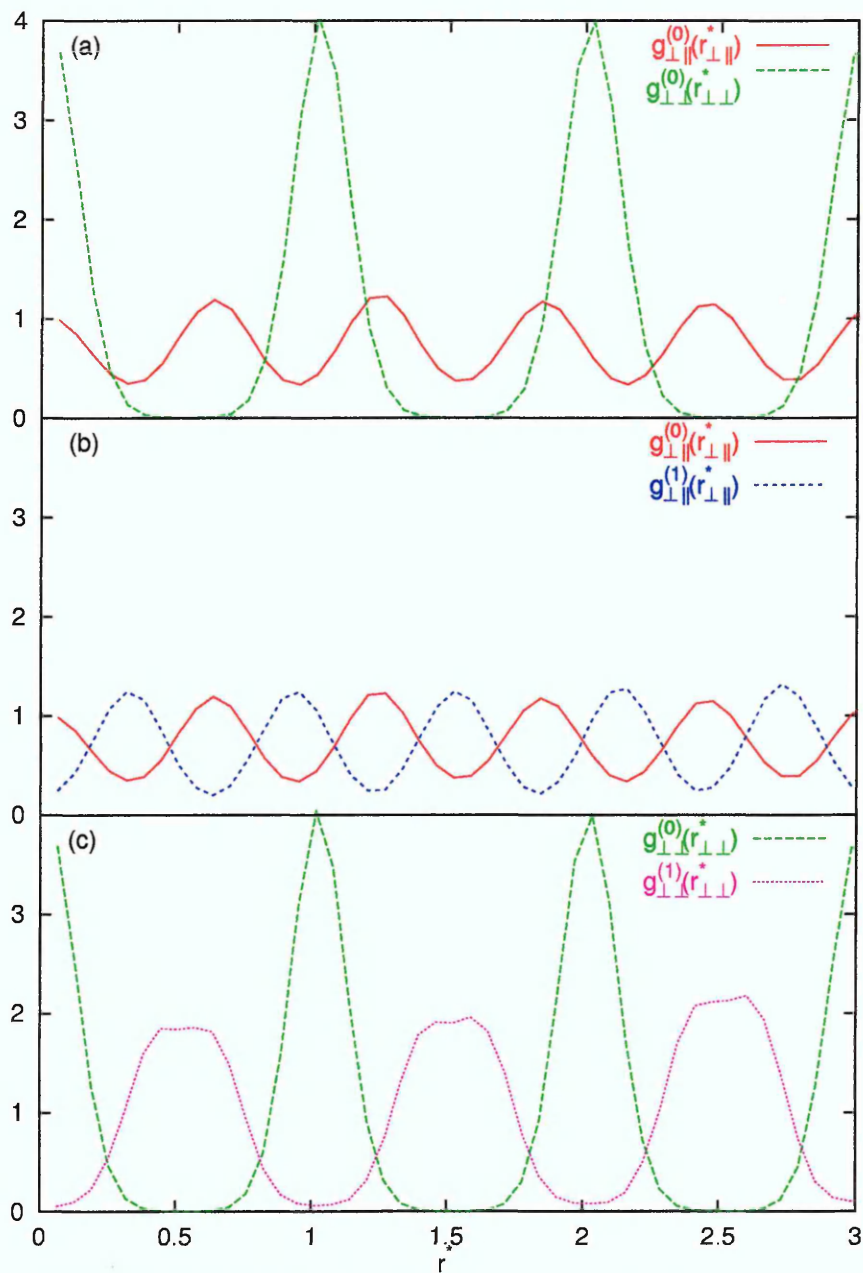
241

Figure 7.16: Radial distribution functions (a) resolved within the layer parallel, $g_{\perp\parallel}^{(0)}(r_{\perp\parallel}^*)$, and perpendicular, $g_{\perp\perp}^{(0)}(r_{\perp\perp}^*)$, to the direction of tilt and between adjacent layers resolved (b) parallel to the direction of tilt and (c) perpendicular to the direction of tilt for 4:1 molecules at $Q^* = 0.40$, $T^* = 1.50$ and $P^* = 2.00$.
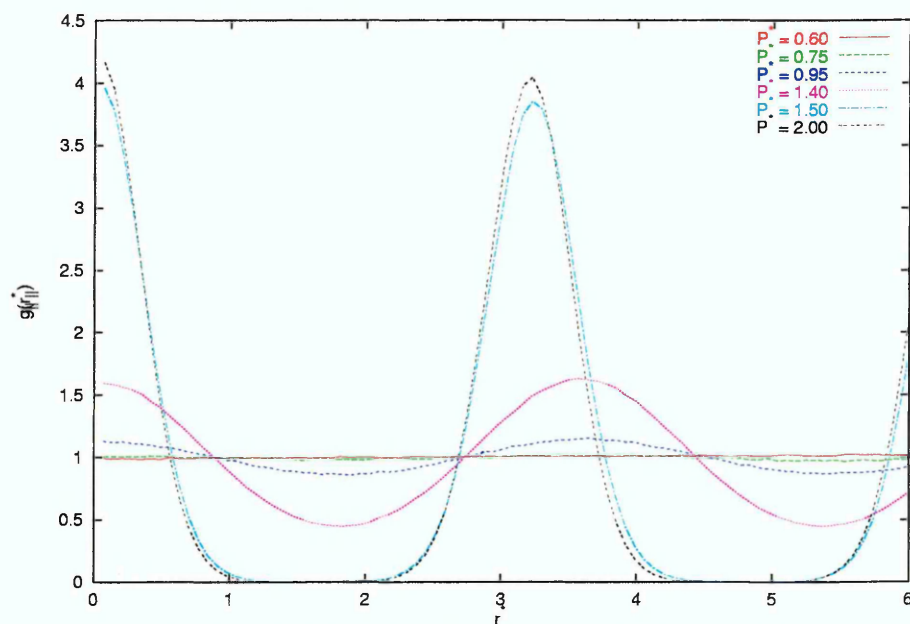
Figure 7.17: Radial distribution function resolved parallel to the layer normal for 4:1 molecules at $Q^* = 0.60$ and $T^* = 1.50$.
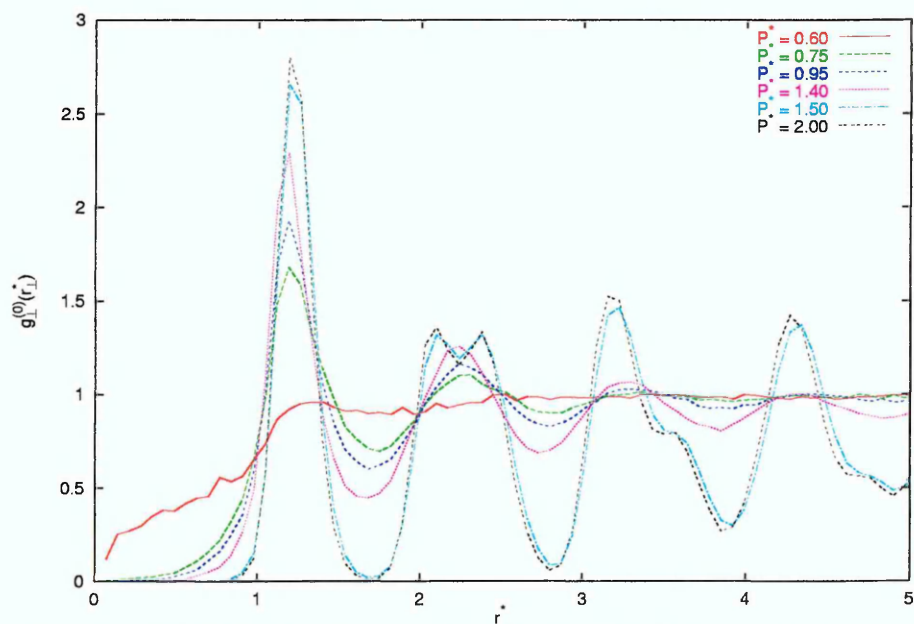

Figure 7.18: Radial distribution function resolved perpendicular to the layer normal for 4:1 molecules at $Q^* = 0.60$ and $T^* = 1.50$.
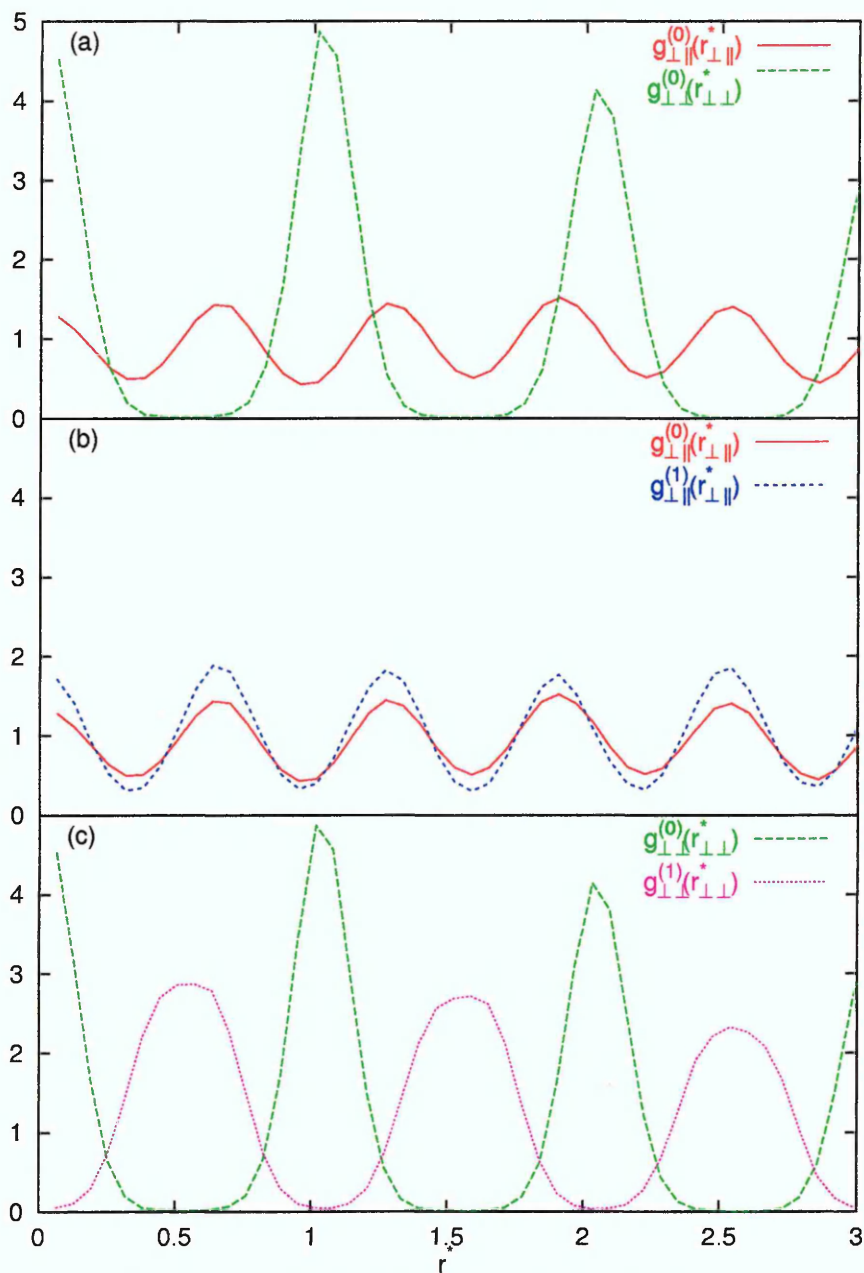
243

Figure 7.19: Radial distribution functions (a) resolved within the layer parallel, $g_{\perp\|}^{(0)}(r_{\perp\|}^*)$, and perpendicular, $g_{\perp\perp}^{(0)}(r_{\perp\perp}^*)$, to the direction of tilt and between adjacent layers resolved (b) parallel to the direction of tilt and (c) perpendicular to the direction of tilt for 4:1 molecules at $Q^* = 0.60$, $T^* = 1.50$ and $P^* = 2.00$.

occurs over the same pressure range as was observed for $Q^* = 0.60$, with the density range of the coexistence region being reduced. Upon further compression a second phase transition is observed in the equation of state over the range $0.80 < P^* < 0.85$, with a corresponding increase in the nematic order parameter also being observed. It is worth noting that this transition occurs at a lower pressure and density than the nematic to smectic A transition observed for the $Q^* = 0.60$ case. Examination of the radial distribution functions shows no evidence of a layered structure being formed, which is surprising since smectic ordering is expected to be observed for phases occuring at densities above the nematic phase. That said, examination of molecular organisation via visualisation techniques (shown in Fig. 7.22(a) for $P^* = 1.50$) suggests a poorly defined layered structure, where some molecules are tilted with respect to a local layer normal, whilst others are not. Thus this phase has a clear smectic character, although the buckled layers make further classification impossible; both the absence of a density wave and a non-uniform direction of molecular though out the simulation box are unexpected observations for a bulk system such as is considered here. An attempt has also been made to quench the system from the nematic phase. Once again liquid-like behaviour is observed in the radial distribution functions (not shown) and visualisation techniques show that a buckled smectic structure is once again formed (Fig. 7.22(b)). Since these simulations have been performed at constant pressure it seems unlikely that this buckled structure arises due to constraints imposed upon the system by the simulation box, however, since periods boundary conditions are being employed, further simulations need to be undertaken to determine any system size effects and temperature dependence that

245

this phenomena may exhibit.

Upon further compression a third phase transition is observed at a higher pressure and range of densities than was observed for $Q^* = 0.60$, with a corresponding increase being observed in the nematic order parameter, and a slight increase in the biaxial order parameter. The orientation of the average director and the layer normal are also not coincident, indicating the formation of a tilted phase, although both the average tilt angle and biaxial order parameter are considerably less than were observed for $Q^* = 0.60$. Examination of the radial distribution functions, once again, shows no evidence of a layered system being formed (Fig. 7.20), however long range translational order is observed in the perpendicular component (Fig. 7.21), although these profiles display a poorly defined *double-peak* structure which is typically ascribed to a hexatic phase. Examination of the molecular organisation with visualisation techniques (shown in Fig. 7.23(a) for $P^* = 2.00$) shows that a buckled hexatic phase is being formed, where the layers are buckled perpendicular to the direction of molecular tilt. This behaviour seems likely to occur due presence of two minima in the attractive well depth in the side-by-side configuration, resulting in the parallel staggered configuration becoming the energetically most favourable for interactions which have components perpendicular to the direction of tilt (i.e. along the r_2 direction defined in Fig. 7.12(a)). As with the smectic phase preceding this hexatic phase, an attempt has been made to quench the system from the nematic phase. Unlike the case considered previously, a buckled structure is not observed here (shown in Fig. 7.23(b)), with the radial distribution functions (not shown) being used to classify this phase as smectic J.
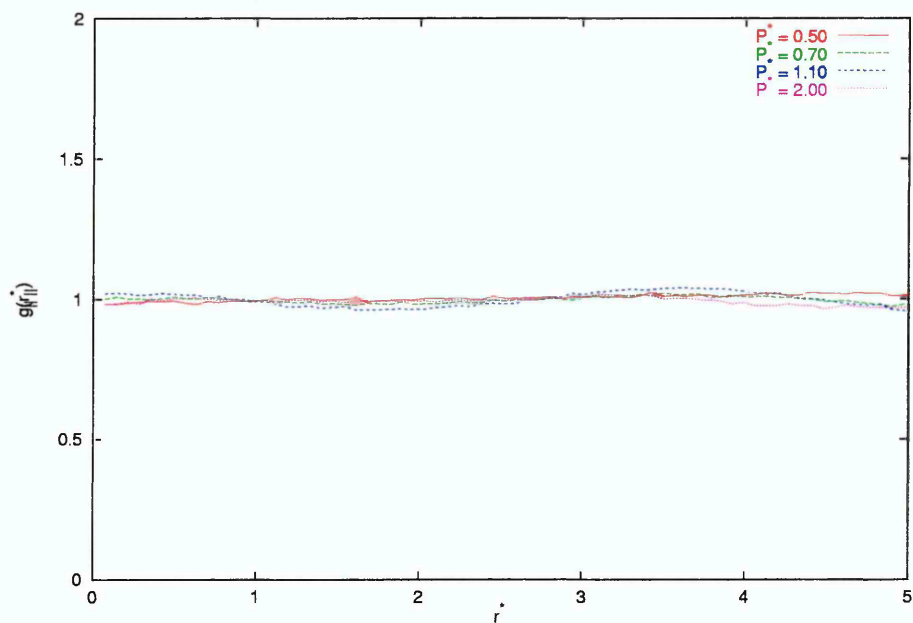
Figure 7.20: Radial distribution function resolved parallel to the layer normal for 4:1 molecules at $Q^* = 0.80$ and $T^* = 1.50$.
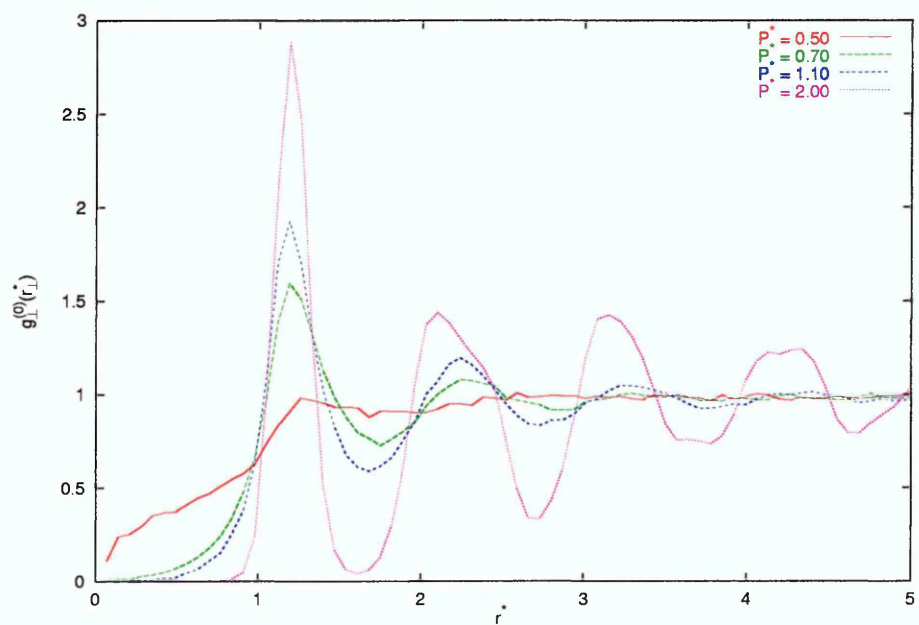

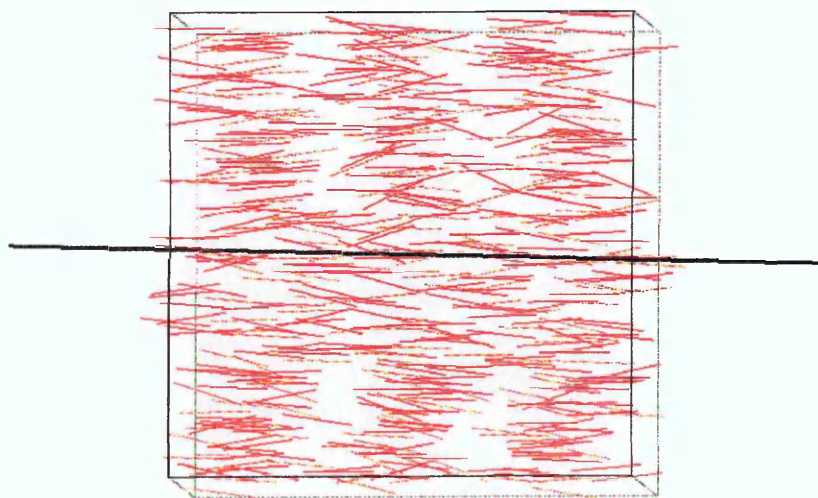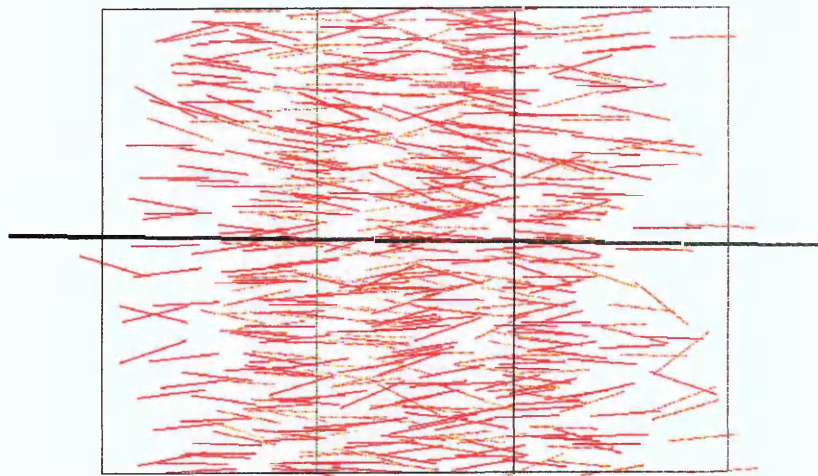Figure 7.21: Radial distribution function resolved perpendicular to the layer normal for 4:1 molecules at $Q^* = 0.80$ and $T^* = 1.50$.

Figure 7.22: Typical configurations for $\delta = 30$ and $Q^* = 0.80$ at $T^* = 1.50$ and $P^* = 1.50$ obtained (a) during the course of the compression run and (b) quenched from $P^* = 0.60$. The black vector represents the average director $\hat{\mathbf{n}}$.
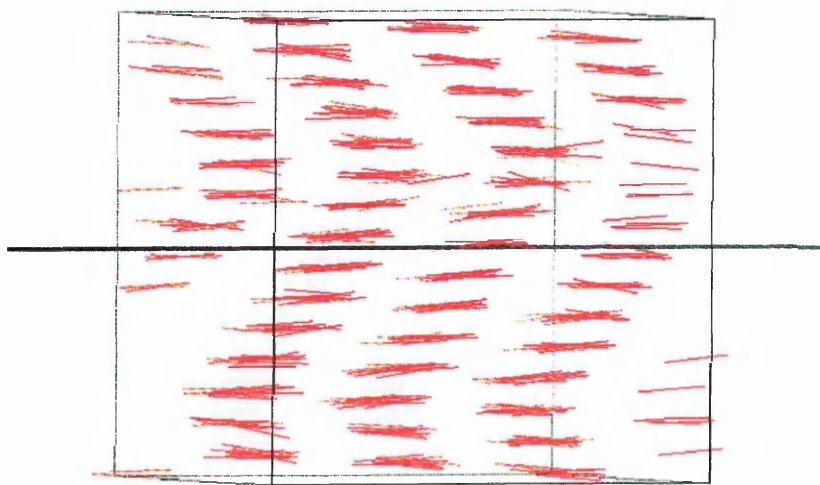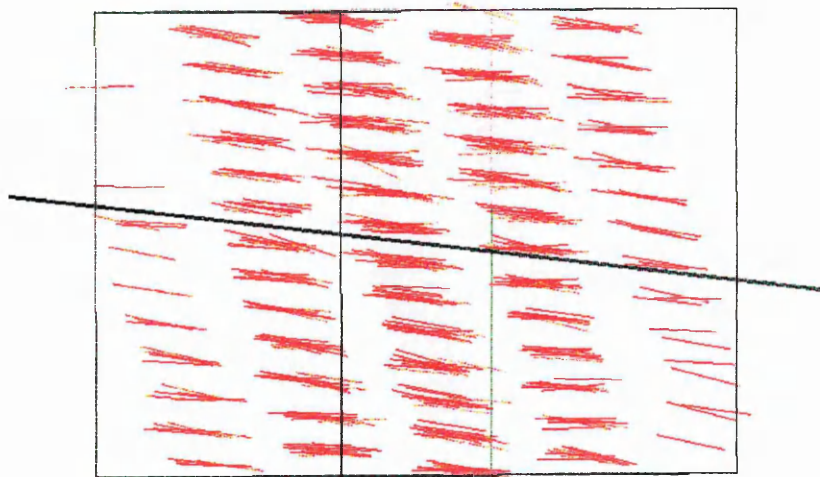
(a)

(b)

(a)

(b)

Figure 7.23: Typical configurations for $\delta = 30$ and $Q^* = 0.80$ at $T^* = 1.50$ and $P^* = 2.00$ obtained (a) during the course of the compression run and (b) quenched from $P^* = 0.60$. The black vector represents the average director $\hat{\mathbf{n}}$.

The reasons as to why an undeformed structure is formed upon quenching the system and why the nematic and first smectic phase are stabilised for this relatively large quadrupole moment are unclear. The effect of finite-size effects should not be overlooked, and further simulations are required to investigate any system size dependence. Rippled smectic layers have been observed previously [98] in constant NPT simulations, with the ripple becoming more marked with a greater wavelength as the temperature is decreased. It would, therefore, also be interesting to investigate the temperature dependence of this phenomenon for this model.

7.4 Conclusions

This chapter has considered the simulation of the biaxial rigid Internally-Rotated Gay-Berne potential with longitudinal linear quadrupoles. The effect upon the phase behaviour of the inclusion of a quadrupole-quadrupole interaction has been studied since theoretical descriptions of the smectic C phase, from the electrostatic interaction category, which rely on dipole-dipole interactions are now not widely accepted and have been succeeded by a number of studies which have focussed upon the effect of electric quadrupole interactions upon the formation of mesophases. The most recent of these studies [39, 40] have have concluded that the inclusion of a quadrupole-quadrupole interaction upon a rod-like molecule of sufficient length will favour the smectic C phase, with onset of smectic ordering being destabilised with increasing quadrupole moment.

The simulations were performed upon systems interacting via the Internally-Rotated Gay-Berne potential plus a longitudinal quadrupole-quadrupole interaction with the stronger ($\epsilon_{ss}/\epsilon_{ee} = 5.0$, $\nu = 2.0$ and $\mu = 1.0$) parameterisation for two different shape anisotropies ($\sigma_{ee}/\sigma_{ss} = 3.0$ and 4.0) at temperatures chosen such that comparison may be made with the phase behaviour already determined in Chapter 5. The effect upon the observed phase behaviour of increasing values of Q^*, the reduced quadrupole moment, was then determined.

Initially, the effect upon the phase behaviour of the shorter 3:1 molecules will be discussed. For $Q^* = 0.20$ the observed sequence of phases was found to be unchanged compared with the standard IRGB potential, with all of the observed phase transitions being shifted to higher pressures and densities, indicating that the inclusion of a small quadrupole moment destabilises all of the orientationally ordered phases. That said, the increased values calculated for the biaxial order parameter and average tilt angle within the tilted smectic J phase for $Q^* = 0.20$ indicates that the inclusion of the quadrupole interaction improves the quality of the tilted structure. Increasing the quadrupole moment to $Q^* = 0.40$ results in the complete destabilisation of the smectic phases, with only the nematic phase being observed. The observation that the isotropic to nematic transition occurs at a lower pressure and density than for $Q^* = 0.20$ may be due to the increased quadrupole moment extending the well depth in the side-by-side configuration such that this configuration becomes move favourable for these biaxial molecules.

For the longer 4:1 molecules, the observed sequence of phases differs from that

observed for the standard IRGB potential for $Q^* = 0.20$ and 0.40, with the smectic G phase being replaced by the smectic J phase. This may be explained by purely intra-layer interactions, since the inclusion of a quadrupole interaction favours the smectic J phase for a perfectly orientated hexagonal unit cell. The coexistence region observed between the isotropic and nematic phases is reduced for $Q^* = 0.20$ (again most probably due to the extension of the well depth in the side-by-side configuration) and occurs at a higher pressure and over a greater density range for $Q^* = 0.40$. The onset of hexatic ordering is suppressed to higher densities in both cases. For $Q^* = 0.60$ the nematic phase is injected into the observed sequence of phases, with the onset of the smectic ordering being observed at a higher density and pressure than was observed for $Q^* = 0.40$. The onset of hexatic ordering is also suppressed further. The biaxial order parameter and average tilt angles calculated within the smectic J phases increases with increasing Q^*, providing further evidence that the inclusion of a quadrupole helps to stabilise the tilted structure.

For $Q^* = 0.80$, the isotropic to nematic and nematic to a buckled smectic phase transitions are stabilised compared with those observed for $Q^* = 0.60$. This observation is surprising since for this quadrupole magnitude, two minima occur in the attractive well in the side-by-side configuration and, as a result, the orientationally ordered phases are expected to be destabilised. Further simulations are required to examine the system size and temperature dependence of this behaviour before definite conclusions may be draw. However, the identification of a buckled smectic structure where some molecules are tilted with respect to a local layer normal is encouraging since it confirms that a tilted smectic structure is being favoured

by the quadrupole component of the potential energy. Indeed, of all the systems considered in this thesis, this observation is the one which most closely resembles the elusive smectic C phase. A buckled hexatic phase is also observed, with the onset of hexatic ordering being suppressed to higher densities than was observed for smaller quadrupole magnitudes. The observation that translationally ordered phases are observed for the 4:1 molecules where no such phases were observed for the 3:1 molecules provides further evidence that increasing molecular elongation does dramatically stabilise mesophase formation.

The absence of an unambiguous smectic C phase here is somewhat disappointing, since a smectic C phase has been observed previously [41] for 4:1 molecules interacting via the Gay-Berne potential and a longitudinal quadrupole, albeit with the weaker well depth parameterisation ($\mu = 2.0$ and $\nu = 1.0$). That said, the smectic C phase, within this previous study, was observed with decreasing quadrupole moment from a previously equilibrated configuration within the nematic phase, and was not found to be accessible simply on cooling from an isotropic configuration. Further simulations of systems interacting via both strong and weak well depth parameterisations for the uniaxial Gay-Berne and biaxial Internally-Rotated Gay-Berne fluids with longitudinal quadrupoles attached are required to allow complete phase diagrams to be constructed, thus allowing a more thorough evaluation of the effect of the quadrupole-quadrupole interaction upon the phase behaviour of these systems to be given.

253

Chapter 8

Conclusions and Future Work

In this chapter, the principal results of this thesis are summarised, and suggestions

for future work are made.

The aim of the work, as specified in Chapter 1, was to use computer simulations

of a modified variant of the Gay-Berne model, to achieve greater understanding of

the mechanism and nature of the molecular tilting within smectic mesophases. An

understanding of this phenomenon is of considerable technological importance since

modern ferroelectric liquid crystal displays are manufactured from such materials. In

particular, we have focussed upon the phase behaviour of a GB model which has been

modified so as to represent a molecule constrained into a rigid *zig-zag* conformation,

the Internally-Rotated Gay-Berne. Subsequently, this has been modified to include

a degree of molecular flexibility and electrostatic interactions.

Since the work has been undertaken for three distinct types of model, each is sum-

marised and suggestions made for future work separately.

8.1 Rigid *Zig-Zag* Shaped Molecule

In Chapter 5 the phase behaviour of systems interacting via both the uniaxial GB and biaxial IRGB potentials were investigated, as a test of the theoretical model proposed by Wulf [42], which assumes that the molecular tilt originates as a result of the packing requirements of *zig-zag* shaped molecules. This has been achieved by constructing approximate phase diagrams for particles with an aspect ratio of 3:1 interacting via the stronger ($\mu = 1.0$ and $\nu = 2.0$) well depth parameterisation, with varying degrees of biaxiality.

It has been shown that the introduction of biaxiality into the intermolecular potential results in the destabilisation of the orientationally ordered phases, since the presence of *zig-zag* shaped molecules are expected to frustrate local packing (an observation which has also be confirmed by a more complicated multi-site model [98]). For particles with a sufficiently pronounced *zig-zag* conformation, the smectic A phase is destabilised completely and the smectic B phase is replaced by the tilted smectic J phase. Whilst the observation that a model which represents a molecule in a *zig-zag* conformation results in the observation of a tilted hexatic phase is encouraging, the absence of the smectic C phase is somewhat disappointing.

The effect of increasing the molecular elongation for the IRGB model was also considered within Chapter 5, since previous studies into the effect of increasing the

elongation of the GB model [87] have shown that this results in the stabilisation of the smectic mesophases. This was also found to be the case here, with the smectic A and smectic G phases replacing the nematic and smectic J phases respectively with an increase in aspect ratio from 3:1 for 4:1. Whilst, once again, no smectic C phase was observed, the observation that the types of tilted hexatic phase formed is dependent upon molecular elongation is an important observation, indicating that the degree of interdigitation and a subtle relationship between the inter- and intra-layer interactions may be controlling factors here.

Examination of the dynamic behaviour of this system has shown that free rotation of the molecules about their molecular long axes is permitted within the nematic and smectic A phases, whereas it is *not* within the tilted hexatic phases. A common criticism of the Wulf model has arisen since it does not allow for free rotation of the molecules within the tilted phases, whilst experimental studies have shown that such rotation does occur [13–15]. Since the form of the IRGB potential is that of the GB potential with the *doughnut* of potential minima rotated about one of the molecular short axes, such that the linear symmetry of the molecule has been broken, the same criticism may be made of this model. Whilst one may argue that free rotation of the individual components of the molecule are permitted, it is only the rotation of the molecule as a whole which is considered by the IRGB model. Thus, it may be concluded, that only tilted phases where free rotation of the molecules is either not permitted or constrained, i.e. tilted hexatic or crystalline solid phases, are accessible using this type of model.

That said, the importance of steric repulsions should not be completely overlooked in future investigations, since the atomistic simulations of Glaser *et al* [101, 102] have shown that the tilted hexatic may be observed for more complicated models which do not consider electrostatic interactions. Whilst atomistic simulations are hoped to eventually provide a complete understanding of the interactions between molecules, they are currently limited, by the available computational power, to the type of molecules which may be modelled and restricted to small system sizes and short time scales.

In terms of future work, the criticism of the basic IRGB model above would indicate that this model is not capable of forming a smectic C phase. That said, modified versions of the model, which have been introduced within this thesis, have shown interesting behaviour, particularly for the particles with an aspect ratio of 4:1, which have been the subject of only a very brief investigation here. It may, therefore, be desirable in the future to determine phase diagrams for differing parameterisations of the IRGB potential than that considered here, which then may be used as reference systems for these modified models, allowing more thorough investigations into these modifications to be undertaken.

8.2 Flexible *Zig-Zag* Shaped Molecule

In Chapter 6 a flexible variant of the IRGB model was introduced, in which the orientation defining the attractive well is linked harmonically to an ideal orientation

with respect to the central core of the molecule. This modification has been introduced since molecules which form mesophases are not rigid structures [6], and such flexibility is considered important since it both promotes reasonably low melting points and is thought to stabilise mesophase structure.

The results presented within Chapter 6 have shown that there are three regimes accessible with varying values of k, the spring constant linking the orientation of the potential well to its ideal orientation. For large values, no flexibility is introduced into the model. Conversely, for small values, the coupling is weak so that the translationally ordered phases are destabilised; either not being observed or suppressed to high densities. For intermediate values of k, a degree of flexibility is introduced into the model, with the translationally ordered mesophase being observed, and it is within this regime that attention was, and should in the future, be focussed.

Simulations performed for particles within this intermediate regime of k, with aspect ratios of 3:1 and 4:1 at a constant temperature, have shown that the nematic and tilted hexatic phases are stabilised by the inclusion of flexibility, whereas the smectic A phase is destabilised. These observations are in agreement with general experimental observations [6, 108], although it should be noted that experimental studies usually consider the temperature dependence, which has not been investigated here. Thus, in terms of future work, the first obvious step would be to examine the effect upon the observed phase behaviour of varying temperature.

Whilst the observations described above are encouraging, criticism of this model may be made since the constraints placed upon the type of flexibility allowed are highly

idealised compared with the complex behaviour which real molecules are expected to exhibit. The observation that the degree of flexibility remains unchanged with increasing density, which results in the destabilisation of the biaxial order parameter within the hexatic phases, is also somewhat worrying since the degree of flexibility is expected to be reduced within these highly ordered phases. This observation appears to arise since no steric hindrance to this type of motion is considered within this model, whereas steric hindrance is expected to be observed within real materials. Unfortunately, the assumptions which have caused this unrealistic behaviour to be observed are inherent in the single-site potential employed. Thus these problems may only be overcome by implementing a more complex flexible multi-site or atomistic model, which will not be able to sample phase space as efficiently as the single-site potential used here.

These criticisms aside, the observation that the results presented here agree with experimentally observed trends means that this model cannot be as easily discounted at the standard IRGB model was. However, since the flexible IRGB potential is a biaxial object it thus falls foul of the criticism that free rotation of the molecules about their long axes is not permitted. Therefore the smectic C phase may also not be expected to be observed using this model, and indeed is not for the brief investigations presented here. That said, systematic investigations into the effect of flexibility upon the GB and IRGB potentials with and without longitudinal quadrupole moments attached are worthy. Since this model has been the subject of a brief, temperature independent, study, definite conclusions as to the validity of this type of model must be deferred until more detailed studies have been performed.

8.3 Rigid Molecules plus a Quadrupole Moment

Within Chapter 7 attention returned to the rigid Internally-Rotated Gay-Berne model, with the effect upon the observed phase behaviour of the inclusion of a longitudinal linear quadrupole interaction being considered. This variant of the IRGB model was implemented since recent theoretical [37–40] and computer simulation [41] studies have shown that the inclusion of a longitudinal quadrupole-quadrupole interaction into linear rod-like objects favours tilted smectic phases, whilst allowing free rotation of the molecules about their long axes. The most recent of these theoretical studies [39, 40] have also shown that the onset of smectic ordering is destabilised with increasing quadrupole moment. Since the IRGB is a biaxial potential, this model has a prefered direction of tilt, with the free rotation of the molecule being energetically more favourable than that of the standard IRGB potential.

Simulations performed for particles with aspect ratios of 3:1 and 4:1 at a constant temperature have shown that the tilted hexatic phase is destabilised, as is expected following Refs. [39, 40]. That said, the observation that the biaxial order parameter and average tilt angle are greater within the tilted hexatic phase for larger quadrupole moments indicates that the inclusion of the quadrupole interaction improves the quality of these tilted structures. The nematic and smectic A phases are variously destabilised and stabilised for different values of the quadrupole moment. This is surprising since only destabilisation of these phases was expected. However, increasing the quadrupole moment results in the extension of the well depth in the side-by-side configuration along the molecular long axis, thus making this

configuration more favourable for these biaxial molecules.

The identification of a buckled smectic structure where some molecules are tilted with respect to a local layer normal for large quadrupole moments for the 4:1 molecules is encouraging since it confirms that a tilted smectic structure is being favoured by the quadrupole component of the potential energy. Of all the systems considered in this thesis, this observation is the one which most closely resembles the elusive smectic C phase. Since these simulations have been performed at constant pressure it seems unlikely that this buckled structure arises due to the constraints imposed upon the system by the simulation box. However, since periodic boundary conditions are being employed, further simulations need to be undertaken to determine any system size effects and temperature dependence that this phenomena may exhibit.

The observation that translationally ordered phases are observed for larger quadrupole moments for the 4:1 molecules where no such phases were observed for the 3:1 molecules provides further evidence that increasing molecular elongation dramatically stabilises mesophase formation. Since no translationally ordered phases were observed for a relatively small quadrupole moment for the 3:1 molecules, it may be concluded that these molecules have insufficient length to provide enough steric hindrance to overcome the destabilising effect of the quadrupole component to the potential energy for the smectic phases to be observed. As a result of this, future investigations should be restricted to the longer molecules.

The absence of an unambiguous smectic C phase here is somewhat disappointing,

since a smectic C phase has been observed in a previous simulations study [41]. That said, the smectic C phase, within this previous study, was observed for a very small range of phase space and only found on discontinuously changing the quadrupole moment. Thus, the most logical progression for this work in the future would be to construct phase diagrams for systems interacting via the Gay-Berne potential with longitudinal quadrupoles attached, initially for the parameterisation used in Ref. [41] for which a smectic C phase is believed to exist. Once the temperature and density dependence of these systems has been determined, they may be used as reference systems to determine whether a *zig-zag* shaped molecule, and the introduction of molecular flexibility helps to stabilise the smectic C phase.

Whatever new studies are conducted in this area, this work has provided a systematic study into the effects that these modifications to the Gay-Berne model have upon the observed phase behaviour. Probably the most encouraging point to be demonstrated by this work is that these systems, even though they can seem highly idealised and are based upon a simple potential, are capable of showing a wide variety of fascinating phenomena. We also note, however, that even using this relatively simple model the long time scales associated with liquid-crystalline behaviour made successful equilibration difficult to achieve. Arguably, the detailed difficulties discussed in this chapter would not, therefore, have been apparent had a significantly more complex model been employed. A cautious, considered approach should, therefore, always be adopted.

Bibliography

[1] F. Reinitzer, *Monatsch Chem.*, **9**, 421 (1888).

[2] O.H. Lehmann, *Physikal Chem.*, **4**, 462 (1889).

[3] L. Gattermann and A. Ritchke, *Ber Deut Chem Ges*, **23**, 1738 (1890).

[4] P.G. de Gennes and J. Prost, *The Physics of Liquid Crystals*, Oxford, Clarendon (1993).

[5] S. Chandrasekhar, *Liquid Crystals*, Cambridge University Press (1992).

[6] P.J. Collings and M. Hird, *Introduction to Liquid Crystals - Chemistry and Physics*, Taylor and Francis (1997).

[7] M.P. Allen and D.J. Tildesley, *Computer Simulation of Liquids*, Oxford, Clarendon (1987).

[8] D. Frenkel and B. Smit, *Understanding Molecular Simulation - From Algorithms to Applications*, Academic Press (1996).

[9] J.G. Gay, B.J. Berne, *J. Chem. Phys*, **74**, 3316 (1981).

[10] S. Chandrasekhar *et al*, *Pramana*, **9**, 471 (1977).

[11] G.W. Gray and J.W. Goodby, *Smectic Liquid Crystals - Textures and Structures*, Leonard Hill (1984).

[12] J. Doucet, A.M. Levelut and M. Lambert, *Mol. Cryst. Liq. Cryst.*, **24**, 317 (1973).

[13] Z. Luz and S. Meiboom, *J. Chem. Phys.*, **59**, 275 (1973).

[14] H. Hervet, F. Volino, A.J. Dianoux and R.E. Lechner, *Phys. Rev. Lett.*, **34**, 451 (1975).

[15] D.J. Photinos, P.J. Bos, M.E. Neubert and J.W. Doane, *Phys. Rev. A*, **23**, 3346 (1981).

[16] R. Bartolino, J. Doucet and G. Durand, *Ann. Phys. Paris*, **3**, 389 (1978).

[17] A. Yoshizawa, H. Kikuzaki and M. Fukumasa, *Liq. Cryst.*, **18**, 351 (1995).

[18] G.W. Gray and J.W. Goodby, *Mol. Cryst. Liq. Cryst.*, **37**, 157 (1976).

[19] J.W. Goodby and G.W. Gray, *Mol. Cryst. Liq. Cryst.*, **48**, 127 (1978).

[20] J.W. Goodby, G.W. Gray and D.G. McDonnell, *Mol. Cryst. Liq. Cryst. Lett.*, **34**, 183 (1977).

[21] R.B. Meyer, L. Liebert, L. Strzelecki and P. Keller, *J. Phys. (Paris) Lett.*, **36**, L69 (1975).

[22] N.A. Clark and S.T. Lagerwall, *Appl. Phys. Lett.*, **36**, 899 (1980).

[23] L. Onsager, *Ann. N.Y. Acad. Sci.*, **51**, 627 (1949).

[24] W. Maier and A.Z. Saupe, *Naturforsch*, **A13**, 564 (1958).

[25] U. Fabbri and C. Zannoni, *Mol. Phys.*, **58**, 763 (1986).

[26] Z.P. Zhang, O.G. Mouritsen and M.J. Zuckermann, *Phys. Rev. Lett.*, **69**, 2803 (1992).

[27] W.L. McMillan, *Phys. Rev. A*, **4**, 1238 (1971).

[28] W.L. McMillan, *Phys. Rev. A*, **6**, 936 (1972).

[29] W.L. McMillan, *Phys. Rev. A*, **8**, 1921 (1973).

[30] R.J. Meyer and W.L. McMillan, *Phys. Rev. A*, **9**, 899 (1974).

[31] D. Cabib and L. Benguigui, *J. Phys. (Paris)*, **38**, 419 (1977).

[32] W.H. de Jeu, *J. Phys. (Paris)*, **38**, 1265 (1977).

[33] B.W. van der Meer and G. Vertogen, *J. Phys. (Paris) Colloq.*, **40**, C3-222 (1979).

[34] W.J.A. Goossens, *J. Phys. (Paris)*, **46**, 1411 (1985).

[35] R.G. Priest, *J. Phys. (Paris)*, **36**, 437 (1975).

[36] R.G. Priest, *J. Chem. Phys.*, **65**, 408 (1976).

[37] W.J.A. Goossens, *Europhys. Lett.*, **3**, 341 (1987).

[38] G. Barbero and G. Durand, *Mol. Cryst. Liq. Cryst.*, **179**, 57 (1990).

[39] A. Poniewierski and T.J. Sluckin, *Mol. Phys.*, **73**, 199 (1991).

[40] E. Velasco, L. Mederos and T.J. Sluckin, *Liq. Cryst.*, **20**, 399 (1996).

[41] M.P. Neal and A.J. Parker, *Chem. Phys. Lett.*, **294**, 277 (1998).

[42] A. Wulf, *Phys. Rev. A*, **11**, 365 (1975).

[43] A.M. Somoza and P. Tarazona, *Phys. Rev. Lett.*, **61**, 2566 (1988).

[44] N. Metropolis, A.W. Rosenbluth, N.M. Rosenbluth, A.H. Teller and E. Teller, *J. Chem. Phys.*, **21**, 1087 (1953).

[45] J.A. Barker and R.O. Watts, *Chem. Phys. Lett.*, **3**, 144 (1969).

[46] H. Goldstein, *Classical Mechanics*, Addison-Wesley (1980).

[47] P.S.Y.Cheung, *Chem. Phys. Lett.*, **40**, 19 (1976).

[48] S.L. Price, A.J. Stone, M. Alderton, *Mol. Phys.*, **52**, 987 (1984).

[49] R.W. Hickney, *Methods Comput. Phys.*, **9**, 136 (1970).

[50] K. Singer, A. Taylor and J.V.L. Singer, *Mol. Phys.*, **33**, 1757 (1977).

[51] D. Fincham, *CCP5 Quaterly*, **8**, 47 (1984).

[52] D.J. Evans, *Mol. Phys.*, **34**, 317 (1977).

[53] D. Fincham, *CCP5 Quaterly*, **2**, 6 (1981).

[54] J.A. Barker, R.A. Fisher and R.O. Watts, *Mol. Phys.*, **21**, 657 (1971).

[55] M.P. Allen, *Liq. Cryst.*, **8**, 499 (1990).

[56] C. Zannoni. in *The Molecular Physics of Liquid Crystals*, G.R. Luckhurst and G.W. Gray editors, chapter 9. Academic Press, 1979.

[57] D. Frenkel and R. Eppenga, *Phys. Rev. Lett.*, **49**, 1089 (1982).

[58] D. Frenkel, B.M. Mulder and J.P. Mctaguq, *Phys. Rev. Lett.*, **52**, 287 (1984).

[59] D. Frenkel and B.M. Mulder, *Mol. Phys.*, **55**, 1171 (1985).

[60] D. Frenkel, *Mol. Phys.*, **60**, 1 (1987).

[61] M.P. Allen and M.R. Wilson, *J. Comp. Aided Mol. Des.*, **3**, 335 (1989).

[62] P.J. Camp and M.P. Allen, *J. Chem. Phys.*, **106**, 6681 (1997).

[63] A. Stroobants, H.N.W. Lekkerkerker and D. Frenkel, *Phys. Rev. Lett*, **57**, 1452 (1986).

[64] D. Frenkel, *J. Chem. Phys.*, **92**, 11 (1988).

[65] J.A.C. Veerman and D. Frenkel, *Phys. Rev. A*, **41**, 3237 (1990).

[66] P. Bolhuis and D. Frenkel, *J. Chem. Phys.*, **106**, 666 (1997).

[67] D. Wei and G.N. Patey, *Phys. Rev. Lett.*, **68**, 2043 (1992).

[68] D. Wei and G.N. Patey, *Phys. Rev. A*, **46**, 7783 (1992).

[69] S.C. McGrother, A. Gil-Villegas and G. Jackson, *J. Phys. Cond. Matt.*, **8**, 9649 (1996).

[70] A. Gil-Villegas, S.C. McGrother and G. Jackson, *Chem. Phys. Lett.*, **269**, 441 (1997).

[71] A. Gil-Villegas, S.C. McGrother and G. Jackson, *Mol. Phys.*, **92**, 723 (1997).

[72] J. Corner, *Roy. Soc. Lond. A*, **192**, 275 (1948).

[73] T. Kihara, *Rev. Mod. Phys.*, **25**, 831 (1953).

[74] S.H. Walmsley, *Chem. Phys. Lett.*, **49**, 320 (1977).

[75] B.J. Berne and P. Pechukas, *J. Chem. Phys*, **56**, 4213 (1972).

[76] J. Kushick and B.J. Berne, *J. Chem. Phys*, **64**, 1362 (1976).

[77] A.J. Stone. in *The Molecular Physics of Liquid Crystals*, G.R. Luckhurst and G.W. Gray editors, chapter 2. Academic Press, 1979.

[78] D.J. Adams, G.R. Luckhurst and R.W. Phippen, *Mol. Phys.*, **61**, 1575 (1987).

[79] G.R. Luckhurst, R.A. Stephens and R.W. Phippen, *Liq. Cryst.*, **8**, 451 (1990).

[80] E. de Miguel, L.F. Rull, M.K. Chalam and K.E. Gubbins, *Mol. Phys.*, **71**, 1223 (1990).

[81] E. de Miguel, L.F. Rull, M.K. Chalam and K.E. Gubbins, *Mol. Phys.*, **72**, 593 (1991).

[82] M.K. Chalam, K.E. Gubbins, E. de Miguel and L.F. Rull, *Mol. Sims*, **7**, 357 (1991).

[83] L.F. Rull, *Physica A*, **220**, 113 (1995).

[84] G.R. Luckhurst and P.S.J. Simmonds, *Mol. Phys.*, **80**, 233 (1993).

[85] R. Berardi, A.P.J. Emerson and C. Zannoni, *J. Chem. Soc. Faraday Trans.*, **89**, 4069 (1993).

[86] E. de Miguel, E. Martin del Rio, J.T. Brown and M.P. Allen, *J. Chem. Phys.*, **105**, 10 (1996).

[87] J.T. Brown, M.P. Allen, E. Martin del Rio and E. de Miguel, *Phys. Rev. E*, **57**, 6685 (1998).

[88] S.J. Mills, C.M. Care, M.P. Neal and D.J. Cleaver, *Phys. Rev. E*, **58**, 3284 (1998).

[89] R. Berardi, C. Fava and C. Zannoni, *Chem. Phys. Lett.*, **236**, 462 (1995).

[90] D.J. Cleaver, C.M. Care, M.P. Allen and M.P. Neal, *Phys. Rev. E*, **54**, 559 (1996).

[91] R. Berardi, C. Fava and C. Zannoni, *Chem. Phys. Lett.*, **297**, 8 (1998).

[92] R. Berardi, S. Orlandi and C. Zannoni, *J. Chem. Soc. Faraday Trans.*, **93**, 1493 (1997).

[93] M.A. Bates and G.R. Luckhurst, *Liq. Cryst.*, **24**, 229 (1998).

[94] K. Satoh, S. Mita and S. Kondo, *Liq. Cryst.*, **20**, 757 (1996).

[95] K. Satoh, S. Mita and S. Kondo, *Chem. Phys. Lett.*, **261**, 357 (1996).

[96] R. Berardi, S. Orlandi and C. Zannoni, *Chem. Phys. Lett.*, **261**, 357 (1996).

[97] M. Houssa, A. Oualid and L.F. Rull, *Mol. Phys.*, **94**, 439 (1998).

[98] M.P. Neal, A.J. Parker and C.M. Care, *Mol. Phys.*, **91**, 603 (1997).

[99] A.G. Petrov and A. Derzhanski, *Mol. Cryst. Liq. Cryst.*, **151**, 303 (1987).

[100] M.R. Wilson, *Structure and Bonding*, **94**, 41 (1998).

[101] M.A. Glaser, R. Malzbender, N.A. Clark and D.M. Walba, *J. Phys. Cond. Matt.*, **6**, A261 (1994).

[102] M.A. Glaser, R. Malzbender, N.A. Clark and D.M. Walba, *Mol. Sims.*, **14**, 343 (1995).

[103] G.R. Luckhurst and B.A. Timini, *Phys. Lett.*, **75A**, 91 (1979).

[104] R.A. Bemrose, C.M. Care, D.J. Cleaver and M.P. Neal, *Mol. Phys.*, **90**, 625 (1997).

[105] E. de Miguel, L.F. Rull and K.E. Gubbins, *Phys. Rev. A*, **45**, 3813 (1992).

[106] B.J. Berne and G.D. Harp, *Adv. Chem. Phys.*, **17**, 63 (1970).

[107] M.D. de Luca. *Molecular Dynamics Simulations of Calamitic and Discotic Liquid Crystals*. PhD thesis, Sheffield Hallam University, 1997.

[108] S.M. Kelly and J. Fünfschilling, *Liq. Cryst.*, **19**, 519 (1995).

[109] A.D. Buckingham, *Adv. Chem. Phys.*, **12**, 107 (1978).

[110] G.W. Gray and K.E. Gubbins, *Theory of Molecular Fluids*, volume 1, Oxford, Clarendon (1984).

[111] S.J. Clark. in *Physical Properties of Liquid Crystals*, volume 1. IEE, 1999.

Appendix A

Derivation of forces and torques

The methods of calculating the explicit forces and torques for systems of linear molecules [47] and multi-site molecules [48] are well understood. These explicit forms are necessary for the simulation of such fluids using the molecular dynamics technique. Within this Appendix, a brief overview of the methods used to arrive at these explicit forms for biaxial molecules, following Price *et al* [48], is given, followed by details of the implementation of these methods to the anisotropic potentials described previously.

271

A.1 Calculation of forces and torques for single-site anisotropic molecules

Consider two single-site biaxial molecules with centre of mass position vectors $\mathbf{r}_i$ for molecule i and $\mathbf{r}_j$ for molecule j, as illustrated in figure A.1.
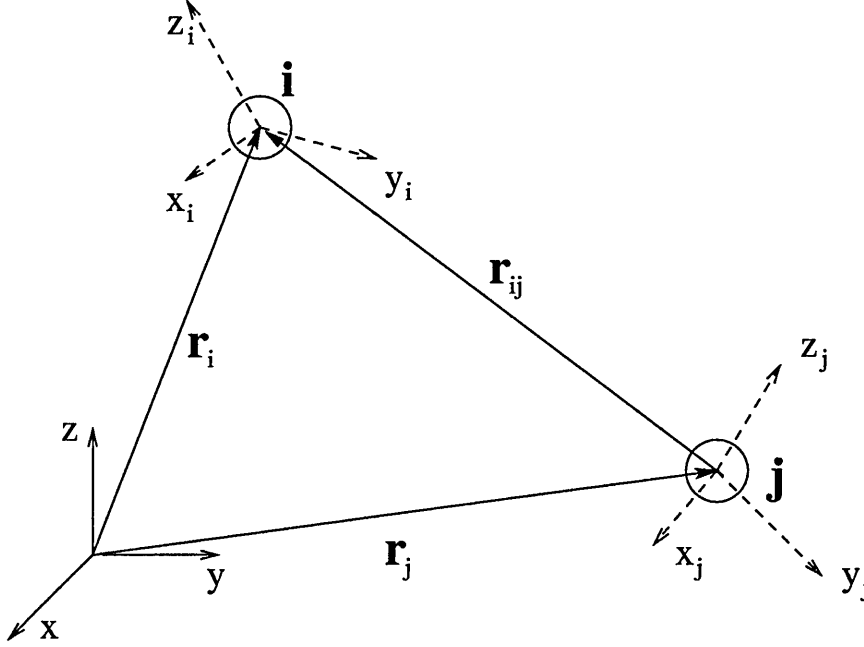

Figure A.1: Representation of interaction between two single-site biaxial molecules

The intermolecular vector $\mathbf{r}_{ij}$ is given by $\mathbf{r}_{ij} = \mathbf{r}_i - \mathbf{r}_j$. The force on the centre of mass of the molecule i is denoted by $\mathbf{F}_i = -\nabla_{\mathbf{r}_{ij}} U_{ij}$. Using the chain rule we obtain,

$$\mathbf{F}_i = -\sum_{\mathbf{r}_{ij}} \frac{\partial U_{ij}}{\partial (\mathbf{s} \cdot \mathbf{r}_{ij})} \nabla_{\mathbf{r}_{ij}} (\mathbf{s} \cdot \mathbf{r}_{ij}) \tag{A.1}$$

in which the notation for the sum indicates that all scalar products involving the intermolecular vector are considered, including $r = (\mathbf{r}_{ij} \cdot \mathbf{r}_{ij})^{1/2}$. Now,

$$\nabla_{r_i}(\mathbf{s}.\mathbf{r}_{ij}) = \mathbf{s}$$

Therefore eqn. A.1 becomes,

$$\mathbf{F}_i = -\sum_{\mathbf{r}_{ij}} \frac{\partial U_{ij}}{\partial(\mathbf{s}.\mathbf{r}_{ij})}\mathbf{s} \qquad \text{(A.2)}$$

The force on molecule j is by necessity the same as that acting upon molecule i except that it acts in the opposite direction.

To evaluate the torque we make use of the fact that the energy is expressed entirely in terms of scalar products s.t of vectors which are either fixed in direction in space or rotating with the molecule. If both are fixed or both are rotating then their scalar product is independent of orientation and does not contribute to the torque, so we need only consider the case where s is fixed in direction in space and t rotates with the molecule. The vectors $\mathbf{x}_i$, $\mathbf{y}_i$ and $\mathbf{z}_i$ describe the orientation of molecule i. The corresponding vectors for molecule j and the intermolecular vector, $\mathbf{r}_{ij}$, are fixed.

If the differential operator which gives the torque is given by $\dot{\mathbf{G}}$, then the torque may be evaluated by invoking the chain rule to give,

$$\tau = \dot{\mathbf{G}}U_{ij} = \sum \frac{\partial U_{ij}}{\partial(\mathbf{s}.\mathbf{t})}\dot{\mathbf{G}}(\mathbf{s}.\mathbf{t}) \qquad \text{(A.3)}$$

273

We therefore now need to evaluate $\dot{\mathbf{G}}(\mathbf{s}.\mathbf{t})$. To do this we write,

$$(\mathbf{s}.\mathbf{t}) = s_\alpha T_{\alpha\beta} t'_\beta$$

where $T_{\alpha\beta}$ is the transformation matrix between space-fixed and molecule-fixed axes, and t'_β is a constant vector in the molecular frame. If $\hat{\mathbf{x}}$, $\hat{\mathbf{y}}$ and $\hat{\mathbf{z}}$ are unit vectors defining the molecular frame, then

$$T = (\hat{\mathbf{x}} \ \ \hat{\mathbf{y}} \ \ \hat{\mathbf{z}})$$

Now a small rotation of the molecule by $\delta\gamma$ about $\hat{\mathbf{z}}$ replaces T with

$$T + \delta T = (\hat{\mathbf{x}} + \hat{\mathbf{y}}\delta\gamma \ \ \hat{\mathbf{y}} - \hat{\mathbf{x}}\delta\gamma \ \ \hat{\mathbf{z}})$$

such that,

$$\frac{\partial T}{\partial \gamma} = (\hat{\mathbf{y}} \ \ -\hat{\mathbf{x}} \ \ 0) = (\hat{\mathbf{z}} \times \hat{\mathbf{x}} \ \ \hat{\mathbf{z}} \times \hat{\mathbf{y}} \ \ \hat{\mathbf{z}} \times \hat{\mathbf{z}})$$

and the z component of the torque in the molecular frame is

$$-\frac{\partial}{\partial \gamma}(\mathbf{s}.\mathbf{t}) = -\mathbf{s}.\hat{\mathbf{z}} \times \mathbf{t} = -s_\alpha \epsilon_{\alpha\beta\gamma} T_{\beta z} t_\gamma$$

Dealing with the other components similarly gives,

$$\dot{\mathbf{G}}'_\delta(\mathbf{s}.\mathbf{t}) = -s_\alpha \epsilon_{\alpha\beta\gamma} T_{\beta\delta} t_\gamma = (\mathbf{s} \times \mathbf{t})_\beta T_{\beta\delta}$$

274

in the molecular frame. Since T is the transformation matrix from the space-fixed frame to the molecular frame, then the torque in the space-fixed frame is

$$\dot{G}(s.t) = (s \times t)$$

and therefore eqn. A.3 becomes,

$$\tau = \sum_{s,t} \frac{\partial U_{ij}}{\partial(s.t)}(s \times t) \tag{A.4}$$

where the notation implies that we sum over all scalar products in which one member, s, is fixed in space while the other, t, rotates with the molecule.

It should be noted that the sum of the torques on molecule i and j need not (and usually will not) equal zero. However, is is necessary, that in the absence of external fields, that the total torque on the system should vanish,

$$\tau_i + \tau_j + \mathbf{r}_i \times \mathbf{F}_i + \mathbf{r}_j \times \mathbf{F}_j = 0 \tag{A.5}$$

We now consider the application of equations A.2 and A.4 to the anisotropic potentials considered previously.

A.2 Application to anisotropic potentials

A.2.1 Internally Rotated Gay-Berne potential

The Internally Rotated Gay-Berne potential may be expressed in the following form,

$$U_{ij}^I = 4\epsilon \left(\frac{a}{r}, \frac{b}{r}, c, \gamma\right) \left(\left(\frac{\sigma_0}{r - \sigma(\frac{\alpha}{r}, \frac{\beta}{r}, \gamma) + \sigma_0}\right)^{12} - \left(\frac{\sigma_0}{r - \sigma(\frac{\alpha}{r}, \frac{\beta}{r}, \gamma) + \sigma_0}\right)^{6}\right)$$

where,

$$\alpha = \mathbf{r}_{ij} \cdot \hat{\mathbf{u}}_i \quad \beta = \mathbf{r}_{ij} \cdot \hat{\mathbf{u}}_j \quad \gamma = \hat{\mathbf{u}}_i \cdot \hat{\mathbf{u}}_j \quad r = (\mathbf{r}_{ij}.\mathbf{r}_{ij})^{1/2}$$

$$a = \mathbf{r}_{ij} \cdot \hat{\mathbf{v}}_i \quad b = \mathbf{r}_{ij} \cdot \hat{\mathbf{v}}_j \quad c = \hat{\mathbf{v}}_i \cdot \hat{\mathbf{v}}_j$$

To obtain an expression for the intermolecular forces, equation A.2 may be used using the relevant scalar products to give,

$$\mathbf{F}_i^I = -\frac{\partial U_{ij}^I}{\partial r}\hat{\mathbf{r}}_{ij} - \frac{\partial U_{ij}^I}{\partial \alpha}\hat{\mathbf{u}}_i - \frac{\partial U_{ij}^I}{\partial \beta}\hat{\mathbf{u}}_j - \frac{\partial U_{ij}^I}{\partial a}\hat{\mathbf{v}}_i - \frac{\partial U_{ij}^I}{\partial b}\hat{\mathbf{v}}_j \tag{A.6}$$

Similarly the torques may be evaluated by the expansion of equation A.4, to give,

$$
\begin{aligned}
\tau_i^I &= \frac{\partial U_{ij}^I}{\partial(\hat{\mathbf{r}}_{ij} \cdot \hat{\mathbf{u}}_i)}\hat{\mathbf{r}}_{ij} \times \hat{\mathbf{u}}_i + \frac{\partial U_{ij}^I}{\partial(\hat{\mathbf{u}}_j \cdot \hat{\mathbf{u}}_i)}\hat{\mathbf{u}}_j \times \hat{\mathbf{u}}_i + \frac{\partial U_{ij}^I}{\partial(\hat{\mathbf{r}}_{ij} \cdot \hat{\mathbf{v}}_i)}\hat{\mathbf{r}}_{ij} \times \hat{\mathbf{v}}_i + \frac{\partial U_{ij}^I}{\partial(\hat{\mathbf{v}}_j \cdot \hat{\mathbf{v}}_i)}\hat{\mathbf{v}}_j \times \hat{\mathbf{v}}_i \\
&= \frac{\partial U_{ij}^I}{\partial \alpha}\mathbf{r}_{ij} \times \hat{\mathbf{u}}_i + \frac{\partial U_{ij}^I}{\partial \gamma}\hat{\mathbf{u}}_j \times \hat{\mathbf{u}}_i + \frac{\partial U_{ij}^I}{\partial a}\mathbf{r}_{ij} \times \hat{\mathbf{v}}_i + \frac{\partial U_{ij}^I}{\partial c}\hat{\mathbf{v}}_j \times \hat{\mathbf{v}}_i \\
&= \hat{\mathbf{u}}_i \times \left(-\frac{\partial U_{ij}^I}{\partial \alpha}\mathbf{r}_{ij} - \frac{\partial U_{ij}^I}{\partial \gamma}\hat{\mathbf{u}}_j\right) + \hat{\mathbf{v}}_i \times \left(-\frac{\partial U_{ij}^I}{\partial a}\mathbf{r}_{ij} - \frac{\partial U_{ij}^I}{\partial c}\hat{\mathbf{v}}_j\right) \tag{A.7}
\end{aligned}
$$

and,

$$\begin{aligned}
\boldsymbol{\tau}_j^I &= \frac{\partial U_{ij}^I}{\partial(\hat{\mathbf{r}}_{ij}\cdot\hat{\mathbf{u}}_j)}\hat{\mathbf{r}}_{ij}\times\hat{\mathbf{u}}_j + \frac{\partial U_{ij}^I}{\partial(\hat{\mathbf{u}}_i\cdot\hat{\mathbf{u}}_j)}\hat{\mathbf{u}}_i\times\hat{\mathbf{u}}_j + \frac{\partial U_{ij}^I}{\partial(\hat{\mathbf{r}}_{ij}\cdot\hat{\mathbf{v}}_j)}\hat{\mathbf{r}}_{ij}\times\hat{\mathbf{v}}_j + \frac{\partial U_{ij}^I}{\partial(\hat{\mathbf{v}}_i\cdot\hat{\mathbf{v}}_j)}\hat{\mathbf{v}}_i\times\hat{\mathbf{v}}_j \\
&= \frac{\partial U_{ij}^I}{\partial\beta}\mathbf{r}_{ij}\times\hat{\mathbf{u}}_j + \frac{\partial U_{ij}^I}{\partial\gamma}\hat{\mathbf{u}}_i\times\hat{\mathbf{u}}_j + \frac{\partial U_{ij}^I}{\partial b}\mathbf{r}_{ij}\times\hat{\mathbf{v}}_j + \frac{\partial U_{ij}^I}{\partial c}\hat{\mathbf{v}}_i\times\hat{\mathbf{v}}_j \\
&= \hat{\mathbf{u}}_j\times\left(-\frac{\partial U_{ij}^I}{\partial\beta}\mathbf{r}_{ij} - \frac{\partial U_{ij}^I}{\partial\gamma}\hat{\mathbf{u}}_i\right) + \hat{\mathbf{v}}_j\times\left(-\frac{\partial U_{ij}^I}{\partial b}\mathbf{r}_{ij} - \frac{\partial U_{ij}^I}{\partial c}\hat{\mathbf{v}}_i\right) \quad\text{(A.8)}
\end{aligned}$$

It is now relatively simple to perform these differentials, and so obtain,

$$\begin{aligned}
\frac{\partial U_{ij}^I}{\partial r} &= \frac{4\epsilon\mu}{\epsilon_2}\left(\left(\frac{\sigma_0}{r-\sigma+\sigma_0}\right)^{12} - \left(\frac{\sigma_0}{r-\sigma+\sigma_0}\right)^6\right)\frac{\chi'}{r^3}\left(\frac{(a+b)^2}{1+\chi'c} + \frac{(a-b)^2}{1-\chi'c}\right) \\
&\quad -4\epsilon\left(12\left(\frac{\sigma_0}{r-\sigma+\sigma_0}\right)^{13} - 6\left(\frac{\sigma_0}{r-\sigma+\sigma_0}\right)^7\right) \\
&\quad \left(\frac{1}{\sigma_0} + \frac{\sigma^3\chi}{2\sigma_0^3 r^3}\left(\frac{(\alpha+\beta)^2}{1+\chi\gamma} + \frac{(\alpha-\beta)^2}{1-\chi\gamma}\right)\right) \quad\text{(A.9)}
\end{aligned}$$

$$\begin{aligned}
\frac{\partial U_{ij}^I}{\partial\alpha} &= 2\epsilon\left(12\left(\frac{\sigma_0}{r-\sigma+\sigma_0}\right)^{13} - 6\left(\frac{\sigma_0}{r-\sigma+\sigma_0}\right)^7\right) \\
&\quad \frac{\sigma^3\chi}{\sigma_0^3 r^2}\left(\frac{\alpha+\beta}{1+\chi\gamma} + \frac{\alpha-\beta}{1-\chi\gamma}\right) \quad\text{(A.10)}
\end{aligned}$$

$$\begin{aligned}
\frac{\partial U_{ij}^I}{\partial\beta} &= 2\epsilon\left(12\left(\frac{\sigma_0}{r-\sigma+\sigma_0}\right)^{13} - 6\left(\frac{\sigma_0}{r-\sigma+\sigma_0}\right)^7\right) \\
&\quad \frac{\sigma^3\chi}{\sigma_0^3 r^2}\left(\frac{\alpha+\beta}{1+\chi\gamma} - \frac{\alpha-\beta}{1-\chi\gamma}\right) \quad\text{(A.11)}
\end{aligned}$$

$$\frac{\partial U_{ij}^I}{\partial a} = -\frac{4\epsilon\mu}{\epsilon_2}\left(\left(\frac{\sigma_0}{r-\sigma+\sigma_0}\right)^{12} - \left(\frac{\sigma_0}{r-\sigma+\sigma_0}\right)^6\right)$$

277

$$\frac{\chi'}{r^2} \left(\frac{a+b}{1+\chi'c} + \frac{a-b}{1-\chi'c} \right) \tag{A.12}$$

$$\frac{\partial U_{ij}^I}{\partial b} = -\frac{4\epsilon\mu}{\epsilon_2} \left(\left(\frac{\sigma_0}{r-\sigma+\sigma_0} \right)^{12} - \left(\frac{\sigma_0}{r-\sigma+\sigma_0} \right)^6 \right)$$

$$\frac{\chi'}{r^2} \left(\frac{a+b}{1+\chi'c} - \frac{a-b}{1-\chi'c} \right) \tag{A.13}$$

$$\frac{\partial U_{ij}^I}{\partial \gamma} = 4 \left(\left(\frac{\sigma_0}{r-\sigma+\sigma_0} \right)^{12} - \left(\frac{\sigma_0}{r-\sigma+\sigma_0} \right)^6 \right) \epsilon\nu\epsilon_1^2\chi^2\gamma$$

$$-\epsilon \left(12 \left(\frac{\sigma_0}{r-\sigma+\sigma_0} \right)^{13} - 6 \left(\frac{\sigma_0}{r-\sigma+\sigma_0} \right)^7 \right)$$

$$\frac{\sigma^3\chi^2}{\sigma_0^3 r^2} \left(\left(\frac{\alpha+\beta}{1+\chi\gamma} \right)^2 - \left(\frac{\alpha-\beta}{1-\chi\gamma} \right)^2 \right) \tag{A.14}$$

$$\frac{\partial U_{ij}^I}{\partial c} = \frac{2\epsilon\mu}{\epsilon_2} \left(\left(\frac{\sigma_0}{r-\sigma+\sigma_0} \right)^{12} - \left(\frac{\sigma_0}{r-\sigma+\sigma_0} \right)^6 \right)$$

$$\frac{\chi'^2}{r^2} \left(\left(\frac{a+b}{1+\chi'c} \right)^2 - \left(\frac{a-b}{1-\chi'c} \right)^2 \right) \tag{A.15}$$

A.2.2 Shifted Internally Rotated Gay-Berne potential

The potential energy may be shifted at a spherical cut-off distance, r_c, such that the potential at the cut-off is equal to zero, thus eliminating a discontinuity in the potential energy due to truncation. For the Shifted Internally Rotated Gay-Berne the potential this shift is expressed as,

$$U_{ij}^{SI} = U_{ij}^I - U_{ij}^C$$

where,

$$U_{ij}^C = U_{ij}^I \big|_{r=r_c}$$

$$= 4\epsilon\left(\frac{a}{r}, \frac{b}{r}, c, \gamma\right)\left(\left(\frac{\sigma_0}{r_c - \sigma(\frac{\alpha}{r}, \frac{\beta}{r}, \gamma) + \sigma_0}\right)^{12} - \left(\frac{\sigma_0}{r_c - \sigma(\frac{\alpha}{r}, \frac{\beta}{r}, \gamma) + \sigma_0}\right)^{6}\right)$$

It should be noted that, due to the notation used within this appendix, ϵ and σ remain functions of r. This is due to these functions being defined [9] as dependent upon scalar products of the form $\hat{\mathbf{r}}_{ij} \cdot \hat{\mathbf{u}}_i$, etc, not $\mathbf{r}_{ij} \cdot \hat{\mathbf{u}}_i$, etc. Therefore the r dependence within ϵ and σ is used to normalise α, etc, such that,

$$\hat{\mathbf{r}}_{ij} \cdot \hat{\mathbf{u}}_i = \frac{\mathbf{r}_{ij} \cdot \hat{\mathbf{u}}_i}{r} = \frac{\alpha}{r} \neq \frac{\mathbf{r}_{ij} \cdot \hat{\mathbf{u}}_i}{r_c}$$

Since this potential is anisotropic in form, the potential energy at the cut-off distance is not constant, but is dependent upon α, β and γ. Therefore the effect of this shift upon the forces and torques must be evaluated.

To evaluate the force we once again turn to equation A.2,

$$\mathbf{F}_i^{SI} = -\sum_{\mathbf{r}_{ij}} \frac{\partial(U_{ij}^I - U_{ij}^C)}{\partial(\mathbf{s} \cdot \mathbf{r}_{ij})}\mathbf{s}$$

$$= -\sum_{\mathbf{r}_{ij}} \frac{\partial U_{ij}^I}{\partial(\mathbf{s} \cdot \mathbf{r}_{ij})}\mathbf{s} + \sum_{\mathbf{r}_{ij}} \frac{\partial U_{ij}^C}{\partial(\mathbf{s} \cdot \mathbf{r}_{ij})}\mathbf{s}$$

$$= \mathbf{F}_i^I - \mathbf{F}_i^C \tag{A.16}$$

where $\mathbf{F}_i^I$ has been evaluated in Section A.2.1. This leaves $\mathbf{F}_i^C$, which may be evaluated by invoking the summation process to give,

$$\mathbf{F}_i^C = -\frac{\partial U_{ij}^C}{\partial r}\hat{\mathbf{r}}_{ij} - \frac{\partial U_{ij}^C}{\partial \alpha}\hat{\mathbf{u}}_i - \frac{\partial U_{ij}^C}{\partial \beta}\hat{\mathbf{u}}_j - \frac{\partial U_{ij}^C}{\partial a}\hat{\mathbf{v}}_i - \frac{\partial U_{ij}^C}{\partial b}\hat{\mathbf{v}}_j \qquad \text{(A.17)}$$

Similar arguments may be used to evaluate the torque, which yields,

$$\tau_i^{SI} = \tau_i^I - \tau_i^C \qquad \text{(A.18)}$$

and,

$$\tau_j^{SI} = \tau_j^I - \tau_j^C \qquad \text{(A.19)}$$

where,

$$\tau_i^I = \hat{\mathbf{u}}_i \times \left(-\frac{\partial U_{ij}^C}{\partial \alpha}\mathbf{r}_{ij} - \frac{\partial U_{ij}^C}{\partial \gamma}\hat{\mathbf{u}}_j \right) + \hat{\mathbf{v}}_i \times \left(-\frac{\partial U_{ij}^C}{\partial a}\mathbf{r}_{ij} - \frac{\partial U_{ij}^C}{\partial c}\hat{\mathbf{v}}_j \right) \quad \text{(A.20)}$$

$$\tau_j^I = \hat{\mathbf{u}}_j \times \left(-\frac{\partial U_{ij}^C}{\partial \beta}\mathbf{r}_{ij} - \frac{\partial U_{ij}^C}{\partial \gamma}\hat{\mathbf{u}}_i \right) + \hat{\mathbf{v}}_j \times \left(-\frac{\partial U_{ij}^C}{\partial b}\mathbf{r}_{ij} - \frac{\partial U_{ij}^C}{\partial c}\hat{\mathbf{v}}_i \right) \quad \text{(A.21)}$$

Evaluation of these derivatives gives the following results,

$$\frac{\partial U_{ij}^C}{\partial r} = \frac{4\epsilon\mu}{\epsilon_2}\left(\left(\frac{\sigma_0}{r_c-\sigma+\sigma_0}\right)^{12} - \left(\frac{\sigma_0}{r_c-\sigma+\sigma_0}\right)^6\right)\frac{\chi'}{r^3}\left(\frac{(a+b)^2}{1+\chi'c} + \frac{(a-b)^2}{1-\chi'c}\right)$$

$$-4\epsilon\left(12\left(\frac{\sigma_0}{r_c-\sigma+\sigma_0}\right)^{13} - 6\left(\frac{\sigma_0}{r_c-\sigma+\sigma_0}\right)^7\right)$$

$$\frac{\sigma^3\chi}{2\sigma_0^3 r^3}\left(\frac{(\alpha+\beta)^2}{1+\chi\gamma} + \frac{(\alpha-\beta)^2}{1-\chi\gamma}\right) \tag{A.22}$$

$$\frac{\partial U_{ij}^C}{\partial\alpha} = 2\epsilon\left(12\left(\frac{\sigma_0}{r_c-\sigma+\sigma_0}\right)^{13} - 6\left(\frac{\sigma_0}{r_c-\sigma+\sigma_0}\right)^7\right)$$

$$\frac{\sigma^3\chi}{\sigma_0^3 r^2}\left(\frac{\alpha+\beta}{1+\chi\gamma} + \frac{\alpha-\beta}{1-\chi\gamma}\right) \tag{A.23}$$

$$\frac{\partial U_{ij}^C}{\partial\beta} = 2\epsilon\left(12\left(\frac{\sigma_0}{r_c-\sigma+\sigma_0}\right)^{13} - 6\left(\frac{\sigma_0}{r_c-\sigma+\sigma_0}\right)^7\right)$$

$$\frac{\sigma^3\chi}{\sigma_0^3 r^2}\left(\frac{\alpha+\beta}{1+\chi\gamma} - \frac{\alpha-\beta}{1-\chi\gamma}\right) \tag{A.24}$$

$$\frac{\partial U_{ij}^C}{\partial a} = -\frac{4\epsilon\mu}{\epsilon_2}\left(\left(\frac{\sigma_0}{r_c-\sigma+\sigma_0}\right)^{12} - \left(\frac{\sigma_0}{r_c-\sigma+\sigma_0}\right)^6\right)$$

$$\frac{\chi'}{r^2}\left(\frac{a+b}{1+\chi'c} + \frac{a-b}{1-\chi'c}\right) \tag{A.25}$$

$$\frac{\partial U_{ij}^C}{\partial b} = -\frac{4\epsilon\mu}{\epsilon_2}\left(\left(\frac{\sigma_0}{r_c-\sigma+\sigma_0}\right)^{12} - \left(\frac{\sigma_0}{r_c-\sigma+\sigma_0}\right)^6\right)$$

$$\frac{\chi'}{r^2}\left(\frac{a+b}{1+\chi'c} - \frac{a-b}{1-\chi'c}\right) \tag{A.26}$$

$$\frac{\partial U_{ij}^C}{\partial\gamma} = 4\left(\left(\frac{\sigma_0}{r_c-\sigma+\sigma_0}\right)^{12} - \left(\frac{\sigma_0}{r_c-\sigma+\sigma_0}\right)^6\right)\epsilon\nu\epsilon_1^2\chi^2\gamma$$

$$-\epsilon\left(12\left(\frac{\sigma_0}{r_c-\sigma+\sigma_0}\right)^{13} - 6\left(\frac{\sigma_0}{r_c-\sigma+\sigma_0}\right)^7\right)$$

$$\frac{\sigma^3 \chi^2}{\sigma_0^3 r^2} \left(\left(\frac{\alpha+\beta}{1+\chi\gamma} \right)^2 - \left(\frac{\alpha-\beta}{1-\chi\gamma} \right)^2 \right) \tag{A.27}$$

$$\frac{\partial U_{ij}^C}{\partial c} = \frac{2\epsilon\mu}{\epsilon_2} \left(\left(\frac{\sigma_0}{r_c - \sigma + \sigma_0} \right)^{12} - \left(\frac{\sigma_0}{r_c - \sigma + \sigma_0} \right)^6 \right)$$

$$\frac{\chi'^2}{r^2} \left(\left(\frac{a+b}{1+\chi'c} \right)^2 - \left(\frac{a-b}{1-\chi'c} \right)^2 \right) \tag{A.28}$$

A.2.3   Flexible Internally Rotated Gay-Berne potential

Within Chapter 6, flexibility is introduced into the model, such that the $\hat{u}_i$ and $\hat{v}_i$ may move with respect to each other. The potential energy per molecule is expressed as,

$$U_i^{FI} = \sum_j U_{ij}^I + k \left[1 - (\hat{v}_i \cdot \hat{v}_0)^2 \right]$$

where k may be considered as a spring constant which links the orientation of $\hat{v}_i$ to its ideal location, $\hat{v}_0$. The notation for the summation indicates that the potential energy of molecule i is given by the sum of all pair potentials within the system (or spherical cut-off), whereas the contribution from the spring need only be considered once for each molecule.

To simulate a bulk system of these flexible molecules using molecular dynamics techniques we consider the interaction of molecules as illustrated in figure A.2.

To evaluate the centre of mass force we return to equation A.2. Since the contribution to the potential energy from the spring term does not include any dependence
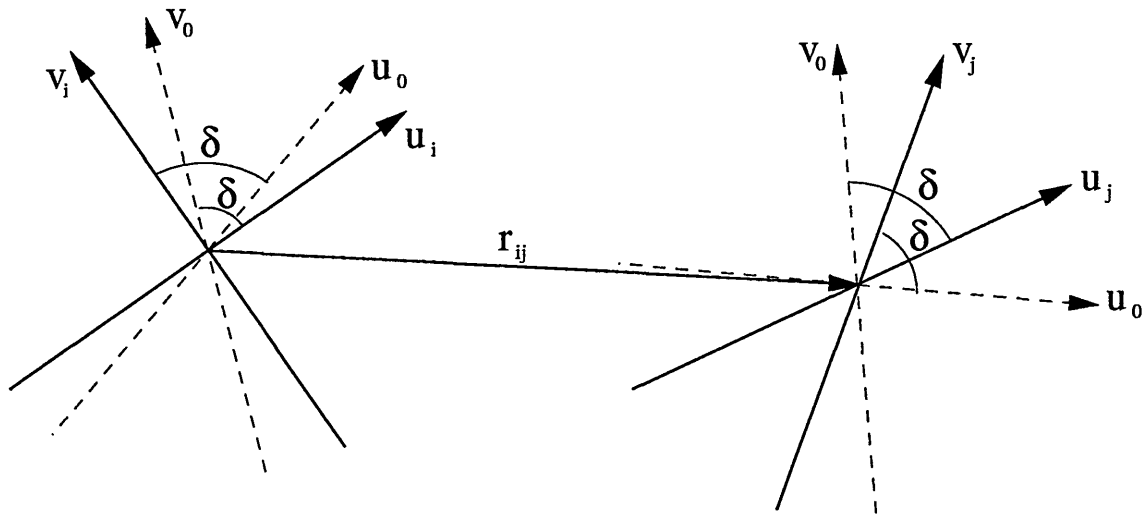
282

Figure A.2: Schematic representation of the interaction between two flexible Internally Rotated Gay-Berne sites

upon r_{ij}, the expansion for the force is identical to that for the rigid molecule (as given by equation A.6).

To evaluate the torque on these molecules, we consider $\hat{u}$ and $\hat{v}$ as separate objects which may rotate independently about the centre of mass of the molecule. To obtain the ideal orientation for both $\hat{u}_i$ and $\hat{v}_i$, we rotate $\hat{u}_i$ about $\hat{u}_i \times \hat{v}_i$ by the ideal shift angle, δ, to obtain $\hat{v}_0$, and $\hat{v}_i$ in the opposite direction to obtain $\hat{u}_0$. Since $\hat{u}_i \cdot \hat{u}_o = \hat{v}_i \cdot \hat{v}_o$, the potential energy contribution from the spring term may be expressed either as a function of $\hat{u}_i \cdot \hat{u}_o$ or $\hat{v}_i \cdot \hat{v}_o$.

Therefore, the torque on molecule i may be evaluated by expanding equation A.4 to give,

$$\begin{aligned}
\tau^I_{u_i} &= \frac{\partial U^{FI}_i}{\partial(\hat{\mathbf{r}}_{ij} \cdot \hat{\mathbf{u}}_i)}\hat{\mathbf{r}}_{ij} \times \hat{\mathbf{u}}_i + \frac{\partial U^{FI}_i}{\partial(\hat{\mathbf{u}}_j \cdot \hat{\mathbf{u}}_i)}\hat{\mathbf{u}}_j \times \hat{\mathbf{u}}_i + \frac{\partial U^{FI}_i}{\partial(\hat{\mathbf{u}}_0 \cdot \hat{\mathbf{u}}_i)}\hat{\mathbf{u}}_0 \times \hat{\mathbf{u}}_i \\
&= \sum_j \left[\frac{\partial U^I_{ij}}{\partial\alpha}\mathbf{r}_{ij} \times \hat{\mathbf{u}}_i + \frac{\partial U^I_{ij}}{\partial\gamma}\hat{\mathbf{u}}_j \times \hat{\mathbf{u}}_i \right] + \frac{\partial U^{FI}_i}{\partial(\hat{\mathbf{u}}_i \cdot \hat{\mathbf{u}}_0)}\hat{\mathbf{u}}_0 \times \hat{\mathbf{u}}_i \\
&= \hat{\mathbf{u}}_i \times \left(\sum_j \left[-\frac{\partial U^I_{ij}}{\partial\alpha}\mathbf{r}_{ij} - \frac{\partial U^I_{ij}}{\partial\gamma}\hat{\mathbf{u}}_j \right] - \frac{\partial U^{FI}_i}{\partial(\hat{\mathbf{u}}_i \cdot \hat{\mathbf{u}}_0)}\hat{\mathbf{u}}_0 \right) \quad\quad \text{(A.29)}
\end{aligned}$$

and,

$$\begin{aligned}
\tau^I_{v_i} &= \frac{\partial U^{FI}_i}{\partial(\hat{\mathbf{r}}_{ij} \cdot \hat{\mathbf{v}}_i)}\hat{\mathbf{r}}_{ij} \times \hat{\mathbf{v}}_i + \frac{\partial U^{FI}_i}{\partial(\hat{\mathbf{v}}_j \cdot \hat{\mathbf{v}}_i)}\hat{\mathbf{v}}_j \times \hat{\mathbf{v}}_i + \frac{\partial U^{FI}_i}{\partial(\hat{\mathbf{v}}_0 \cdot \hat{\mathbf{v}}_i)}\hat{\mathbf{v}}_0 \times \hat{\mathbf{v}}_i \\
&= \sum_j \left[\frac{\partial U^I_{ij}}{\partial a}\mathbf{r}_{ij} \times \hat{\mathbf{v}}_i + \frac{\partial U^I_{ij}}{\partial c}\hat{\mathbf{v}}_j \times \hat{\mathbf{v}}_i \right] + \frac{\partial U^{FI}_i}{\partial(\hat{\mathbf{v}}_i \cdot \hat{\mathbf{v}}_0)}\hat{\mathbf{v}}_0 \times \hat{\mathbf{v}}_i \\
&= \hat{\mathbf{v}}_i \times \left(\sum_j \left[-\frac{\partial U^I_{ij}}{\partial a}\mathbf{r}_{ij} - \frac{\partial U^I_{ij}}{\partial c}\hat{\mathbf{v}}_j \right] - \frac{\partial U^{FI}_i}{\partial(\hat{\mathbf{v}}_i \cdot \hat{\mathbf{v}}_0)}\hat{\mathbf{v}}_0 \right) \quad\quad \text{(A.30)}
\end{aligned}$$

where $\tau^I_{u_i}$ and $\tau^I_{v_i}$ are the torques on $\hat{\mathbf{u}}_i$ and $\hat{\mathbf{v}}_i$ respectively. The derivatives of U^I_{ij} have already been evaluated in section A.2.1. The remaining derivatives may be evaluated to give,

$$\frac{\partial U^{FI}_i}{\partial(\hat{\mathbf{u}}_i \cdot \hat{\mathbf{u}}_0)} = \frac{\partial U^{FI}_i}{\partial(\hat{\mathbf{v}}_i \cdot \hat{\mathbf{v}}_0)} = -2k(\hat{\mathbf{u}}_i \cdot \hat{\mathbf{u}}_0) \quad\quad \text{(A.31)}$$

The shifted form of this potential has been defined within Chapter 6 as,

$$\begin{aligned}
U^{SFI}_i &= \sum_j \left[U^I_{ij} - U^C_{ij} \right] + k\left[1 - (\hat{\mathbf{v}}_i \cdot \hat{\mathbf{v}}_0) \right] \\
&= U^{FI}_i - \sum_j U^C_{ij}
\end{aligned}$$

where,

$$
\begin{aligned}
U_{ij}^{C} &= \left. U_{ij}^{I}\right|_{r=r_c} \\
&= 4\epsilon\left(\frac{a}{r},\frac{b}{r},c,\gamma\right)\left(\left(\frac{\sigma_0}{r_c-\sigma(\frac{\alpha}{r},\frac{\beta}{r},\gamma)+\sigma_0}\right)^{12}-\left(\frac{\sigma_0}{r_c-\sigma(\frac{\alpha}{r},\frac{\beta}{r},\gamma)+\sigma_0}\right)^{6}\right)
\end{aligned}
$$

Since the shifted part of the potential does not include the spring term, the effect of this shift upon the force is identical to that considered in Section A.2.2.

The torques may be evaluated by manipulation of equation A.4 in a similar manner to that described within Section A.2.2, bearing in mind that for the flexible model we are treating the $\hat{u}$ and $\hat{v}$ as separate objects and the torque on each must be calculated independently.